

**Modelling of methane emissions utilising a Lagrangian  
atmospheric dispersion model in combination with Earth  
observation data**

Thesis submitted for the degree of  
Doctor of Philosophy  
at the University of Leicester

by

Laimonas Zubas  
Earth Observation Science Group  
Department of Physics and Astronomy  
University of Leicester

January 2014

© Laimonas Zubas, 31<sup>st</sup> January, 2014

This thesis is copyright material and no quotation from it may be published without proper acknowledgement.

## **Declaration**

I hereby declare that no part of this thesis has been previously submitted to this or any other University as part of the requirement for a higher degree. The work described herein was conducted by the undersigned except for contributions from colleagues as acknowledged in the text.

Laimonas Zubas  
31<sup>st</sup> January, 2014

I would like to dedicate this thesis to my family; Mum and step-Dad Danute and Paul Meek, my Sister Ruta and my Grandparents Aleksas and Genovaite. I could not have done this without your support.

# **Modelling of methane emissions utilising a Lagrangian atmospheric dispersion model in combination with Earth observation data**

**by Laimonas Zubas**

## **Abstract**

Space-borne methane observations provide increased spatial coverage and complement the precise, but sparse network of in-situ measurement sites. In this study, a method has been developed to investigate regional-scale methane budgets using space-borne methane observations, utilising the UK Met Office Numerical Atmospheric Modelling Environment (NAME). Lagrangian atmospheric dispersion models, such as NAME, allow us to investigate fluxes at a lesser computational cost and potentially, a higher spatial resolution.

An inversion algorithm was created and tested on synthetic ground measurement data. The NAME based inversion algorithm was then developed to utilise column CH<sub>4</sub> concentrations, with an intention of applying it to Greenhouse Gases Observing SATellite (GOSAT) observations. A study utilising synthetic GOSAT-like observations was carried out, as well as synthetic inversions quantifying the performance of future methane sensing space-borne missions (CarbonSat and Sentinel-5 Precursor), when used to study fluxes over the British Isles. The results were obtained for 2 months, January and July, 2011. Sentinel-5 Precursor can reduce the flux uncertainty over England by ~30% over England and Wales in July, with the remaining regions (Scotland, Republic of Ireland, Northern Ireland and northern France) achieving a reduction of ~8-14%. In contrast, CarbonSat error reduction values are expected to range from 3% to 18%.

Finally, we used the forward model to relate bottom-up inventories to satellite observations of atmospheric XCH<sub>4</sub> from GOSAT. For selected regions, we have inferred patterns in atmospheric XCH<sub>4</sub> from the spatial distribution of the surface emissions, factoring in the atmospheric transport using an atmospheric dispersion model. The forward model was found to perform poorly over Western Europe ( $r=0.43$ ) and North America ( $r=0.48$ ). The agreement between the observations and simulations of  $r=0.72$  were calculated over South America,  $r=0.60$  over South East Asia and  $r=0.60$  over Australasia.

## ACKNOWLEDGEMENTS

I would like to thank my Ph.D. supervisors: Paul Monks and Hartmut Boesch, who helped me shape my vision for the thesis. My thanks also goes to Rob Parker, for the GOSAT data and support throughout my Ph.D., Zoe Fleming and Alan Hewitt for your help with teaching me how to use NAME. Finally, a shout out to the fellow EOS students - it was a pleasure!

I would also like to thank the following people based at other institutions: Anthony Bloom (University of Edinburgh) for the wetland and rice paddy emission estimates, Anne-Marie (University of Edinburgh) for the GEOSCHEM data and all of the other institutions, whose data was used in the course of the project. A big thanks to Alistair Manning (Met Office) for his insights into inversions and the NAME dispersion model and providing me with the assimilated meteorological data.

I would also like to say a huge thanks to Tomasz Augustynek and Alessio Bortoluzzi for being great housemates over the last few years.

Finally, thanks to National Centre of Earth Observation for providing funding for my Ph.D.

# Contents

<b>1 Methane in the Earth System</b>	<b>1</b>
1.1 Introduction . . . . .	1
1.2 Atmospheric methane and climate change . . . . .	1
1.3 Temporal variability in observed CH <sub>4</sub> concentrations . . . . .	3
1.3.1 Stabilisation of 1999-2007 . . . . .	4
1.3.2 Recent growth (2007-onwards) . . . . .	6
1.4 Sources . . . . .	7
1.4.1 Biogenic . . . . .	7
1.4.2 Thermogenic . . . . .	17
1.4.3 Pyrogenic . . . . .	18
1.4.4 Aerobic formation of CH <sub>4</sub> . . . . .	19
1.5 Sinks . . . . .	20
1.6 Methane and air quality . . . . .	23
1.7 Summary . . . . .	24
<b>2 Atmospheric Measurements and Modelling of Methane</b>	<b>26</b>
2.1 Introduction . . . . .	26
2.2 In situ CH <sub>4</sub> measurements . . . . .	26
2.3 Remote sensing . . . . .	31
2.3.1 Thermal Infrared (TIR) . . . . .	32
2.3.2 Short Wave Infrared (SWIR) . . . . .	36

2.3.3	Active sensing (LIDAR) . . . . .	43
2.4	Bottom-up emission estimation . . . . .	44
2.5	Modelling methane emissions . . . . .	46
2.5.1	Eulerian and Lagrangian models . . . . .	48
2.5.2	Inverse modelling of methane using global models . . . . .	50
2.5.3	Atmospheric modelling using Lagrangian models . . . . .	53
2.5.4	Numerical Atmospheric Modelling Environment (NAME) . . . . .	56
2.6	Summary . . . . .	60
2.7	Thesis Overview . . . . .	61
<b>3</b>	<b>Methods and Data</b>	<b>63</b>
3.1	Aims . . . . .	63
3.2	Methodology - Bayesian inversion framework . . . . .	64
3.3	Formulating the forward model - simulating ground measurements with NAME . . . . .	67
3.3.1	Linking emissions to observations . . . . .	68
3.3.2	Inversion spatial resolution . . . . .	72
3.3.3	Simulated measurement . . . . .	74
3.3.4	Notation . . . . .	76
3.3.5	Inversion and analysis . . . . .	78
3.4	Modelling the satellite measured column with NAME . . . . .	86
3.4.1	Pressure weighting . . . . .	88
3.5	Modifying the inversion system . . . . .	90
3.6	Data used in the study . . . . .	90
3.6.1	Leicester retrieved GOSAT methane XCH <sub>4</sub> . . . . .	91
3.6.2	Emission Inventories . . . . .	93
3.7	Summary . . . . .	97

<b>4</b>	<b>Synthetic inversion of space-borne instrument methane measurements</b>	<b>98</b>
4.1	Aims . . . . .	98
4.2	Simulation setup . . . . .	99
4.3	Initial synthetic inversion results . . . . .	100
4.4	Reducing the number of unknown flux regions . . . . .	102
4.5	Reduced number of grids - results . . . . .	106
4.6	Decreasing the observation density and inversion spatial resolution . . .	106
4.6.1	Application to simulated GOSAT-like instrument measurements	111
4.7	Future CH <sub>4</sub> observing space-borne instruments . . . . .	112
4.7.1	Application to simulated CarbonSat measurements . . . . .	120
4.7.2	Application to Sentinel-5 Precursor measurements . . . . .	122
4.7.3	Suitability of future instruments for inversion studies . . . . .	125
4.8	Conclusion . . . . .	126
<b>5</b>	<b>Application of a forward model to GOSAT data</b>	<b>129</b>
5.1	Introduction . . . . .	129
5.2	Regions to be simulated . . . . .	130
5.3	Combining emission inventories . . . . .	134
5.4	Determining the atmospheric background . . . . .	138
5.5	Simulating satellite XCH <sub>4</sub> observations . . . . .	141
5.6	Results and analysis . . . . .	146
5.6.1	Analysis of inventory contribution to enhancement . . . . .	150
5.6.2	Comparison of GOSAT measurements, simulated observations and the GEOSCHEM model . . . . .	159
5.6.3	Comparison with TCCON sites . . . . .	165
5.7	Conclusion . . . . .	171
<b>6</b>	<b>Conclusion</b>	<b>176</b>
6.1	Future work and potential applications . . . . .	180

# List of Figures

1.1	Main drivers of climate change. The radiative balance between incoming solar shortwave radiation (SWR) and outgoing longwave radiation (OLR) is influenced by the drivers of global climate. (Stocker et al., 2013)	2
1.2	Principal components of the radiative forcing of climate during the industrial era, between the years of 1750 – 2011. Positive forcing leads to warming of climate and negative radiative forcing to a cooling. (Stocker et al., 2013)	3
1.3	Atmospheric concentrations of the three main anthropogenic greenhouse gases for the last 2000 years. Measurements for N <sub>2</sub> O and CH <sub>4</sub> are stated in parts per billion (ppb) and in parts per million (ppm) for CO <sub>2</sub> . (Solomon et al., 2007)	4
1.4	Recent CH <sub>4</sub> concentrations and trends as measured by the NOAA Mauna Loa laboratory in Hawaii (Dlugokencky et al., 1995). Note the units of nmol mol <sup>-1</sup> is equivalent to ppbv.	4
1.5	EDGAR anthropogenic bottom-up methane emission estimates for the year of 2008. Emissions as shown, are in grams, per metre squared, per second (EDGAR, 2009).	9
1.6	Microbiological process of methane production. (Hornibrook, 2005; Whiticar, 1999)	10
1.7	Methane production from wetlands: production, oxidation and pathways of emission. (United States Environmental Protection Agency, 2010)	12
1.8	The effect of temperature on the pathway of CH <sub>4</sub> production (Conrad, 2002)	13
1.9	The biodegradation of organic waste. The timeline of methane and other pollutant production (Agency for Toxic Substances and Disease Registry, 2001).	16

1.10	Contribution of the different regions of the troposphere to the total removal of CH <sub>4</sub> throughout the year calculated from a global CTM (Monks et al., 2009). . . . .	24
2.1	The locations of the stations reporting to the Global Atmosphere Watch Station Information System (GAWSIS) network (Barrie, 2005). . . . .	27
2.2	The left panel shows flight paths of HIPPO missions I and II during January and October - November 2009 respectively. The panels in the centre and on the right show methane concentrations as a function of latitude and pressure measured during southbound and northbound flight paths of HIPPO I and II. Black lines show the aircraft profiles with methane data. Solid contours are interpolated (Wecht et al., 2012). . . . .	30
2.3	Remote sensing of greenhouse gases: active and passive methods. . . . .	32
2.4	Black body emission spectra of the Sun and the Earth. Energy is in relative units, that of the Sun on the left whilst the right side of the diagram displays the energy emitted by the Earth. . . . .	32
2.5	AIRS averaged methane mixing ratio observation for 2011 (NASA, 2013)	35
2.6	The weighting functions for a number of Earth observation instruments. Variations due to different surface types and temperature variations is not shown. GOSAT weighting function is similar to SCIAMACHY and OCO. A-SCOPE (1.6 and 2.0 micron) LIDAR concepts have been proposed for the monitoring of CO <sub>2</sub> from space. The instruments did not, however, pass the ESA selection process (Bron and Ciaï, 2010). . . . .	37
2.7	Global and seasonal maps of SCIAMACHY measured atmospheric CH <sub>4</sub> concentrations. The red curve is a smoothed time series (Buchwitz, 2007).	38
2.8	GOSAT observation modes (Hamazaki, 2005). . . . .	39
2.9	The spectral range of the TROPOMI, as well as SCIAMACHY, OMI and GOME instruments. (Veefkind et al., 2012). . . . .	41
2.10	The measurement principle of the TROPOMI instrument onboard Sentinel-5P. All of the ground pixels in the swath are measured simultaneously (Veefkind et al., 2012). . . . .	41
2.11	Map of the operational TCCON sites (as of July, 2014). . . . .	42

2.12	Atmospheric modelling: forward and inverse approaches. An atmospheric transport model provides the link between the emission and the observation of a pollutant. The model must model the atmospheric transport of the pollutant, taking into account atmospheric variables, such as the temperature and wind speed, as well as the chemical processes acting on it. Methane has a relatively long atmospheric lifetime, thus the atmospheric sink can be ignored owing to the short run time of 10 days in this work. . . . .	47
2.13	Lagrangian (a) and Eulerian (b) approaches to modelling flow. . . . .	49
2.14	Modelling with Lagrangian Particle Dispersion Models (LPDMs): source-oriented (left) and receptor-oriented (right) approaches (Lin et al., 2007). . . . .	53
3.1	The geographical location of the Mace Head station. The domain within which dispersion will be simulated, is shown. Fluxes within this region will contribute towards the synthetic measurement at the station. The a priori fluxes used to model the measurements will then be inverted. . . . .	68
3.2	The effect of NAME simulation spatial resolution on the surface topography. The plots show the m (asl) height of the surface as modelled by the LPDM for two different scenarios i.e. model is run with a horizontal resolution of 0.25° (a) and 1° (b). Decreasing the resolution results in lost detail of the model surface, as well as meteorological data . . . . .	70
3.3	The overview of the developed inversion system. . . . .	71
3.4	Mace Head measurement time series and NAME tracer concentration maps for selected measurements. The influence of meteorology on the measurement magnitude is demonstrated (see text for more details). . . . .	73
3.5	A variable resolution grid for which the fluxes are going to be inverted. . . . .	74
3.6	Emissions Database for Global Atmospheric Research (EDGAR) methane flux estimates over the United Kingdom and Ireland for 2005. The units are: tons per 0.1° grid square (EDGAR, 2009). . . . .	75
3.7	EDGAR emission estimates, regridded and converted to $\text{g m}^{-2} \text{ s}^{-1}$ . Europe was divided into 45 regions. The areas distant from the measurement site have decreased resolutions, as the site is most sensitive to the emissions nearest to Mace Head. . . . .	76

3.8	Simulated observations at Mace Head. EDGAR emissions utilised as an a priori are assumed to be constant. The synthetic baseline to which the local methane enhancement is added, is shown in red. . . . .	77
3.9	The a posteriori flux. The random measurement noise is simulated to be $1 \times 10^{-10}$ ppbv. . . . .	79
3.10	The a posteriori flux error. The random measurement noise is simulated to be $1 \times 10^{-10}$ ppbv. . . . .	79
3.11	The a posteriori flux error, as a percentage of the a posteriori flux. The random measurement noise is simulated to be $1 \times 10^{-10}$ ppbv. . . . .	80
3.12	The inverted error as a percentage of the flux. The measurement error is 1 ppbv. . . . .	81
3.13	The inverted error as a percentage of the flux. The measurement error is 2 ppbv. . . . .	82
3.14	The inverted error as a percentage of the flux. The measurement error is 5 ppbv. . . . .	82
3.15	The inverted error as a percentage of the flux. The measurement error is 10 ppbv. . . . .	83
3.16	The inverted error as a percentage of the flux. The measurement error is 20 ppbv. . . . .	83
3.17	The inverted fluxes plotted up against the known a priori fluxes. The measurement errors are: (a) $1 \times 10^{-10}$ ppbv, (b) 1 ppbv, (c) 2 ppbv, (d) 5 ppbv, (e) 10 ppbv and (f) 20 ppbv. . . . .	84
3.18	The error reduction for each individual flux cell for simulated measurement errors of $1 \times 10^{-10}$ (top left), 1 (top right), 2 (centre left), 5 (centre right), 10 (bottom left) and 20 (bottom right) ppbv. Bars in green denote flux magnitudes below $1 \times 10^{-8}$ g m <sup>-2</sup> s <sup>-1</sup> . It is expected that simulated flux reductions are lowest for these grid boxes. . . . .	85
3.19	The combined cell error reduction values as a fraction of the flux magnitude with the simulated measurement errors of (a) 1, 2, 5, 10 and 20 ppbv (b) $1 \times 10^{-10}$ ppbv. . . . .	85

3.20	The wind direction and speeds at different heights in the atmosphere as given by the UK Met Office Unified model. (a) shows the wind vectors at 10 metres above the ground level. (b) the wind directions and velocities at 5000 m a.g.l. Only the x and y components are displayed. The z component (ie. the vertical transport) is not shown. . . . .	87
3.21	The release of tracer particles occurs at discrete pre-defined levels (m agl) within the column. The model is asked to output the pressures ( $p_n$ ) and temperatures ( $t_n$ ), where $n=1\dots N$ is the number of levels. At each level $i$ , there is a corresponding value of the calculated volume mixing ratio given shown as $u_n$ . . . . .	88
3.22	The time series of the GOSAT and GEOSCHEM XCH <sub>4</sub> between August 2009 and July 2010 globally and for the 7 regions outlined on the map (Parker et al., 2011). The error bars and shaded areas represent the standard deviation of the GOSAT and GEOSCHEM data respectively. .	92
3.23	The monthly mean gridded 2° × 2° maps of the (top) GOSAT XCH <sub>4</sub> and (middle) GEOSCHEM XCH <sub>4</sub> for August 2009, September 2009, June 2010 and July 2010 sampled at GOSAT measurement times and locations (Parker et al., 2011). The zonal means between 40°S and 50°N in 5° bins for these months are also shown with error bars (red) and the shaded areas (blue) represent the standard deviation of the GOSAT and GEOSCHEM data respectively. The correlation coefficient ( $r$ ) is also shown. . . . .	92
3.24	EDGAR methane emissions inventory, excluding rice and fire emissions (EDGAR, 2009). . . . .	94
3.25	Wetland and rice paddy emission inventory for the 1st of August, 2009 (Bloom et al., 2012). . . . .	95
3.26	Termite emission inventory used by the modelling system (Fung et al., 1991). . . . .	95
3.27	Aseasonal methane soil absorption (Fung et al., 1991). . . . .	96
3.28	GFED fire emission estimates for September, 2009 (van der Werf et al., 2010). . . . .	96

4.1	(a) GOSAT measurement locations and the number of total measurements in the month of August, 2009. (b) The measurement locations of synthetic measurements to be produced. The total number of simulated measurements is 5084. . . . .	100
4.2	The EDGAR emission inventory utilised to produce the synthetic measurements. This is also used as the a priori in the inversion algorithm. .	101
4.3	The average dilution values over the region of interest. This can be taken as a geographical footprint of the measurement. . . . .	102
4.4	Inversion result with a measurement error of $1 \times 10^{-10}$ ppbv. (a) the inverted flux, (b) the inverted flux error, (c) the error reduction of the inverted flux, assuming a 100% uncertainty in the a priori data, (d) the difference between a known flux value and the inverted flux. . . . .	103
4.5	Inversion result with a measurement error of 1 ppbv. (a) the inverted flux, (b) the inverted flux error, (c) the error reduction of the inverted flux, assuming a 100% uncertainty in the a priori data, (d) the difference between a known flux value and the inverted flux. . . . .	104
4.6	The sea flag, produced utilising the MODIS instrument. The low-emitting boxes over the ocean are combined into a single value, with the exception of high-emitting oil rigs in the North Sea. The islands north of Scotland were manually assigned a water flag, as the a priori emissions for these regions are very low. . . . .	105
4.7	Inversion result (grouped mainland and water boxes) with a measurement error of $1 \times 10^{-10}$ ppbv. (a) the inverted flux, (b) the inverted flux error, (c) the error reduction of the inverted flux, assuming 100% uncertainty in the a priori data and (d) the difference between the known and the inverted flux. . . . .	107
4.8	Inversion result (grouped mainland and water boxes) with a measurement error of 1 ppbv. (a) the inverted flux, (b) the inverted flux error, (c) the error reduction of the inverted flux, assuming 100% uncertainty in the a priori data and (d) the difference between the known and the inverted flux. . . . .	108

4.9	Inversion result (grouped mainland and water boxes) with a measurement error of 5 ppbv. (a) the inverted flux, (b) the inverted flux error, (c) the error reduction of the inverted flux, assuming 100% uncertainty in the a priori data and (d) the difference between the known and the inverted flux. . . . .	109
4.10	Inversion result (grouped mainland and water boxes) with a measurement error of 10 ppbv. (a) the inverted flux, (b) the inverted flux error, (c) the error reduction of the inverted flux, assuming 100% uncertainty in the a priori data and (d) the difference between the known and the inverted flux. . . . .	110
4.11	(a) EDGAR emission inventory gridded to a spatial resolution of 1° and (b) The land sea flag utilised for the inversion at the spatial resolution of 1°. The ocean grid cells are combined to a single average, as is the flux over France. The analysis is concentrated on the the fluxes over the British Isles only. . . . .	111
4.12	The locations and the number of the simulated daily measurements. The inversions were repeated with a decreasing number of simulated measurements. A total of 10 simulations were carried out, ranging from 16 daily measurements over the United Kingdom and Ireland (496 total measurements during August) to 164 measurements (a total of 5084 during August). . . . .	112
4.13	The combined error reduction values for the region, with varying number of simulated measurements and error values of 10, 5 and 1 ppbv. (a) The inversion at the spatial resolution of 0.5° and (b) spatial resolution of 1.0°	113
4.14	The combined error reduction values for the region, with varying number of simulated measurements and error value of $1 \times 10^{-10}$ ppbv. (a) The inversion at the spatial resolution of 0.5° and (b) spatial resolution of 1.0°	113
4.15	The combined cell error reduction values as a fraction of the flux magnitude (measurement errors of 1, 5 and 10 ppbv). The error reduction is greatest at largest fluxes. (a) the inversion at the spatial resolution of 0.5° (b) the inversion at the spatial resolution of 1.0°. The $x$ scale is changed for the spatial resolution of 1.0° inversion due to largest and lowest fluxes decreasing with decreasing resolution. . . . .	114

4.16	The combined cell error reduction values as a fraction of the flux magnitude (measurement error of $1 \times 10^{-10}$ ppbv). The error reduction is greatest at largest fluxes. The inversions at the spatial resolutions of (a) $0.5^\circ$ and (b) $1.0^\circ$ . The $x$ scale is changed for the spatial resolution of $1.0^\circ$ inversion due to the largest and lowest fluxes decreasing with decreasing resolution. . . . .	114
4.17	The simulated XCO <sub>2</sub> retrieval errors from a SWIR-sensing instrument (OCO-2) as a function of SZA and AOD for nadir simulations for the five different surface types (and in turn, albedo) with a surface pressure of 1000 hPa. A similar effect will be observed for CarbonSat and Sentinel-5 Precursor instruments (Boesch et al., 2011). . . . .	116
4.18	The Simulated XCO <sub>2</sub> retrieval errors for a SWIR-sensing instrument (OCO-2) as a function of SZA and AOD for glint simulations for the four different surface types (and in turn, albedo) with a surface pressure of 1,000 hPa. A similar effect will be observed for CarbonSat and Sentinel-5 Precursor instruments (Boesch et al., 2011). . . . .	117
4.19	The reduced errors as a fraction of a number of observations when calculated using Equation 4.3 for (a) CarbonSat, assuming a single observation error of 10 ppbv and (b) Sentinel-5 Precursor, assuming a single observation error of 18 ppbv. . . . .	118
4.20	The combined CH <sub>4</sub> emission inventory for (a) January 2011 and (b) July 2011, used as the a priori to simulate the CarbonSat and Sentinel-5 Precursor observations taken during the month. . . . .	118
4.21	The solar zenith angle at (a) 13:00 UTC 19/01/2011 and (b) 13:00 UTC 19/07/2011. 13:00 is the simulated overpass time for the proposed instruments. . . . .	119
4.22	The cloud cover derived from the NAME meteorological data at (a) 13:00 UTC 19/01/2011 and (b) 13:00 UTC 19/07/2011. 0 represents a cloud-free scene, whilst 8 signifies a scene that is completely covered by clouds. . . . .	119
4.23	CarbonSat simulated orbit with a 12 day repeat cycle. The overpass locations for days 1-12 are shown. . . . .	121

4.24	The number of measurements that would be expected to be obtained by CarbonSat on (a) 19/01/2011 and (b) 19/07/2011. The SZA, cloud cover and the simulated orbit are taken into account. . . . .	122
4.25	The error reduction in uncertainty of CH <sub>4</sub> fluxes achieved over Britain and Ireland utilising CarbonSat measurements on (a) January, 2011 and (b) July, 2011. The calculation assumes a 100% uncertainty in the a priori and that the reduced error decreases by a square root of a number of observations in a grid box. (c) and (d) show the error reduction achieved for the months of January and July, respectively, when Equation 4.3 is used to calculate the reduced error. . . . .	123
4.26	The error reduction in uncertainty of CH <sub>4</sub> fluxes achieved over Britain and Ireland utilising Sentinel-5 Precursor on (a) January, 2011 and (b) July, 2011. The calculation assumes a 100% uncertainty in the a priori and that the reduced error decreases by a square root of a number of observations in a grid box. (c) and (d) show the error reduction achieved for the months of January and July, respectively, when Equation 4.3 is used to calculate the reduced error. . . . .	124
4.27	The number of measurements that would be expected to be obtained by Sentinel-5 Precursor on (a) 19/01/2011 and (b) 19/07/2011. The SZA, cloud cover and the simulated orbit are taken into account. . . . .	125
4.28	The regions for which the total error reduction is calculated. . . . .	127
5.1	The regions of for which simulations are carried out. . . . .	130
5.2	The locations of GOSAT measurements, Western Europe for the time period of 1 <sup>st</sup> - 7 <sup>th</sup> Jun /Jul /Aug /Sep, 2009. . . . .	131
5.3	The locations of GOSAT measurements, South America for the time period of 1 <sup>st</sup> - 7 <sup>th</sup> Jun /Jul /Aug /Sep, 2009. . . . .	131
5.4	The locations of GOSAT measurements, Australasia for the time period of 1 <sup>st</sup> - 7 <sup>th</sup> Jun /Jul /Aug /Sep, 2009. . . . .	131
5.5	The locations of GOSAT measurements, South East Asia for the time period of 1 <sup>st</sup> - 7 <sup>th</sup> Jun /Jul /Aug /Sep, 2009. . . . .	131
5.6	The locations of GOSAT measurements, North America for the time period of 1 <sup>st</sup> - 7 <sup>th</sup> Jun /Jul /Aug /Sep, 2009. . . . .	132

5.7	North America - the mean GOSAT proxy XCH <sub>4</sub> measurements retrieved at Leicester (gridded to 1 degree). . . . .	132
5.8	South America - the mean GOSAT proxy XCH <sub>4</sub> measurements retrieved at Leicester (gridded to 1 degree). . . . .	132
5.9	Western Europe - the mean GOSAT proxy XCH <sub>4</sub> measurements retrieved at Leicester (gridded to 1 degree). . . . .	133
5.10	South East Asia - the mean GOSAT proxy XCH <sub>4</sub> measurements retrieved at Leicester (gridded to 1 degree). . . . .	133
5.11	Australasia - the mean GOSAT proxy XCH <sub>4</sub> measurements retrieved at Leicester (gridded to 1 degree). . . . .	134
5.12	Western Europe - The final combined methane emission inventory. . . .	135
5.13	North America - The final combined methane emission inventory. . . .	135
5.14	South America - The final combined methane emission inventory. . . .	136
5.15	South East Asia - The final combined methane emission inventory. . . .	137
5.16	Australasia - The final combined methane emission inventory. . . . .	137
5.17	(a) GEOSCHEM XCH <sub>4</sub> concentration over Western Europe on 24/07/2009. (b) The GEOSCHEM modelled XCH <sub>4</sub> from the highlighted regions is taken into account when calculating the baseline. (c) NAME outputs the residence time of the particles 10 days prior to reaching the measurement co-ordinate at the border region around the domain of interest. . . . .	140
5.18	An overview of the forward modelling system used to simulate the GOSAT measured XCH <sub>4</sub> . The time and location of the GOSAT measurements are used to produce the NAME inputs. High-resolution, multi-level model output is converted to the dilution matrix and combined with the emission inventories to obtain the enhancement in concentration due to local emission. The emission inventory is different for each release day. The low-resolution NAME output, in conjunction with the GEOSCHEM concentrations, provides the baseline. . . . .	141
5.19	Western Europe - the requested nested NAME output. The low-resolution output (within the white borders) is used for calculating the background, whilst the high-resolution tracer concentration is used to calculate the XCH <sub>4</sub> enhancement due to local emissions. . . . .	143

5.20	North America - the requested nested NAME output. The low-resolution output (within the white borders) is used for calculating the background, whilst the high-resolution tracer concentration is used to calculate the XCH <sub>4</sub> enhancement due to local emissions. . . . .	143
5.21	South America - the requested nested NAME output. The low-resolution output (within the white borders) is used for calculating the background, whilst the high-resolution tracer concentration is used to calculate the XCH <sub>4</sub> enhancement due to local emissions. . . . .	144
5.22	South East Asia - the requested nested NAME output. The low-resolution output (within the white borders) is used for calculating the background, whilst the high-resolution tracer concentration is used to calculate the XCH <sub>4</sub> enhancement due to local emissions. . . . .	145
5.23	Australasia - the requested nested NAME output. The low-resolution output (within the white borders) is used for calculating the background, whilst the high-resolution tracer concentration is used to calculate the XCH <sub>4</sub> enhancement due to local emissions. . . . .	145
5.24	North America - simulated GOSAT measurements. . . . .	146
5.25	South America - simulated GOSAT measurements. . . . .	146
5.26	Western Europe - simulated GOSAT measurements. . . . .	147
5.27	South East Asia - simulated GOSAT measurements. . . . .	147
5.28	Australasia - simulated GOSAT measurements. . . . .	148
5.29	Simulated GOSAT observations compared with actual measurements - 1 <sup>st</sup> to 7 <sup>th</sup> June, 2009. . . . .	151
5.30	Simulated GOSAT observations compared with actual measurements - 1 <sup>st</sup> to 7 <sup>th</sup> July, 2009. . . . .	152
5.31	Simulated GOSAT observations compared with actual measurements - 1 <sup>st</sup> to 7 <sup>th</sup> August, 2009. . . . .	153
5.32	Simulated GOSAT observations compared with actual measurements - 1 <sup>st</sup> to 7 <sup>th</sup> September, 2009. . . . .	154
5.33	North America: GOSAT measurements minus simulated GOSAT measurements. . . . .	155

5.34	South America: GOSAT measurements minus simulated GOSAT measurements. . . . .	155
5.35	Western Europe : GOSAT measurements minus simulated GOSAT measurements. . . . .	156
5.36	South East Asia: GOSAT measurements minus simulated GOSAT measurements. . . . .	156
5.37	Australasia: GOSAT measurements minus simulated GOSAT measurements. . . . .	157
5.38	GOSAT observations vs simulated GOSAT measurements. All four months included in the analysis. . . . .	158
5.39	1 <sup>st</sup> to 7 <sup>th</sup> of June, 2009 - the breakdown of the inventory contributions to the enhanced concentration over the atmospheric background. The ppbv volume enhancement by the different emission inventories is highlighted in different colours. All of the individual measurements for the week are listed here . . . . .	160
5.40	1 <sup>st</sup> to 7 <sup>th</sup> of July, 2009 - the breakdown of the inventory contributions to the enhanced concentration over the atmospheric background. The ppbv volume enhancement by the different emission inventories is highlighted in different colours. All of the individual measurements for the week are listed here . . . . .	161
5.41	1 <sup>st</sup> to 7 <sup>th</sup> of August, 2009 - the breakdown of the inventory contributions to the enhanced concentration over the atmospheric background. The ppbv volume enhancement by the different emission inventories is highlighted in different colours. All of the individual measurements for the week are listed here. . . . .	162
5.42	1 <sup>st</sup> to 7 <sup>th</sup> of September, 2009 - the breakdown of the inventory contributions to the enhanced concentration over the atmospheric background. The ppbv volume enhancement by the different emission inventories is highlighted in different colours. All of the individual measurements for the week are listed here. . . . .	163
5.43	June 1 <sup>st</sup> - 7 <sup>th</sup> , a comparison of the GOSAT measurement with the simulated GOSAT observations and the GEOSCHEM model. . . . .	166
5.44	July 1 <sup>st</sup> - 7 <sup>th</sup> , a comparison of the GOSAT measurement with the simulated GOSAT observations and the GEOSCHEM model. . . . .	167

5.45	August 1 <sup>st</sup> - 7 <sup>th</sup> , a comparison of the GOSAT measurement with the simulated GOSAT observations and the GEOSCHEM model. . . . .	168
5.46	September 1 <sup>st</sup> - 7 <sup>th</sup> , a comparison of the GOSAT measurement with the simulated GOSAT observations and the GEOSCHEM model. . . . .	169
5.47	North America - The time-series of TCCON measurements in the North America region (Parkfalls and Lamont). The actual GOSAT measurements within 2° of the measurement site are overplotted in red and the simulated measurements in blue. . . . .	171
5.48	South East Asia - The time-series of TCCON measurements in the South East Asia region (Tsukuba). The actual GOSAT measurements within 2° of the measurement site are overplotted in red and the simulated measurements in blue. . . . .	172
5.49	Western Europe - The time-series of TCCON measurements in the Western Europe region (Bialystok, Bremen and Garmisch). The actual GOSAT measurements within 2° of the measurement site are overplotted in red and the simulated measurements in blue. . . . .	173
5.50	Australasia - The time-series of TCCON measurements in the Australasia region (Darwin and Wollongong). The actual GOSAT measurements within 2° of the measurement sites are overplotted in red and the simulated measurements in blue. . . . .	174

# List of Tables

1.1	Estimated methane sources and sinks for the time period of 2000-2009, derived using top-down and bottom-up approaches in Tg year <sup>-1</sup> . The ranges of estimates are shown in brackets. (Kirschke et al., 2013) . . . . .	8
2.1	Specifications of TANSO-FTS onboard GOSAT. . . . .	40
3.1	The different model experiments to be carried out in this study and the required technical developments. The work highlighted in red, blue and green is carried out in the current chapter and Chapters 4, 5 respectively.	64
4.1	A list of the current and planned methane sensing space-borne instruments. The instrument footprint characteristics and the corresponding percentage predicted clear-sky fractions are shown. The CarbonSat specifications are still not finalised and are subject to change (Buchwitz et al., 2013; Meijer et al., 2012; Miller et al., 2007). . . . .	115
4.2	The error reduction values achieved for the different regions in the inversion domain. The results are for January and July 2011, utilising two methods for calculating the reduced error of an observation within a single model grid box. . . . .	127
5.1	The percentage contribution of a priori emission inventories to the modelled XCH <sub>4</sub> enhancement over the background. . . . .	164

## LIST OF ABBREVIATIONS

4D-VAR	Four-dimensional variational assimilation
ACOS	Atmospheric CO <sub>2</sub> Observations from Space
ACTM	Atmospheric Chemistry Transport Model
AGAGE	Advanced Global Atmospheric Gases Experiment
AIRS	Aqua-advanced Infrared Radiation Sounder
AMSU	Advanced Microwave Sounding Unit
CAI	Cloud and Aerosol Imager
CARIBIC	Civil Aircraft for the Regular Investigation of the atmosphere based on an Instrument Container
CASA	Carnegie-Ames-Stanford-Approach
CH <sub>4</sub>	Methane
CMS	Carbon Monoxide and Methane Spectrometer
CNES	Centre National dEtudes Spatiales
CO	Carbon Monoxide
CO <sub>2</sub>	Carbon Dioxide
DAOD	Differential Atmospheric Optical Depth
DIAL	Differential Absorption Lidar
DMCM	Dynamic Methanogen-available Carbon Model
DOAS	Differential Optical Absorption Spectroscopy
ECMWF	European Centre for Medium Range Weather Forecasts
EE	Earth Explorer
ESGAR	The Emissions Database for Global Atmospheric Research
ENVISAT	ENVironment SATellite
EnKF	Ensemble Kalman Filter
ESA	European Space Agency
ESRL	Earth System Research Laboratory
EUMETSAT	European Organisation for the Exploitation of Meteorological Satellites
EPH	Equivalent Water Height
FTS	Fourier Transform Spectrometer
GAW	Global Atmosphere Watch
GAWSIS	Global Atmosphere Watch Station Information System

GC-MD	Gas Chromatograph Multidetector
GC-MS	Gas Chromatography with Mass Spectrometry
GEOS	Goddard Earth Observing System
GFED	Global Fire Emissions Database
GHG	Greenhouse Gas
GOSAT	Greenhouse gases Observing SATellite
GWP	Global Warming Potential
H <sub>2</sub>	Hydrogen
H <sub>2</sub> O	Water
HIPPO	HIAPER Pole-to-Pole Observations
HSB	Humidity Sounder for Brazil
IASI	Infrared Atmospheric Sounding Interferometer
IPCC	Intergovernmental Panel on Climate Change
IPDA	Integral-Path Differential-Absorption
IR	Infrared
JAXA	Japan Aerospace Exploration Agency
KIEs	Kinetic Isotope Effects
KNMI	Royal Netherlands Meteorological Institute
LIDAR	a portmanteau of "light" and "radar"
LPDM	Lagrangian Particle Dispersion Model
MERLIN	Methane Remote Sensing Lidar Mission
MODIS	MODderate REsolution Imaging Spectroradiometer
MSU	Microwave Sounding Unit
MTP	Microwave Temperature Profiler
N <sub>2</sub>	Nitrogen
NASA	National Aeronautics and Space Administration
NAME	Numerical Atmospheric Modelling Environment
NCAR	National Center for Atmospheric Research
NCEP	National Centers for Environmental Prediction
NIES	National Institute for Environmental Studies
NIR	Near Infra-Red
NOAA	National Oceanic and Atmospheric Administration

NO <sub>x</sub>	Nitrogen Oxides
NMHC	Non-methane hydrocarbon
NWP	Numerical Weather Prediction
O <sub>2</sub>	Oxygen
O <sub>3</sub>	Ozone
OH	Hydroxyl Radical
OSSE	Observing System Simulation Experiment
PAN	Peroxyacetyl Nitrate
PBL	Planetary Boundary Layer
PANTHER	PAN and other Trace Hydrohalocarbon Experiment
QCLS	Quantum Cascade Laser Spectrometer
RF	Radiative Forcing
SAR	Second Assessment Report
SCIAMACHY	SCanning Imaging Absorption SpectroMeter for Atmospheric Cartography
SF <sub>6</sub>	Sulphur hexafluoride
SOGE	Observation of Halogenated Greenhouse Gases in Europe
SRR	Source Receptor Relationship
SWIR	Short Wave Infra-Red
SZA	Solar Zenith Angle
TANSO	Thermal And Near infrared Sensor for carbon Observations
TAR	Third Assessment Report
TCCON	Total Column Carbon Observing Network
TIR	Thermal Infra-Red
TOVS	TIROS Operational Vertical Sounder
TROPOMI	The TROPOspheric Monitoring Instrument
UNFCCC	United Nations Framework Convention on Climate Change
UOL-FP	University of Leicester Full Physics
USA	United States of America
UV	Ultra Violet
VIS	Visible
VMR	Volume Mixing Ratio

VOC Volatile Organic Compound  
WMO World Meteorological Organization  
XCH<sub>4</sub> Column averaged dry air mole fraction of CH<sub>4</sub>

# Chapter 1

## Methane in the Earth System

### 1.1 Introduction

Methane ( $\text{CH}_4$ ) is the simplest hydrocarbon and the most abundant organic trace gas in the Earth's atmosphere. It is the second most important anthropogenic greenhouse gas after Carbon Dioxide ( $\text{CO}_2$ ) (Solomon et al., 2007). This chapter introduces methane and describes the role that the gas plays in the Earth system. The description includes an overview of historical atmospheric concentration trends and the more recently observed increases. The effect of  $\text{CH}_4$  on global warming and the impact it has on air quality is also discussed, as are the most important  $\text{CH}_4$  sources and sinks. This includes the natural sources, such as wetlands and termites, as well as emissions due to anthropogenic activity, including rice fields, ruminant animals and fossil fuel mining.

### 1.2 Atmospheric methane and climate change

Climate is defined by the IPCC as "the average weather, or more rigorously, as the statistical description in terms of the mean and variability of relevant quantities over a period of time ranging from months to thousands or millions of years" (Stocker et al., 2013). The Earth's climate system is dictated by the state of balance between the incoming solar radiation from the sun and the outgoing radiation (Trenberth and Fasullo, 2012; Trenberth and Stepaniak, 2004). The Earth receives the energy from the sun in the form of UV, visible, and near IR radiation. Of the total amount of shortwave radiation (SWR) the planet is exposed to at the top of the atmosphere, about half is absorbed by the Earth's surface. The rest is reflected back to space by gases and aerosols, clouds and by the

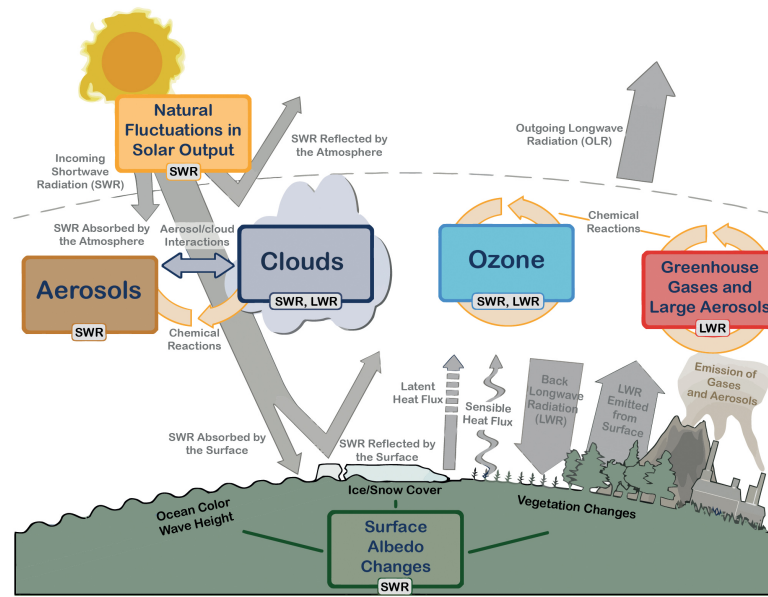


FIGURE 1.1: Main drivers of climate change. The radiative balance between incoming solar shortwave radiation (SWR) and outgoing longwave radiation (OLR) is influenced by the drivers of global climate. (Stocker et al., 2013)

surface. The majority of the outgoing energy from the Earth is in the thermal infrared part of the spectrum, as determined by the local temperature. The longwave radiation (LWR) emitted from the Earth's surface is largely absorbed by atmospheric constituents, such as water vapour, carbon dioxide ( $\text{CO}_2$ ), methane ( $\text{CH}_4$ ), nitrous oxide ( $\text{N}_2\text{O}$ ), other greenhouse gases (GHGs) and clouds, which themselves emit LWR into all directions. The downward directed component of this LWR adds heat to the lower layers of the atmosphere and to the Earth's surface (known as the greenhouse effect, Figure 1.1).

Humans influence the climate by changing the composition of the atmosphere and thus disturbing the Earth's radiative equilibrium. The increase of the concentrations of  $\text{CO}_2$  and other greenhouse gases, have led to a post-2000 imbalance at the top of the atmosphere of  $0.9 \pm 0.5 \text{ Wm}^{-2}$  (Trenberth et al., 2009). This energy imbalance leads to global warming. Humans also affect both the energy and water budget of the planet by changing the land surface. Conversion of forests to cultivated land for example, change the characteristics of vegetation, including its colour, seasonal growth and carbon content. The changes in atmosphere, land, ocean, biosphere and cryosphere can perturb the Earth's radiation budget, producing a radiative forcing (RF) that affects climate. The contributions to radiative forcing from various human activities are shown in Figure 1.2.

$\text{CH}_4$  is the second biggest contributor to the total forcing from 1750 - 2011, after  $\text{CO}_2$ . Although the radiative forcing efficiency of  $\text{CH}_4$  is  $\sim 21$  times that of  $\text{CO}_2$ , the contribu-

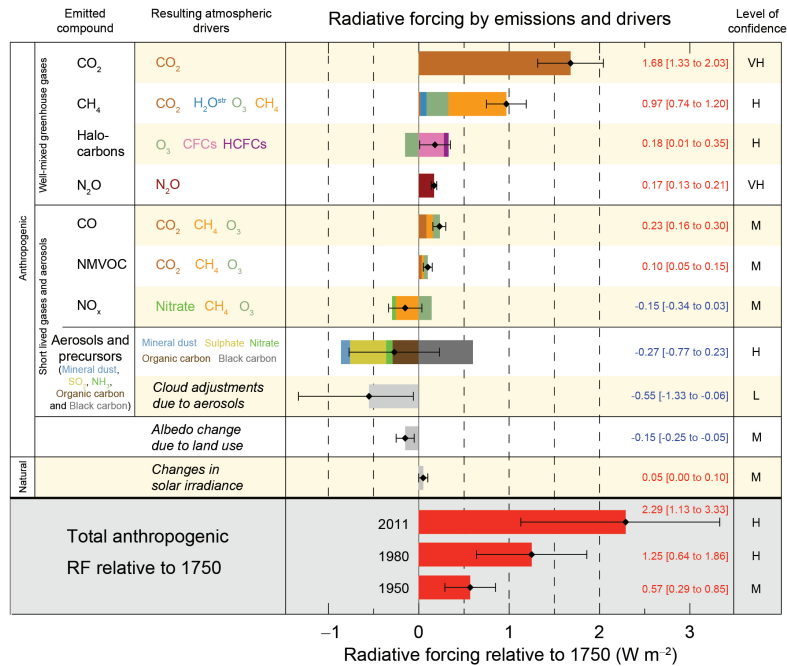


FIGURE 1.2: Principal components of the radiative forcing of climate during the industrial era, between the years of 1750 – 2011. Positive forcing leads to warming of climate and negative radiative forcing to a cooling. (Stocker et al., 2013)

tion towards global warming is limited by the relatively short lifetime of  $\sim 10$  years. The estimated radiative forcing contribution is calculated to be  $+0.48 \text{ Wm}^{-2}$  as in responsible for about 20% of the warming induced by greenhouse gases since pre-industrial times (Kirschke et al., 2013). Four indirect radiative forcing effects of methane have been identified (Rigby et al., 2008): methane is a factor in the amplification of climate change, as the amount released is sensitive to moisture conditions and temperature. Release of methane into the atmosphere causes an increase in global warming, resulting in more CH<sub>4</sub> being released. In effect, a positive-feedback mechanism is established that has contributed to global warming during the last glacial cycle (Brook et al., 2000).

### 1.3 Temporal variability in observed CH<sub>4</sub> concentrations

The atmospheric concentration of CH<sub>4</sub> has varied greatly over the last 650k years, from about 400 ppb during glacial periods to highs of about 700 ppb during inter-glacials (Levine et al., 2011). More recently (last 2000 years), the concentration of methane, along with N<sub>2</sub>O and CO<sub>2</sub>, has remained fairly constant until the onset of the industrial revolution. Since then, the atmospheric concentrations of the three main GHGs have been on a steep rise, despite political attempts at cutting emissions (such as the Kyoto

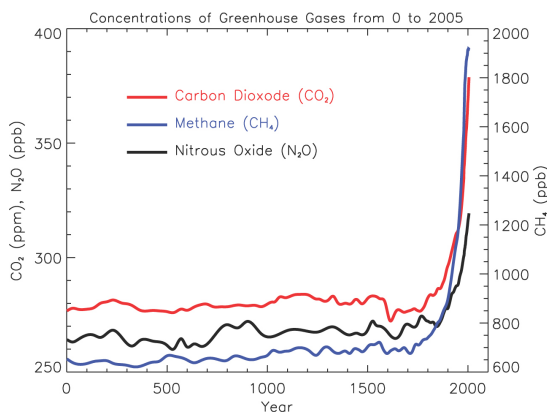


FIGURE 1.3: Atmospheric concentrations of the three main anthropogenic greenhouse gases for the last 2000 years. Measurements for  $\text{N}_2\text{O}$  and  $\text{CH}_4$  are stated in parts per billion (ppb) and in parts per million (ppm) for  $\text{CO}_2$ . (Solomon et al., 2007)

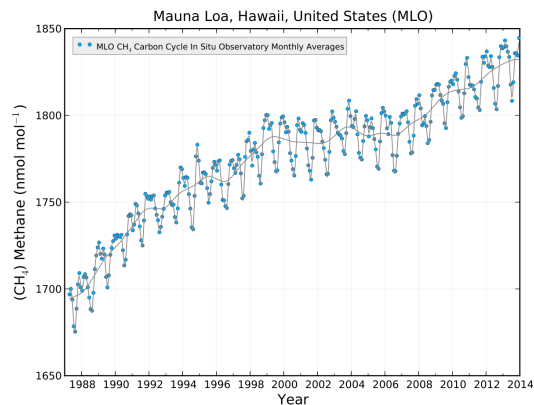


FIGURE 1.4: Recent  $\text{CH}_4$  concentrations and trends as measured by the NOAA Mauna Loa laboratory in Hawaii (Dlugokencky et al., 1995). Note the units of  $\text{nmol mol}^{-1}$  is equivalent to ppbv.

agreement). At  $\sim 1.8$  ppm, the present average measured atmospheric mole fraction is higher than observed throughout the existing ice-core record (Montzka, Dlugokencky and Butler, 2011). The growth rate of atmospheric methane was more than 10% per decade before the 1980s, after which it had dropped (Figure 1.4). This has been interpreted as an approach to a steady state, where emissions were approximately constant (Dlugokencky et al., 2011). A period of stabilisation in atmospheric  $\text{CH}_4$  followed in the time period of 1999 - 2007 and has since increased significantly (Dlugokencky et al., 1995; Rigby et al., 2008).

### 1.3.1 Stabilisation of 1999-2007

The growth rate of the atmospheric methane concentrations reflects the global methane budget, however the variability in atmospheric  $\text{CH}_4$  concentrations is difficult to attribute to sinks or individual sources. One technique used to explain the recent stabilisation of methane concentrations makes use of the fact that most of the source processes have a distinct geographical signature (Heimann, 2011). Emissions from fossil fuels for example, occur in the Northern Hemisphere, causing a north-south concentration gradient that is visible in in situ and space-borne observations. As anthropogenic  $\text{CH}_4$  emissions only change gradually with time, it has been suggested that the dominant factors in the observed year-to-year variability of methane are the fluctuations of the natural sources, particularly wetlands in the tropics and biomass burning emissions (Bousquet

et al., 2011). The emissions of wetlands are sensitive to meteorological conditions, such as dry periods. A possible explanation is that from 1999 onwards, extended droughts have depressed the magnitude of natural methane emissions, which along with a fall in fossil fuel emissions in the 1990s are identified as the main drivers of the global decline in the growth rate of atmospheric methane (Bousquet et al., 2006). Bousquet et al. also suggests that this could in turn result in less methane being broken down by the loss of the hydroxyl radical. The number of vegetation fires would increase in the dry period, releasing large amounts of carbon monoxide (CO). CO also reacts with OH leading to less CH<sub>4</sub> being broken down owing to the loss of the hydroxy radical (Bousquet et al., 2006). The trends in the OH sink magnitude are uncertain in over decadal timescales and could therefore also play a part in the stabilisation of atmospheric CH<sub>4</sub> over the time period of 2000 - 2006 (Montzka et al., 2011).

Emissions from the the fossil fuels in the Northern and Southern hemisphere have also been investigated using ethane (C<sub>2</sub>H<sub>6</sub>) trapped in porous snow-ice as a proxy for methane (Aydin et al., 2011). Ethane, like CH<sub>4</sub> is emitted to the atmosphere during mining, processing, transport and consumption of fossil fuels, during use of biofuels, and during biomass burning. With the help of an atmospheric chemistry model, ethane concentration record can be translated into source strengths, which can then be used to estimate the history of fossil fuel emissions. It was found that the ethane-based fossil-fuel emissions display a steep ramp-up at ~1920 and a sharp decline after 1980, where as the bottom-up methane fossil-fuel emission inventories display a generally increasing trend through the entire twentieth century. Other studies have also used ethane observations to model methane emissions. Simpson et al. (2012) attributed the decreasing ethane observations to decreased venting and flaring of natural gas in oil fields, which is also thought to have significantly contributed to methane's slowing atmospheric growth rate since the mid-1980s.

Monitoring isotopic composition of  $\delta^{13}\text{C}$ ,  $\delta\text{D}$ , and  $\delta^{14}\text{C}$  can also be a powerful tool in determining the sources of methane. Methane released from different sources can be enriched or depleted in  $\delta^{13}\text{C}$ ,  $\delta\text{D}$  relative to ambient background air (Heimann, 2011). CH<sub>4</sub> formed at high temperatures (combustion) is enriched in heavier isotopes, whilst methane produced by biogenic sources is depleted. Emissions from sources, such as wetlands, agriculture and waste management therefore tends to diminish the <sup>13</sup>C/<sup>12</sup>C ratio in the atmospheric methane, whilst fossil fuels and biomass burning (as well as all the methane sinks) induce the <sup>13</sup>CH<sub>4</sub> enrichment (Monteil et al., 2011; Neef et al., 2010). Furthermore, variations in the <sup>2</sup>H/<sup>1</sup>H hydrogen ratio in methane are primarily affected by the changes in the photochemical sink (Heimann, 2011).

Analysis of isotopic information has also been used to try and explain the decadal evolution of the methane budget. Kai et al. (2011) found that the CH<sub>4</sub> growth rates are best explained by reduced microbial sources in the Northern Hemisphere, contradicting the results of Aydin et al. (2011). The authors attribute the decreasing emissions from rice agriculture for some of the observed source reductions in the Northern Hemisphere, as well as improved management of landfills. The study concludes that the observed changes in the interhemispheric difference of  $\delta^{13}\text{C}$  effectively exclude reduced fossil fuel emissions as the primary cause of the slowdown. A paper by Levin et al. (2012) did challenge these results, showing that the experimental data used by Kai et al. are probably biased because the authors used only one continental mountain station (Niwot Ridge, Colorado, USA) as representative of the entire Northern Hemisphere. Data from Antarctica, in combination from two other networks used to estimate long-term trends and the interhemispheric difference (IHD) in methane isotopes, found that the  $\delta^{13}\text{C}$  IHD has been mostly uniform over the last three decades. Kai et al. responded, stating that even when the stabilising emissions from both fossil and microbial sources during 1990 - 2005 are taken into account, the forward biogeochemical modelling analysis of rice agriculture provides evidence that emissions from this sector of the budget declined as a consequence of changes in fertiliser application and water management. The authors of these papers highlight the value of isotope observations in constraining the global methane budget.

### **1.3.2 Recent growth (2007-onwards)**

The methane concentrations in the atmosphere have begun to increase again in 2007. Studies of atmospheric methane concentration gradients, isotopic composition and emissions of proxy pollutants can provide us with clues to the causes of the observed trend. In 2007, CH<sub>4</sub> mixing ratios increased most rapidly at polar northern latitudes and in the Southern Hemisphere, whilst in 2008 methane increased most rapidly in the tropics, with a near zero growth in the Arctic (Montzka, Dlugokencky and Butler, 2011). As mixing ratios increases attributed to anthropogenic emissions tend to be observed in the low-to-mid-latitude Northern Hemisphere, it has been suggested that the rise in emissions from wetlands is the cause (Dlugokencky et al., 2009; Kirschke et al., 2013). The abnormally high temperatures in northern high latitudes and increased rainfall over tropical wetlands during 2008 - 2009 and 2010 - 2011 is likely to have resulted in increased methane emissions.

The hypothesis is further supported by isotopic composition analysis. Methane mea-

sured in Canada in the summer of 2007 was depleted in  $^{13}\text{C}$ , suggesting a natural source in the northern high latitudes (Dlugokencky et al., 2009). Biomass burning is not likely to be a significant contributor to the  $\text{CH}_4$  mixing ratio enhancements during 2007 - 2008, based on the observed levels of carbon monoxide, ethane and  $\text{CH}_3\text{Cl}$  (chemicals co-emitted during biomass burning) in the atmosphere (Dlugokencky et al., 2009).

## 1.4 Sources

A methane source can be classed as being biogenic, thermogenic or pyrogenic. Biogenic sources contain methanogens, methane generating microbes which generate  $\text{CH}_4$  when breaking down organic materials under anaerobic conditions. Examples of biogenic sources are rice fields, wetlands, digestive systems of ruminant animals or landfill sites. Thermogenic methane sources are formed under high pressures and temperatures, deep underground over millions of years. Thermogenic  $\text{CH}_4$  can be leaked into the atmosphere through natural venting or fossil fuel mining. Pyrogenic  $\text{CH}_4$  is formed under incomplete combustion of biomass, fuel and soil carbon during wildfires. The most important emitters of methane from the biogenic, thermogenic and pyrogenic sources are outlined in Sections 1.4.1, 1.4.3, 1.4.2 respectively.

The spatial and temporal variability of individual  $\text{CH}_4$  sources and sinks is still poorly understood and is highly uncertain (Lasey et al., 2011). The total global emissions are estimated using the top-down approach to be 526 - 569 Tg  $\text{CH}_4$  year $^{-1}$ , whilst bottom-up estimates put the emissions in the range of 542 - 852 Tg  $\text{CH}_4$  year $^{-1}$  (Kirschke et al., 2013). The sources are mainly biogenic in nature (more than 70% of the global emission total), although it is also released by industrial processes, such as fossil fuel mining and burning. During the years of 2000 - 2009, anthropogenic sources of  $\text{CH}_4$  account for 50% to 65% of the decadal mean global emissions. Figure 1.5 shows the EDGAR bottom up modelled geographical distribution of anthropogenic  $\text{CH}_4$  emissions (see Table 1.1 for the top-down and bottom-up derived methane budgets).

### 1.4.1 Biogenic

The pathway of biogenic methane production is similar regardless of whether decomposition is occurring within a body of water or a ruminant animal. Methane is produced as a metabolic by-product when complex organic compounds are decomposed by

**CH<sub>4</sub> Budget 2000 – 2009** Units: Tg year<sup>-1</sup>

	<b>Top Down</b>	<b>Bottom-up</b>
<b>NATURAL SOURCES</b>	218 [179-273]	347 [238-484]
Natural wetlands	175 [142-208]	217 [177-284]
Other sources	43 [37-65]	130 [61-200]
Fresh water lakes And rivers		40 [8-73]
Wild animals		15 [15-15]
Wild fires		3 [1-5]
Termites		11 [2-22]
Geological (incl. oceans)		54 [33-75]
Permafrost (excl. lakes and wetland)		6 [2-9]
<b>ANTHROPOGENIC SOURCES</b>	335 [273-409]	331 [304-368]
Agriculture and waste	209 [180-241]	200 [187-224]
Biomass burning (incl. biofuels)	30 [24-45]	35 [32-39]
Fossil fuels	96 [77-123]	96 [85-105]
<b>SINKS</b>		
Soils	32 [36-42]	28 [9-47]
Total chemical loss	518 [510-538]	604 [483-738]
Tropospheric OH		528 [454-617]
Stratospheric loss		51 [16-84]
Tropospheric Cl		25 [13-37]
<b>TOTALS</b>		
Sum of sources	553 [526-569]	678 [542-852]
Sum of sinks	540 [514-560]	632 [592-785]
Imbalance (sources – sinks)	13 [-4-19]	
Atmospheric growth rate	6	

Table 1.1: Estimated methane sources and sinks for the time period of 2000-2009, derived using top-down and bottom-up approaches in Tg year<sup>-1</sup>. The ranges of estimates are shown in brackets. (Kirschke et al., 2013)

methanogens in an anaerobic environment (Figure 1.6). These methanogens are members of archaea, single-celled microorganisms which function similarly to bacteria. Archaea have a distinctive line of evolution alongside the bacteria and the eukarya. There are over 50 described species of archaea capable of producing CH<sub>4</sub>. The process begins with complex polymers being decomposed into simple sugars and amino acids. Bacteria then metabolise these further, producing acetates and H<sub>2</sub> as waste products. Methane fermentation therefore is a sequence of a series of metabolic interactions amongst various

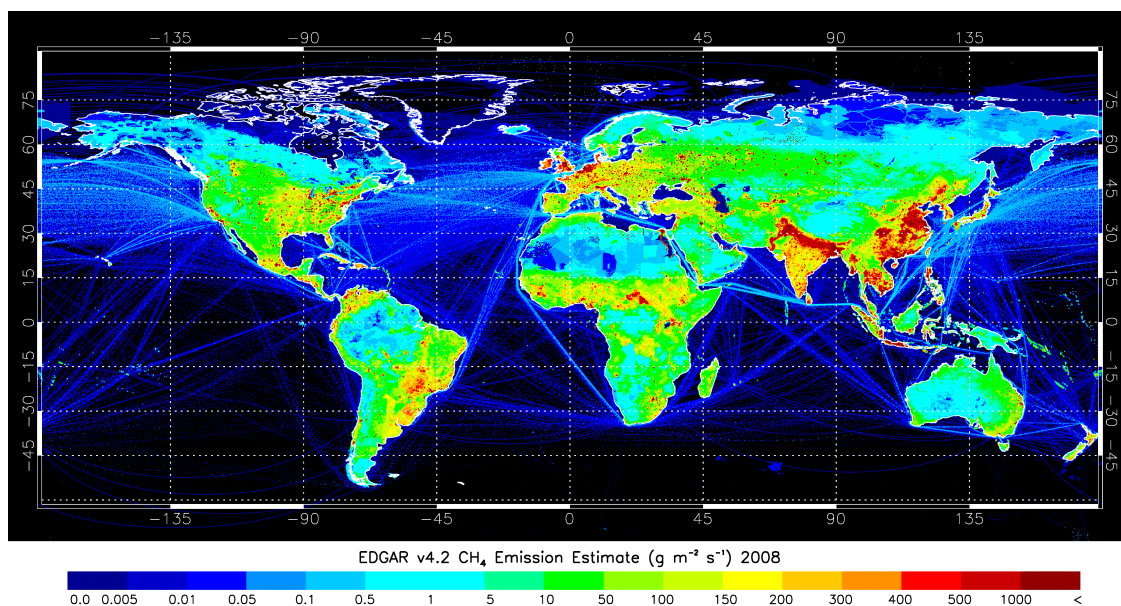


FIGURE 1.5: EDGAR anthropogenic bottom-up methane emission estimates for the year of 2008. Emissions as shown, are in grams, per metre squared, per second (EDGAR, 2009).

groups of microorganisms. The fermenters supply the methanogens with the substrates, such as  $H_2$ ,  $CO_2$  and acetate, whilst the archaea prevents the hydrogen build-up.  $H_2$  inhibits the acetogens, thus removal of hydrogen by archaea allows for acetate formation. Acetate can then be broken down to methane. In most freshwater systems, 2/3 of methanogenesis occurs via the acetate fermentation and 1/3 by  $CO_2$  reduction. The pathway of methanogenesis has been observed to shift from acetoclastic in surface peat to hydrogenotrophic in more oligotrophic deeper peat. Availability of fresh organic matter favours acetoclastic methanogenesis, whereas hydrogenotrophic pathway dominates in more oligotrophic and recalcitrant peat (Juottonen, 2008). Sulphur-reducing bacteria can however compete with methanogens for the substrates. Sulphate reducers use acetate or  $H_2$  as electron donors in anaerobic respiration and using  $SO_4^{2-}$  as an electron acceptor, produce  $H_2S$  as the final product (Schimel, 2004).  $SO_4^{2-}$  reduction is energetically favourable, meaning the sulphate reducing bacteria can out-compete methanogens for substrates. Anthropogenic sulphate emissions have therefore already reduced the natural wetland methane source by 5 Tg below pre-industrial levels (Schimel, 2004).

## Wetlands

The biggest and the most uncertain single source of methane are wetlands, which are estimated to emit between 177 to 284 Tg  $y^{-1}$  using the bottom up approach (Kirschke

et al., 2013). Wetlands may be the main drivers of the global inter-annual variability of  $\text{CH}_4$ , according to the Stocker et al. (2013) report.

Wetlands are estimated to cover a global area of  $5.2$  to  $5.86 \times 10^6 \text{ km}^2$  (Prigent et al., 2007). Wetlands are characterised by water logged soils and are different from both, terrestrial and aquatic environments (Karamouz et al., 2012). Around half of the wetlands are peat-rich, temperature-regulated northern wetlands located  $50^\circ\text{N}$  -  $70^\circ\text{N}$ . Approximately 35% of the global wetland area is broadly distributed in the latitude zone extending from  $20^\circ\text{N}$  to  $30^\circ\text{S}$  and are dominated by precipitation and flood cycles (Khalil, 2000). Annual patterns of  $\text{CH}_4$  emission are influenced by the wetland latitude. Arctic and boreal peat lands are characterised by a temperature-restricted thaw season, which results in pronounced  $\text{CH}_4$  emissions second to third quarter of the year. Temperate wetlands show less seasonal variability due to more restricted range of air temperatures, while tropical  $\text{CH}_4$  emissions are linked to the annual high and low water cycles (Whalen, 2005). The source of the water in the wetlands also determines how much methane is produced. In salty sediments for example, practically no methane is formed due to presence of sulphates (Bartlett et al., 1987).

Methanogens break down the organic matter into methane in an anaerobic soil. As methane is formed, it then travels up to the surface through a variety of different mechanisms, affecting the quantity released to the atmosphere. Methane can diffuse across the soil or water interface by ebullition (bubbling) when concentrations are high and exceed saturation levels. It is possible for methane to enter the atmosphere simply by

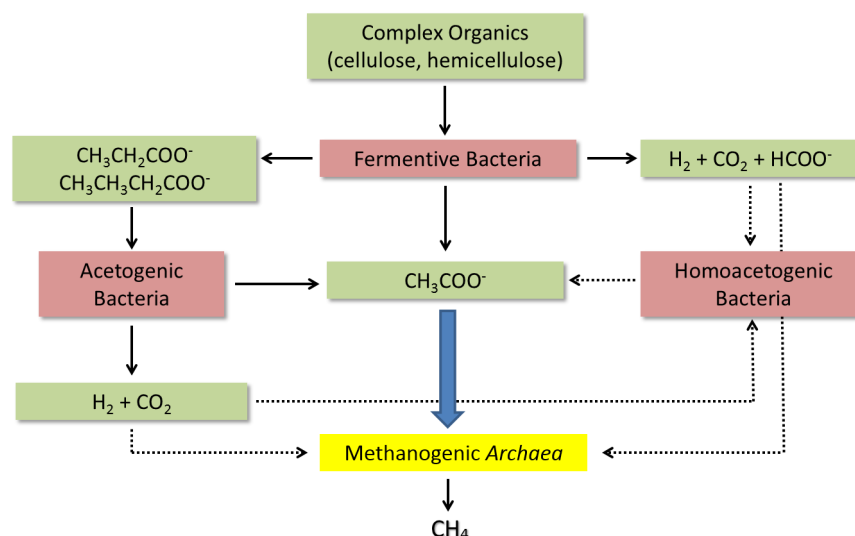


FIGURE 1.6: Microbiological process of methane production. (Hornibrook, 2005; Whiticar, 1999)

plant-mediated transport also. If methane diffuses upwards towards the aerobic zone, most will be oxidised by the methanotrophs. Plants can also mediate the transport to the surface, thus bypassing this important layer. By moving rapidly through the air spaces in plant stems and leaves, greater portion of the gas produced will be released to the atmosphere (Whalen, 2005) (see Figure 1.7).

There are considerable differences in the emission rates in different types of wetlands. It is extremely difficult to estimate the true emissions and extrapolation from one wetland to another can lead to considerable errors. A number of studies have attempted to quantify the magnitude and the seasonality of emissions. This included bottom-up inventory approach, as well as top-down inversions. Aselmann and Crutzen (1989) extrapolated average measured CH<sub>4</sub> emissions in individual ecosystems to global methane emission estimates of 40 - 160 Tg year<sup>-1</sup> from natural wetlands. More recently, Bloom et al. (2010) estimated the wetland and rice paddy contributions to space-borne CH<sub>4</sub> measurements during the years of 2003 - 2005 using satellite observations of gravity anomalies, a proxy for water-table depth and surface temperature analyses. Bloom et al. correlated the ground water table depth data from NASA's GRACE instrument to ESA's SCIAMACHY methane measurements. The authors estimate that tropical wetlands contribute 52 - 58% of total global wetland and rice paddy emissions, with the remainder coming from the extra-tropics. Despite recent developments and improvements in a number of process-based models of wetland methane emissions (Melton et al., 2013; Spahni et al., 2011), confidence in modelled wetland CH<sub>4</sub> emissions remains low. The WETland and Wetland CH<sub>4</sub> Inter-comparison of Models Project (WETCHIMP) investigated our present ability to simulate large-scale wetland characteristics and corresponding CH<sub>4</sub> emissions (Melton et al., 2013). A suite of models was found to demonstrate an extensive disagreement in their simulations of wetland areal extent and CH<sub>4</sub> emissions, in both space and time. The ability to validate the models is limited by the low number of observations in these regions. It was also found that all models tested showed a strong positive response to increased atmospheric CO<sub>2</sub> concentrations in both CH<sub>4</sub> emissions and wetland area. This is supported by other studies (van Groenigen et al., 2011), where such increases in CH<sub>4</sub> emissions from natural wetlands are attributed to increasing soil moisture due to the reduced plant demand for water under higher CO<sub>2</sub>.

### **Northern Lakes**

Ebullition from northern lakes is a globally significant source of atmospheric CH<sub>4</sub>, although one that has not been incorporated into global methane budgets. The emissions

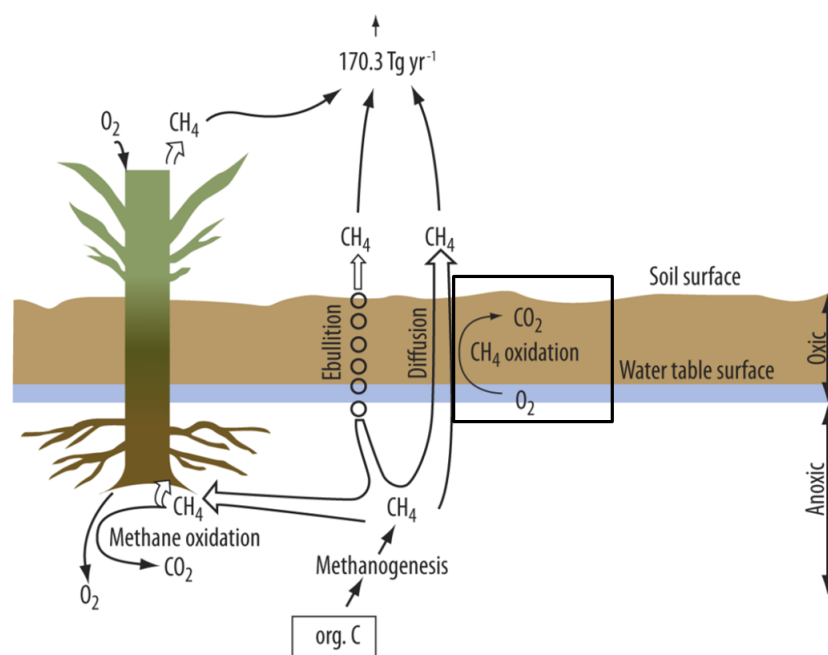


FIGURE 1.7: Methane production from wetlands: production, oxidation and pathways of emission. (United States Environmental Protection Agency, 2010)

from the northern lakes were underestimated due to extrapolation from short-term measurements with randomly placed bubble traps or floating chambers not capturing a particular type of ebullition. Point source or hotspot-bubbling points, although spatially rare, can dominate whole-lake emissions. Walter et al. (2007) mapped the distribution and abundance of point sources and hotspots of methane emissions by walking on the surface of early winter lake ice and observing a specific classes of bubble clusters or open holes in lake ice distinct from background ebullition. Together, point-source and hotspot ebullition was calculated to account for 70% of total emissions from Siberian thermokarst lakes, while molecular diffusion accounts for only 5%. Finally, the authors calculated that all lakes north of 45 degrees are thought to emit 13.7 - 34.7 Tg year<sup>-1</sup>.

## Rice Fields

Rice fields are also a significant source of methane and are estimated to emit 33 - 40 Tg year<sup>-1</sup> in the decade of the 2000s (Stocker et al., 2013). The emissions are largely localised to Asia - over 90% of the area is estimated to be located on this particular continent. A number of factors can influence the magnitude of methane production. These can be temperature, fertilisers used, as well as soil properties and plant phenology.

Temperature affects the rates of all microbiological reactions. The local temperature

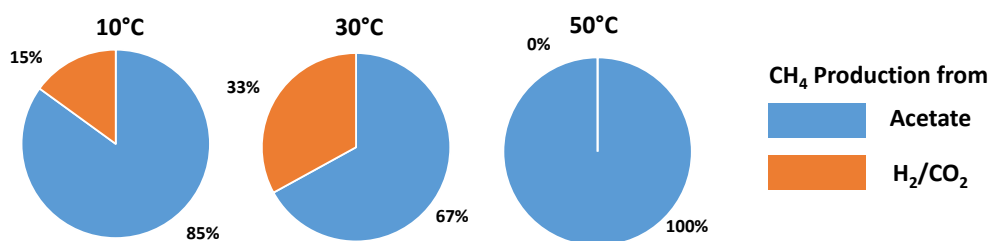


FIGURE 1.8: The effect of temperature on the pathway of CH<sub>4</sub> production (Conrad, 2002)

is critical in determining the magnitude in production of CH<sub>4</sub> following flooding of the rice field. The temperature dependence is due to the rate of reduction of ferric iron and sulfate being enhanced by increasing temperature immediately following flooding, so that steady state CH<sub>4</sub> production is reached earlier (Conrad, 2002). Once steady state of emission is reached, the temperature also affects the pathway of carbon flow. Some microbial processes are more sensitive to temperature than others. Formation of acetate is favored relative to the formation of propionate at lower temperatures, thus CH<sub>4</sub> is increasingly produced from acetate rather than from H<sub>2</sub>/CO<sub>2</sub> (Figure 1.8).

At intermediate temperatures (approximately 30°C), H<sub>2</sub>/CO<sub>2</sub> contributes about 33% to the total CH<sub>4</sub> production. Methane was also found to be produced at high temperatures, indicating the presence of thermophilic methanogens in the rice field soil. Experiments with <sup>14</sup>C-labelled bicarbonate showed that at the temperature of 50°C, methane was exclusively produced from H<sub>2</sub>/CO<sub>2</sub>, while acetate is no longer consumed and accumulates (Fey et al., 2001). The rate of methane production is dependant on the production pathway taken.

CH<sub>4</sub> emission rates can be decreased by draining the rice fields. Experiments have shown that drainage of rice microcosms for 48 hours results in drastically decreased CH<sub>4</sub> emission rates (Ratering and Conrad, 1998). It also resulted in increased sulphate concentrations which decreased slowly back to zero after flooding. Interestingly, the emission rates of CH<sub>4</sub> only slowly recovered to the rates of the undrained controls. This was found to be due to the production of sulphate and ferric iron from their reduced precursors, following the exposure of soil to O<sub>2</sub>. Ratering and Conrad (1998) found that elevated sulphate and ferric iron concentrations allowed sulphate-reducing and ferric-iron reducing bacteria to outcompete methanogenic bacteria on H<sub>2</sub> as a common substrate.

Addition of phosphate fertilizer also results in decreased CH<sub>4</sub> emissions. Lu et al. (1999) evaluated the impact of phosphate supply on rice plant development and the

methane budget of rice fields. It was found that phosphate deficiency leads to higher CH<sub>4</sub> concentrations in soil solution being detected as well as significant increases of CH<sub>4</sub> emission rates during the later stages of rice plant growth.

### **Ruminant Animals**

Emissions from domestic animals may be one of the better quantified sources. This is due to the statistics of animal populations in the developed countries being reasonably reliable (see Section 2.4 on bottom-up emission estimation). Significant uncertainties however exist for wild animals and less developed countries. Production of methane in an animal is affected by a number of factors: body weight, age and feed consumed. There are also variations within individuals of the same species due to differences in bacterial culture within the digestive system of an animal. Domestic ruminant animals are estimated to emit 87 - 94 Tg CH<sub>4</sub> a year (Dentener et al., 2005; EDGAR, 2009; Solomon et al., 2007), whilst wild animals are thought to release 15 Tg CH<sub>4</sub> (Solomon et al., 2007) a year into the atmosphere. Methanogenesis allows the ruminants to utilise the energy in low-quality feeds, like grass and fodder with high cellulose content. Pseudo-ruminants like pigs and horses also produce methane but in much smaller quantities.

### **Termites**

Savannas play an important part in global carbon cycle, as they cover 20% of the Earth's surface and produce almost 30% of the global net primary production (Jamali et al., 2013). Methane exchange in tropical savannas is dominated by fire emissions and to a lesser extent, soil-derived fluxes which includes termites. Termites do play an important role in nutrient cycling. This is especially true in regions such as Australia, which lack dominant grazing and browsing mega-fauna. They can also be a significant source of greenhouse emissions, both CH<sub>4</sub> and CO<sub>2</sub>. The total source strength of termites, however, is largely uncertain. The yearly methane emission estimates range from the minimum of 2 to the maximum of 20 Tg (Kirschke et al., 2013).

Methane production by termites was first reported by Cook (1932), who described the gas evolved from a species of termite as hydrogen and/or methane (Seiler et al., 1984). Later studies have shown that CH<sub>4</sub> (and CO<sub>2</sub>) are the metabolic end products of oxic/anoxic degradation of organic matter by symbiotic microbial communities within termite digestive tract. A number of factors can effect the magnitude of termite CH<sub>4</sub> emissions. The amount of methane produced is affected by the feeding behavior of

termites; whether termites are wood-feeding, fungus-cultivating or soil-feeding. It was found, that soil-feeding and fungus-growing termites emit more methane than wood-feeding termites for example (Brauman et al., 1992). Temperature has also been found to affect the magnitude of emissions. A study by Sawadogo et al. (2011) aimed to quantify CH<sub>4</sub> and CO<sub>2</sub> productions from termites and from the microflora of their gut, with regard to temperature of incubation and feed consumed, under laboratory conditions. In the study, 20 worker termites were put into flasks containing damp cotton and were incubated at 30, 33 and 37° C, respectively, in the dark for 18 days. Different substrates were introduced into separate flasks prior to them being sealed. 1 ml of headspace gas was then analysed regularly and the concentrations of CO<sub>2</sub> and CH<sub>4</sub> recorded. It was found that globally, CH<sub>4</sub> production increased with increasing temperature in the beginning and then continued to increase slightly at lower temperature (30°C) up to 18 days. Sawadogo et al. found that the termite species under investigation produced highest concentrations of CH<sub>4</sub> when the substrates used were mango hull and peanut foliage. Methane emissions were found to be constant on the other substrates. Also, a clear CH<sub>4</sub> concentration decrease (from 160.50 ppm to 0.03 ppm) was observed in the presence of termite mound soil from 11 days. The existence of methanotrophic bacteria involved in CH<sub>4</sub> uptake in soils is therefore suggested.

## **Landfill Sites**

Landfill sites are thought to emit 69 - 90 Tg CH<sub>4</sub> year<sup>-1</sup> (Dentener et al., 2005; EDGAR, 2009; Solomon et al., 2007). Measurement of methane emissions from landfills is however problematic due to the large area and heterogeneous nature of most landfill sites (Mosher et al., 1999). A high variability in local factors affect the amount of methane produced, consumed and emitted in these sites. These include climate, age of refuse and landfill design as well as management practices.

The bacterial decomposition of landfill waste is identified and designated as being in one of the 4 stages: Phase I Aerobic; Phase II Anaerobic Non-Methanogenic; Phase III Anaerobic Methanogenic Unsteady and Phase IV; Anaerobic Methanogenic Steady (Farquhar and Rovers, 1973) (see Figure 1.9).

In phase I, complex organic matter is reduced to smaller, soluble components by extracellular enzymes. The landfill waste at phase I of decomposition has a high nitrogen content, which decreases as the landfill develops through the 4 phases. Phase I continues until oxygen is depleted, the time of which can vary according to factors such as how loose or compressed the waste was when it was buried. Phase II begins once the oxygen

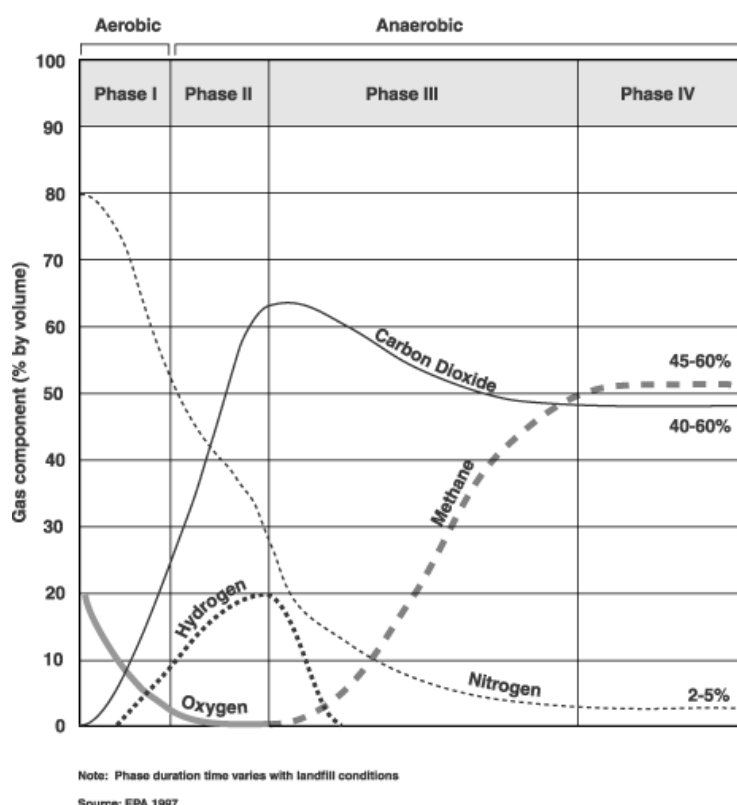


FIGURE 1.9: The biodegradation of organic waste. The timeline of methane and other pollutant production (Agency for Toxic Substances and Disease Registry, 2001).

in the landfill site has been depleted. During this stage, the CO<sub>2</sub> and H<sub>2</sub> production increases. The production of methane has not yet begun. The lag in CH<sub>4</sub> production after anaerobiosis may be owing to the need for adequate amounts of CO<sub>2</sub> in solution, to act as an H<sub>2</sub> acceptor (Farquhar and Rovers, 1973). The microbial processes may return to Phase I, if oxygen is somehow introduced into the landfill (due to disturbance, for example) During phase III of decomposition, the landfill produces increasing amounts of CH<sub>4</sub>. Hydrogen disappears at this stage and the concentrations of CO<sub>2</sub> and N<sub>2</sub> reduce to some terminal value. During Phase IV, the composition of the gases produced and the rates of production remain steady, containing approximately 45% to 60% methane by volume. The CH<sub>4</sub> production is constant for around 20 years, however gas will continue to be emitted for 50 or more years after the waste is initially placed into the site (Agency for Toxic Substances and Disease Registry, 2001).

A number of environmental factors can influence the amount of gas produced. The bacteria producing methane is sensitive to the moisture content in the landfill and the temperature. Moisture encourages bacterial growth and transports nutrients and bacteria to all areas within a landfill, thus increasing water content, which then increases the

amount of methane produced. Increasing temperatures also increases bacterial activity, which in turn speeds up landfill gas production.

### **Methane Hydrates**

A big potential source of atmospheric CH<sub>4</sub> is methane hydrate. This is a crystalline solid consisting of methane and water located in the northern latitude regions. The permafrost covers more than 1 million km<sup>2</sup> of the northern Siberia and Central Alaska to an average depth of ~25 metres (Zimov et al., 2006). It is a large carbon reservoir, representing the steppe-tundra ecosystem that occupied these territories during the glacial periods. These deposits contain 10 - 30 times the carbon found in normal mineral soils. The Northern Hemisphere permafrost is estimated to contain a total of 950 Gt of carbon. Between 50 and 70 Gt is thought to reside in peatbogs of Western Siberia, ~500 Gt in the frozen yedoma and ~400 Gt in the non-yedoma permafrost (Zimov et al., 2006). It is therefore clear, that a rise in temperatures would cause the melting of permafrost resulting in the release of gaseous CH<sub>4</sub>. Gas hydrate decomposition represents an important positive CH<sub>4</sub> feedback to be considered in global warming scenarios. Permafrost regions have already begun to thaw, with some projections indicating that all of yedoma will thaw by the end of the 21st century (Zimov et al., 2006). The time-scale over which methane would be released into the atmosphere is also an important factor in the potential impact on the environment. If the release was to occur very quickly. i.e. emissions spanning over less than 10 years (the lifetime of CH<sub>4</sub>), the atmospheric concentrations would peak and then decay back to a steady state (Archer, 2005). Release on the time-scale of 500-1000 years would on the other hand result in a strong positive atmospheric forcing and warming (Archer et al., 2009).

### **1.4.2 Thermogenic**

Gas and oil industry combined with coal mining are estimated to emit ~97 Tg CH<sub>4</sub> year<sup>-1</sup>. Coal mining is an important source of methane, release of which occurs at a number of stages of extraction. This includes the coal removal process itself as well as releases from coal left in the mine in overlying and underlying seams. The quantity of methane gas emitted from mining operations is a function of two primary factors: coal rank and coal depth (EPA, 2012). Coal rank is a way of measuring the total carbon content of the coal. If the coal rank is higher, it is expected to release an increased amount of CH<sub>4</sub> gas during mining. Coals such as anthracite and semi-anthracite have the

highest coal ranks, while peat and lignite have the lowest (EPA, 2012). The depth the coal is mined at also affect the magnitude of emissions, as at higher depths natural methane escape to the surface is minimised as a result of reduced permeability, owing to increased pressure. Underground mining operations therefore emit more CH<sub>4</sub> than mining done at the surface. Default emission factors are usually used to relate the quantity of coal mined to CH<sub>4</sub> emissions (see Chapter 2 for more detail on forming bottom-up emission estimates).

CH<sub>4</sub> is the principal component of natural gas (95% of pipeline quality natural gas) and is also emitted at various stages of natural gas production, processing, transmission and distribution. Methane emissions associated with natural gas production include losses during extraction, venting and flaring at oil and gas wells and losses during transmission and distribution. Data on venting and flaring is collected by oil companies but is not made readily available making the estimation of this source a major uncertainty. In some countries in Middle East and South America, gas is vented due to the lack of local markets for the gas. Leaking of gas in transit is also a problem in certain regions. The leaking of gas from the Russian and Siberian oil and gas industry results in up to 1.4 % of gas being lost due to low maintenance and permafrost problems which destabilises the pipelines (Lelieveld et al., 2005).

### 1.4.3 Pyrogenic

Biomass burning is known to be a major source of aerosols and gases in the atmosphere (Seiler and Crutzen, 1980). It is estimated to emit 14 – 88 Tg CH<sub>4</sub> year<sup>-1</sup>. Biomass burning is a process of oxidising organic material, which under ideal conditions produces carbon dioxide (CO<sub>2</sub>) and water (H<sub>2</sub>). A simplified equation for complete combustion is:



where (CH<sub>2</sub>O) represents the average composition of organic matter. In natural fires, the supply of oxygen is never sufficient for complete combustion. Owing to the lack of oxygen, incomplete combustion occurs leading to the formation of reduced compounds such as methane, carbon monoxide (CO), non-methane hydrocarbons (NMHCs) and particulate carbon. The contribution of biomass burning to the global total emission of methane is highly uncertain due to the variability of the process itself, as well as data limitations. Fires can be started naturally, by lightning for example. Humans are, however responsible for almost all of the various burning activities, which vary across

different regions (Delmas, 1994). The activities might be burning the land for permanent use for agriculture and ranching, burning of agricultural waste or merely owing to the use of wood as fuel. Prescribed burning is also a method of forest management, commonly used in countries such as Australia or the United States (Delmas, 1994).

The emission of a specific compound depends on the amount of material and the area that is burning. An estimate of the impact of emissions from biomass burning on the atmosphere therefore requires the knowledge of either the total emission of a compound per unit area by a specific fire, or the total emission of a compound per unit mass of the burnt material (Koppmann et al., 2005). The total emission of any species  $n$  per unit area ( $n_{te}$  in  $\text{g m}^2$ ) by a specific fire can be expressed as:

$$n_{te} = m_f \times f_c \times c_f \times \langle EF_n \rangle \quad (1.2)$$

where  $m_f$  is the amount of fuel mass available for combustion in  $\text{kg m}^2$ ,  $f_c$  is the mass fraction of carbon in the fuel,  $c_f$  is the combustion factor (fraction of that mass combusted during the course of a fire) and  $\langle EF_n \rangle$  is the combustion averaged emission factor for species  $n$ , in grams produced per kg of carbon burned, averaged over the time-frame of the fire. The fuel load,  $m_f$ , and  $f_c$  are uncertain in larger regions, but can be observed directly. The mass fraction of carbon in the fuel ( $c_f$ ) can be measured post-fire. The emission factor  $\langle EF_n \rangle$  is the least known on a fire-to-fire basis and the most variable.

More recently, satellites have helped improve the understanding of the spatial and temporal distribution of fires, as well as their inter-annual variability using satellite information on fire activity (utilising ATSR data, for example) and/or aerosol optical depths from the Total Ozone Mapping Spectrometer (TOMS). The datasets of global satellite-derived burned area information been used in combination with biogeochemical or dedicated fuel load models to estimate fire emissions (Lelieveld et al., 2005; Schultz, 2002; van der Werf et al., 2010; Werf et al., 2009).

#### 1.4.4 Aerobic formation of $\text{CH}_4$

A paper by Keppler et al. (2006) did challenge the current understanding of methane production and current global emission estimates. It was demonstrated using carbon isotopes, that methane is formed in situ under aerobic conditions. This was only noticed when the plants were incubated in an  $\text{CH}_4$  free air, as the quantities released were insignificant to those currently in the atmosphere. The release was temperature sensitive, with the concentrations doubling in the temperature range of 30-70°C. This suggests a

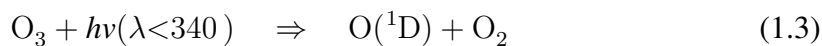
non-enzymic process. To rule out production by anaerobic bacteria, the samples were irradiated with  $\gamma$  radiation. No difference in emission was noted between sterilised and non-sterilised samples, thus microbial activity had to be excluded as the cause. The process via which methane is produced is unknown and sparked a discussion within the scientific community. Keppler et al. estimated that living vegetation released between 62-236 Tg year<sup>-1</sup>. If this was true, a significant source would have been missed by the community. A number of papers were published both in support of the group and contradicting the findings. Vigano et al. (2008) found that emissions from UV irradiated plants are almost instantaneous, indicating a direct photochemical process. In the long term irradiation experiments, the authors argued that concentration of methane produced is large enough to rule out potential interference from degassing or desorption processes.

Frankenberg et al. (2005) did report an unexpectedly high methane concentrations observed with SCIAMACHY over the tropical regions. This would have confirmed the findings of Keppler et al. It was later found that the enhanced concentrations were due to an error in the retrieval algorithm. It was caused by erroneous H<sub>2</sub>O spectroscopic database, which led to a systematic overestimation of tropical methane abundances (Frankenberg et al., 2008). Keppler's findings did at the time, also help explain the stabilisation in the observed atmospheric concentrations of CH<sub>4</sub>. Anthropogenic deforestation would reduce the tropical biomass, decreasing the amount of methane produced. The concentrations have now, as discussed previously, been on the increase again, indicating that the stabilisation was due to another process. The importance of Keppler's work in the view of the global methane budget remains highly uncertain and emissions from plants have not, as yet, been ruled out.

## 1.5 Sinks

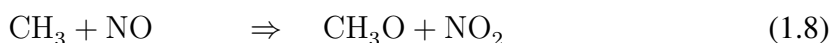
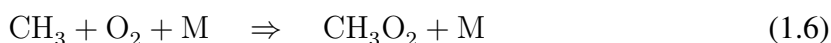
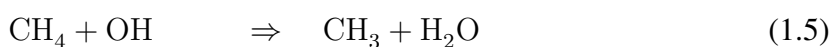
The main atmospheric sink for methane, as well as the other pollutants in the troposphere, is the hydroxyl radical (OH). Oxidation by the hydroxyl radical accounts for approximately 90% of the global sink, or 528 Tg year<sup>-1</sup> (using bottom-up estimates, Kirschke et al. (2013)). Any changes in OH can therefore affect the tropospheric chemical lifetime of CH<sub>4</sub>.

OH is produced when electronically excited O(<sup>1</sup>D) atoms, produced by ozone photolysis, react with water vapour (Naik et al., 2013).

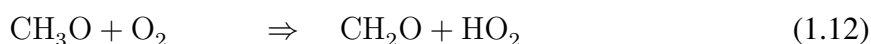
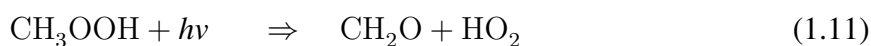
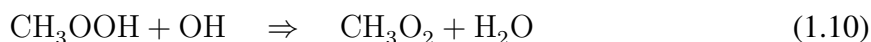
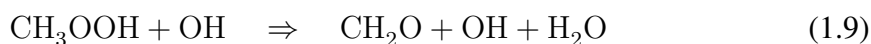


The OH production is therefore highest in regions with the highest levels of water vapour and highest incident UV radiation, ie. tropical lower to middle troposphere.

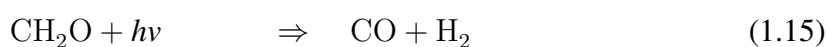
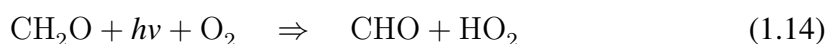
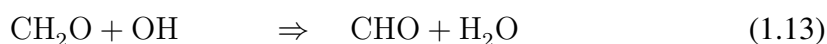
Methane is oxidised by OH to form methyl radical and H<sub>2</sub>O. The methyl radical then rapidly reacts with O<sub>2</sub> to form CH<sub>3</sub>O<sub>2</sub>. The methylperoxy radical (CH<sub>3</sub>O<sub>2</sub>) produced can then either react with HO<sub>2</sub> or NO, giving CH<sub>3</sub>OOH and CH<sub>3</sub>O (Jacob, 1999).



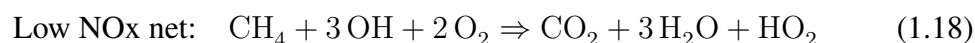
Methylhydroperoxide (CH<sub>3</sub>OOH) can either react with OH or photodissociate. Hydrogen abstraction can occur at the methyl branch or the hydroperoxide group when reacting with OH, producing CH<sub>2</sub> or CH<sub>2</sub>OOH or CH<sub>3</sub>O<sub>2</sub> respectively. The CH<sub>2</sub>OOH radical rapidly decomposes to formaldehyde (CH<sub>2</sub>O) and OH. The methoxy radical produced in steps 1.8 and 1.12 can react with oxygen, also producing formaldehyde.



Formaldehyde has 2 photolysis branches. It can also react with OH producing CHO, which in turn reacts rapidly with O<sub>2</sub> to yield CO and HO<sub>2</sub>. CO can then be oxidised to CO<sub>2</sub> as is shown in the following equations:



The product of CH<sub>4</sub> oxidation is determined by the concentration of NO<sub>x</sub> in the atmosphere. Under high NO<sub>x</sub> conditions the net reaction yields five O<sub>2</sub> molecules and two OH radical molecules. Under low NO<sub>x</sub> conditions, no O<sub>3</sub> is produced and three HO<sub>x</sub> molecules are consumed.



Methane can also produce ozone as the final product, when oxidised in the presence of high NO<sub>x</sub> concentrations (see Section 1.6). Indirect radiative effects of CH<sub>4</sub> are due to increasing its own lifetime through changes in the OH concentration. A decrease in the concentration of atmospheric hydroxyl radical leads to changes in tropospheric ozone, enhanced stratospheric water vapour levels, and increase in CO<sub>2</sub> concentrations (Solomon et al., 2007).

The chlorine free radical atom is a second, minor sink of atmospheric CH<sub>4</sub>. The reaction with Cl occurs predominantly in the stratosphere (10-50 km altitude), owing to the low abundances of oxygen and chlorine free radicals in the troposphere. Methane can also be removed from the atmosphere by uptake in soils. This is a small, but important sink, estimated to be 30 Tg CH<sub>4</sub> a year (Solomon et al., 2007). Methane is removed by methanotrophs, bacteria that are able to metabolise CH<sub>4</sub> as their only source of carbon and energy. This process can be divided into 2 forms: low and high-affinity oxidation. High-affinity oxidation occurs in soils that have close to atmospheric CH<sub>4</sub> concentrations. These are upland, dry soils. Forest soil is the most efficient sink and cultivated land, the least (Mer and Roger, 2001). The species responsible for high affinity oxidation remain poorly understood. Low-affinity oxidation on the other hand occurs in soils that have high methane concentrations (> 40 ppm). Examples of such environments are wetlands and rice paddies. Low-affinity methanotropic bacteria break-down significant quantities of methane in wetland soils. It is estimated that in such environments, bacteria annually consume well in excess of the 600 Tg of methane (Hornibrook et al., 2008). These microorganisms, also known as Type I (gamma) and Type II (alpha) methanotrophs, therefore serve as an efficient filter, removing CH<sub>4</sub> that otherwise would enter the atmosphere.

## 1.6 Methane and air quality

Methane also plays a role in air quality, as it is an ozone precursor (Crutzen, 1973). Ozone at ground level is the primary constituent in photochemical smog and has detrimental effect on human health, reducing life expectancy. The increased background ozone concentration levels since the industrial revolution are largely due to the increased anthropogenic emissions of methane, volatile organic compounds (VOCs) and nitrogen oxides (NO<sub>x</sub>). The methane oxidation pathway is dependent on the concentrations of NO<sub>x</sub> present. In high NO<sub>x</sub> concentrations, O<sub>3</sub> is produced via reactions of peroxy free radicals with nitrogen oxides. Where the concentrations of background NO<sub>x</sub> are low, ozone formation is suppressed by methyl hydroperoxide. This may result in a net loss of O<sub>3</sub>. It is expected that ozone produced from methane oxidation is independent of the location of CH<sub>4</sub> emissions, as it is well-mixed within the troposphere. The spatial pattern of O<sub>3</sub> from CH<sub>4</sub> oxidation would be controlled by the distributions of OH and NO<sub>x</sub>, which affect the location of the reaction and in turn, the amount of O<sub>3</sub> produced.

A number of studies have attempted to characterise the response of tropospheric O<sub>3</sub> to controls on CH<sub>4</sub> emissions and quantify the resulting benefits to air quality and climate (Dentener et al., 2005; Fiore et al., 2008; West et al., 2012). Fiore et al. (2008) used a tropospheric chemistry model MOZART-2 to show that global tropospheric O<sub>3</sub> responds approximately linearly to changes in CH<sub>4</sub> emissions. It was found that decrease in surface and tropospheric ozone column concentrations arising from CH<sub>4</sub> emission controls are largely independent of source locations. The decrease in O<sub>3</sub> is not however uniform, reflecting the sensitivity to local meteorological and chemical conditions. Importantly, the model results show that O<sub>3</sub> is nearly twice as sensitive to CH<sub>4</sub> in the planetary boundary layer than to CH<sub>4</sub> in the free troposphere. This results in strong O<sub>3</sub> enhancement in response to methane in NO<sub>x</sub>-saturated areas. Examples of such conditions would be urban environments, power plants and industrial facilities. Locations experiencing mixing with the free troposphere expectedly display a weaker response.

West et al. (2012) have investigated the benefits of controlling methane to reduce ozone atmospheric concentration in terms of premature human mortality rate reductions and cost-benefit calculations. Three scenarios of future methane emissions abatement over the period of 2005-2030 were modelled relative to a base scenario. The base scenario projects a global anthropogenic methane emission increase of 40%, which falls in the middle of IPCC projections (Solomon et al., 2007). It is estimated that 38k mortalities can be avoided globally in 2030, assuming a decrease in global emissions of 125 Mton year<sup>-1</sup>. The model calculation predicts a global average ozone concentration de-

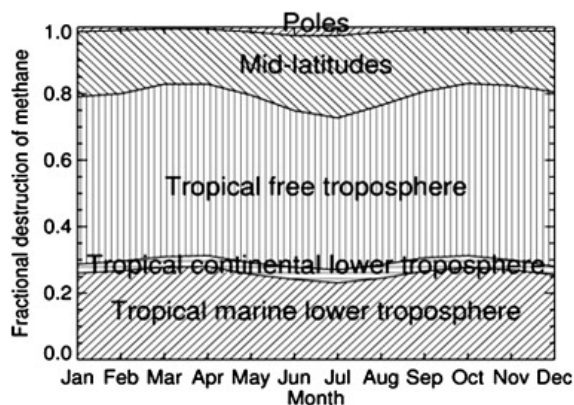


FIGURE 1.10: Contribution of the different regions of the troposphere to the total removal of  $\text{CH}_4$  throughout the year calculated from a global CTM (Monks et al., 2009).

crease of 1.3 ppb relative to the base scenario. Under 2 of the 3 scenarios modelled (emission reductions of  $75 \text{ Mton year}^{-1}$  and  $125 \text{ Mton year}^{-1}$ ), the incremental benefits far outweigh the incremental costs. The third scenario (emission reductions of  $180 \text{ Mton year}^{-1}$ ) assumes technological advancement, but has costs that roughly equals benefits. Overall, the authors conclude that the mitigation of methane emissions for climate purposes provides an important co-benefit for air quality and human health (see also a study by Morgenstern et al. (2013)).

## 1.7 Summary

Atmospheric methane ( $\text{CH}_4$ ) plays a significant role in global warming, despite being present in the atmosphere in smaller quantities than carbon dioxide ( $\text{CO}_2$ ) and has a radiative forcing efficiency or global warming potential 21 times greater than that of  $\text{CO}_2$ . The annual global source strength of  $\text{CH}_4$  is estimated by inverse studies to be between  $526\text{-}569 \text{ CH}_4 \text{ Tg year}^{-1}$ . The quantification of individual methane sources and sinks is still however largely uncertain, which leaves question, such as the reason for the slowdown and recent recovery of the atmospheric  $\text{CH}_4$  trend, unanswered. These uncertainties are particularly large for the various biogenic  $\text{CH}_4$  sources, such as wetland emissions or emissions from rice paddies owing to their large spatial and temporal variation. Satellite instruments can provide a top-down view of the integrated atmospheric signals in atmospheric  $\text{CH}_4$ , thus helping to constrain the magnitude of  $\text{CH}_4$  emissions from larger regions.

This chapter described how  $\text{CH}_4$  is formed and the main sources and sinks of atmospheric methane. Over 50% of the methane source is estimated to be due to an-

thropogenic activity and over 70% are biogenic in origin. Biogenic methane is produced as a metabolic byproduct when complex organic compounds are decomposed by methanogens in an anaerobic environment. Methane can also be formed in fires, due to incomplete combustion of organic matter (pyrogenic) or leaked in the process of fossil fuel mining (thermogenic).

## **Chapter 2**

# **Measuring and modelling atmospheric methane**

### **2.1 Introduction**

This chapter describes the current methods of measuring atmospheric methane. Each method has its advantages and can be used to investigate fluxes at different spatial and temporal scales. In situ measurements are accurate and contain information on the local and regional fluxes. Surface point flask observations are sensitive to pollutant emissions in the near vicinity of the measurement site, whilst air samples taken on tall towers and by aircraft are influenced by emissions further up-wind. Earth observation instruments provide the greatest spatial coverage, although they are the least accurate. This chapter describes passive instruments, sensing in the thermal infrared (TIR) and shortwave infrared (SWIR) regions of the spectrum and gives a quick introduction to active systems. Each of these has its own distinct advantages and weaknesses, although SWIR sensing instruments are of most relevance here, as the performance of three of such systems (GOSAT, Sentinel 5-Precursor and CarbonSat) is modelled in this study.

### **2.2 In situ CH<sub>4</sub> measurements**

There are currently over 200 flask and in situ continuous measurement stations providing measurements of various atmospheric constituents (Ciais et al., 2013). The measurement network is dense in highly populated areas, such as North America, Europe and Japan (locations of the stations reporting to the World Meteorological Organization (WMO)

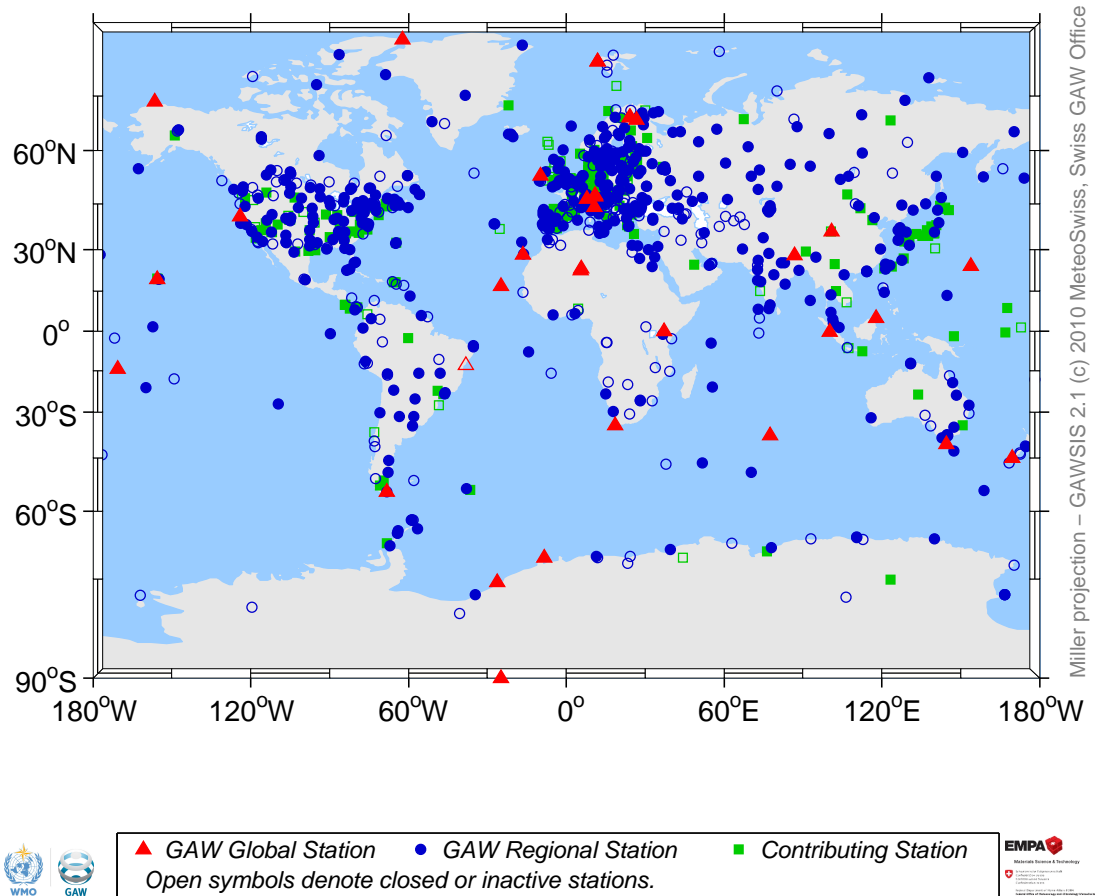


FIGURE 2.1: The locations of the stations reporting to the Global Atmosphere Watch Station Information System (GAWSIS) network (Barrie, 2005).

can be seen in Figure 2.1). Data is however sparse over large areas of the globe. South America, mid-Australia and central Asia are very poorly sampled. The lack of measurements in the a fore-mentioned areas hampers the ability of models to obtain flux estimates in these regions.

Historically, flask sampling was the first method to be used to measure greenhouse gases. Mauna Loa observatory in Hawaii, the oldest continuous measuring station has been utilising the method to measure  $\text{CO}_2$  concentrations in the atmosphere since 1958 (Keeling and Whorf, 2004). First, glass containers are filled with ambient air taken at the measurement location. The discrete air samples are then transported to a laboratory, to be analysed. The amount of  $\text{CO}_2$  present in the sample is obtained using IR spectroscopy, whilst vacuum-UV resonance fluorescence is utilised to quantify the CO present in the air sample (National Oceanic and Atmospheric Administration, 2013).  $\text{N}_2\text{O}$ ,  $\text{SF}_6$ ,  $\text{H}_2$  and  $\text{CH}_4$  have to be separated from the air mixture using gas chromatography. The different

constituents are then detected utilising different methods, flame ionisation detector being used to measure the concentration of CH<sub>4</sub> in a gas stream. Flask sampling is still widely used today, however the atmosphere is poorly sampled in time when GHGs are measured in this manner. In remote regions, samples can be obtained monthly or weekly at best, resulting in temporal measurement gaps. National Institute for Environmental Studies (NIES) for example, collects air samples on voluntary observation ships sailing between Japan and Australia/New Zealand and between Japan and North America (Terao et al., 2011). Observations between Japan and Australia/New Zealand are collected every 35 - 42 days, whilst average sampling interval for northern Pacific cruises is 60 days. The background maritime air is therefore only sampled ~10 times per year.

The time-discontinuity has been addressed by equipping observatories with continuous measurement systems. These are expensive to install and maintain, thus are not as numerous as dedicated flask measurement sites. Advanced Global Atmospheric Gases Experiment (AGAGE) network currently contains 9 such stations. The original stations (Mace Head, Trinidad Head, Ragged Point, Cape Matalula, and Cape Grim) occupy coastal sites around the world chosen to provide accurate measurements of trace gases whose lifetimes are long compared to global atmospheric circulation times. Four more observatories have been added later: Ny-Ålesund and Jungfraujoch in Europe as well as Shangdianzi and Gosan in Southeast Asia. AGAGE sites contain two instrumental components: a gas chromatograph multidetector (GC-MD) system and a Medusa Gas Chromatography with Mass Spectrometry (GC-MS) instrument (Miller et al., 2008). The frequency of measurements is 36 times per day and 60 minutes per measurement for GC-MD and Medusa GC-MS instruments respectively, thus providing considerably more data than discrete flask measurements

Tall towers also provide continuous measurements, whilst also having an advantage of being able to measure the vertical profile of pollutant concentrations. A tower typically has a number of inlet points, which vary in height from ground level. Air from each individual line is analysed separately, thus providing information on the influence of local and more remote sources. A measurement taken at ground level will mainly be affected by fluxes in the local vicinity of the instrument. An observation taken higher up in the tower provides us with information on the emissions on a regional scale. It has been estimated that a typical sampling footprint for a tall tower is of an order of 10<sup>6</sup> km<sup>2</sup> (Gloor et al., 2001).

The towers can be purpose built (KNMI-mast Cabauw, Netherlands) or existing infrastructure can be adapted for atmospheric measurements. For example, the tall tower greenhouse gas observing network of the Earth System Research Laboratory (ESRL)

uses very tall ( $> 300$  m) television and radio transmitter towers as a convenient platform for mid-boundary layer trace gas sampling (Andrews et al., 2013). Towers are typically automated, although flask samples are also taken, providing independent validation to the aforementioned measurements.

Aircraft measurements are also an integral part of the methane observation and modelling network. Global-scale atmospheric chemistry transport models (ACTMs) have difficulty resolving sharp chemical gradients which are present at air mass boundaries, at the tropopause (Pan, 2010), or in plumes released from strong source regions. Aircraft measurements enable us to measure the concentrations of various gases at different altitudes, allowing us to validate vertical mixing in models (Saito et al., 2013; Wecht et al., 2012) and Fourier Transform Spectrometer (FTS) observations (TCCON and satellite) (Tanaka et al., 2012). The measurements have been taken using a variety of different aircraft on a number of campaigns. Most aircraft datasets span the depth of the atmosphere on a limited temporal scale (Wofsy, 2011), but few datasets have long transects covering extended time periods. Missions, such as HIPPO and CARIBIC described below, are examples of such long running measurement campaigns.

HIAPER Pole-to-Pole Observations (HIPPO) project was a sequence of five global aircraft measurement programmes that sampled the atmosphere from  $87^{\circ}\text{N}$  to  $67^{\circ}\text{S}$ , with vertical profiles approximately every  $2.2^{\circ}$  of latitude, from the surface to 14 km in altitude (Wofsy, 2011). The measurements were taken on the National Science Foundation's Gulfstream V, High-performance Instrumented Airborne Platform for Environmental Research (HIAPER) aircraft, operated by the National Center for Atmospheric Research (NCAR). The goal of HIPPO was to obtain global-scale, fine-grained data for a large number of atmospheric constituents, including  $\text{CH}_4$ . The obtained data allows for improved modelling of transport in ACTMs, addresses the errors in the spatial/temporal representation of surface fluxes and reaction rates. The vertical greenhouse gas profile also allows to rigorously test satellite algorithms. The aircraft carried a number of instruments, capable of measuring  $\text{CH}_4$ , which worked independently thus providing redundancy and allowing to check the calibration of the said spectrometers. Quantum Cascade Laser Spectrometer (QCLS), measuring  $\text{CO}_2$ ,  $\text{CO}$ ,  $\text{CH}_4$  and  $\text{N}_2\text{O}$ , was a mid-infrared (IR) sensor developed by Harvard University and Aerodyne Corp. UCATS and the PAN (PeroyAcylNitrate) and other Trace Hydrohalocarbon Experiment (PANTHER) were the on-board gas chromatographs, measuring  $\text{CH}_4$  at 13 min intervals. Data from the HIPPO campaign has been used to calibrate total column measurements of  $\text{CO}_2$ ,  $\text{CO}$  and  $\text{CH}_4$  from the Total Carbon Column Observing Network (TCCON) of Fourier transform spectrometers (Wunch et al., 2010).

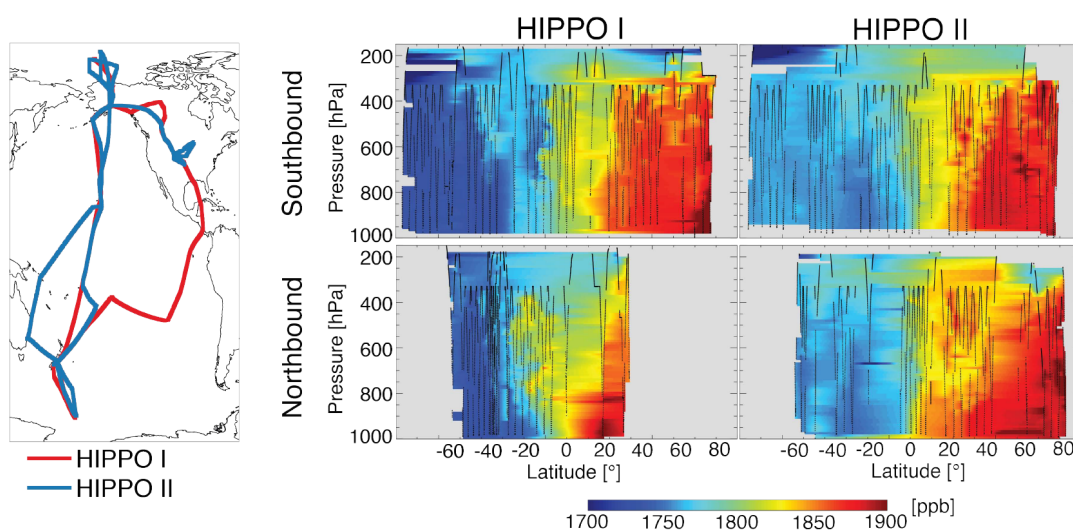


FIGURE 2.2: The left panel shows flight paths of HIPPO missions I and II during January and October - November 2009 respectively. The panels in the centre and on the right show methane concentrations as a function of latitude and pressure measured during southbound and northbound flight paths of HIPPO I and II. Black lines show the aircraft profiles with methane data. Solid contours are interpolated (Wecht et al., 2012).

The SOLVE (2000), POLARIS (1997), and STRAT (1996) (Hurst et al., 2000) campaigns collected air samples covering latitudes from 1°S to 89°N and altitudes from 11 to 21 km (Rice et al., 2003). NASA ER-2 aircraft has been used to probe the upper troposphere and lower stratosphere providing measured CH<sub>4</sub> mixing ratios that range from 1744 to 716 ppbv respectively (Rice et al., 2003). The aim of the campaign was to measure the carbon isotope ratios. It was noted that the dearth of stratospheric isotopic data, in particular, has limited the ability of the models to evaluate CH<sub>4</sub> source strengths and distributions, the seasonality of CH<sub>4</sub> source functions and experimentally determined kinetic isotope effects (KIEs) in CH<sub>4</sub> sink processes. The campaign organisers hoped that additional stratospheric isotopic CH<sub>4</sub> observations obtained in the study, will promote a better understanding of stratospheric CH<sub>4</sub> isotope fractionation, which in turn, will provide tighter constraints on the influence of stratospheric photochemistry on free tropospheric isotope values. The results indicated that a combination of chemistry and transport determines the isotope:tracer relationships observed, with underlying chemical kinetic isotope effects associated with CH<sub>4</sub> sink reactions enriching CH<sub>4</sub> in the heavy isotopes (<sup>13</sup>C and deuterium), as CH<sub>4</sub> is oxidized in the stratosphere.

In situ measurements are still mostly restricted to individual campaigns employing research aircraft, however instruments have also been fitted to scheduled passenger carrying aircraft. Atmospheric chemistry and composition programs based on commercial passenger aircraft allow us to probe the tropopause region and the lowermost

stratosphere. CARIBIC (Civil Aircraft for the Regular Investigation of the atmosphere Based on an Instrument Container) is one such long-term atmospheric measurement program, utilising a comprehensive scientific instrument package aboard a Lufthansa Airbus A340-600 (Schuck et al., 2009). The use of this type of aircraft ensures that large sections of the globe are covered and allows for the background tropospheric air to be probed regularly. The system allows for real-time measurements of aerosols and trace gases to be taken. The onboard payload also collects air samples to be analysed for the main greenhouse gases CO<sub>2</sub>, CH<sub>4</sub>, N<sub>2</sub>O, and sulfur hexafluoride (SF<sub>6</sub>) as well as for various non-methanehydrocarbons (NMHCs), halocarbons, and isotope ratios of CO<sub>2</sub>, CH<sub>4</sub>, and H<sub>2</sub>. The use of spectrometers onboard commercial aircraft helps to gain a better understanding of the mixing processes that take place in the tropopause region, making it possible to access this part of the atmosphere regularly during all seasons.

## 2.3 Remote sensing

Remote sensing refers to identifying, observing, and measuring an object without coming into direct contact with it. In the context of greenhouse gas monitoring, the concentration is inferred by detection and measurement of radiation at different wavelengths. The term can refer to ground-based, aircraft or space-borne instruments, although this section will focus on satellites. Description of the TCCON sites will also be provided, as data from these sites is used to calibrate and validate space-borne measurements.

Satellites are an increasingly important platform for remote sensing of CH<sub>4</sub> in the atmosphere. The current in situ network does not cover significant parts of the globe, including the oceans and areas of low population density. Satellites can fill in the measurement gaps by providing a high density of observations over most of the Earth's surface. This makes it possible to observe highly forested regions, such as the Amazon or Siberia, which could otherwise be difficult to access.

Several techniques can be used to measure the atmospheric concentration of greenhouse gases. Instruments can be passive or active depending on the source of the radiation that the sensor measures to infer the concentration of the greenhouse gas of interest. Passive sensors utilise an external source of energy, such as the Sun or the energy emitted by the Earth and the atmosphere itself. Sections 2.3.1 and 2.3.2 describe passive techniques, i.e. satellites carrying out observations in the SWIR and TIR regions of the electromagnetic spectrum and Section 2.3.3, an active technique, i.e. LIDAR (a portmanteau of "light" and "radar") measurements (see Figure 2.3).

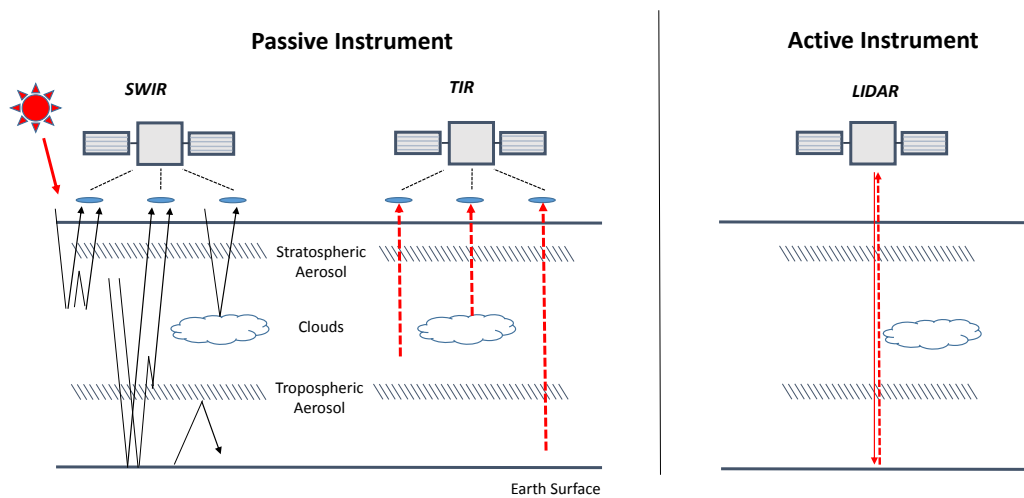


FIGURE 2.3: Remote sensing of greenhouse gases: active and passive methods.

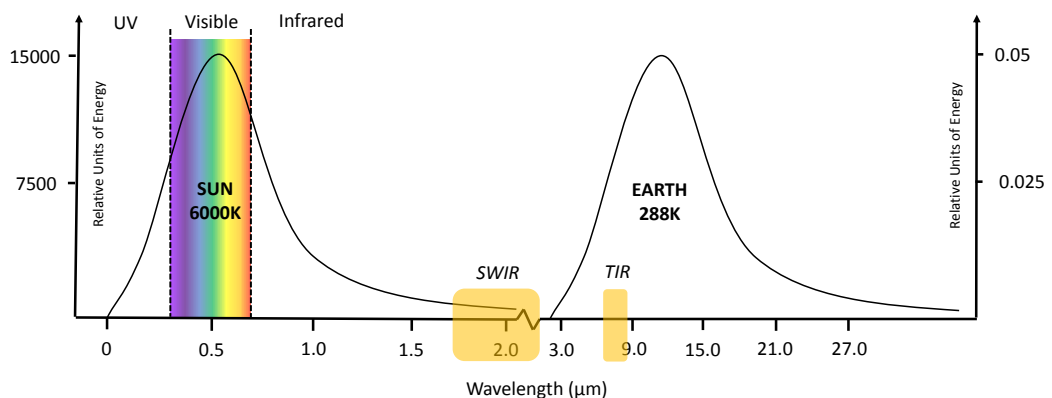


FIGURE 2.4: Black body emission spectra of the Sun and the Earth. Energy is in relative units, that of the Sun on the left whilst the right side of the diagram displays the energy emitted by the Earth.

### 2.3.1 Thermal Infrared (TIR)

Any object with a temperature of above 0 K emits radiation. The radiation has a specific spectrum and intensity, which is dependant on the temperature of the body in question. The black body emission spectrum, as this is known, is shown for the Sun and the Earth in Figure 2.4. However, the spectrum shown is for a body that is in thermodynamic equilibrium with its environment. This means the object absorbs all radiation incident upon it and re-radiates energy which is characteristic of this radiating system only.

In the thermal infrared region of the spectrum (wavelength greater than 4  $\mu\text{m}$ ), the radiance emitted by the Earth is significantly larger than that emitted by the Sun and reflected by the Earth. The radiance of the planet's atmosphere is a function of its temperature and its composition. As the atmosphere is not a perfect black body, the observed spectrum can be used to infer the composition of the atmosphere due to radiation of different wavelengths being absorbed by different greenhouse gases.

The radiance  $I(\lambda)$  observed by an instrument at the top of the atmosphere at wavelength  $\lambda$  can be written as (Schuck et al., 2009):

$$I(\lambda) = \epsilon_{surf} B(\lambda, T_{surf}) \tau(\lambda, P_{surf}) + \int_{P_{surf}}^0 B(\lambda, T) \frac{\delta\tau(\lambda, P)}{\delta P} dp, \quad (2.1)$$

where  $B$  is the Planck function,  $\lambda$  is the wavelength,  $T$  = temperature and  $\tau$  is the atmospheric transmission between a pressure level  $p$  and the top of the atmosphere. The radiance, as shown in Equation 2.1, is composed of 2 terms. The first term is the surface and the second is the atmospheric contribution to the radiance. The surface contribution is proportional to the emissivity. The atmosphere radiance is the integral of the Planck function over the atmospheric column weighted by the derivative of the transmission. Depending on the wavelength, some channels will be highly absorbent whilst others will be transparent. TIR instruments are most sensitive to absorbers in the upper troposphere. The weighting function in the atmospheric term is, on the other hand, close to zero in the boundary layer and at the top of the atmosphere. The Earth observation instruments probing this particular part of the atmosphere are not therefore, on the short timescale, sensitive to surface emissions. The enhanced sensitivity to the upper troposphere makes TIR sensing instruments more suited for studies of total budgets of various greenhouse gases.

$$\tau(\lambda, P) = \exp\left(-\frac{1}{\cos(\Theta_v)} \int_0^P K_p(\lambda, T, p) dp\right) \quad (2.2)$$

For a given wavelength, absorption  $K_P(\lambda, T, p)$  depends on the atmospheric composition, temperature and pressure (Equation 2.2). This dependence makes it possible, if the temperature and pressure profile is known, for the concentrations of the absorbing gas can be retrieved from the inferred  $K$ . As the concentration of the said gas increases, the channel of interest sees higher in the atmosphere and for a troposphere peaking channel, the measured radiance corresponds to a colder temperature. By adjusting the measured and modelled radiance using the known temperature profile, the absorbing gas concentration can be estimated. Finally, there are several intrinsic advantages when using the

thermal infrared region for atmospheric remote sensing (Clerbaux et al., 2011). Since the processes of absorption and emission of infrared photons are governed by Planck's law, they are very sensitive to temperature, as are the molecular line strengths owing to the temperature-dependent population of the molecular energy levels. This allows for vertical information to be extracted from atmospheric spectra in the thermal infrared - even when using observations obtained in the nadir geometry, from space. The pressure-dependence of the molecular line-widths also provides additional vertical information, although a high spectral resolution is required to observe this effect. The biggest advantage of TIR, is that observations can be made both day and night, therefore diurnal cycles can be observed, as can species that are only present in significant concentrations during the night.

### **Atmospheric Infrared Sounder (AIRS)**

AIRS, launched onboard the AQUA platform on May 4<sup>th</sup>, 2002, is a nadir cross-track scanning infrared spectrometer aimed at obtaining temperature profiles within the atmosphere and a variety of additional Earth/atmosphere products. It is part of a closely coupled triplet of instruments that include the Advanced Microwave Sounding Unit (AMSU) and Humidity Sounder for Brazil (HSB). The products include water vapour concentrations and profiles, as well as that of gases such as CO<sub>2</sub>, CO, CH<sub>4</sub>, O<sub>3</sub>, and SO<sub>2</sub>. The primary scientific achievement of AIRS has been to improve weather prediction and to study the water and energy cycle (Chahine et al., 2006).

The AIRS instrument views the atmospheric infrared spectrum, with 2378 spectral samples obtained with a nominal spectral resolution of 1200 ( $\lambda/\delta\lambda$ ), covering more than 95% of the Earth's surface and returning about three million spectra daily. AIRS 2378 channels cover wavelengths 649–1136, 1217–1613 and 2169–2674 cm<sup>-1</sup>. A ground footprint is scanned every 22.4 ms, the total scan period being 2.667 s. The AIRS IR spatial resolution is 13.5 km at nadir from the 705.3 km orbit (AIRS, 2013). The instrument requires no moving parts for spectral encoding and all spectral samples are measured simultaneously in time and space. Simultaneity of measurement is an essential requirement for accurate temperature retrievals under partly cloudy conditions.

AIRS channels near 7.6  $\mu\text{m}$  are used for CH<sub>4</sub> retrieval, and they are most sensitive to the middle to upper troposphere, i.e., 200–300 hPa in the tropics and 400–500 hPa in the polar region (Xiong et al., 2008). It is possible to use the stand-alone AIRS infrared observations for these retrievals, but the results will be more strongly affected by clouds. The primary AIRS products are obtained when CH<sub>4</sub> retrievals are carried out

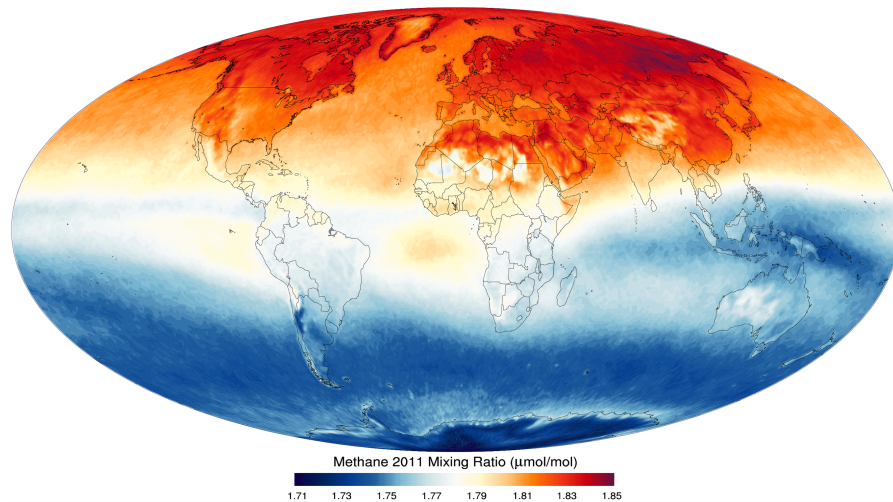


FIGURE 2.5: AIRS averaged methane mixing ratio observation for 2011 (NASA, 2013)

utilising both AIRS and AMSU observational data. The Advanced Microwave Sounding Unit (AMSU-A), is a 15-channel microwave sounder designed primarily to obtain temperature profiles in the upper atmosphere (especially the stratosphere) and to provide a cloud-filtering capability for tropospheric temperature observations. The atmospheric temperature-humidity profiles, surface skin temperature, and emissivity are required to derive  $\text{CH}_4$  concentrations in the atmosphere, which are retrieved using combinations of different AIRS channels and AMSU data. AIRS  $\text{CH}_4$  products include the  $\text{CH}_4$  profiles, plus averaging kernels and information contents. The information content was found to be larger in the tropics than that at high latitudes, and the altitude with the most sensitivity in the tropics is higher than in the polar region (Xiong et al., 2008). AIRS has been validated against thousands of aircraft profiles (convolved using the AIRS averaging kernels), demonstrating that its RMS error is mostly less than 1.5% from 2003 to 2009 (Xiong et al., 2010). Figure 2.5 shows the average methane column concentrations for 2011 as observed by AIRS.

### **Infrared Atmospheric Sounding Interferometer (IASI)**

Developed by the French Space Agency CNES, IASI was launched into space on October 19<sup>th</sup>, 2006, onboard the MetOp platform. MetOp is a series of three polar orbiting meteorological satellites operated by the European Organisation for the Exploitation of Meteorological Satellites (EUMETSAT) and is Europe's first polar orbiting satellite used for operational meteorology. The satellites are planned to be launched at approximately 5 year intervals (Metop-B launched successfully on 17<sup>th</sup> September, 2012), maintaining the service until at least 2020. As with AIRS, the main goal of the IASI mission is to

provide temperature and humidity profiles, for use in the improving our understanding and making of atmospheric forecasts. The long time series of planned instruments will allow for long time trends to be studied.

IASI is a Fourier Transform Spectrometer based on a Michelson interferometer that measures the Earth's atmospheric TIR emission. IASI provides 8461 spectral samples, aligned in three bands between 645.00 and 2760.00  $\text{cm}^{-1}$  (15.5 and 3.63  $\mu\text{m}$ ), with a spectral resolution of 0.50  $\text{cm}^{-1}$  (Level 1C data) (Xiong et al., 2013). The instrument has a 112 km swath width and a spatial resolution of 12 km at nadir, from a 837 km orbit (PLANETA, 2013).

Similarly to AIRS, MetOp carries an Advanced Microwave Sounding Unit (AMSU) which offers independent information on temperature that can be used to retrieve  $\text{CH}_4$  profiles. IASI retrieved methane concentrations, in combination with high resolution methane aircraft-based observations in the upper tropical troposphere, provide a means to improve our knowledge on the mechanisms that transport methane emissions from the surface to the upper atmosphere as well as detect the atmospheric transport pathways (Xiong et al., 2013).

### 2.3.2 Short Wave Infrared (SWIR)

At short wavelengths ( $\lambda < 3 \mu\text{m}$ ), the Earth's surface and atmosphere does not emit significant amounts of radiation. Instruments sensing this part of the electromagnetic spectrum measure the light emitted by the Sun and reflected either through atmospheric scattering or at the surface. The change in the radiation spectral signature from the signature prior to it entering the atmosphere, is a function of the amount of absorbing material in the atmosphere. The measured radiance seen by a satellite ( $I(\lambda)$ ) is equal to (first order approximation) (Bron and Ciaia, 2010):

$$I(\lambda) = E_0(\lambda)R(\lambda)T(\lambda), \quad (2.3)$$

where  $E_0(\lambda)$  is the top of atmosphere solar irradiance,  $R(\lambda)$  is the surface reflectance, and  $T(\lambda)$  is the atmospheric transmittance. The atmospheric transmittance varies due to individual absorption lines of the atmospheric constituents. The depth of these lines is a direct response to the amount of absorbing material along the atmospheric path. Therefore it is possible to identify the absorption lines of various gases and to retrieve their concentration from the relative depth, when a measurement of high spectral resolution is obtained. Contrary to the spectroscopic emission technique, the weighting is significant

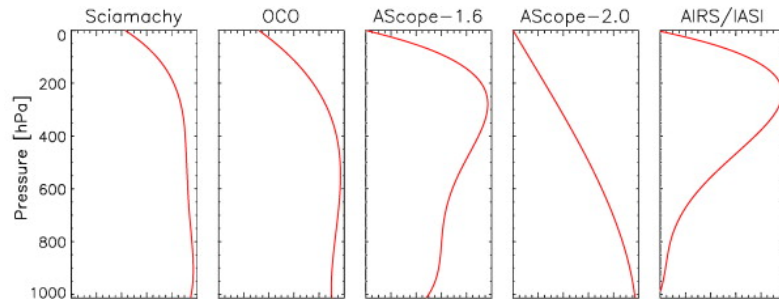


FIGURE 2.6: The weighting functions for a number of Earth observation instruments. Variations due to different surface types and temperature variations is not shown. GOSAT weighting function is similar to SCIAMACHY and OCO. A-SCOPE (1.6 and 2.0 micron) LIDAR concepts have been proposed for the monitoring of CO<sub>2</sub> from space. The instruments did not, however, pass the ESA selection process (Bron and Ciaï, 2010).

in the lowermost atmosphere: the weighting function is either nearly constant along the vertical or gives more weight to the high-pressure levels. For methane, the favourable absorption wavelengths are at around 1.65  $\mu\text{m}$  and 2.33  $\mu\text{m}$ . The surface reflectance does show some spectral variations (i.e.,  $R$  varies with  $\lambda$ ), but these variations are relatively smooth. For a limited spectral range,  $R$  may be approximated by a constant or a linear function of wavelength. Similarly, the solar irradiance  $E_0$  varies smoothly with wavelength, except for a few well-identified so-called Fraunhofer lines.

The disadvantage of SWIR sensing of greenhouse gases is that the technique requires a clear line of sight between the top of the atmosphere and the surface. The presence of thick clouds over the measurement location renders the data unusable. It also requires the Sun to be sufficiently high above the horizon to limit scattering in the atmosphere. The measurements also cannot be carried out over the ocean, except when the sunglint mode is used. Water is dark at the wavelengths of interest and the use of sunglint coverage is spatially limited. GOSAT, for example, makes it possible to use the mode in the tropics only ( $\sim 30^\circ\text{N}$  to  $\sim 30^\circ\text{S}$ ). Another constraint is that the surface reflectance must be sufficiently high, as it has a direct impact on the signal-to-noise ratio. Snow is also relatively dark, thus high latitudes are not sampled during the winter season. Of the current and planned SWIR observing satellites, GOSAT, Sentinel 5-P and CarbonSat are of particular interest, as the ability of the developed inversion algorithm to constrain methane inventories using measurements from these instruments is investigated in this thesis.

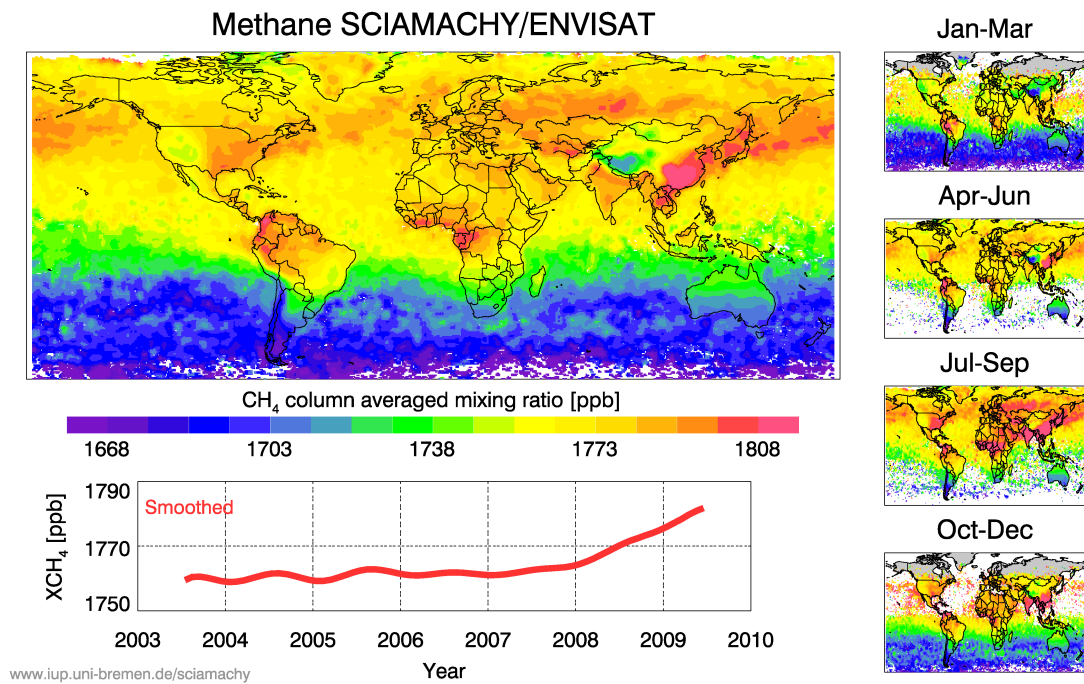


FIGURE 2.7: Global and seasonal maps of SCIAMACHY measured atmospheric CH<sub>4</sub> concentrations. The red curve is a smoothed time series (Buchwitz, 2007).

### SCIAMACHY onboard ENVISAT

Launched in 2002, ENVISAT was Europe's largest Earth observation satellite to date, with a total mass of 8211 kg. The contact with the satellite was lost on 8<sup>th</sup> of April, 2012 and ESA formally announced the end of ENVISAT's mission on 9<sup>th</sup> of May, 2012. SCanning Imaging Absorption SpectroMeter for Atmospheric Cartography (SCIAMACHY) was one of the ten instruments onboard ESA's ENVISAT. SCIAMACHY was an imaging spectrometer, whose primary mission objective was to perform global measurements of trace gases in the troposphere and in the stratosphere. SCIAMACHY had 8 spectral channels, ranging in wavelength from 214 (UV) to 2386 nm (Short Wave IR). SCIAMACHY was used to obtain the concentrations of CH<sub>4</sub>, CO<sub>2</sub> and O<sub>2</sub> in addition to clouds and aerosols. Channels 6 (971–1773 nm) and 8 (2259–2386 nm) were used for retrieving methane, although retrievals from channel 8 had been problematic due to a build up of an ice layer (Frankenberg et al., 2006). SCIAMACHY had a typical ground pixel size of ~30 × 60 km (Buchwitz et al., 2005).

### GOSAT

Greenhouse gases Observing SATellite (GOSAT) was launched on January 2009 by JAXA and is the first satellite dedicated to GHG monitoring. The primary purpose of

the GOSAT project is to estimate emissions and absorptions of greenhouse gases on a subcontinental scale.

The instrument has two sensors onboard: TANSO-FTS and TANSO-CAI (Center for Global Environmental Research, NIES, 2010). Tanso-FTS is a Fourier transform spectrometer that senses radiation from the Sun that has been reflected from the Earth in the SWIR and in the TIR spectral regions. The SWIR region is measured in three spectral bands and the TIR in one band as shown in Figure 2.1. The sensor is able to observe any selected point on Earth, as it has a two-axis pointing mechanism. In the normal observation pattern (mode 5), five points are observed in a single sweep. A zigzag sequence results in a mesh of exposures, where the total number of global measurements is about 56000, every 3 days. The column measurements of CO<sub>2</sub> and CH<sub>4</sub> can only be obtained under clear sky conditions and therefore only 2 - 5% of the data collected is usable (Center for Global Environmental Research, NIES, 2010). GOSAT also has a so-called sunglint mode, where the sensor is pointed point at an angle where the sunlight is reflected off of the surface of the water. The sunglint mode gives brighter sun reflection and consequently, more accurate observation. Retrievals over water when the sunglint mode is not used, are usually impossible owing to low radiance.

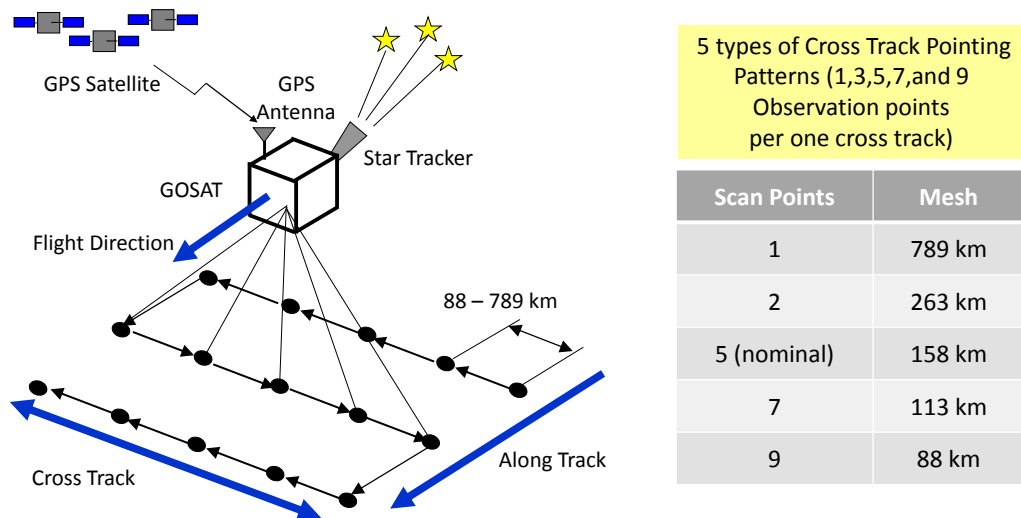


FIGURE 2.8: GOSAT observation modes (Hamazaki, 2005).

The instrument uses a solar irradiance calibration for the SWIR observations and a blackbody calibration for the TIR observations. The ground pixel of GOSAT is in the shape of a skewed ellipse, with a diameter of approximately 13 km.

TANSO-CAI (Cloud and Aerosol Imager) is the second sensor fitted on the GOSAT satellite. It can be used to measure cloud coverage and thickness, as well as aerosol type

Band	1	2	3	4
	Visible	SWIR	SWIR	TIR
Polarised light observation	Yes	Yes	Yes	No
Spectral Coverage (cm <sup>-1</sup> )	12900 - 13200	5800 - 6400	4800 - 5200	700 - 1800
Spectral Resolution (cm <sup>-1</sup> )	0.2	0.2	0.2	0.2
Out of Band Characteristics	Transmittance of 0.1% or less in the spectral range of < 12700 cm <sup>-1</sup> > 13400 cm <sup>-1</sup>	Transmittance of 0.1% or less in the spectral range of < 5000 cm <sup>-1</sup> > 6800 cm <sup>-1</sup>	Transmittance of 0.1% or less in the spectral range of < 4500 cm <sup>-1</sup> > 5500 cm <sup>-1</sup>	Transmittance of 0.1% or less in the spectral range of < 600 cm <sup>-1</sup> > 3800 cm <sup>-1</sup>
FWHM of the instrument function	0.6 cm <sup>-1</sup> or less	0.27 cm <sup>-1</sup> or less	0.27 cm <sup>-1</sup> or less	0.27 cm <sup>-1</sup> or less
Targeted Gases	O <sub>2</sub>	CO <sub>2</sub> , CH <sub>4</sub> , H <sub>2</sub> O	CO <sub>2</sub> , CH <sub>4</sub> , H <sub>2</sub> O	CO <sub>2</sub> , CH <sub>4</sub> , H <sub>2</sub> O

Table 2.1: Specifications of TANSO-FTS onboard GOSAT.

and thickness. TANSO-CAI helps to filter out any observations made by TANSO-FTS that do not receive radiance from the Earth's surface, hence excluding cloudy or partially cloudy observations that can not be used to retrieve the concentration of methane near the surface.

### Sentinel-5 Precursor

The Sentinel-5 Precursor mission is intended to provide data continuity for SCIAMACHY and for NASA's OMI instrument aboard the Aura satellite, in the interim between the end of the Envisat and Aura missions and the launch of Sentinel-5. The Sentinel-5P will extend the data records of these missions as well as be a preparatory mission for Sentinel-5. The TROPospheric Monitoring Instrument (TROPOMI) aboard the Sentinel-5P is a pushbroom imaging spectrometer with four spectrometers covering the spectral range from UV to SWIR (Maresi et al., 2013) (Figure 2.9 shows the spectral range of the instrument). It is able to measure a number of compounds, such as NO<sub>x</sub> (NO+NO<sub>2</sub>), CO, CH<sub>4</sub>, aerosols, SO<sub>2</sub>, and VOCs (Volatile Organic Compounds) (via CH<sub>2</sub>O and CHO-CHO). The SWIR band in the spectral range of 2305–2385 nm is for imaging CH<sub>4</sub>, as well as CO. The spectral resolution varies from 1 nm in the shortest UV band, to 0.25 nm in SWIR and to about 0.5 nm in the remainder of the bands (Veefkind et al., 2012). The Sentinel-5P reference orbit is a near-polar frozen sun-synchronous orbit with a mean Local Solar Time at Ascending Node (LTAN) of 13:30 h and a repeat cycle of 17 days. The TROPOMI observations will also have a synergy with the MetOp GOME-2 and IASI morning observations, thus providing two observations during the day.

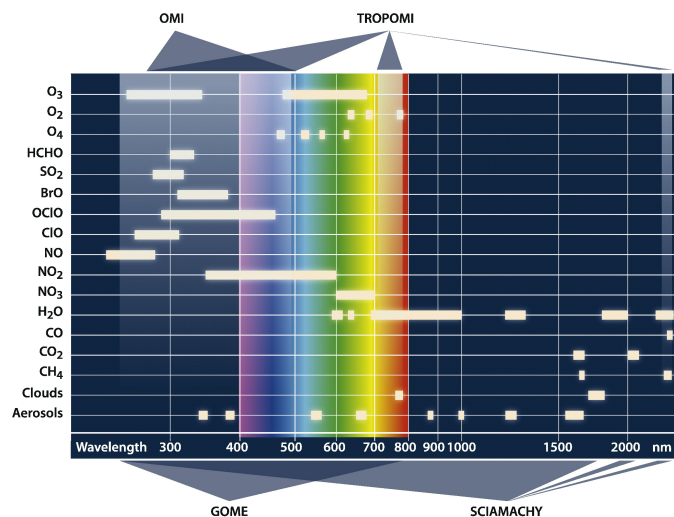


FIGURE 2.9: The spectral range of the TROPOMI, as well as SCIAMACHY, OMI and GOME instruments. (Veefkind et al., 2012).

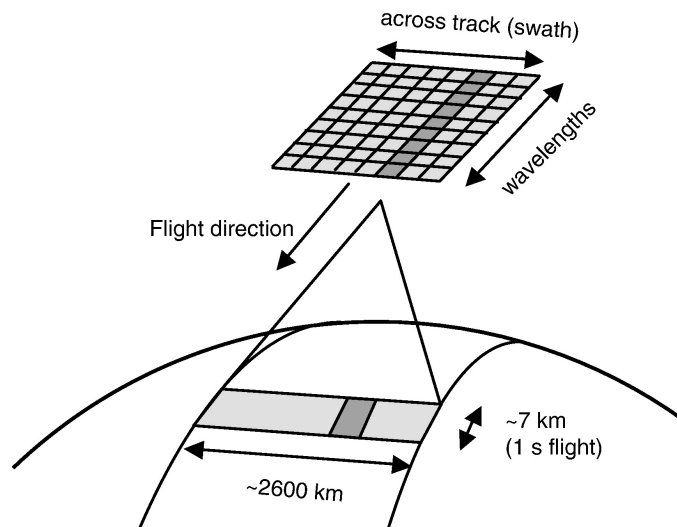


FIGURE 2.10: The measurement principle of the TROPOMI instrument onboard Sentinel-5P. All of the ground pixels in the swath are measured simultaneously (Veefkind et al., 2012).

### CarbonSat

CarbonSat has been selected by ESA to be one of the two candidate Earth Explorer Opportunity Missions (EE-8) to be launched in 2018 (Buchwitz, 2010). The instrument has been proposed to continue the CO<sub>2</sub> and CH<sub>4</sub> global measurement time series after SCIAMACHY and GOSAT, i.e. after 2014, and to deliver important additional information on CO<sub>2</sub> and CH<sub>4</sub>. The instrument is proposed to have a high spatial resolution (2 x 3 km<sup>2</sup>) and a good spatial coverage (300 km gap-free across and along track ground swath). The instrument specifications have not yet however, been finalised. CarbonSat

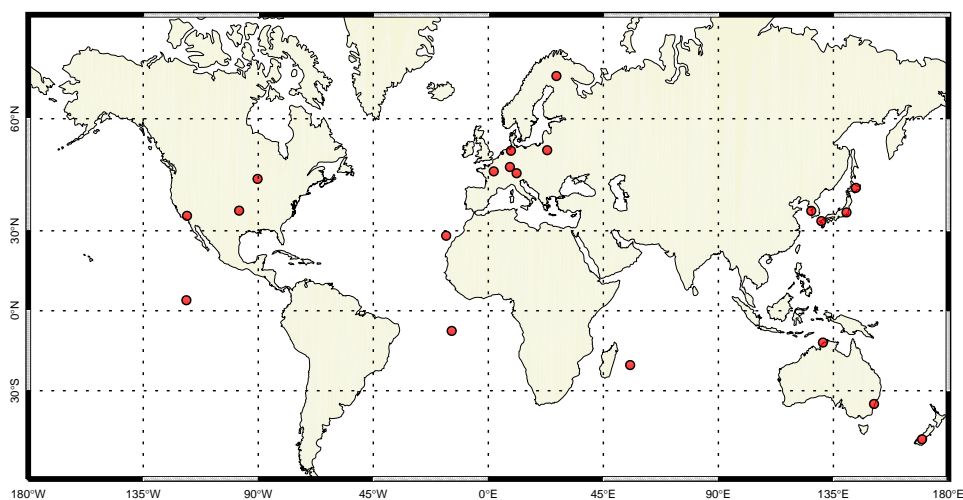


FIGURE 2.11: Map of the operational TCCON sites (as of July, 2014).

will enable the global imaging of localised strong emission sources such as cities, power plants, methane seeps, landfills and volcanos (Buchwitz et al., 2013). The sunglint mode will also be available to be used over water, allowing to track strong marine geological  $\text{CH}_4$  emission sources including large seeps, mud volcanoes or methane releases from the destabilization of shallow marine arctic gas hydrates. The single measurement error is modelled to be typically  $\sim 10$  ppb (Buchwitz et al., 2013).

### TCCON network

TCCON was setup in 2004 with the installation of the first instrument in Park Falls, Wisconsin, USA, and has since grown to 19 operational sites worldwide (Figure 2.11). It is a network of ground-based Fourier transform spectrometers (FTSs), designed to retrieve column abundances of  $\text{CO}_2$ ,  $\text{CH}_4$ ,  $\text{N}_2\text{O}$  and  $\text{CO}$  from near-infrared (NIR) solar absorption spectra. Column measurements help disentangle the effects of atmospheric mixing from the surface exchange. The retrieved column mixing ratios are insensitive to variations in surface pressure and atmospheric water vapour, in contrast to the in situ surface measurements which are greatly affected by local sources and vertical transport. The observed concentration values are therefore more directly related to the underlying regional-scale fluxes. The scientific goals of the network are to improve our understanding of the carbon cycle, to provide the primary validation dataset for retrievals of  $\text{XCO}_2$  and  $\text{XCH}_4$  from space-based instruments, and to provide a transfer standard between the satellite measurements and the ground-based in situ network (Wunch et al., 2011).

The TCCON sites at Park Falls, Darwin, Lamont, Orléans, Bialystok and Lauder are

also co-located with, or near tall towers or surface in situ measurements. This makes it possible to make intercomparisons with aircraft measurements, as well as assimilated data products such as Carbontracker. These measurements are directly comparable with the near-infrared total column measurements from space-based instruments, thus providing the primary validation dataset for space-based XCO<sub>2</sub> and XCH<sub>4</sub> retrievals (Dils et al., 2013; Yoshida et al., 2013). TCCON makes it possible to identify temporal drifts and spatial biases in calibration in the calibration of the comparison instruments. The accuracy of the retrievals from TCCON spectra is also minimally influenced by aerosol, uncertainty in airmass or variation in land surface properties, in contrast to the reflected sun observations of the space-based sensors.

### **2.3.3 Active sensing (LIDAR)**

Active sensing differs from the previously described methods, as it makes use of an artificial radiation source. LIDARs have their own light source emitting pulsed narrow-line laser radiation, not relying on sunlight or radiation emitted by the Earth. Differential Absorption Lidar (DIAL) measurements of trace gases in the atmosphere rely on the highly wavelength-selective absorption of laser light by molecules. When considering the selection of appropriate absorption lines, a number of factors have to be considered, such as overlaps by other absorbing trace gases have to be avoided, and temperature-insensitive absorption lines with suitable strength have to be selected. For methane, lines with appropriate strength are found in two water vapour transmission windows at around 1.6 and 2.3  $\mu\text{m}$  (Kiemle et al., 2011). The retrieval makes use of the difference in atmospheric transmission between a laser emission with a wavelength placed at or near the centre of a methane absorption line, denoted on-line, and a reference off-line wavelength with significantly less absorption. Radiation of the two distinct wavelengths is first 'fired' at the surface of the Earth. A small fraction of the emitted photons are scattered by cloud, or reflected from the surface of the Earth back towards the instrument's receiver. The Integral-Path Differential-Absorption (IPDA) implementation of the DIAL principle exploits this reflected radiation to obtain the column mixing ratio of the greenhouse gas of interest (Ehret et al., 2012).

LIDAR instruments have a number of advantages over sensing sensing with other techniques. Greenhouse gas retrievals from SWIR sensing instruments, such as GOSAT and SCIAMACHY, are complex and error prone as they involve complex bias correction schemes to deal with aerosol/cloud scattering in the light path. Using a range-gated receiver and a pulsed laser transmitter, any biases from aerosols and clouds in the light path

can be avoided. This eliminates the largest error contributor to the solar spectroscopy method, which greatly affects passive instruments. The use of TIR sensing instrument measurements are on the other hand limited by the instrument being more sensitive to the middle and the upper troposphere rather than the lower troposphere, where the sources and sinks reside. Figure 2.6 shows the typical weighting functions for existing or proposed space-borne greenhouse gas monitoring instruments. LIDARs can also obtain measurements during the night as well as day. The on-board radiation source gives active instruments the ability to measure at high latitudes during all seasons, in contrast to the passive method, which requires the Sun to be relatively high above the horizon. There are currently no space-borne operational LIDAR missions, although a Methane Remote Sensing Lidar Mission (MERLIN) is scheduled for launch at 2019.

## **2.4 Bottom-up emission estimation**

Methane emissions can be estimated utilising two approaches, which are bottom-up and top-down. Bottom-up is a calculation of the total emissions based on emission factors: the amount of pollutant gas typically released per unit of coal or natural gas sold, or the amount released by a single ruminant animal. This section gives example approaches taken to compile two such inventories, rice field and emissions by animals. A top-down approach on the other hand relies on the current atmospheric measurement at a given time and using meteorological data and statistical analysis to trace it back to the sources. An advantage of inverse modelling is that it can provide an independent verification of the emission factor based flux estimates. This section gives an overview of both, bottom-up and inverse approaches of forming emission inventories, with a particular emphasis on inversions of space-borne methane observations.

Compiling accurate emission inventories for natural methane, such as rice fields, is a problematic process. While the emission processes for gases of such as  $\text{CO}_2$  are well understood, the emission sources of  $\text{CH}_4$  are very heterogeneous. Currently, emissions from rice fields are reported using a method defined by the IPCC. Annual harvested areas and seasonally integrated emission factors based on an area are used to form an inventory. The emission factors are first calculated experimentally. The amount of gas emitted in a small area of a rice field is collected and the emissions are then up-scaled to the whole of the rice field. It has to be remembered that methane is formed by archaea, therefore a sample collected on one end of the field might not necessarily be representative of the whole field. The assumption of uniformity when scaling up a measurement from a small area can lead to big errors, as it cannot be guaranteed that the same amount of mi-

croorganisms is present somewhere else under exactly same conditions. The variability in water management practices, the used fertiliser and the soil type will all affect CH<sub>4</sub> emissions. Where the data on the growing conditions is not available (such as more rural areas in third world countries), assumptions have to be made. The emissions from wetlands are just as variable - sampling then up-scaling does not necessarily represent the production of methane in the whole of the wetlands. Walter et al. (2007) estimated the amount of methane released from northern lakes utilising a bottom-up approach. This was done by estimating point-source ebullition for 16 lakes in Alaska and Siberia, representing several different lake types. The measurements are then extrapolated from these 16 sites to all lakes North of 45° using circumpolar databases and permafrost distributions.

Livestock methane emission estimates are usually based on the multiplication of the heads of the livestock by emission factors, such as provided by IPCC (Eggleston et al., 2006) (Quantifying Methane Emissions from Livestock, 2012). The IPCC Guidelines for National Greenhouse Gas Inventories provide definitions of livestock annual population subcategories, whilst higher tier reporting requires details of feed intake and characterisation.

The emissions of CH<sub>4</sub> in livestock occurs during enteric fermentation and release from manure. Suggested feed digestibility coefficients for various livestock categories have been provided by the IPCC, to help estimation of feed intake for use in calculation of emissions from these sources. Tier 1, or basic characterisation for livestock populations requires animal species and categories to be defined as well as annual populations. Initially a complete list of all livestock populations in a country that have default emission factor values are developed (e.g, dairy cows, deer and poultry). Waste characteristics among the different populations of certain animal species, such as poultry, varies significantly. For increased accuracy the poultry populations can further be subdivided (e.g., layers, broilers, turkeys, ducks, and other poultry). The tier 2 livestock characterisation requires more detail, such as livestock population by subcategory along with the feed intake estimates for each. The emission factors then can be estimated for each subgroup in terms of a mass of methane released. The step can rely on default emission factors which is drawn from literature (tier 1), or require detailed country-specific data on gross energy intake and methane conversion factors for specific livestock categories (tier 2). The sum of the emission factors multiplied by the calculated subgroup populations results in the total CH<sub>4</sub> emission estimate. Estimating emissions from manure can also be complex and can take into consideration a number of factors. Climate region, or the temperature along with manure management practices, can be taken into account, depending on the

tier the country is reporting its emissions at.

Emissions from the oil and gas industry are also reported utilising provided emission factors (U.S. Government, 2013). The total sum of the calculations has to take into account a number of possible release points for methane, in the production and storage of oil and natural gas. CH<sub>4</sub> emissions are reported from onshore production storage tanks, gas well venting during completions and workovers from hydraulic fracturing and natural gas pneumatic device venting. To calculate the total mass of CH<sub>4</sub> released from natural gas pneumatic device venting for example, the calculation has to take into account the total number of natural gas pneumatic devices of different types, the concentration of methane in the gas, as well as the emission factors.

## **2.5 Modelling methane emissions**

An atmospheric transport model is a mathematical model constructed around a set of primitive dynamical equations that govern atmospheric motions. Modern complex models, such as the Numerical Atmospheric Modelling Environment (NAME), which is the primary tool used in this thesis and which will be discussed in Section 2.5.4 in more detail, also include parameterisations for turbulent diffusion, the kinematic effects of terrain and convection. These models in effect can provide a mathematical link between emissions and atmospheric observations (Figure 2.12). The models can use existing emission inventories to predict the concentration of a gas at a location (known as forward modelling). Inverse modelling on the other hand is the identification of sources or sinks from an atmospheric observation of an atmospheric constituent. For inverse modelling, three pieces of information are needed to statistically map the emissions: the observation of the trace gas of interest, an a priori to provide the inversion algorithm the best current estimate of fluxes and a description of atmospheric transport from the observation to the potential sources (provided by an atmospheric transport model).

The choice of a model depends on a number of factors, such as the temporal and spatial scale of the atmospheric processes involving the pollutants, as well as complexity of the topography of the region in question. In terms of spatial scale, models can be classed as local, regional, continental or global. Microscale models operate at approximately 1 km and higher spatial resolution and can be used to model phenomena, such as turbulence in an urban street canyon. Mesoscale models have dispersion modelling capabilities up to a few hundred kilometres and are typically used to quantify the transport and deposition of pollutants, such as sulphur and nitrogen oxides and photo-oxidants,

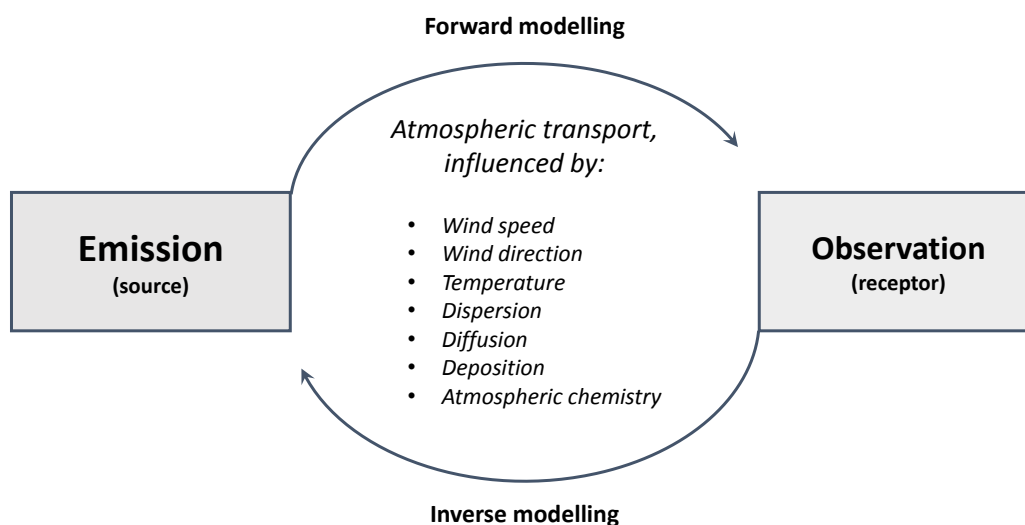


FIGURE 2.12: Atmospheric modelling: forward and inverse approaches. An atmospheric transport model provides the link between the emission and the observation of a pollutant. The model must model the atmospheric transport of the pollutant, taking into account atmospheric variables, such as the temperature and wind speed, as well as the chemical processes acting on it. Methane has a relatively long atmospheric lifetime, thus the atmospheric sink can be ignored owing to the short run time of 10 days in this work.

such as ozone. Continental and global scale models are used for long range transport of pollutants and their interaction with climate (from hundreds to thousands of km). Global scale models cannot resolve sub-grid scale effects, such as man-built obstacles and terrain variations below the resolution of the model run.

Gaussian plume models were widely applied when studying dispersion of pollutants. Gaussian models assume steady-state conditions and homogeneous flow within the domain of interest. This method is computationally cheap to run, however the assumptions of homogeneous turbulence and homogeneous underlying surface are too restrictive for many practical applications. The method is not suitable if the pollutant is chemically reactive in nature and is unable to predict concentrations beyond the radius of approximately 20 km. If the scenario is more complex, the use of 3-D Lagrangian and Eulerian models is preferred. The differences between the two approaches will be described in Section 2.5.1.

On the subcontinental scale, inversions of the data from the ground measuring sites can provide a good estimate of regional emissions. To calculate the emissions on a larger scale reliably, remote sensing instruments have to be used. The aim of this project is to develop a method to constrain these uncertain emissions of methane utilising spaceborne measurements. Data from the GOSAT instrument has not yet been used along with

a Lagrangian transport model for testing emission inventories and mapping CH<sub>4</sub> fluxes.

### 2.5.1 Eulerian and Lagrangian models

Atmospheric transport models can be based on either Eulerian or Lagrangian formulations of the fluid transport process (Pillai et al., 2012) (Figure 2.13). Both of these approaches are used by the inverse modelling community (Bergamaschi et al., 2013; Gerbig et al., 2003; Manning et al., 2003; Rodenbeck et al., 2003). The Lagrangian approach assumes a moving frame of reference and the Lagrangian atmospheric transport models work by releasing tracer particles into the model atmosphere. The tracer particles represent the atmospheric constituent, which is then carried by the local 'mean wind' and other processes, such as diffusion, as well as a random walk scheme. The particles can represent a number of chemical species, the mass of which can be depleted by chemical and various physical processes during its lifetime, such as wet or dry deposition; the Lagrangian equations of mass and momentum are solved in each time step. Let  $\psi$  represent the particle concentration (or any other required state variable) and  $S$  be the source term.  $D\psi/Dt$  represents the rate of change of concentration as it is carried by the fluid. The change of  $\psi$  in the Lagrangian frame of reference is therefore:

$$\frac{D\psi}{Dt} = S. \quad (2.4)$$

Eulerian models assume a stationary frame of reference. The concentration of the pollutant is calculated as a function of space and time, instead of calculating the trajectories of tracer particles. The calculation is done on a fixed three-dimensional grid of points. The Lagrangian perspective can be converted to the Eulerian frame of reference with the addition of the nonlinear advection term  $u \times \nabla\psi$ .  $D\psi/Dt$  now represents the rate of change at the fixed position and  $\nabla$  is the spatial gradient operator at the said position (Lin, 2013). Eulerian reference frame is described as:

$$\frac{D\psi}{Dt} + u \times \nabla\psi = S \quad (2.5)$$

If  $u$  is defined as  $Dx/Dt$ , the velocity  $u$  can be integrated over time to yield the position of the air parcel  $x$ , at various time steps. Integrating the equation  $Dx/Dt = u$  gives the simplest first-order solution:

$$x(t_0 + \nabla t) = x(t_0) + u(t_0) * \nabla t + \dots, \quad (2.6)$$

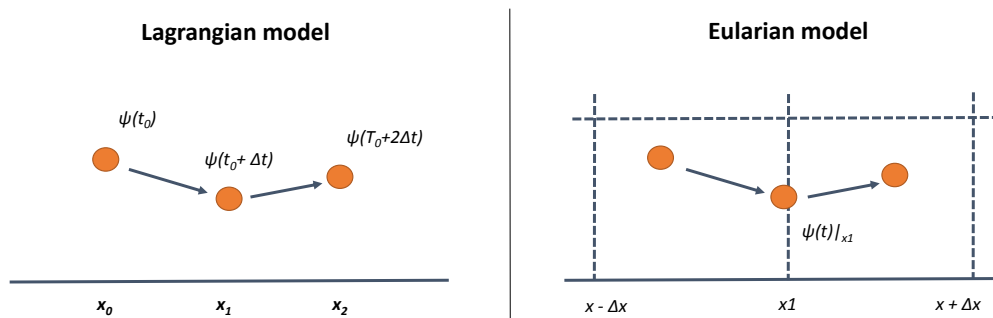


FIGURE 2.13: Lagrangian (a) and Eulerian (b) approaches to modelling flow.

Lagrangian models hold a number of advantages over Eulerian models (Lin, 2013):

- *Trajectory Information:* The model simulations contain trajectory information absent in the Eulerian model outputs. The knowledge of air-parcel trajectories contain a wealth of information that can be analysed to answer a number of scientific questions. This allows us to carry out cluster analysis or more complex inversions to compute the fluxes of required pollutants.
- *Near source representation:* Lagrangian models are efficient close to the source of the pollutant, where gridded computations utilising a Eulerian model would require a very fine resolution to handle large gradients.
- *Realistic physical representation:* The atmosphere could be said to be a Lagrangian system. The pollutant molecules are carried by the flow of the wind, which gives the Lagrangian models the potential to better model phenomena, such as mixing and convection.
- *Lack of numerical diffusion:* The Lagrangian approach has the advantage against Eulerian models due to the fact that no grid is used for computation, thus spatial discretisation errors like numerical diffusion are avoided. The result can be interpolated to any grid, which means that the model error is independent of the output resolution.
- *Resolving subgrid scale variability:* Lagrangian models offer good representation of near source effects which would be sub-grid in a Eulerian model. This is made possible by the fact that the air parcels are not tied to regular grid cells.

The disadvantages of Lagrangian models are (Lin, 2013):

- *Computational cost:* The computational cost of running a Lagrangian models can be significant if run with a large number of particles when small time steps are adopted. The disadvantage associated with the running cost can be mitigated when the run is 'parallelised' i.e. the model run load can be split among a number of individual processors when dispersion of a chemically inert gas is simulated.
- *Irregularity of grids:* Lagrangian model air parcel positions are not fixed (in contrast to the grid cells in Eulerian models). A grid comprised by the ensemble of trajectories is irregular, thus requiring an additional step of parcel insertion or merging.
- *Inconsistencies with Eulerian model derived met data:* The Lagrangian models run on the Numerical Weather Prediction (NWP) model gridded meteorological data. The lack of close integration with the NWP models and the lack of access to meteorology with Lagrangian model run time-step resolution can lead to inconsistencies with one another. Disparity is noticeable when variables are interpolated from internal model coordinates to common pressure levels.

## 2.5.2 Inverse modelling of methane using global models

Eulerian models have been utilised to invert surface greenhouse gas measurements (Bergamaschi et al., 2005, 2010; Bousquet et al., 2011; Houweling et al., 1999; Meirink, Bergamaschi and Krol, 2008; Pison et al., 2009; Rigby et al., 2011; Rodenbeck et al., 2003) and more recently, space-borne column observations of methane (Bergamaschi et al., 2009, 2013; Fraser et al., 2013; Meirink et al., 2008; Spahni et al., 2011) as well as other greenhouse gases. The studies utilise the Bayes theory to constrain the emissions from atmospheric measurements. The Bayes theory describes how to determine the distribution of a set of parameters (in this case, emissions) consistent with estimates of the remotely observed quantity that are closest to the distribution of these observations, while simultaneously accounting for prior information regarding reasonable values of these parameters (Streets et al., 2013). The methods used vary based on the desired spatial and temporal scales of the analysis in question and errors in the inversion inputs are determined and propagated throughout the analysis.

Traditionally, inverse modelling studies have been based on the synthesis approach (Houweling et al., 1999). The method involves seeking a linear combination of fluxes, such that the linear combination of the calculated responses matches the observed data (Enting et al., 1995). This approach is mainly applicable when emissions are optimised

for a limited number of pre-defined regions (i.e. a coarse resolution). An example of such study, utilising only NOAA surface network recorded greenhouse gas concentrations is described by Rodenbeck et al. (2003). The authors of the study estimated the inter-annual variations and spatial patterns of surface CO<sub>2</sub> fluxes in the period of 01/1982–12/2000 using a time-dependent Bayesian inversion technique. The simulations are based on the observed CO<sub>2</sub> concentration data measured by NOAA network of sites during the years of 1980–2001. The concentration data of the individual measurements are used directly, i.e. no gap filling or smoothing is done. However data sets with temporal gaps of longer than two months were not utilised to avoid trends being introduced by the changes in the sampling network in time. The transport of carbon dioxide was simulated using a global off-line Eulerian atmospheric transport model TM3 (Heimann, 2006), driven by meteorological fields derived from the NCEP reanalysis. The simulation was run at a spatial resolution of 4° latitude × 5° longitude and with 19 vertical levels. To compute the relationships between fluxes and concentrations computationally efficiently, an adjoint version of the model was used.

With the availability of GOSAT and SCIAMACHY data, Earth observation satellite measurements have also been assimilated into Eulerian models. The synthesis approach described earlier is used when inverting relatively small sets of observational data. To take a full advantage of satellite measurements, approaches that can handle large amounts of observations together with a large control vector are required. One such approach, a four-dimensional variational (4D-Var) data assimilation system for inverse modelling of atmospheric methane emissions, was developed by Meirink et al. (2008) and Bergamaschi et al. (2013). The Bergamaschi et al. 4D-Var system is based on the off-line Eulerian transport model TM5 and is driven by meteorological fields from the European Centre for Medium-Range Weather Forecasts (ECMWF) ERA-Interim reanalysis. The model is run at a spatial resolution of 6° longitude × 4° latitude, with 25 vertical levels.

The set of model parameters (state vector  $x$ ) is optimized by iteratively minimising the cost function, shown in Equation 2.7. The state vector includes the emissions per model grid cell, month, and emission group, the initial 3-D CH<sub>4</sub> fields at the beginning of each inversion series, and the parameters for the bias correction of the SCIAMACHY retrievals:

$$j(x) = \frac{1}{2}(x - x_B)^T B^{-1}(x - x_a) + \frac{1}{2} \int_{i=1}^n (H_i(x) - y_i)^T R_i^{-1}(H_i(x) - y_i), \quad (2.7)$$

where  $x_B$  is the a priori estimate of  $x$ ,  $B$  the parameter error covariance matrix,  $y$  the set of observational data,  $R$  the observation error covariance matrix, and  $H(x)$  the model simulations corresponding to the observations. A semi-exponential description of the probability density function for the a priori emissions was applied to avoid negative a posteriori flux emissions.

Bergamaschi et al. derived the global total emissions for 2007–2010 to be 16–20 Tg CH<sub>4</sub> year<sup>-1</sup> higher compared to 2003–2005. Most of the inferred emission increase was located in the tropics (9 - 14 Tg CH<sub>4</sub> year<sup>-1</sup>) and mid-latitudes of the northern hemisphere (6 - 8 Tg CH<sub>4</sub> year<sup>-1</sup>). The authors state that the derived emissions are largely consistent among all inversions, however significant differences in the exact latitudinal attribution of the inter-annual variations of CH<sub>4</sub> emissions were apparent between the inversions using SCIAMACHY + NOAA data and those using only the NOAA surface observations. The differences were calculated to be largest in the tropics. Comparison with BARCA aircraft campaign data (November, 2008 and May, 2009), used to validate the model, shows a significant improvement of the SCIAMACHY + NOAA inversions compared to the NOAA only inversions in the free troposphere over the Amazon. The concluding remark is that one has to be cautious regarding conclusions about the derived inter-annual variations, as potential artefacts in the SCIAMACHY retrievals cannot be ruled out.

Inversions using GOSAT observations have been carried out with GEOSCHEM chemistry transport model utilising an ensemble Kalman filter (EnKF) (Fraser et al., 2013). The simulated time period was from June 2009, until December 2010, which also used proxy dry-air NOAA ESRL and CSIRO GASLAB (Global Atmospheric Sampling Laboratory) CH<sub>4</sub> surface mole fraction measurements. The global a posteriori estimates using GOSAT and/or surface measurements are found to be between 510–516 Tg year<sup>-1</sup>. In the study, a series of Observing System Simulation Experiments (OSSEs) were also carried out to test the ability of the EnKF to retrieve reliable fluxes using the observed distribution of clear-sky GOSAT measurements in the presence of random and systematic errors. The GOSAT data was initially simulated by sampling the GEOS-Chem model at the location of the clear-sky GOSAT observations. A randomly generated error was then added to the model based on the error of the actual GOSAT measurement and assuming a Gaussian distribution. In addition, a global bias of 10 ppb was added as well as a latitudinally varying bias with minima at the poles (5 ppb) and a maximum at the equator (15 ppb). In these idealised experiments, it was found that the inversion scheme is able to retrieve fluxes within 10% of the known true fluxes in most regions. In tropical regions with only a few observations, retrieved fluxes are within 15% of the true values.

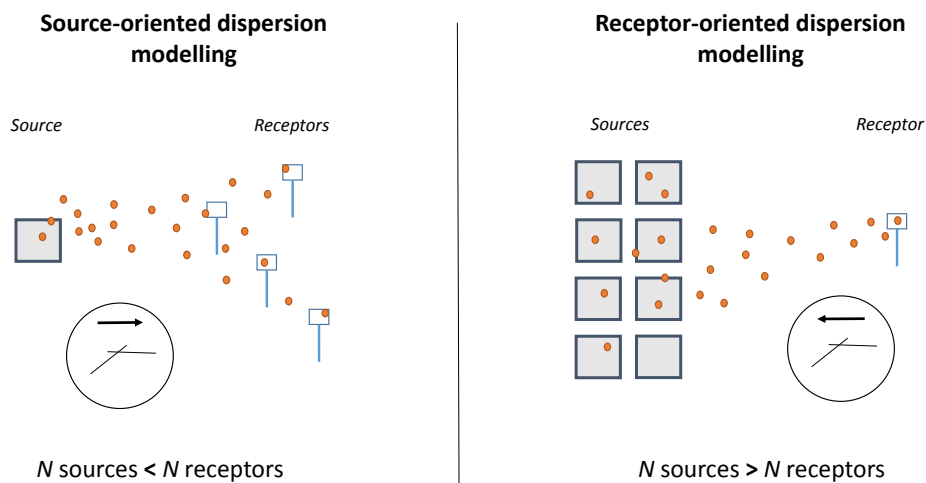


FIGURE 2.14: Modelling with Lagrangian Particle Dispersion Models (LPDMs): source-oriented (left) and receptor-oriented (right) approaches (Lin et al., 2007).

### 2.5.3 Atmospheric modelling using Lagrangian models

Two approaches could theoretically be used to model the atmospheric transport of a trace gas to the receptor (measuring location). The Lagrangian Particle Dispersion Model (LPDM) could be run in the forwards or in a receptor-oriented, backwards mode (Figure 2.14). The forward mode would involve the release of the tracer particles at each possible source grid in the domain of interest, which would then be 'followed' to the receptor site. The concentration of each individual tracer at the measurement site would then be obtained, thus linking all the potential emitter cells to the observation. In the receptor-oriented mode, the tracer particles are released at the measurement location and the mean wind trajectories are reversed. The concentration of the tracer at the source location grids are then calculated. The receptor-oriented mode has been used in a number of studies owing to increased computational efficiency (Manning et al., 2011; Ryall et al., 2001; Stohl et al., 2009). It is advantageous to utilise the backward mode if there is greater number of sources than receptors (Seibert and Frank, 2004).

#### Previous studies

A number of studies have made use of Lagrangian models to help understand long-lived trace gas emissions (Kort et al., 2008; Lin et al., 2004; Manning et al., 2011, 2003; Polson et al., 2011; Stohl et al., 2009; Uglietti et al., 2011; Zhao et al., 2009). Most studies run the model in a backward-time mode, due to there being a larger number

of source elements than emitter cells (see Figure 2.14). In addition, all of the current studies have used in-situ measurement sites and no known studies have utilised Earth observation systems.

Manning et al. (2011) developed a method to estimate the emissions of CH<sub>4</sub> and N<sub>2</sub>O for each year in the time period of 1990–2007 for the United Kingdom and for Northwest Europe. In the study, only the data from Mace Head monitoring site on the west coast of Ireland is used in conjunction with NAME. An a priori is not used, thus the calculated fluxes are derived independently of any existing estimates. The Lagrangian model is run in backward mode to estimate the history of air over 12 days en route to Mace Head. An air history map has been calculated for each 3 h period from 1995 until 2008, amounting to more than 90,000 maps in total. The model output gives the time-integrated air concentration dosage at each grid box (40 km horizontal resolution and 0 - 100 m above ground level). It can be said that the boxes identified will contribute towards the observed concentration at Mace Head with addition of the atmospheric background. The background calculation is based on the NAME dilution calculations. A 3 h period is classed as background if it meets certain criteria with respect to a dilution sensitivity limit (a threshold above which an emission would generate a discernible signal at the measurement point). The dilution sensitivity is also used to define the inversion grid, which gets more coarse as the distance from the site is increased. Grid boxes that are distant from the observation site, contribute relatively little to the observation at Mace Head, whereas those that are close, can have a large impact. In order to balance the contribution from different grid boxes, those that are more distant are grouped together into increasingly larger blocks.

The iterative best-fit technique, simulated annealing, is used to derive these regional emission estimates. The inversion process works by iteratively choosing different emissions, varying the emission magnitudes and distributions, with the aim of minimising the mis-match between the observations and the modelled concentrations. The relative skill of a derived emission map is tested by comparing the modelled and the observed time series by using a cost function:

$$j = [r(1 - r)] + [0.5NMSE] + [4(1 - fac2)] + [20(1 - facNoise)], \quad (2.8)$$

where  $r$  is Pearson correlation coefficient,  $NMSE$  is a normalised mean square error,  $fac$  is the fraction within a factor of 2 of observations and  $facNoise$  is the fraction of the model values within  $Noise$  of the observations.  $Noise$  is the standard deviation of the background observations about the defined smoothed baseline value.

The simulated annealing best-fit technique and NAME have also been used in a study by Polson et al. (2011) to estimate the UK emissions of a number of trace gases, including CO, CO<sub>2</sub>, CH<sub>4</sub>, N<sub>2</sub>O and various HCFCs. In this particular study, aircraft measurements were inverted to obtain the emission estimates of the gases measured. A FAAM BAe 146 aircraft was used to circumnavigate the UK offshore, measuring the upwind and downwind gas concentrations in the boundary layer. 17 flights were conducted, with measurements that were obtained during periods of westerly wind and absent of deep convection, used in the inversion. The concentration of the pollutants measured upwind was used as the background in the simulations. There was not sufficient time to completely circumnavigate the UK, therefore it was assumed that the background concentration would be constant across the whole inflow region. The inversion predicts the total annual CH<sub>4</sub> emissions of 3500 kt year<sup>-1</sup> on average, with a range of 0–8000 kt year<sup>-1</sup>. It was found that the weighted average used to derive the average emission results biased the average emission to the east coast. Thus the result is less reliable than for the inversions for other gases in the study.

Stohl et al. (2009) constrained the fluxes of halocarbons using in situ measurement data from three global networks, which were the AGAGE, System of System for Observation of Halogenated Greenhouse Gases in Europe (SOGE) and NIES. In contrast to studies by Manning et al., a priori estimates were used as well as inclusion of increased number of measurement points to help better constrain the trace gas emissions. The inversion procedure was based on backward simulations with the LPDM FLEXPART. The transport model represented only concentration fluctuations caused by emissions during a 20 day time window of the air mass history. Older emissions produced a background or baseline mixing ratio in the observations, to which the explicitly modelled part was added. The emission information was extracted from the observed concentration with the baseline, that was itself objectively determined by the inversion algorithm, removed. Stohl et al. defined the baseline as that part of the measured concentration averaged over 31 days that could not be explained by emissions occurring on the 20 d time scale of the model calculations.

Rigby et al. (2011) carried out an inversion of long-lived trace gas emissions using a combination of Eulerian and Lagrangian chemical transport models. The aim was to make use of the strongest aspects of both for simultaneous global and regional emission estimations. The method aimed to address the problem of estimating the atmospheric background of the trace gas, as described earlier. Manning et al. identified Mace Head observations that represented background air and interpolating between them to obtain the baseline. A limitation of this approach was that background mole fractions that were

lower than the observed values cannot be identified. Stohl et al. statistically estimated an offset that is applied to the observations over a time period. The drawback here, is that constant background levels must be assumed over the simulation time-scale. Rigby et al. proposes to use the Lagrangian model to calculate the sensitivity of observations at a particular site to emissions in the near vicinity to the monitoring site. The long-term fate of the emissions, as they were mixed into the global background and the impact of the emissions from one LPDM region on observations at another, were estimated using the Eulerian CTM. The method was then used to derive the global SF<sub>6</sub> emissions using measurements from AGAGE, between 2007 and 2009. The global total trace gas fluxes calculated using the method and large-scale emission patterns agreed well with previous studies, whilst allowing emissions to be determined at higher resolution than in previous studies.

#### **2.5.4 Numerical Atmospheric Modelling Environment (NAME)**

In principle, any Lagrangian model could be used to link sources to observations; models such as FLEXPART (Stohl et al., 2005) or STILT (Lin et al., 2003) could also be suitable for this work. NAME was chosen, owing to the model being installed and available for use at the university of Leicester.

NAME is a Lagrangian atmospheric dispersion model developed by the U.K. Met Office. It was commissioned by the central government following the Chernobyl nuclear accident, as no other operational long-range model was available for use and the Met Office used trajectory techniques to provide specialist forecast at the time. The then so-called 'Nuclear Accident Model' was ready for use by 1988 undergoing major upgrades at 1994 (NAMEII) and 2004 (NAMEIII). The model gave the Met Office the capability to model the transport and deposition of radioactive material in future incidents (Jones et al., 2007). It is now used in a wide range of applications by the Met Office as well as by a number of academic institutions owing to the subsequent developments that have greatly enhanced the model capabilities. The "Numerical Atmospheric Modelling Environment", NAMEIII has been used to model the dispersion of volcanic ash clouds (Devenish et al., 2012; Webster et al., 2012), fire plumes (Webster et al., 2007) and the spread of air-borne diseases (Burgin et al., 2009; Gloster et al., 2003; Sanders et al., 2010). The model has also been used to help constrain national greenhouse gas emission inventories, as was described in Section 2.4.

## Operation

The main principles of the Lagrangian (and Eulerian) perspectives of modelling flow were described in Section 2.5.3. NAME is driven by a combination of meteorological data from the UK Met Office Unified Model and a random walk turbulence scheme. The general equation of motion used in the model is given by Equation 2.9:

$$x_{t+\Delta t} = x_t + (\bar{u}(x_t) + u'(x_t) + u'_l(x_t))\Delta t, \quad (2.9)$$

where the change of a position of a particle ( $x$ ) at time  $t$  over a time period  $\Delta t$  is expressed as the sum of the mean wind at the position of the particle  $\bar{u}$  and the turbulent velocities  $u'$  and  $u'_l$  (Jones, 2013). The turbulent velocities  $u'$  and  $u'_l$  arise from a separate treatment of the turbulence and low-frequency 'meander' scales respectively. NAME uses random-walk techniques to parameterise the dispersion by small-scale atmospheric turbulence and the low-frequency horizontal eddies (known as meander). The aim of the random-walk (representing dispersion) model is to compute an ensemble of random trajectories of Lagrangian particles through a flow field whose statistics are known (Jones, 2013).

Standard Brownian motion, or diffusion, is the simplest example of a random-walk model. The diffusion of a Lagrangian particle is described by its diffusivity,  $K = (K_x, K_y, K_z)$ , which is related to the turbulent velocities and timescales of atmospheric motions. Turbulence profiles can be constant with height within the planetary boundary layer (PBL), known as homogeneous turbulence or may vary with height (inhomogeneous turbulence). NAME assumes the along-wind and cross-wind spreads to be equal, therefore diffusivity is assumed to take the form:

$$K = (\sigma_u^2\tau_u, \sigma_u^2\tau_u, \sigma_w^2\tau_w), \quad (2.10)$$

where  $\sigma_u$  and  $\sigma_w$  are the standard deviations of the horizontal and vertical velocity fluctuations, respectively.  $\tau_u$  and  $\tau_w$  represent the corresponding horizontal and vertical Lagrangian timescales. The long-range diffusive random walk scheme is given by the stochastic differential Equation 2.11, where  $r$  is a random variable drawn from a random distribution

$$x(t + \Delta t) = x(t) + \sqrt{2K\Delta t}r. \quad (2.11)$$

The advection of the particle is governed by the mean winds and random displacements representing turbulence and meander components (Jones, 2013). The turbulence and meander components in this long-range scheme have no memory from one time step to the next. The short-range dispersion scheme used by NAME obtains a more complex description of dispersion by including a 'memory' for the particle velocity. For a full description, refer to Jones (2013) and Jones et al. (2007).

Turbulence parameters within the PBL, ( $\sigma_u^2$  and  $\sigma_w^2$  in Equation 2.10) have been derived from published empirical fits to observational data large eddy simulations. The vertical profile of turbulence parameters depend on the stability of the atmosphere, determined by the sign of the calculated Monin-Obukhov length ( $L$ ). The inhomogeneous profiles are functions of height and homogeneous profiles can be calculated as the boundary-layer mean values of the inhomogeneous profiles. The meander scheme parameterises the low-frequency horizontal eddies with scales that lie between the resolved motions of the input meteorological data and the small three-dimensional turbulent motions covered by the turbulence parameterisations. The meander parameters are given as  $\sigma_u = \sigma_v = 0.8 \text{ m s}^{-1}$  (velocity variance) and  $\tau_u = \tau_v = 14400 \text{ s}$  (Lagrangian timescale) when using NWP data.

The model is able to simulate other physical processes, such as dry and wet depositions, particle sedimentation and plume rise schemes representing buoyancy and momentum-driven releases. NAME also has a comprehensive sulphur / nitrogen / hydrocarbon chemistry scheme based on the global atmospheric chemistry model STOCHEM. The species concentrations in a chemistry grid box are obtained by summing the contributions from all particles occupying that grid box at a given time. The updated mass of each species in the chemistry box is reassigned back to these particles following the completion of the chemistry calculations by Jones et al. (2007). Fixed background fields generated by the STOCHEM are required to run the chemistry scheme and are not used in this study.

NAME is very flexible and can be optimised for a variety of uses. The pollutant can be released on a specified timescale, either instantly or constantly throughout the run of the model. It is also possible to modify the source time-dependency such that a source emits more during set hours. This could for example represent a manufacturing plant that operates only during the day. NAME can be run in both, the forward and the backward modes. When NAME is run in the forward mode, the tracer particles can represent the density of a pollutant and are followed in time from a source. This would be done when modelling the evolution of a volcanic ash cloud for example. When the model is run backwards, the origin of the air reaching the point or source region can be identified.

This allows the potential locations and their relative strengths of the polluting sources upwind to be calculated.

### **Meteorological Data**

NAME allows the model meteorology to be defined using a variety of approaches. NAME can use data from a single site, where a record of the basic weather parameters measured at the location is read in and used during the simulation. Using single-site meteorology in NAME does not represent horizontal variations in the flow field and might not always capture the correct vertical structure of the atmosphere, thus use of such data might not produce accurate results, especially in meteorological complex cases. Commonly, NAME reads in the gridded meteorological fields from a numerical weather prediction model, such as the Met Offices Unified Model or ECMWF. This data can be a forecast, as is necessary to simulate the dispersion of a pollutant or re-analysed NWP datasets from the past. The meteorological files in each archived dataset consist of a series of short-range forecasts obtained from successive operational forecast cycles of the weather forecast model. Such 3-dimensional meteorological datasets contain parameters such as temperature, mean wind speeds and directions, cloud cover and boundary layer height. The horizontal resolution of the meteorological data can vary from 1.5 to 120 km depending on the geographical location required to be modelled. In this study, the met data used is the UK Met Office reanalysis data with a  $0.5625^\circ \times 0.375^\circ$  resolution (approximately 40 km) for 2009. Met data for 2011 has a higher resolution of  $0.3516^\circ \times 0.2344^\circ$  (approximately 25 km). The meteorological data has a 3 hourly temporal resolution and a vertical ceiling height of 19 km in 2009 and 29 km in 2011.

### **Outputs**

The output of NAME is greatly customisable. The output quantity(-ies) to be produced by the model can range from the concentration of the tracer in the grid box to the deposition rates and boundary layer depths. Typically four dimensional (latitude, longitude, height, time) grid is produced by NAME, so that for every time step in the model, the parameter requested for that grid box is computed. The time step length can also be changed and this can be decreased when dealing with short-range dispersion. This is set to 900 seconds for intermediate and long-range transport modelling. As an example, the concentration matrix of the tracer released could be produced - this could be at the end of the run or every time step. One could also request the model to display the total number

of particles on the whole of the run domain for a certain time period. The output in this case would have just two dimensions: the number of particles and time.

## 2.6 Summary

In this chapter, methods used to measure and model atmospheric  $\text{CH}_4$  were discussed. In situ methods are accurate and contain information on sources local to the flask measurement location. Aircraft and tall tower measurements on the other hand can provide information on fluxes on the regional scale. Earth observation instruments provide the greatest spatial coverage, although they are the least accurate. The main physical principles of Earth observation instruments utilising two passive methods (SWIR, TIR) an active method (LIDAR) were described. Satellites sensing the TIR region of the spectrum allow us to probe the upper troposphere. The weighting function in the atmospheric term is close to zero both in the boundary layer and at the top of the atmosphere. The Earth observation instruments probing this particular part of the atmosphere are not, therefore sensitive to surface emissions on a short timescale. Instruments sensing the SWIR region of the spectrum allow us to probe the boundary layer. The disadvantages of SWIR sensing of greenhouse gases is that the technique requires a clear line of sight between the top of the atmosphere and the surface. The presence of thick clouds or aerosols over the measurement location renders the data unusable. LIDARs, on the other hand, are not sensitive to aerosols and can also obtain measurements during the night. The onboard radiation source also gives active instruments the ability to measure at high latitudes.

Modelling of methane utilising Lagrangian and Eulerian models were also described. Traditionally, inverse modelling studies have been based on the synthesis approach. The method involves seeking a linear combination of fluxes, such that the linear combination of the calculated responses matches the observed data. With the availability of GOSAT and SCIAMACHY data, Earth observation satellite measurements have also been assimilated into Eulerian models. To take full benefit from satellite measurements, approaches that can handle large amounts of observations together with a large control vector are required. Examples of two such approaches, which have been utilised in previous studies, are 4D-Var and EnKF.

## 2.7 Thesis Overview

As described in Section 2.5.3, previous studies have utilised in situ site measurements to constrain greenhouse gas emission estimates. Surface sites and flask measurements are sensitive to local and regional fluxes. Surface sites are geographically sparse and satellite CH<sub>4</sub> observations can provide an increased spatial measurement coverage. It is therefore desirable to investigate the feasibility of using current and future SWIR sensing instruments in combination with a Lagrangian model to investigate methane fluxes on a regional scale. Lagrangian models can be, as described in Section 2.5.1, less computationally expensive to run and potentially simulate dispersion at a higher resolution. In summary, the main scientific questions to be answered in this study are:

1. Can a high-resolution inversion system be set up to use a Lagrangian dispersion model in conjunction with space-borne XCH<sub>4</sub> observations?
2. Can GOSAT be used to constrain high-resolution CH<sub>4</sub> emission inventories over the UK?
3. How well can future instruments, such as Sentinel-5 Precursor and CarbonSat constrain CH<sub>4</sub> emissions inventories over the UK?
4. How well do the synthetic GOSAT measurements, modelled utilising the forward modelling component of the inversion framework compare against the University of Leicester retrieved XCH<sub>4</sub> data?

The thesis is organised as follows:

- Question 1 is answered in Chapter 3. In this chapter an algorithm is developed to invert surface CH<sub>4</sub> fluxes over the United Kingdom and Ireland utilising measurement from a GOSAT-like instrument. The mathematical framework is tested on synthetic measurements from the Mace Head ground measurement station. Mace Head is a well-characterised site with a number of studies utilising the measurements to invert surface fluxes of various pollutants. The algorithm is then modified to simulate column measurements from a space-borne instrument. This chapter also outlines the data used in the later sections, such as the emission inventories and GOSAT data used in Chapter 5.
- Chapter 4 provides the results of a synthetic study, where simulated measurements are produced using the EDGAR emission inventory and the NAME Lagrangian

atmospheric dispersion model used to simulate atmospheric transport. An increasing measurement error is then added to the simulated observations and the ability of the inversion algorithm to reproduce the known fluxes is assessed. The simulated measurements in question assume a uniform, arbitrarily chosen background concentration of CH<sub>4</sub>. The performance of the inversion algorithm when inverting the measurements from future instruments (Sentinel-5 Precursor and CarbonSat), is also simulated. Chapter 4 therefore answers the questions 2 and 3.

- Chapter 5 uses the forward model of the algorithm developed in Chapter 3 to simulate GOSAT measurements in selected regions, thus answering question 4. The Chapter 3 describes the different flux inventories used to construct combined flux estimates used to generate the simulated GOSAT XCH<sub>4</sub> observations. Measurements from the 1<sup>st</sup> until the 7<sup>th</sup> of June, July, August and September, 2009 are simulated to capture the increased rice field emissions in August and September over South East Asia. The synthetic measurements are compared to actual GOSAT observations allowing us to critically evaluate the performance of the a priori forward model as well as the inventory data used in the experiment. Finally, Chapter 6 summarises the main developments of this thesis and draws final conclusions.

## Chapter 3

# Development of the inversion algorithm and data

### 3.1 Aims

In this chapter, the inversion framework linking satellite observations to ground level CH<sub>4</sub> emissions, utilising NAME is developed. Initially, NAME is set up to run in receptor-oriented mode, providing a tracer dosage matrix (see Chapter 2.5.3). The output of the model can be converted to a dilution matrix (also called a source-receptor matrix (SRR)) and in combination with flux estimates, be used to simulate measurements at the release point using the forward modelling approach. The NAME modelled source-receptor matrix can also be used to invert (Figure 2.12) the observations to obtain flux estimates over the region of interest.

First, a mathematical inversion framework is set up and tested utilising modelled synthetic observations at a ground measurement station. Mace Head ground station observations are simulated utilising a forward modelling approach by combining the NAME modelled dilution matrix with The Emissions Database for Global Atmospheric Research (EDGAR) CH<sub>4</sub> emission inventory. It is assumed that EDGAR methane emission inventory represents the true emissions over the simulation domain. The inversion algorithm is then used to infer back the known emission estimates, when synthetic measurements are assimilated into the system. This mathematical exercise allows us to test the robustness of the inverse model, assuming various synthetic observation error magnitudes. Next, the framework is developed to use column XCH<sub>4</sub> observations. A synthetic study utilising the column measurements from instruments such as GOSAT, Sentinel-5 Precursor and CarbonSat will be carried out in Chapter 4. The current chapter also describes the data to

Model Experiment	Description	Required Steps
1	Develop a forward and inverse modelling framework for ground measurement stations.	<ul style="list-style-type: none"> <li>a) Forward model ground measurements with NAME, utilising existing emission estimates as an a priori.</li> <li>b) Produce the inversion code.</li> <li>c) Test the inversion system.</li> </ul>
2	Apply the framework to satellite data.	<ul style="list-style-type: none"> <li>a) Model the atmospheric column within NAME.</li> <li>b) Forward model the synthetic column measurements utilising existing emissions estimates as an a priori.</li> <li>c) Apply the framework to current and future SWIR remote sensing instruments (GOSAT, Sentinel-5 P and CarbonSat respectively).</li> </ul>
3	Utilise the GEOSCHEM Eulerian global chemistry model to initialise the background.	<ul style="list-style-type: none"> <li>a) Use NAME model in combination with a global chemistry model to initialise the background.</li> </ul>

Table 3.1: The different model experiments to be carried out in this study and the required technical developments. The work highlighted in red, blue and green is carried out in the current chapter and Chapters 4, 5 respectively.

be used later in the study, such as various bottom-up emission inventories to be used as an a priori. Table 3.1 summarises the required technical developments and gives a short description of the work to be carried out in this and the later chapters.

## 3.2 Methodology - Bayesian inversion framework

Inverse modelling is frequently used to estimate the magnitudes and distributions of GHG fluxes using atmospheric observations, as was described in Section 2.5.3. Here, the Bayesian framework to be used in this study is described. At its simplest, the equation below describes the relationship between the observation and the sources of an atmospheric constituent:

$$y = Kx. \quad (3.1)$$

The inversion algorithm needs to retrieve  $n$  unknowns in the vector  $x$ , which contains all the possible defined emitter grid cells that would contribute towards the observation. The  $m \times n$  matrix  $K$  is the dilution matrix, obtained from the NAME model output. The Lagrangian atmospheric dispersion model output provides the magnitude of the influence the various defined source regions have on the measurement. The contribution of the modelled sources to the observation  $y$  can be calculated by multiplying the  $x$  and  $K$ .

This implies a linear relationship between the dilution matrix and the fluxes. Adding a background atmospheric concentration to this enhancement yields the measured concentration at the observation site. In practice, this relationship is more complex owing to the presence of errors:

$$y = Kx + e. \quad (3.2)$$

Real world observations contain a measurement error ( $e$ ), as well as a so-called 'representation error'. The representation error arises due to the imperfect understanding of the physics of atmospheric transport and is incorporated into  $K$ . It is not computationally feasible to model the Earth atmosphere for the whole of the globe at extremely high resolutions. Approximations have to be made, resulting in the aforementioned errors. A measurement error is the difference between a measured value of a quantity and its true value. This variability is inherent in all observation systems and can be limited but not eliminated.

Typically, the observations do not constrain all the elements of the source vector. It is often the case, that the inversion solution is very unstable. It is said that the inverse problem is ill-conditioned, meaning that even a small change in the measurement ( $y$  in Equation 3.2) can lead to a big change in the estimated flux magnitude. A constraint to this problem is possible, utilising an a priori estimate of the source. This imposes additional constraints that bias the solution, a process that is generally referred to as regularisation. The difficulty lies in the fact that a real world inverse problem, in contrast to a simulated observation, does not have a unique mathematical solution. Commonly, there are a high number of solutions, aside from the true flux, that fit the observations - even in a noise-free system.

For the model tests carried out in this chapter, a Bayesian approach will be taken to solve the under-determined problem i.e. there are more state variables (emitter grid cells) than there are observations (Rodgers, 2000; Tarantola, 2005). An a priori will help constrain the emissions, although the same emission inventory will be used to model the simulated observations initially. The true solution for this inverse problem is therefore known. When solving Bayesian inverse problems, prior probabilities of the model parameters are updated using information from the measured data to give posterior probabilities of the model parameters. It is a way of characterising the class of possible solutions, considering all possible states and assigning a probability density to each. A linear least squares (Equations 3.8 and 3.9) was chosen as the algorithm to be used in this study (Rodgers, 2000). The method is relatively simple to manipulate and is not resource

intensive.

The Bayes' theorem describes the relationship between the two different conditional probability density functions (*pdfs*). Generalised for the vector case, the Bayes' theorem states:

$$P(y|x) = \frac{P(y|x)P(x)}{P(y)}, \quad (3.3)$$

where  $P(x|y)$  is the conditional *pdf* of  $x$  given  $y$ .  $P(x|y)dx$  is the probability that  $x$  lies in  $(x, x + dx)$  when  $y$  has a given value. i.e. it is the posterior *pdf* of the state when the measurement is given.  $P(x)$  is the prior *pdf* of the state,  $P(y|x)$  describes the knowledge of  $y$  that would be obtained if the state were  $x$ .  $P(y)$  is the prior *pdf* of the measurement (Rodgers, 2000). Gaussian statistics are used to approximate the measurements, so  $P(y|x)$  is expressed as:

$$-2\ln P(y|x) = (y - Kx)^T S_e^{-1} (y - Kx) + c_1, \quad (3.4)$$

where  $c_1$  is independent of  $x$  and  $S_e$  is the measurement error covariance. The prior knowledge of  $x$  is also described by a Gaussian *pdf*:

$$-2\ln P(x) = (x - x_a)^T S_a^{-1} (x - x_a) + c_2, \quad (3.5)$$

where  $x_a$  is the a priori value of  $x$  and  $S_a$  is the associated covariance matrix. Substituting Equations 3.4 and 3.5 into, Equation 3.3, the posterior *pdf* is obtained:

$$-2\ln P(x|y) = (y - Kx)^T S_e^{-1} (y - Kx) + (x - x_a)^T S_a^{-1} (x - x_a) + c_3, \quad (3.6)$$

where  $c_3$  is independent of  $x$ . The maximum a posteriori (MAP) solution is the value of  $x$  that yields the maximum of  $P(x|y)$ , or equivalently the minimum of the scalar-valued cost function  $J(x)$ :

$$J(x) = (x - x_a)^T S_a^{-1} (x - x_a) + (y - Kx)^T S_e^{-1} (y - Kx). \quad (3.7)$$

The maximum a posteriori solution (flux,  $x$ ) and its corresponding a posteriori error covariance ( $S$ ) can therefore be calculated as shown in Equations 3.8 and 3.9 respectively. This algorithm was coded up by the author using IDL, version 7.1 (Exelis, Inc.) and used to carry out the inversions in Chapters 3 and 4. NAME outputs are provided

in a text format, which are then read into arrays in IDL, allowing us to carry out the necessary calculations:

$$\hat{\mathbf{x}} = (K^T S_e^{-1} K + S_a^{-1})^{-1} (K^T S_e^{-1} y + S_a^{-1} x_a) \quad (3.8)$$

$$S = (K^T S_e^{-1} K + S_a^{-1})^{-1}, \quad (3.9)$$

where  $K$  is the weighting function matrix (also known as the Jacobian),  $S_e$  is the methane measurement error covariance matrix.  $S_a$  is the a priori covariance matrix,  $y$  is the measurement vector and  $x_a$  is the a priori flux vector.  $x$  is the calculated methane flux for each of the emitter grid cells and  $S$  gives us the calculated flux error.  $K$  is calculated by NAME and has the dimensions of the number of measurements  $\times$  the number of emitter grid cells.  $K$  relates the observed concentration to the methane emissions in the defined grids.  $S_e$  is a diagonal matrix with the following dimensions: number of measurements  $\times$  number of measurements. This is the uncertainty in the atmospheric observation. The a priori flux ( $x_a$ ) and the corresponding covariance ( $S_a$ ) are used to constrain the inversion to known fluxes, whilst also quantifying the uncertainty of the said emissions.

### 3.3 Formulating the forward model - simulating ground measurements with NAME

The first step in building the inversion system is to run NAME for a test measurement site. This allows us to utilise the dispersion model output in producing synthetic measurements at the said location. The next step is to invert the fluxes from the observations. The Mace Head ground measurement station, on the western coast of Ireland, was chosen as the test site (Figure 3.1). Mace Head is part of the AGAGE network and is also a baseline station in the WMO network of GAW sites (WMO, 2013). The location of the station has previously been exploited to define the baseline concentrations of a number of pollutants (Manning et al., 2011). The station is suitably placed for studying local greenhouse gas sources and sinks, as it receives clean air from the Atlantic, as well as polluted air from Europe. Data from the station has been utilised in a number of studies and it is considered to be a well characterised site. (Manning et al., 2011, 2003; Rigby et al., 2011; Ryall et al., 2001; Stohl et al., 2009). The station has a long record of measurements of various ozone-depleting and other pollutant compounds and methane has

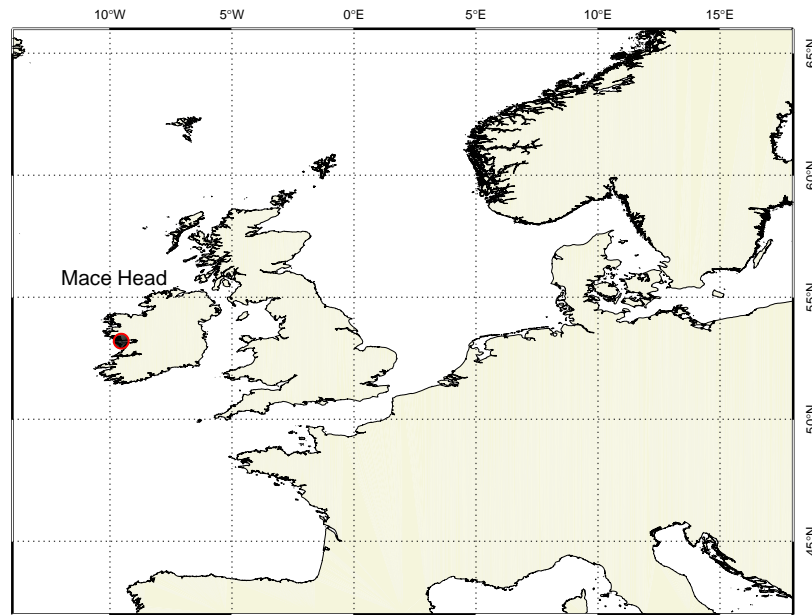


FIGURE 3.1: The geographical location of the Mace Head station. The domain within which dispersion will be simulated, is shown. Fluxes within this region will contribute towards the synthetic measurement at the station. The a priori fluxes used to model the measurements will then be inverted.

been measured in Mace Head since 1987. The currently used, state of the art AGAGE GC-MS (Miller et al., 2008) system has been in place since November 2003. It currently measures over 40 species (Section 2.2).

### 3.3.1 Linking emissions to observations

A number of challenges present themselves when trying to model observed concentrations of greenhouse gases at certain locations, as well as inverting fluxes from real-world observations. The central component of the work described here is the transport between the source and the measurement site (also referred to as the receptor). NAME needs to be set up to provide this link. The dispersion model simulates the upwind flux grid box influence on a measurement, providing a quantitative estimate of sensitivity of the receptor to the source regions (Figure 2.12).

In this model experiment, data from a single station (receptor) is used. A single run from the receptor can reveal multiple upwind source regions. Initialising the simulations from all the potential sources would entail greater computational cost, getting more inefficient with increasing spatial resolution.

Choosing an appropriate spatial resolution for the simulation is important when considering inversion modelling. It is expected that running the model at higher spatial resolutions would result in more accurate source-receptor maps. This is true, if the meteorological data driving the dispersion model matches (or is higher) than the resolution of the LPDM simulation. Although NAME can run at any defined grid, driving the model with low resolution inputs will force the model interpolate available wind fields. It will not therefore capture the actual higher resolution meteorology (Manning, 2011). Decreasing the resolution does decrease the ability of the model to represent the real-world conditions. The wind speeds are averaged and the surface topography detail is lost (Figure 3.2 shows the effect of different run resolution on the model surface topography). This becomes a problem, when trying to map fluxes using data from a measurement station located in a mountainous region, such as Jungfraujoch. Jungfraujoch is situated on a mountain saddle in the central Swiss Alps, at the altitude of 3580 m asl. The 40 km horizontal resolution UK Met office meteorological data driving NAME puts the surface of the grid box containing the station at 1760 metres (Manning, 2011). Modelling at resolutions below that of the native meteorological data would result in even greater inaccuracies for this station. The issues described here can be overlooked for the synthetic tests, as the same model output is used to derive the observations and invert the emissions. This means a unique known emission solution to the inversion problem exists. They do, however have to be taken into account when inverting real-world ground station data. It must be remembered, that the wind fields themselves are taken from three-dimensional weather prediction models, the use of which brings its own errors and inaccuracies. NWP models do not capture sub-grid processes, such as land-sea breezes, well. The ability to model convection in tropical regions is also problematic (Browning and Gurney, 1999).

### **Defining the test simulation - Mace Head**

For NAME to run, a number of variables have to be specified. NAME must be provided with the release location, date and time. First, the atmospheric dispersion model was chosen to run at a spatial resolution of  $1^\circ$ . The simulations were then initialised with the tracer particles being released at the geographical location of the Mace Head station. A single gram of the inert tracer was released into the model atmosphere, 8 m above sea level, at the exact time of each of the real Mace Head measurements over a 6 month time window from the 1<sup>st</sup> of April until the 30<sup>th</sup> of September, 2009. The tracer particles would represent air and in effect, methane arriving at the stations. The dates were chosen arbitrarily, but the time period was long enough for the station to be under the in-

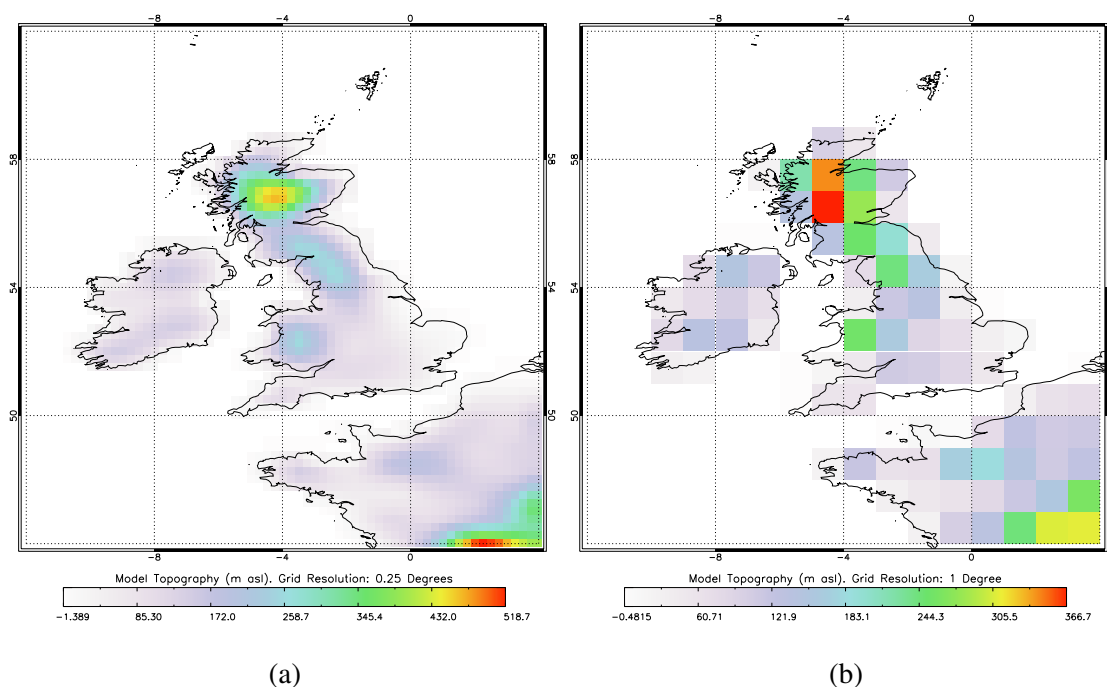


FIGURE 3.2: The effect of NAME simulation spatial resolution on the surface topography. The plots show the m (asl) height of the surface as modelled by the LPDM for two different scenarios i.e. model is run with a horizontal resolution of  $0.25^\circ$  (a) and  $1^\circ$  (b). Decreasing the resolution results in lost detail of the model surface, as well as meteorological data

fluence of various meteorological conditions. The total number of measurements during this time period was 5793. Figure 3.4 (top) shows the time-series of  $\text{CH}_4$  measurements taken at the station. The source-receptor matrix was calculated for each of these measurements individually (Section 3.3.1). If the simulation time period was longer, it would be possible to save computational resources by running the model every 3 hours. There is very little information to gain in computing the source-receptor relationship (SRR) matrix for each measurement owing to meteorological data driving NAME having aforementioned temporal resolution. Calculating a 3-hour SRR matrix would decrease the required number of runs to 1464 for the 6 months investigated here.

The release location had a length, width and the height of 1 metre, which is representative of the air inlet into the GC-MS instrument at the station. 10000 particles were released instantaneously, and followed back in time for 10 days. The choice of releasing 10000 particles was considered a good compromise between accuracy and computational efficiency. Releasing more particles should result in better accuracy, however the simulations would be more computationally expensive to run. The 10-day run was chosen as the sensitivity to the sources outside this time period decreases quite rapidly with time. The

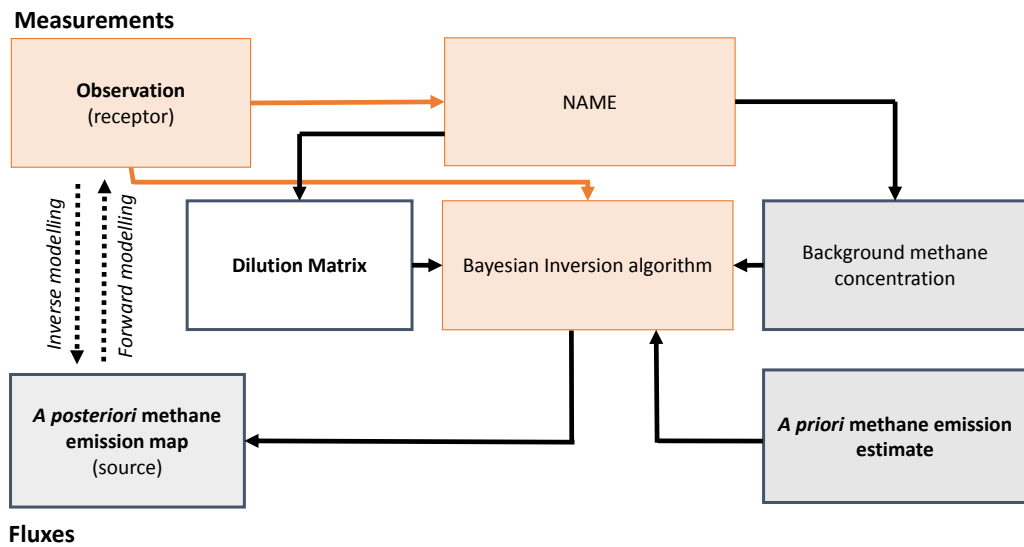


FIGURE 3.3: The overview of the developed inversion system.

surface emission sensitivity is largest just before the arrival of air at the receptor. Prior to this, air is most likely to reside above the boundary layer. The volume, over which the tracer particles are distributed, grows larger over time, making it more difficult to extract information on individual sources, as the simulation run length is increased. Eventually, the emissions from the different regions become well-mixed and start forming the baseline concentration.

### NAME output

The overview of the developed inversion system is shown in Figure 3.3. NAME initially outputs the so called tracer dosage matrix. This matrix is the integrated 10-day concentration of the tracer in the defined grid boxes with units of  $\text{g s m}^{-3}$ . The grid boxes have a horizontal resolution of  $1^\circ$  and a height of 100 m above ground level, which is the assumed footprint layer height. The simulation domain was left unbounded and the particles were free to move above and back down below the 100 m threshold. This threshold was chosen as the height of interest owing to the fact that most emissions occur close to the surface. The chosen altitude represents the PBL and it is also assumed that methane is mixed by the time it arrives at the receptor. Tracer particles (representing air mass) arriving from below this altitude is assumed to be under the influence of the surface fluxes and any particles above this are considered to be unaffected by said emissions.

To be used in the inversion algorithm ( $K$ , Section 3.2), the dosage matrix has to be converted to a dilution matrix. The NAME tracer dosage outputs are read into IDL,

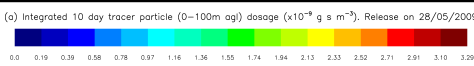
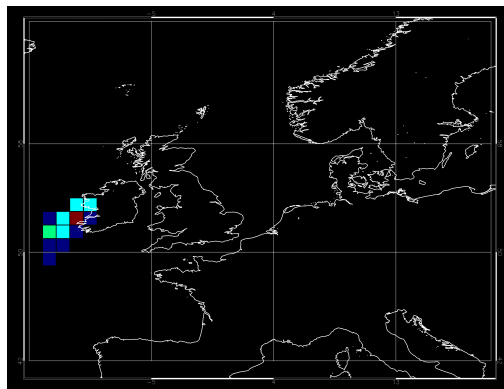
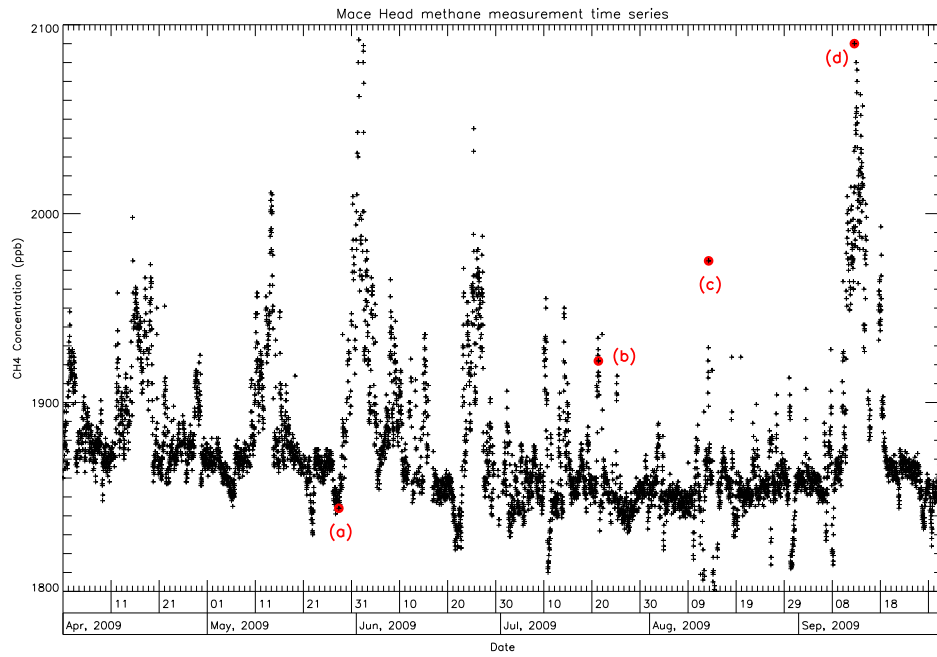
where the tracer concentration in a particular grid box is divided by the total mass emitted (1 gram) and is multiplied by the geographical area of each grid box (as described fully by Manning et al. (2011)). The dilution matrix ( $D$ ) has the units of  $\text{s m}^{-1}$  and dilutes a continuous emission ( $e$ ) of  $1 \text{ g m}^{-2} \text{ s}^{-1}$  from a given box over the previous 10 days to the air concentration in  $\text{g m}^{-3}$  at the measurement site  $m$ ,

$$De = m. \quad (3.10)$$

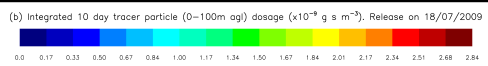
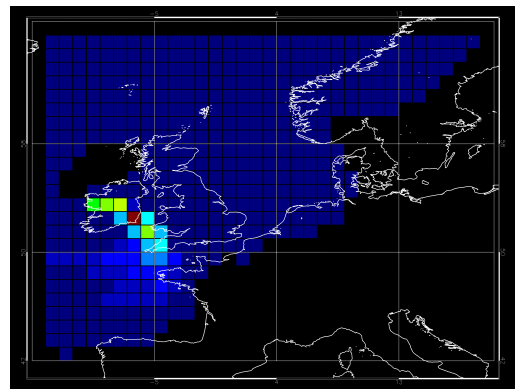
Figures 3.4a, b, c and d highlight the effect of the meteorology on the particles released at Mace Head at different times. A full time series of the station measurements can be seen, as well as the corresponding NAME run outputs. Figure 3.4a shows air at the measuring site being received from the Atlantic. This air can be considered to be baseline and will not be sensitive to European emissions. The observed concentration does not therefore carry any useful information on the fluxes in the region of interest. This is reflected in the low observed value at the station as can be seen in the measurement time series. Figure 3.4b on the other hand, shows the sampled air being under a strong influence of the regional Irish and British fluxes. The modelled influence of the regional emissions results in an increased measurement compared to the baseline case (Figures 3.4a). Figures 3.4c, d show that the air arriving at Mace Head at both of these times are influenced by local emissions. The high observed  $\text{CH}_4$  concentrations at these times indicates stable meteorological conditions. The measurement being under the influence of low speed winds could mean that the local emissions might not be well mixed within the PBL, which could disproportionately influence the measurement, resulting in enhanced observed  $\text{CH}_4$  concentrations. Figure 3.4d shows low concentrations of the tracer north of Ireland which indicates that the particles have risen above the 100 metre detection threshold followed by decrease in altitude as well particles being under the influence of lower wind speeds.

### 3.3.2 Inversion spatial resolution

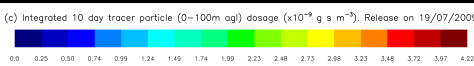
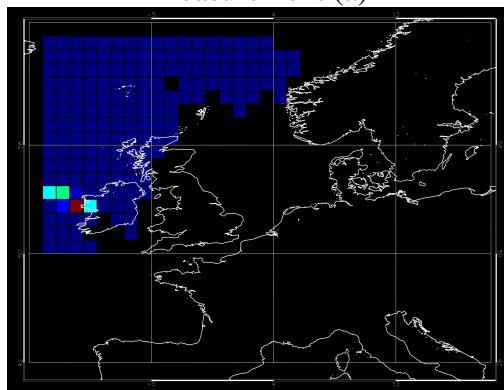
Ground-based measurements are most sensitive to trace-gas emissions in the near-field, with sensitivity decreasing as the distance increases from the measurement location. Ideally, each flux grid cell would contribute to the measured air concentration equally. This is not the case for poorly sampled regions. The distant emissions do not contribute much to the observation at Mace Head, thus the number of grid boxes for which the fluxes are to be obtained, have to be decreased. The approach used in other studies is to start with



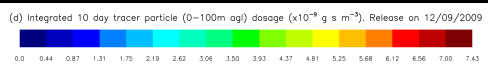
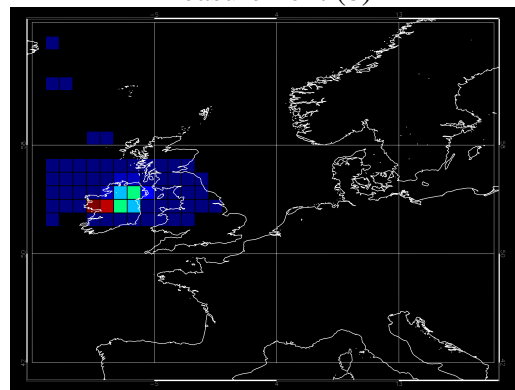
Measurement (a)



Measurement (b)



Measurement (c)



Measurement (d)

FIGURE 3.4: Mace Head measurement time series and NAME tracer concentration maps for selected measurements. The influence of meteorology on the measurement magnitude is demonstrated (see text for more details).

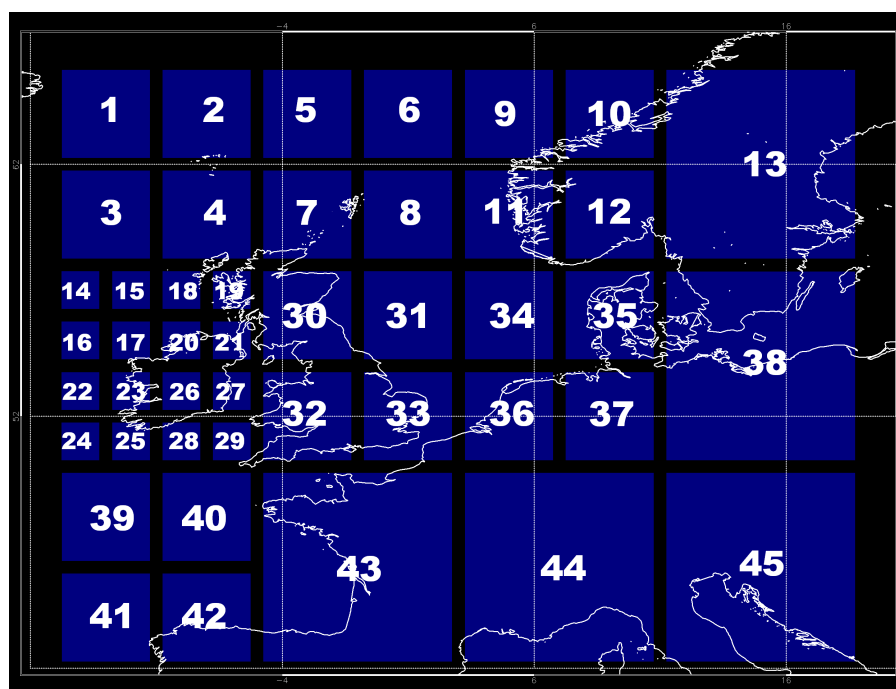


FIGURE 3.5: A variable resolution grid for which the fluxes are going to be inverted.

a high resolution grid aggregating the potential source grid cells, as the distance from the measurement station increases (Manning et al., 2011; Stohl et al., 2009; Vermeulen et al., 1999). A variable-resolution grid therefore allows for high-resolution boxes to be present in the vicinity of the receptor, and decreased in the poorly sampled regions. The approach described in previous studies is utilised here. As the LPDM in this study is run at  $1^\circ$  resolution, this equates to 768 ( $32^\circ \times 24^\circ$ ) unknown flux grid boxes. The grid box resolution is therefore incrementally decreased ( $1^\circ \times 1^\circ$  through to  $8^\circ \times 8^\circ$ ) as the distance from Mace Head is increased. The resulting inversion grid is shown in Figure 3.5

### 3.3.3 Simulated measurement

EDGAR methane emission estimates for 2005 were used to simulate the observations at Mace Head (shown in Figure 3.6). No other emission sources were assumed to influence the Mace Head measurement site. This is not fully representative of the emissions Mace Head would be influenced by, as EDGAR emission inventory does not include natural emission estimates. It provides anthropogenic flux estimates only, thus peatland, termite and wetland emissions are not included in the inventory. Fluxes are considered to be constant during the 6-month simulation time period.

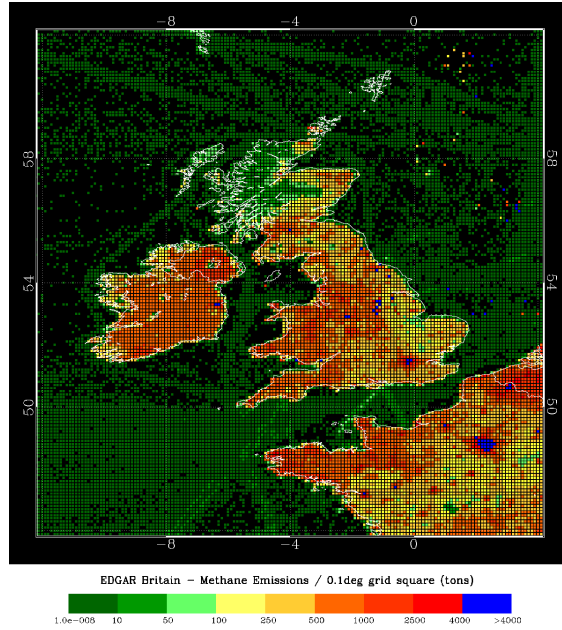


FIGURE 3.6: Emissions Database for Global Atmospheric Research (EDGAR) methane flux estimates over the United Kingdom and Ireland for 2005. The units are: tons per  $0.1^\circ$  grid square (EDGAR, 2009).

The a priori emission estimates have been re-gridded to the inversion resolution determined in Section 3.3.2 and converted to  $\text{g m}^{-2} \text{s}^{-1}$  from tons per  $0.1^\circ$  grid box (Figure 3.7). The inversion algorithm is expected to obtain the flux map shown in the figure, as this is the exact mathematical solution to the inversion problem. The EDGAR, as shown in Figure 3.7 is used to generate the synthetic measurements.

The EDGAR emission inventory was multiplied by the dilution matrices, calculated from the NAME outputs, giving us the enhancement in local methane observations due to fluxes in the simulation region. The enhancement calculated was in grams, which then had to be converted to ppbv. Equation 3.11 was used to achieve this:

$$conc = \frac{\frac{g}{m^3}}{\frac{P}{RT} * MW} \quad (3.11)$$

Where  $P$  is pressure in kPa,  $R$  is a gas constant ( $8.314 \text{ m}^3 \text{ Pa K}^{-1} \text{ mol}^{-1}$ ),  $T$  is the temperature in Kelvin,  $MW$  is the molecular weight (16 for methane). Finally, the ppbv enhancement was added to the background atmospheric methane, giving the observation at the Mace Head station. The baseline was arbitrarily chosen to be constant, at 1870 ppbv. The baseline concentration in this study is defined as the fraction of the observed concentration that cannot be attributed to the sources by dispersion modelling. It is, in essence, the concentration of methane that cannot be accounted for by the 10-day

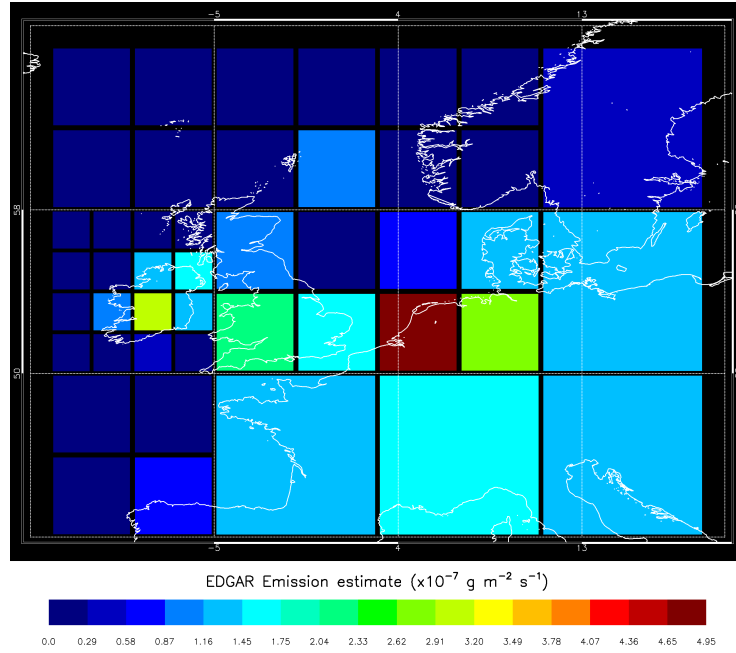


FIGURE 3.7: EDGAR emission estimates, regridded and converted to  $\text{g m}^{-2} \text{s}^{-1}$ . Europe was divided into 45 regions. The areas distant from the measurement site have decreased resolutions, as the site is most sensitive to the emissions nearest to Mace Head.

backward NAME runs. Calculating the baseline when using real-world measurements presents a great challenge, which shall be tackled Chapter 5. The resulting synthetic measurement time series can be seen in Figure 3.8. The next step would be to test the inversion algorithm by attempting to obtain the known EDGAR flux map used to produce measurements i.e. inverting the observations.

### 3.3.4 Notation

In this section, the notation used when analysing inversion results in this thesis, is explained. The error of the inverted flux refers to the square root of the diagonal elements of the a posteriori flux covariance,  $\sigma_{apost} = \sqrt{S_{i,i}}$  ( $i$  is the  $i$ th diagonal entry of the covariance matrix). See Equation 3.9 for a description of how the flux covariance is calculated. The error reduction ( $\gamma$ ) is the primary way of assessing the performance of the inversion algorithm, i.e. the ability of the algorithm to reduce the error variance of the state vector from  $\sigma_a$  to  $\sigma_{apost}$ . The error reduction is calculated:

$$\gamma = \frac{\sqrt{S}}{\sqrt{S_a}}. \quad (3.12)$$

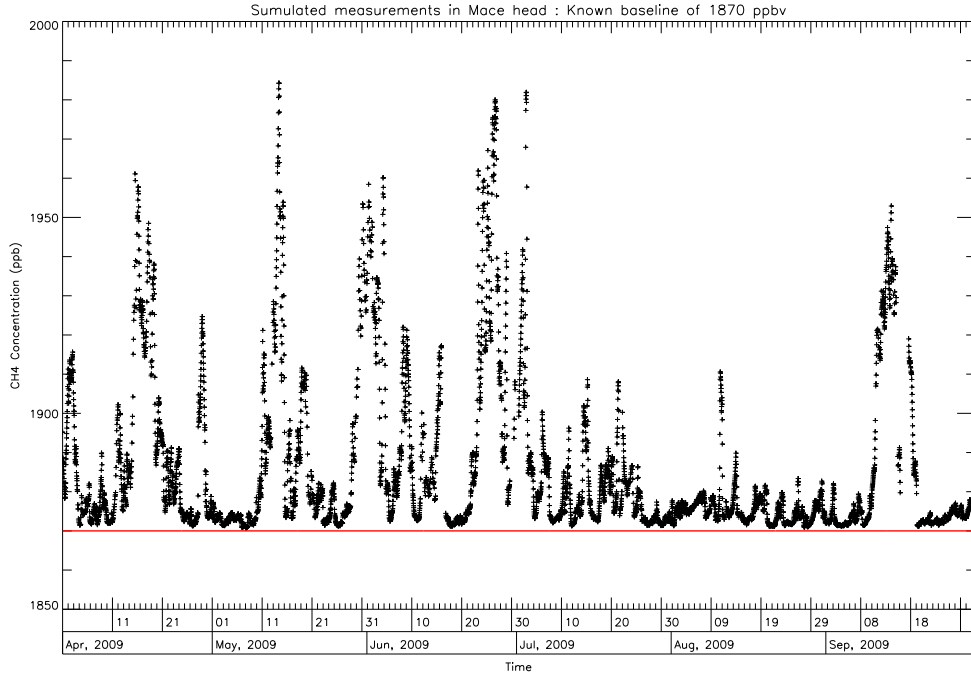


FIGURE 3.8: Simulated observations at Mace Head. EDGAR emissions utilised as an a priori are assumed to be constant. The synthetic baseline to which the local methane enhancement is added, is shown in red.

The reduction in error from  $\sigma_a$  to  $\sigma_{apost}$  assumes that the observational error is random and that error covariances in the observations are fully accounted for. An error reduction value of 1 therefore signifies that no error reduction has been achieved by the algorithm. The lower the error reduction value, the lower the a posteriori error as a fraction of the initially assumed a priori uncertainty. An error reduction of 0.01 would mean the inverted flux has a error of 1% of the prior assumed error (or a 99% reduction). Calculating the error reductions for whole regions is done utilising the following equation:

$$\sigma_{region} = \sqrt{(\sigma_{apost\ box\ n})^2 + (\sigma_{apost\ box\ n+1})^2 + (\sigma_{apost\ box\ n+2})^2 \dots}, \quad (3.13)$$

where *box* is a flux grid cell within a region. Again, it is assumed that the errors are not correlated and the errors propagate linearly. The total inverted flux error over Britain would, for example be calculated by taking a square root of all the individual calculated variances for all the boxes in the region.

### 3.3.5 Inversion and analysis

In this section, the results of the synthetic inversion, utilising the simulated Mace Head measurements are discussed. The inversion algorithm was successful in returning the known flux map, which in conjunction with the NAME model outputs was used to simulate the ground measurements. The inversion carried out here was a purely technical exercise to test the inversion algorithm, (Section 3.2). The outcome makes it possible to quantify the sensitivity of the system to measurement noise when Mace Head measurements are used.

Initially, the measurements were set to have a negligible measurement noise ( $1 \times 10^{-10}$  ppbv, thus they can be considered to be noise-free) and were fed straight into the inversion system. NAME outputs (tracer dosage) were converted to dilution matrices, as described in Section 3.3.1 and used as  $K$  in the inversion algorithm (Equation 3.8). The a priori uncertainty was set to 100%. The a priori variance value is therefore equal to the EDGAR flux magnitude multiplied by itself.

The algorithm was able to reproduce the fluxes accurately, with a Pearson correlation coefficient between the known flux and the inverted flux of 1 (Figures 3.9, 3.17). The model calculated error on the inverted flux can be seen in Figure 3.10. The a posteriori flux error is very low, orders of magnitude lower than the flux itself. The algorithm can be said to invert the emission fields perfectly. Figure 3.10 does make it difficult to visualise the relative flux errors, owing to the varying emission strengths in different grid boxes. Figure 3.11 shows the inverted flux error as a percentage of the inverted flux. It is shown that the greatest percentage error is present in the low emitting grid boxes placed over water, north of Britain. The large error over the sea grid boxes will most likely be due to low sampling of these regions.

Real measurements, in contrast to the first test performed here, will however have a random measurement noise present. The next step was to re-run the inversion adding measurement noise to each simulation. The noise added to the simulated measurements were 1, 2, 5, 10 and 20 ppbv. All of the inversion returned the EDGAR flux value (Figure 3.9). Figures 3.12 through to 3.16 show the effects of the increasing noise on the uncertainty of the a posteriori flux. The errors get progressively larger as the measurement noise increases. Even with an observation error of 1 ppbv (Figure 3.12), the algorithm cannot achieve error reduction in flux uncertainty over low emitting ocean boxes north of Britain or west of Ireland. The inverted flux error is equal to 100% of the a priori flux error in these grid boxes. The number of boxes, where the algorithm cannot reliably place the emissions increases, as the measurement error increases in magnitude.

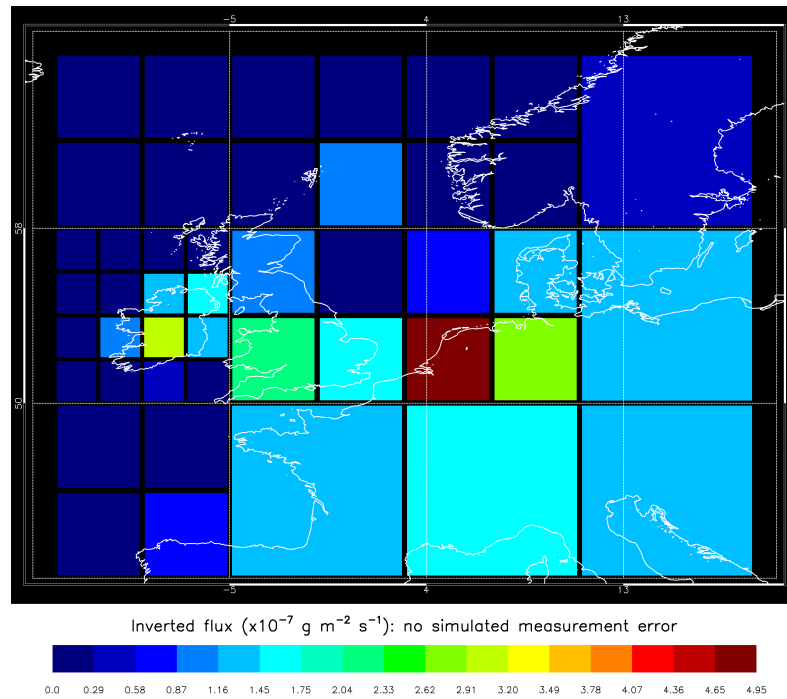


FIGURE 3.9: The a posteriori flux. The random measurement noise is simulated to be  $1 \times 10^{-10}$  ppbv.

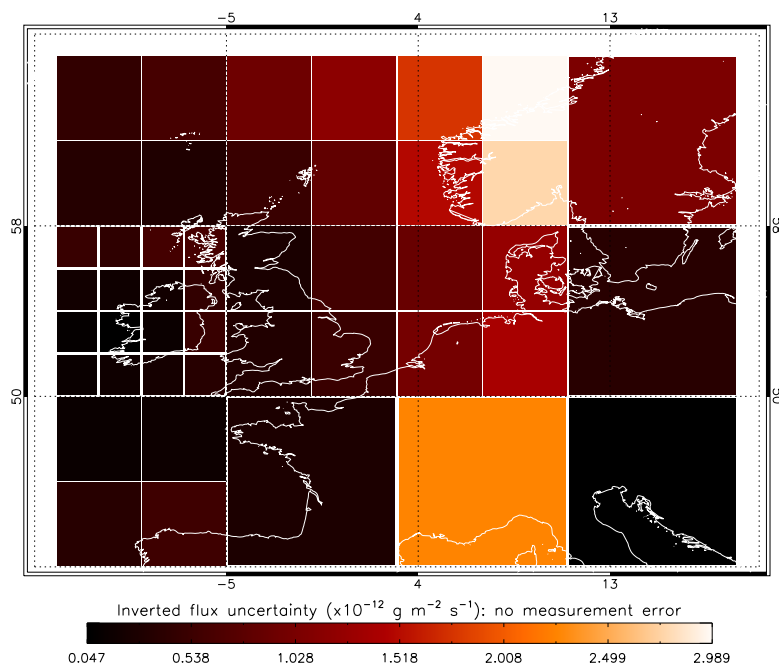


FIGURE 3.10: The a posteriori flux error. The random measurement noise is simulated to be  $1 \times 10^{-10}$  ppbv.

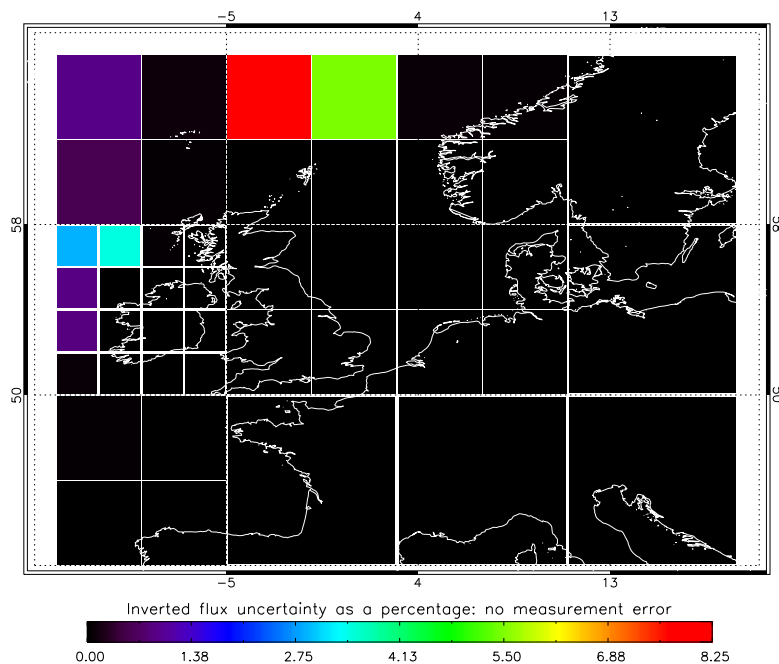


FIGURE 3.11: The a posteriori flux error, as a percentage of the a posteriori flux. The random measurement noise is simulated to be  $1 \times 10^{-10}$  ppbv.

Figure 3.17 shows the inverted fluxes plotted up against the known emissions used to simulate the synthetic measurements. When an error of 20 ppbv is simulated (Figure 3.12), no error reduction is achieved in Norway or Sweden. Generally, the relative error (error in the inverted flux as a percentage of the flux magnitude) is greatest in the low flux regions. The error could be a result of under sampling in the regions by the NAME model. A viable solution could be to merge the grid boxes, where the percentage error is greatest. Regions 1, 2, 5, 6, 14, 16, 22, 24 (grid numbering is shown in Figure 3.5) all have relatively low emission values, therefore the loss in resolution is a good trade-off, if greater flux error reduction in these grid boxes is to be achieved. Another solution could be to constrain the ocean fluxes to the a priori, as these are unlikely to vary significantly from the estimates. The emissions over the oceans are mainly from shipping and are orders of magnitude lower than those from the mainland. Despite the few problem regions, the inversion algorithm is generally speaking able to reproduce the known fluxes in higher emitting dry land areas. Figure 3.18 shows the error reduction values of the inverted fluxes for each individual emission grid cell. The green bars mark the grid boxes with the lowest a priori flux values (below  $1 \times 10^{-8}$   $\text{g m}^{-2} \text{s}^{-1}$ ). It is expected and demonstrated, that simulated error reductions for these grid cells are lowest.

Figure 3.19 shows the error reductions as function of grid box methane flux interval. It is shown that for the lowest emitting regions of  $1 \times 10^{-10}$  to  $1 \times 10^{-9}$   $\text{g m}^{-2} \text{s}^{-1}$ , the

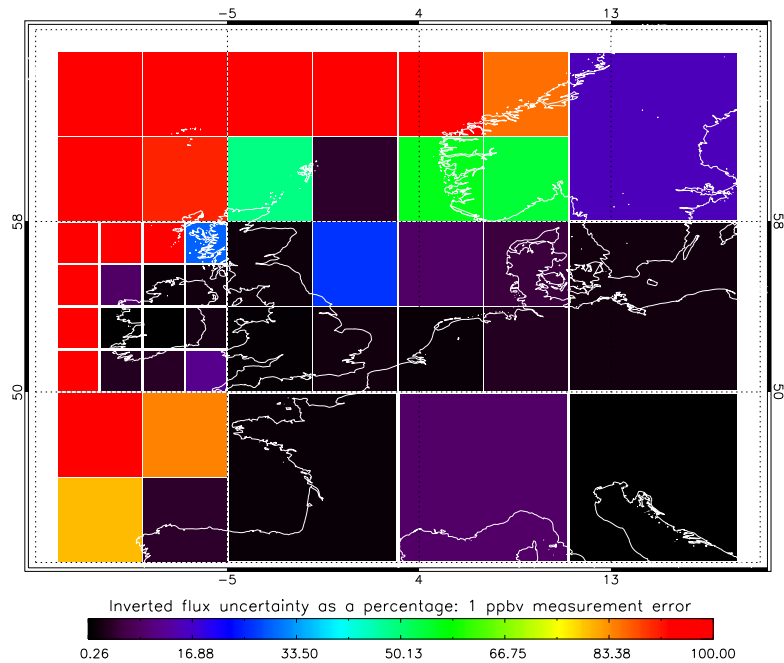


FIGURE 3.12: The inverted error as a percentage of the flux. The measurement error is 1 ppbv.

combined error reduction of  $\sim 6.0 \times 10^{-4}$  is modelled. The error reduction values are consistently low throughout all of the flux ranges, assuming an error-free measurement ( $1 \times 10^{-10}$  ppbv). When a random measurement error of 1 ppbv is simulated, a mean error reduction of 0.90 is obtained. No error reduction is observed if the measurements have random measurement errors of 5, 10 or 20 ppbv. For the fluxes higher than  $1 \times 10^{-8}$   $\text{g m}^{-2} \text{s}^{-1}$ , the inversion algorithm is able to achieve a greater error reduction (error reduction value gets lower). A clear advantage of a measurement having the lowest possible measurement error can be seen for flux values higher than  $1 \times 10^{-7}$ . Here, error reduction is  $\sim 0.04$  when a measurement error of 1 ppbv is assumed. The error reduction decreases to  $\sim 0.05$  and  $\sim 0.15$ , as the measurement error is increased to 2 and 5 ppbv. An error reduction of  $\sim 0.36$  is achieved, when a maximum measurement error of 20 ppbv is simulated.

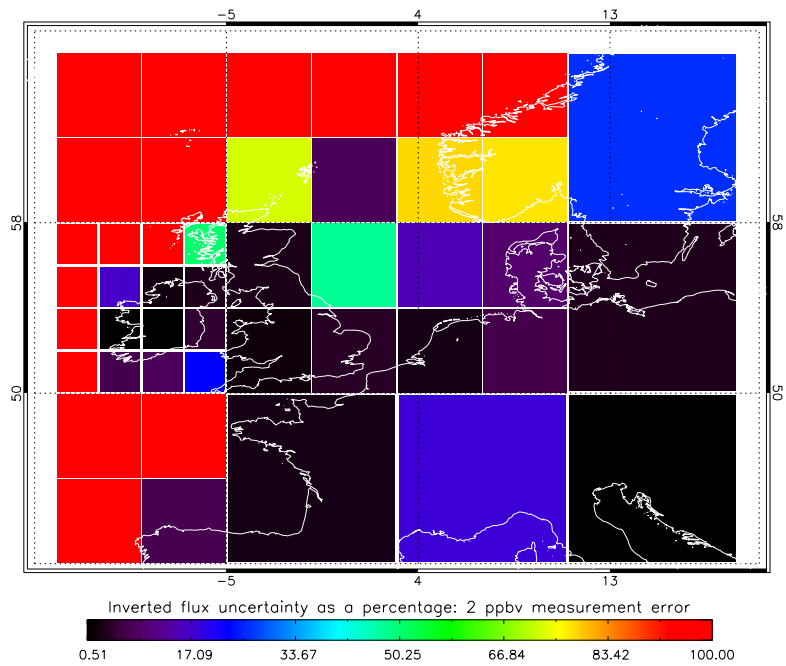


FIGURE 3.13: The inverted error as a percentage of the flux. The measurement error is 2 ppbv.

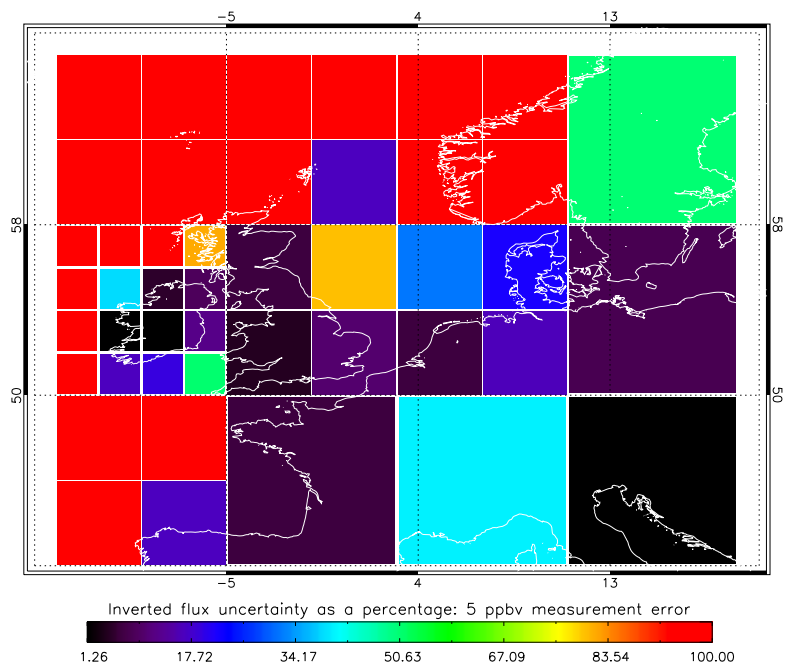


FIGURE 3.14: The inverted error as a percentage of the flux. The measurement error is 5 ppbv.

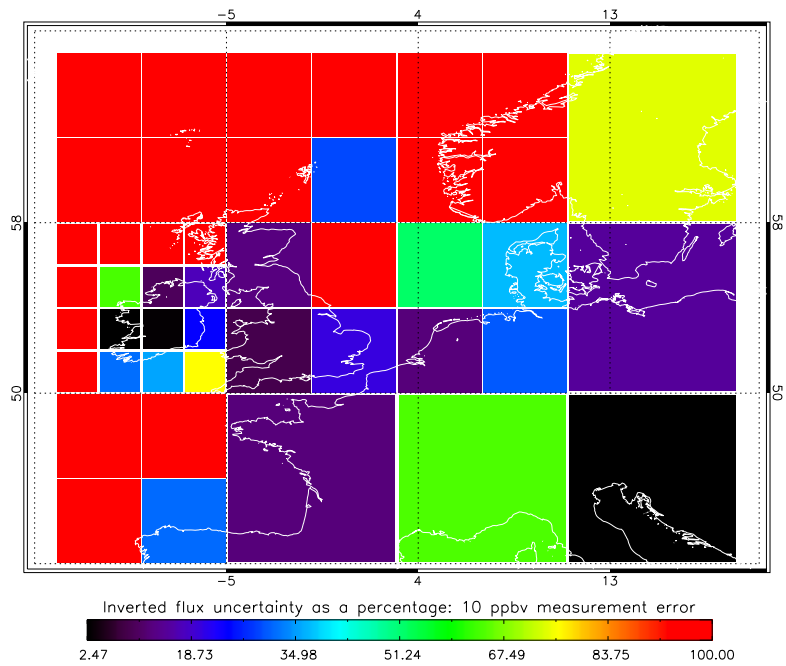


FIGURE 3.15: The inverted error as a percentage of the flux. The measurement error is 10 ppbv.

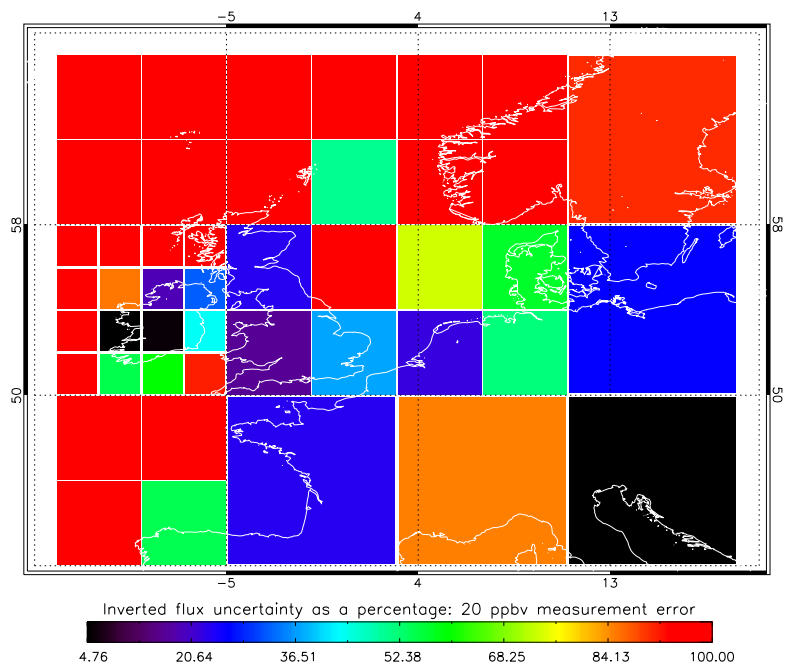


FIGURE 3.16: The inverted error as a percentage of the flux. The measurement error is 20 ppbv.

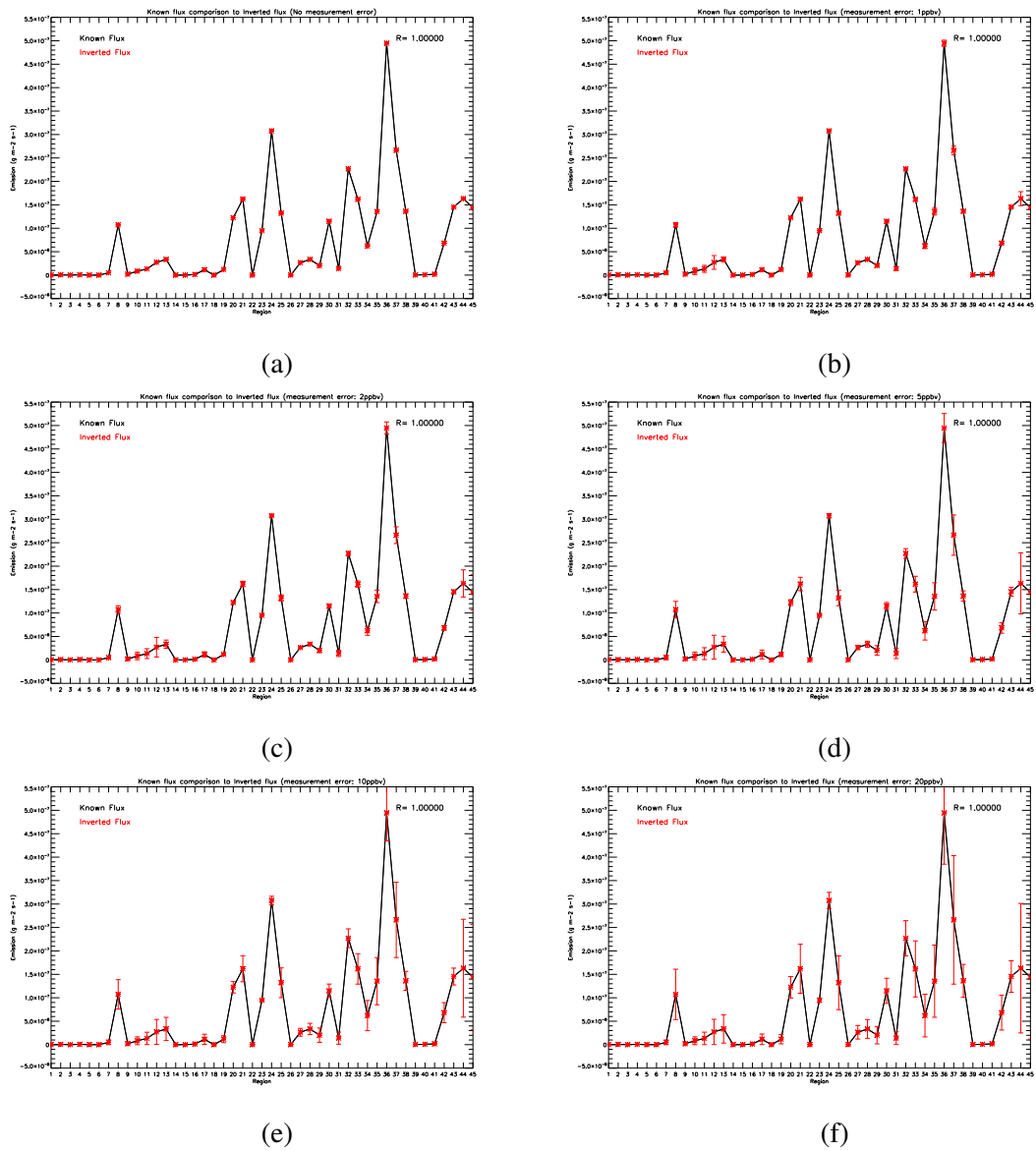


FIGURE 3.17: The inverted fluxes plotted up against the known a priori fluxes. The measurement errors are: (a)  $1 \times 10^{-10}$  ppbv, (b) 1 ppbv, (c) 2 ppbv, (d) 5 ppbv, (e) 10 ppbv and (f) 20 ppbv.

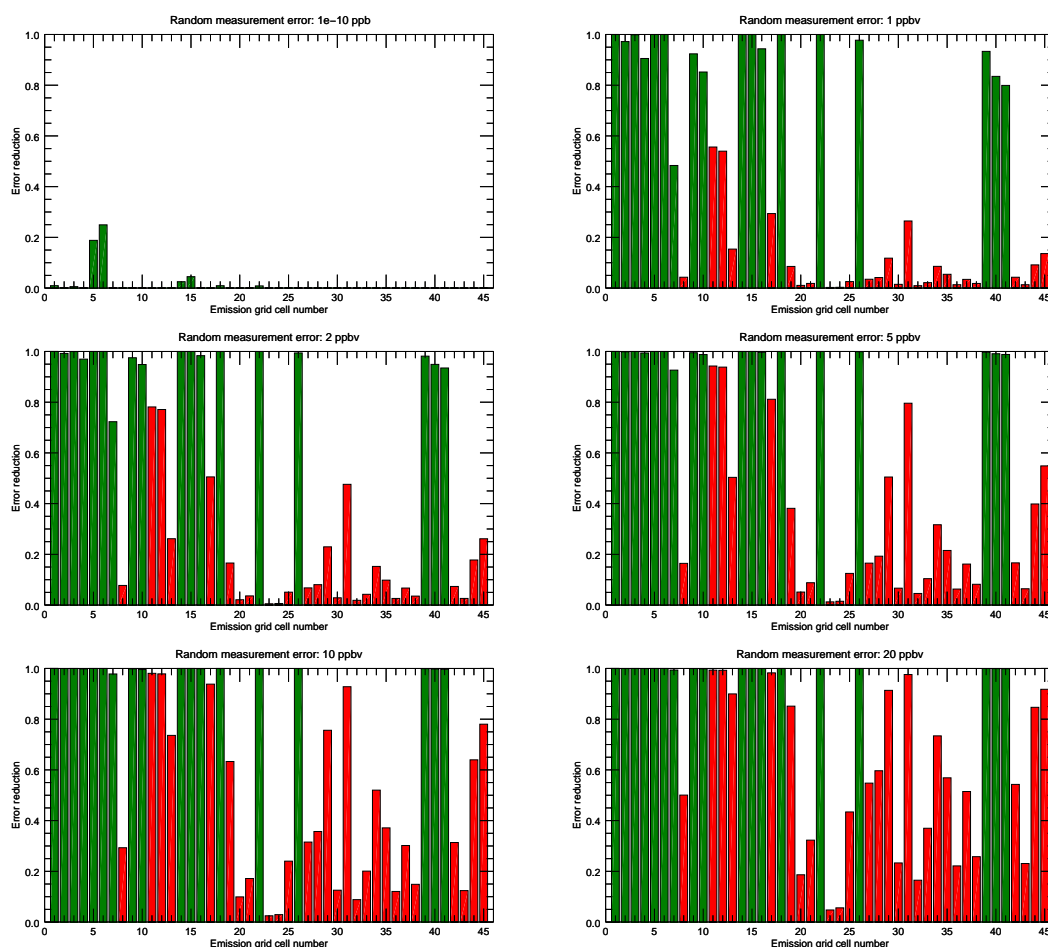


FIGURE 3.18: The error reduction for each individual flux cell for simulated measurement errors of  $1 \times 10^{-10}$  (top left), 1 (top right), 2 (centre left), 5 (centre right), 10 (bottom left) and 20 (bottom right) ppbv. Bars in green denote flux magnitudes below  $1 \times 10^{-8} \text{ g m}^{-2} \text{ s}^{-1}$ . It is expected that simulated flux reductions are lowest for these grid boxes.

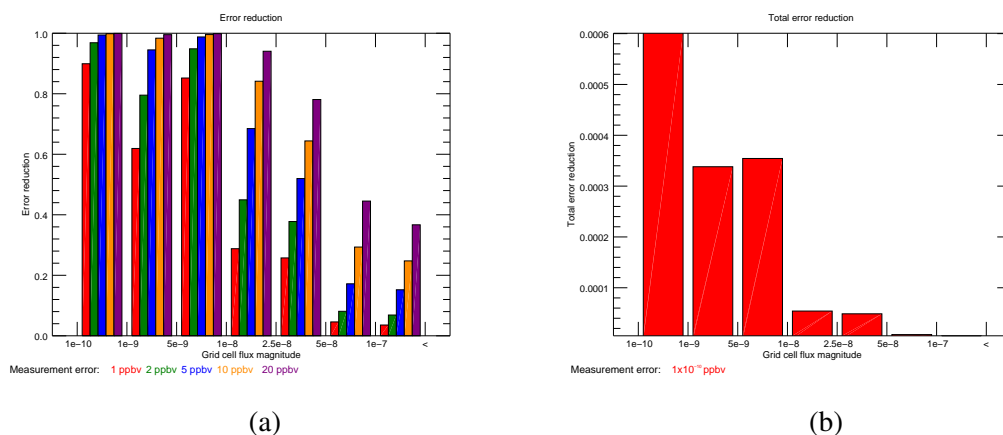


FIGURE 3.19: The combined cell error reduction values as a fraction of the flux magnitude with the simulated measurement errors of (a) 1, 2, 5, 10 and 20 ppbv (b)  $1 \times 10^{-10}$  ppbv.

### 3.4 Modelling the satellite measured column with NAME

In this section, the inversion algorithm is adapted to utilise Earth observation instrument observations. A satellite, in contrast to ground measuring stations, does not sample the air at a single point in the atmosphere. Data from a methane sensing Earth observing instrument, such as GOSAT, represents a column-averaged dry mixing ratio (referred to simply as concentration here). For the column  $X_{CH_4}$  to be retrieved, the retrieval algorithm first obtains the sub-column  $CH_4$  masses at different altitude layers. The column-averaged dry air mixing ratios are obtained by summing up the sub-columns to get the total column values, which are then divided by the dry-air columns obtained from the ECMWF model data. The mass of the gas of interest arriving at different altitudes of the column will be affected by different emission sources. It is not unreasonable to expect the lower column to be under the influence of the nearby emitters. Air sampled higher up should carry mainly the well-mixed background value and a lesser enhancement due to the tracer particles touching the PBL further distance away from the column. The spatial extent of source influences on column concentrations of short-lived gases has been modelled in previous studies (Turner et al., 2012). Turner et al. found that in the case of  $NO_x$  for example, emissions outside the base of the column may govern more than 50% of the model column concentration. To retrieve 90% of the total column influence may require accounting for emissions from more than 500 km away. The area of influence for methane is expected to be less, as it is not produced by chemical reactions in the atmosphere. In contrast, reservoir species and chemical modes allow the short-lived species to impact the chemical state of the atmosphere beyond their own lifetime. The finding of the extended spatial influence in column contributions does however still apply in our case. Wind at different altitudes varies in strength and direction. Figure 3.20 shows an example of modelled wind speeds and directions at different heights above the ground level. This results in different region emissions having an impact on any air arriving at the different altitudes.

To best represent the air column in the dispersion model, the tracer release should be a volume and not a single point in space. Particles have to be released from the ground level to a height that would no longer be influenced by surface fluxes in the run time period. The maximum height the model can run at is also limited by the meteorology data driving the model. During test runs, the model would give erroneous outputs if source releases were initiated above 20 km m. a.g.l. A simulation ceiling height of 9 km was found to be appropriate, as any particles released above this height are not likely to travel down below the 200 m threshold. This hypothesis was later confirmed by NAME

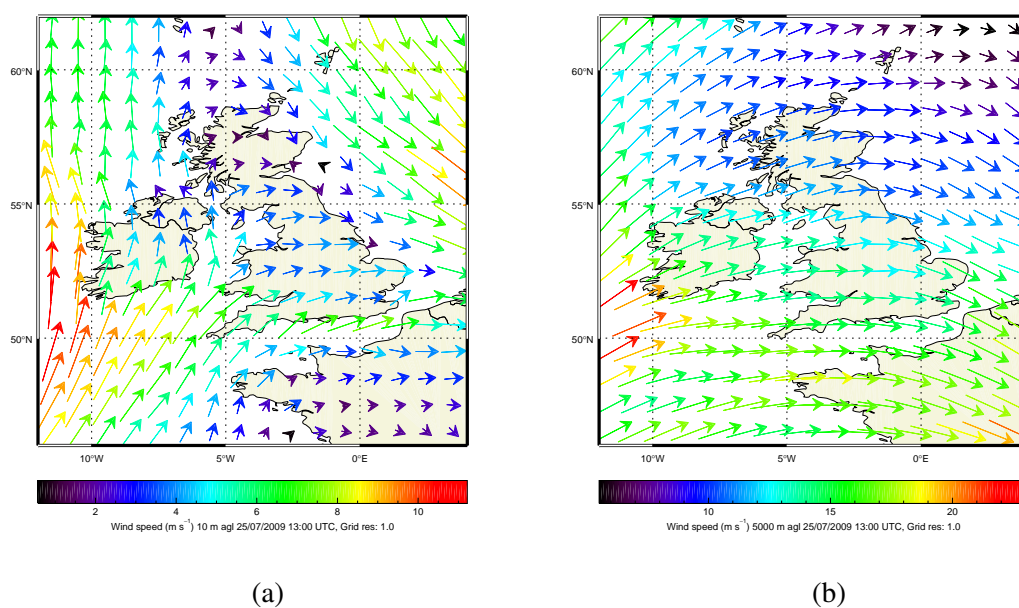


FIGURE 3.20: The wind direction and speeds at different heights in the atmosphere as given by the UK Met Office Unified model. (a) shows the wind vectors at 10 metres above the ground level. (b) the wind directions and velocities at 5000 m a.g.l. Only the x and y components are displayed. The z component (ie. the vertical transport) is not shown.

simulations.

To simulate the air column, it was divided into 10 discrete levels. Ten separate tracers were emitted within NAME, at heights starting at ground level and increasing by 1000 metres at each release. Ground level was defined as 0 m, level 2 at 1000 m etc. In each case 10000 separately tagged particles were released and followed back in time for 10 days in time (see Figure 3.21). A multi-level output i.e. the dosage of the individual tracer in the footprint layer, was calculated by the model. NAME was also requested to output temperatures and pressures at each discrete height. The latter output was used to calculate the  $XCH_4$  values at each sub-level.

The next step was to convert the dosage maps to dilution matrices, as described in Chapter 3. The method followed is identical for each of the runs, each essentially being treated as an individual point source in the column. The dilution matrix is multiplied by the EDGAR emission inventory, resulting in a concentration enhancement ( $g\ m^{-3}$ ) at the particle release point. This is then converted to a mixing ratio,  $XCH_4$  using Equation 3.11.

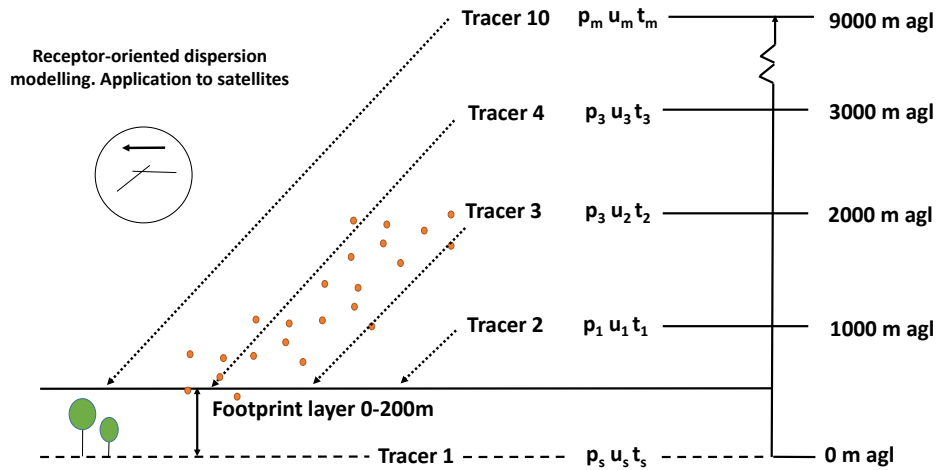


FIGURE 3.21: The release of tracer particles occurs at discrete pre-defined levels (m agl) within the column. The model is asked to output the pressures ( $p_n$ ) and temperatures ( $t_n$ ), where  $n=1\dots N$  is the number of levels. At each level  $i$ , there is a corresponding value of the calculated volume mixing ratio given shown as  $u_n$

### 3.4.1 Pressure weighting

To obtain the total column mixing ratio, the individual pressure level  $\text{XCH}_4$  enhancement values have to be pressure weighted. A single profile-weighted synthetic column measurement can then be calculated ( $\text{XCH}_4 = hx$ ). The vector  $h$  represents the pressure intervals assigned to the state vector levels. The method used to do this was described by Connor et al. (2008).

The pressure weighting function,  $h$ , is defined so that  $\text{XCH}_4 = hTx$ . The calculation of the elements of  $h$  and  $h_i$ , where  $i = 1, q$ , where  $q$  is the number of levels, is described here. Note that  $h_i = 0$  for  $i = q + 1, n$ , where  $n$  is the number of elements in the state vector. In order to calculate  $h$ , the pressure interval in each layer must be conceptually divided by assigning fractions of it to the two adjacent levels, in such a way that an integration over all levels conserves both the total pressure and the  $\text{CH}_4$  column. Let  $u(p)$  be the  $\text{CH}_4$  mixing ratio as a function of pressure, and let an infinitesimal pressure interval  $dp$ , between levels  $i$  and  $i + 1$ , be divided between the adjacent levels in proportions given by:

$$i : dp = \frac{u_{i+1} - u(p)}{u_i - u(p)} = dg_i \quad (3.14)$$

$$i + 1 : dp = \frac{u(p) - u_i}{u_{i+1} - u_i} = dg_{i+1}, \quad (3.15)$$

Then the pressure interval assigned to the level  $i$  is the integral of  $dg_i$  from level  $i - 1$  to level  $i + 1$ . Now if  $u$  varies linearly with a function  $F(p)$ , then

$$u(p) = F_i(p) \Delta u_i + u_i, \quad (3.16)$$

If we interpolate according to the rule that  $u(p)$  varies linearly in  $\ln p$ , this implies

$$F_i(p) = \frac{\ln(p/p_i)}{\ln(p_{i+1}/p_i)} \quad (3.17)$$

followed by

$$dg_i = dp(1 - F_i(p)) \quad (3.18)$$

and

$$dg_{i+1} = dpF_i(p). \quad (3.19)$$

Now  $h_i$  equals the integral of  $dg_i$  over the two layers adjacent to level  $i$ , divided by the surface pressure

$$h_i = \frac{1}{p_{surf}} \left[ \int_i^{i+1} (1 - F_i(p)) dp + \int_{i-1}^i F_{i-1}(p) dp \right]. \quad (3.20)$$

For the edge layers, if  $i = 1$ , only the first term applies, while if  $i = q$ , only the second term applies. After some algebra,

$$h_i = \left| \left( -p_i + \frac{p_{i+1} - p_i}{\ln(p_{i+1}/p_i)} \right) \left( p_i + \frac{p_i - p_{i-1}}{\ln(p_i/p_{i-1})} \right) \right| \frac{1}{p_{surf}} \quad (3.21)$$

where the two terms are separated to simplify the calculation of the edge layers. Note that if  $p$  decreases with increasing  $i$ ,  $h_i$  is formally negative and thus the absolute value is taken.

### 3.5 Modifying the inversion system

The inversion algorithm, as described in Section 3.2, needs to be able to accept the multi-level outputs produced by NAME. The algorithm needs to be presented with a Jacobian,  $K_{satellite}$ , that contains the multi-level output information obtained from the model. We must, therefore, produce a single value weighting function for each potential flux cell to be assimilated into the inversion algorithm. To achieve this, the dosage maps obtained by NAME were first converted to dilution matrices ( $D$ ), as described in Section 3.3.1. This was done for each individual tracer particle release, presenting us with 9 dilution maps. Each map indicates how sensitive that particular layer is to emissions from different emission regions. The dilution matrix was then multiplied by the pressure weighting function  $h$ . The sum of the resulting weighted dilution maps provides us with  $K$  to be used in the inversion.  $K$  now contains vertical the weighted sensitivity information:

$$K_{satellite} = \sum(Dh). \quad (3.22)$$

In the case of Mace Head observations, the difference between the background and the measurement was put into the algorithm as the measurement ( $y$  vector). In these simulations,  $y$  shall be defined as the final observed value. The system will then be asked to estimate the background. It is essentially being treated as another unknown quantity to be retrieved. The algorithm will not however have much independent weighting information to help it determine this value. An extra element of  $K$  will be added with a pre-defined value of 1 for the background. The value estimated by the system will be the the fraction of the concentrations, which cannot be assigned to flux grid boxes, using the information contained in NAME obtained weighted dilution vector. In other words, the NAME output will be used to distribute the observed  $XCH_4$  value across the potential emitting grids and any residual will be the background. The baseline is treated as a flux region, thus an error will also be estimated. In Chapter 4, the framework developed here shall be used to carry out a synthetic inversion study for a number of instruments.

### 3.6 Data used in the study

In Chapter 5, the forward model component of the inversion system will be used to model the  $XCH_4$ , which GOSAT would be expected to observe in various geographical regions. In this section, data to be used in Chapter 5 is introduced. This includes the a priori emission estimates used to model synthetic satellite measurements, as well as

the introduction to GOSAT XCH<sub>4</sub> data to which the synthetic satellite measurements are compared. The combined emission inventories will also be used in Chapter 4, when simulating the performance of CarbonSat and Sentinel-5 Precursor instruments.

### 3.6.1 Leicester retrieved GOSAT methane XCH<sub>4</sub>

The XCH<sub>4</sub> measurements used in this study were retrieved at the University of Leicester utilising the proxy retrieval approach (Parker et al., 2011). The proxy method does not in contrast to the full physics retrieval-rely on Bayesian optimal estimation to retrieve a set of atmospheric / surface / instrument parameters from measured spectral radiances. CH<sub>4</sub> and CO<sub>2</sub> retrievals are carried out sequentially with channels at 1.65 and 1.61  $\mu\text{m}$  respectively. In order to obtain the volume mixing ratio (VMR) of CH<sub>4</sub>, the XCH<sub>4</sub>/XCO<sub>2</sub> ratio is multiplied by a model XCO<sub>2</sub> (from CARBONTRACKER). CO<sub>2</sub> is known to vary in the atmosphere much less than CH<sub>4</sub> and as the CO<sub>2</sub> absorption band is spectrally close to that of CH<sub>4</sub>, CO<sub>2</sub> can be used as a proxy for the light path to minimize common spectral artefacts due to aerosol scattering and instrumental effects (Frankenberg et al., 2011). Column integrated concentration data is available from June 2009 onwards at the University of Leicester.

The XCH<sub>4</sub> has been validated against TCCON data and compared to a global chemistry models (such as GEOSCHEM) XCH<sub>4</sub>. Figure 3.23 shows the monthly mean in gridded 2° × 2° maps of the GOSAT and GEOSCHEM XCH<sub>4</sub>, as well as the zonal means between 40°S and 50°N in 5° bins for the months of August 2009, September 2009, June 2010 and July 2010. Natural methane sources are not expected to vary greatly in the timescale of two years, therefore June and July 2010 are considered as representative months of the agreements between GEOSCHEM and GOSAT in the previous year. The agreement between the model and the observed zonal mean hemispheric gradients is very good ( $r \sim 0.99$ ), varying from month to month, as expected with seasonal sources and sinks, with the model reproducing most of the observed variability. Figure 3.22 shows a time series of GOSAT and GEOSCHEM XCH<sub>4</sub> between August 2009 and July 2010 for various regions. The differences between the model and the observed XCH<sub>4</sub> values of up to 20 ppb are found over latitude bands which include strong emission sources. The discrepancy is problematic, as regions under investigation in Chapter 5, do include such strong sources (South America and South East Asia).

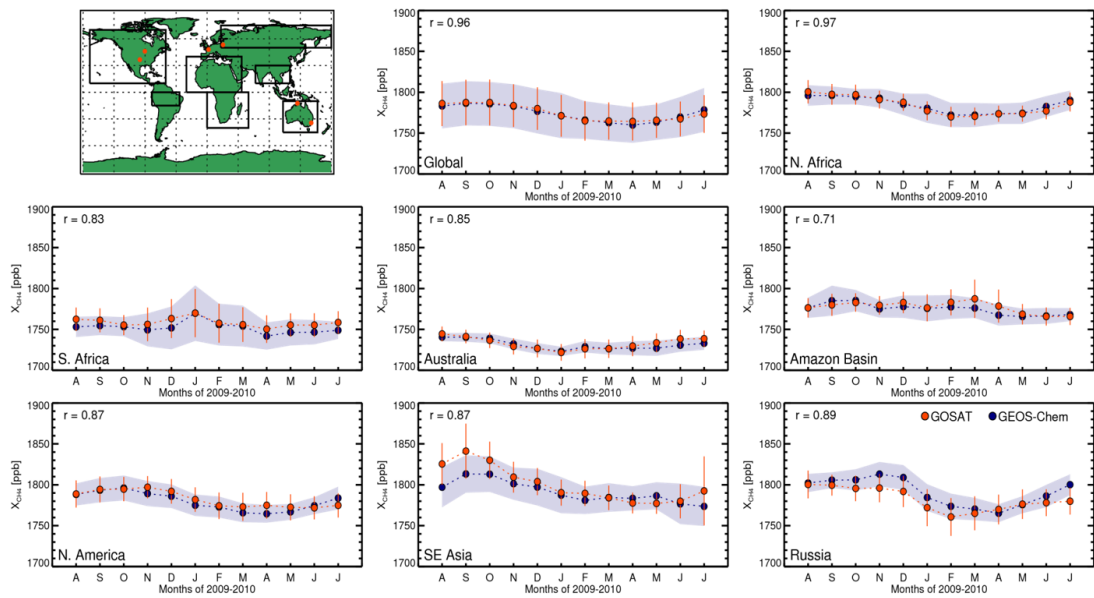


FIGURE 3.22: The time series of the GOSAT and GEOSCHEM  $X_{CH_4}$  between August 2009 and July 2010 globally and for the 7 regions outlined on the map (Parker et al., 2011). The error bars and shaded areas represent the standard deviation of the GOSAT and GEOSCHEM data respectively.

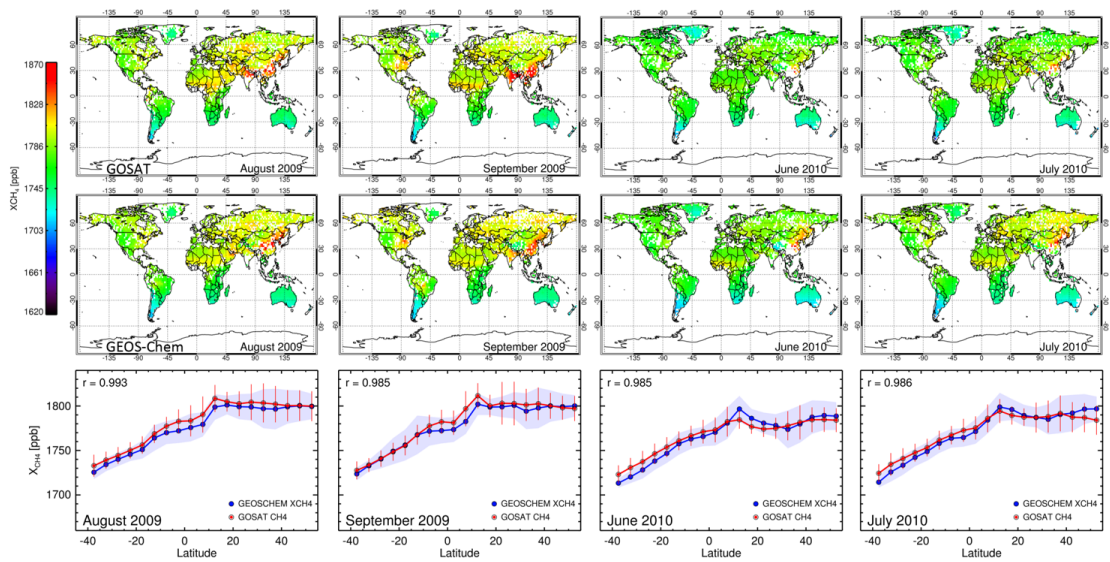


FIGURE 3.23: The monthly mean gridded  $2^\circ \times 2^\circ$  maps of the (top) GOSAT  $X_{CH_4}$  and (middle) GEOSCHEM  $X_{CH_4}$  for August 2009, September 2009, June 2010 and July 2010 sampled at GOSAT measurement times and locations (Parker et al., 2011). The zonal means between  $40^\circ S$  and  $50^\circ N$  in  $5^\circ$  bins for these months are also shown with error bars (red) and the shaded areas (blue) represent the standard deviation of the GOSAT and GEOSCHEM data respectively. The correlation coefficient ( $r$ ) is also shown.

### 3.6.2 Emission Inventories

The forward modelling system used in Chapter 5 (as shown in Figure 5.18) and Chapter 4 (see Figures 4.20a and 4.20b), utilises existing emission estimates from various sources to simulate the observed concentrations of  $XCH_4$  using the method developed in this chapter. Bottom-up anthropogenic and inverse-modelled natural sources are combined to be used by the forward modelling system. The datasets described here have also been used to initialise the global GEOSCHEM model at Edinburgh, which will be used to initialise the background (see Section 5.4). Use of the same inventories will minimise errors that could potentially be introduced by using different inventories. The notable exception to this is the EDGAR emission inventory. Edinburgh utilise EDGAR version 3, whilst in this thesis, the latest available data (version 4.2) is used.

#### EDGAR

EDGAR provides anthropogenic greenhouse gas and air pollutant emission estimates, including  $CH_4$  (EDGAR, 2009). The underlying sectors considered in the production of EDGAR database are: energy; industrial processes; solvents and other product use; agriculture; land-use change; waste and other. These encompass sub-groups of even more detailed emission estimates. An example would be: road, aviation, rail transportation amongst other emissions within the energy source header. The geographical database has been built on data such as location of energy and manufacturing facilities, road networks, shipping routes, human and animal population density and agricultural land use. The emissions are reported on a spatial grid of  $0.1^\circ$ . EDGAR as used here, has rice and fire emissions removed. The rice and fire emission estimates included in EDGAR have a temporal resolution of one year. Both, Bloom et al. (2010) rice paddy and the Global Fire Emissions Database (GFED) estimates (van der Werf et al., 2010) used here, have a higher temporal resolution. This is important, as rice fields for example show significant variations in emission magnitudes on a monthly timescale. Rice fields tend to emit more in the late summer months in South East Asia. Fire emissions show even more temporal variation. Fires can last days and the vast fraction of the emissions are going to occur during the period the fire is active. EDGAR, if used, would calculate the average over the year, thus smoothing out any potential enhancement that could be potentially observed. This in effect would neutralise one of the greatest advantages of using a high-resolution dispersion model. As each simulated exposure has a Lagrangian model footprint of 10 days only, this is bound to have a significant impact on the final result. EDGAR emissions discussed here are calculated for the year of 2008, therefore the fires occurring in

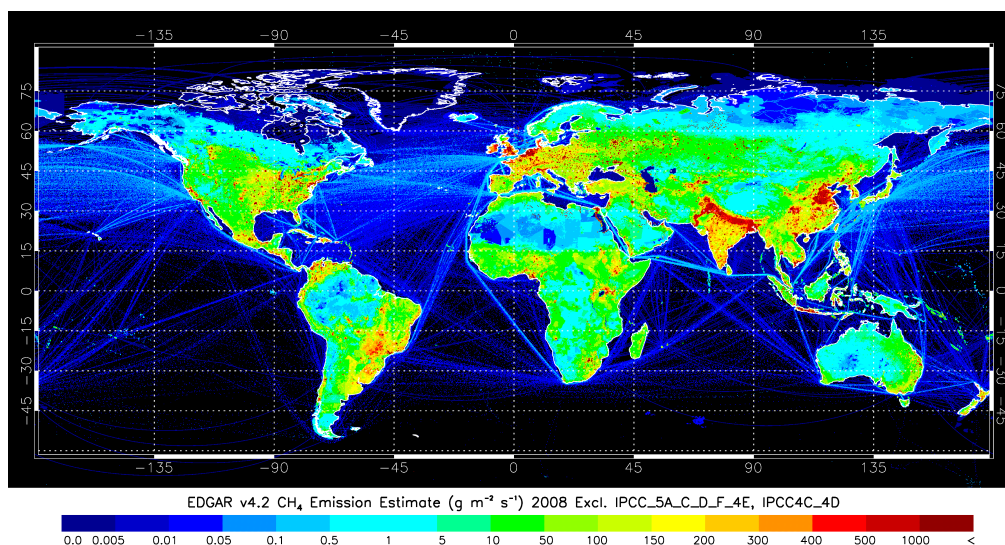


FIGURE 3.24: EDGAR methane emissions inventory, excluding rice and fire emissions (EDGAR, 2009).

2009 or 2011 would not be taken into account when compiling the combined emission inventory.

### **Bloom et al. wetland and rice emission inventory**

EDGAR provides anthropogenic emission estimates only, thus an additional dataset containing significant wetland and rice field emissions had to be used. Bloom et al. (2012) have developed a Dynamic Methanogen-available Carbon Model (DMCM) to quantify the role of the methanogen-available carbon pool in determining the spatial and temporal variability of the tropical wetland CH<sub>4</sub> emissions. DMCM parameters were fitted to satellite observations of CH<sub>4</sub> columns from SCIAMACHY together with the equivalent water height (EWH) from NASA GRACE instrument. The global CH<sub>4</sub> emissions were derived at a daily temporal resolution and at a spatial resolution of 3° × 3°.

### **Termite emission inventory and soil sink**

The termite emission estimates and the soil methane sink were calculated by Fung et al. (1991). The signatures of each of the sources and sinks in the atmosphere were simulated using a global three-dimensional transport model. Candidate methane budget scenarios were constructed according to the mass balance of methane and its carbon isotopes. A number of scenarios were then tested by their ability to reproduce atmospheric observations. The termite emissions are greatest at the tropical and sub-tropical regions and can

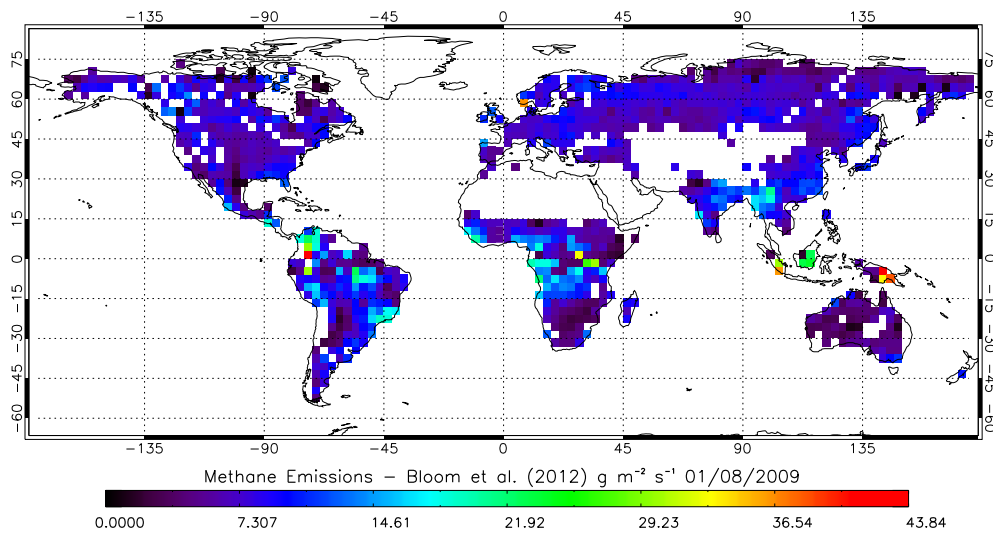


FIGURE 3.25: Wetland and rice paddy emission inventory for the 1st of August, 2009 (Bloom et al., 2012).

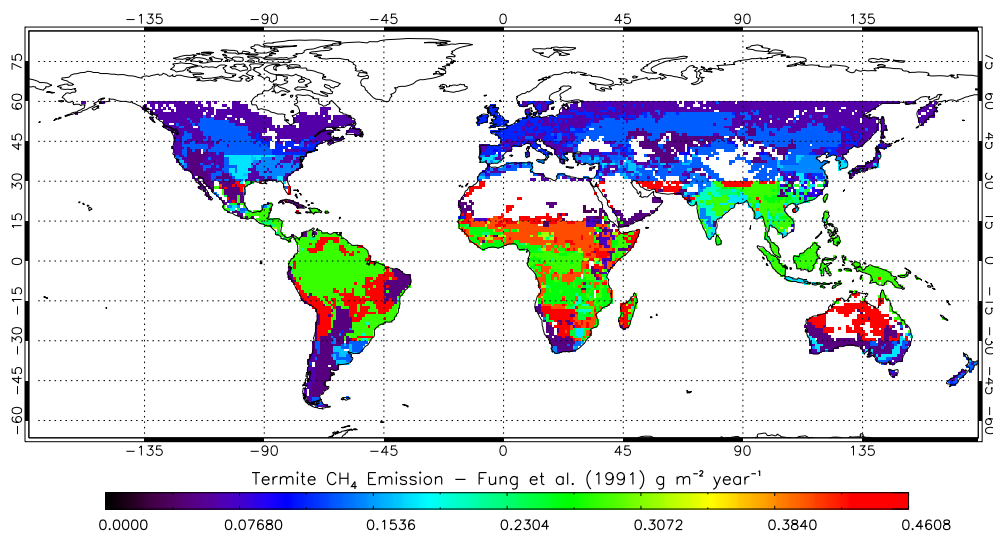


FIGURE 3.26: Termite emission inventory used by the modelling system (Fung et al., 1991).

be considered aseasonal. The total assumed source strength was  $50 \text{ Tg year}^{-1}$ , which was distributed among ecosystems according to the tabulations of Zimmerman et al. (1982) and Fraser et al. (1986). The model experiment soil absorption was run with an aseasonal source with a basis strength of  $50 \text{ Tg year}^{-1}$ . Absorption was modelled to be constant throughout the year, as microbial transport was assumed to be controlled by the soil gas transport rather than temperature.

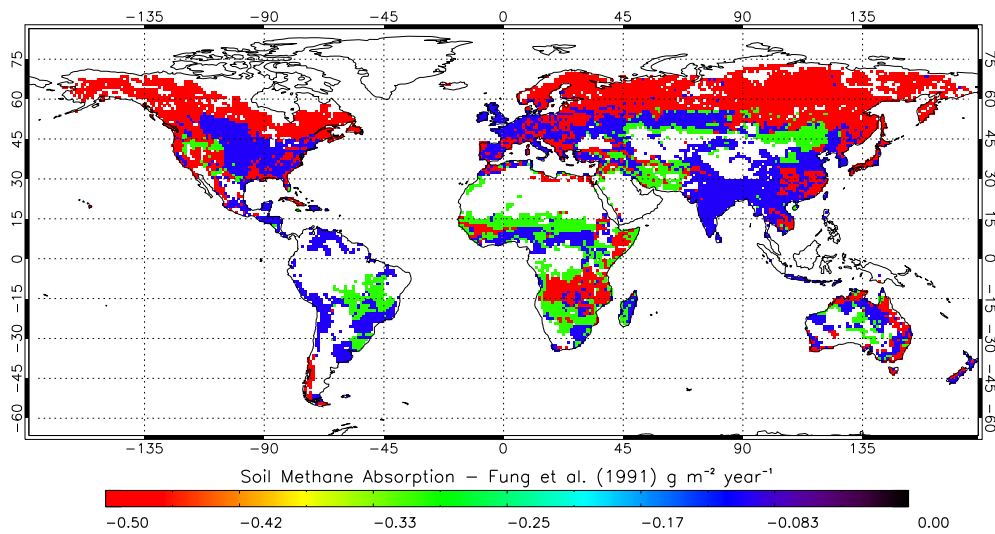


FIGURE 3.27: Aseasonal methane soil absorption (Fung et al., 1991).

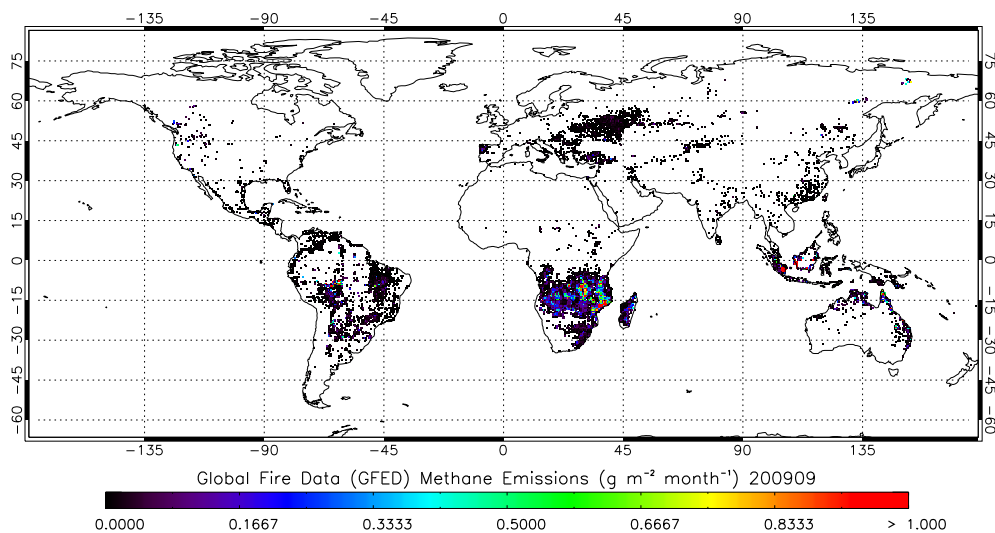


FIGURE 3.28: GFED fire emission estimates for September, 2009 (van der Werf et al., 2010).

### GFED Fire Emission Inventory

The GFED fire emission have been calculated by using a revised version of the Carnegie-Ames-Stanford-Approach (CASA) biogeochemical model and improved, satellite-derived estimates of the burned area, fire activity, activity and plant productivity. GFED methane emission estimates have a temporal resolution of a day and a spatial resolution of  $0.5^\circ$  (van der Werf et al., 2010). The primary data source used to create the burned area maps is the Moderate Resolution Imaging Spectroradiometer (MODIS) surface reflectance imagery.

## 3.7 Summary

In this chapter, the mathematical framework described by Rodgers (2000) to find the optimal state of  $\text{CH}_4$  fluxes given atmospheric methane measurements is implemented. The method relies on a Bayesian inference of flux, taking into account the uncertainties in the measurements and the a priori flux emission estimates, as well as a modelled link between the emissions and the observations. NAME is set up to provide this link, as an operator connecting the measurement space to the flux space. The diagram of the inversion system can be seen in Figure 3.3. The mathematical inversion framework is initially tested on synthetic data from the Mace Head ground measurement site. The data is modelled using a known methane emission map, which can then be inverted back to the fluxes. A measurement noise of various magnitudes is simulated, demonstrating the ability of the inversion algorithm to successfully invert observations. Next, NAME is set up to model the dispersion from a column measurement, as would be observed by an Earth observation instrument. This work will form the basis of the next chapter, where the use of GOSAT, Sentinel-5 Precursor and CarbonSat measurement data with the inversion framework to help reduce the uncertainties in  $\text{CH}_4$  fluxes, will be assessed. This chapter also provides an introduction to the data to be used later in the thesis. This includes a description of the emission inventories and GOSAT data. The emission inventories will be combined when simulating the observations of the instruments studied in this thesis.

# Chapter 4

## Synthetic inversion of space-borne instrument methane measurements

### 4.1 Aims

The aim of this chapter is to utilise the previously developed inversion algorithm to quantify the ability of GOSAT and other space-borne instruments to help constrain methane fluxes over the United Kingdom and Ireland. The analysis will consist of a series of observation system simulation experiments, assuming various observation error scenarios. The forward model component will be used to simulate  $XCH_4$  observed by a GOSAT-like instrument over the United Kingdom and Ireland. The inversion algorithm will then be used to retrieve the known land flux map, used to model the enhancement as well as a known background. The experiments will also simulate the effect of clouds, which will be modelled by removing a varying number of observations from the inversion. The effect of reducing the inversion spatial resolution will also be investigated.

The performance of future methane sensing space-borne missions, such as Carbon-Sat and Sentinel-5 Precursor, will be simulated assuming that multiple potential measurements within a region can be reduced to a single observation with a square root decrease of the measurement error, as well as adopting a more realistic approach. The future instruments will potentially make it possible to obtain more measurements owing to smaller measurement footprints.

The overview of the chapter is as follows:

- In Section 4.3, synthetic inversion results utilising GOSAT-like instrument observations at a spatial resolution of  $0.5^\circ$  are presented.

- In Section 4.4, an inversion is carried out with low emitting water grid boxes combined into a single flux region, thus reducing the number of unknowns in the state vector.
- Section 4.6 repeats the tests with a decreased grid box spatial resolution and simulations of the cloud cover effects on the error reduction.
- In Section 4.7, the results of the observation system simulation experiments carried out with synthetic, future XCH<sub>4</sub> sensing instruments (CarbonSat and Sentinel-5 Precursor), are presented.

## 4.2 Simulation setup

In this section, inversions of the column XCH<sub>4</sub> data, measured by a space-borne instrument, are carried out and the corresponding NAME simulations are described in more detail. The number of available retrieved GOSAT measurements over Britain and Ireland during August 2009, is 12 (the locations can be seen in Figure 4.1a and for more detail on the instrument, see Section 2.3.2). The number of observations is low, mostly due to extensive cloud cover in the region. A vast majority of measurements in these conditions are screened out during the retrieval, resulting in little useful data over Britain and Ireland over the time frame in consideration. 12 measurements are not enough to reliably invert fluxes of CH<sub>4</sub>. It was therefore decided to produce a synthetic measurement map over the United Kingdom and Ireland for the month. The simulated measurement locations represent observations from a GOSAT-like instrument, capable of taking measurements over the whole of Britain once daily. The observation points are spaced out 0.5° apart, all taken at 13:00 simultaneously. It is initially assumed that no clouds are present and all of the observations pass the quality filter. This results in a total of 5084 simulations (164 × 31 days, see Figure 4.1b for the geographical distribution of synthetic measurements). A negligible measurement error of  $1 \times 10^{-10}$  ppbv was assumed.

The methodology developed in Section 3.4 was utilised for this simulation. NAME was run for each of the synthetic observation columns. The simulation region was defined as spanning from -11.25° to 3.75° in longitude and from 47° to 63° in latitude. In the initial test simulation, the geographical resolution of NAME was set to 0.5°, resulting in the fluxes from 960 grid boxes to be retrieved. An atmospheric background is also directly retrieved by the inversion algorithm. The NAME output in combination with EDGAR emission inventories was used to first simulate the satellite observations, utilising the equation

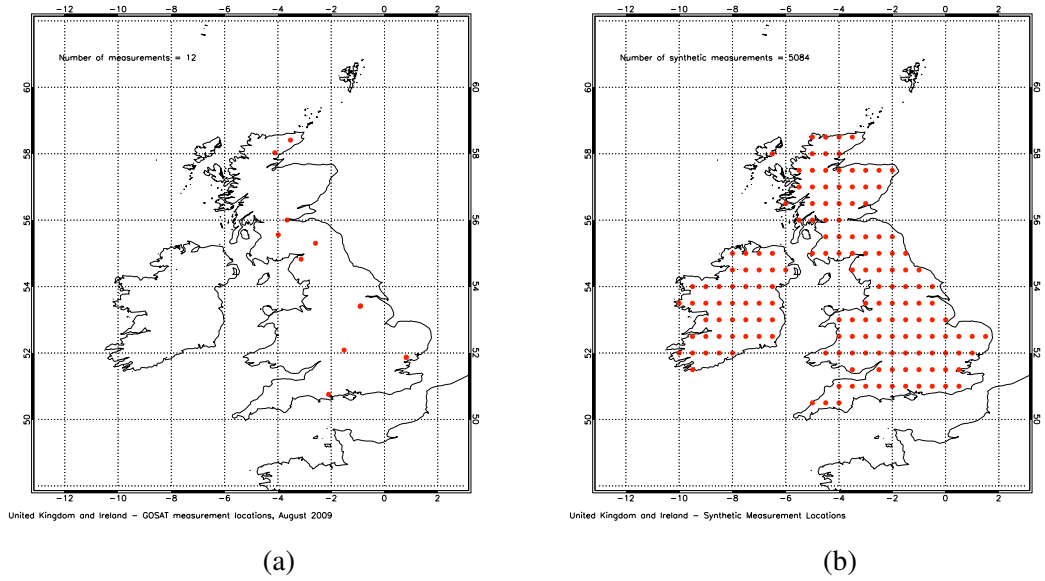


FIGURE 4.1: (a) GOSAT measurement locations and the number of total measurements in the month of August, 2009. (b) The measurement locations of synthetic measurements to be produced. The total number of simulated measurements is 5084.

$$\text{Observed } XCH_4 = (K \times \text{EDGAR inventory}) + \text{background}, \quad (4.1)$$

where,  $K$  is the pressure weighted, multi-level NAME output, which has been converted to a dilution matrix (see Section 3.5). The background was chosen arbitrarily and was assigned a value of 1770 ppbv. The background is treated as an extra unknown in the state vector in the inversion ( $x$ , Equation 3.8). As can be seen in Figure 4.2, the simulation region includes all of Britain and Ireland, as well as large areas of water. The land fluxes are a number of magnitudes higher than the  $CH_4$  emissions from the water grid boxes, which are mainly due to shipping. The exceptions are due to oil rigs in the North Sea, which emit significant quantities of  $CH_4$ . It is desirable to investigate how well the inversion algorithm is able to constrain the low-flux grid boxes over the ocean.

### 4.3 Initial synthetic inversion results

In this section the results for the initial synthetic test are presented. As can be seen in Figure 4.4a, the algorithm struggles to estimate the flux value over the ocean and the southern border of the domain. It places negative emissions next to positive fluxes (known as a dipole). The combined total flux of the two boxes cancel each other out and

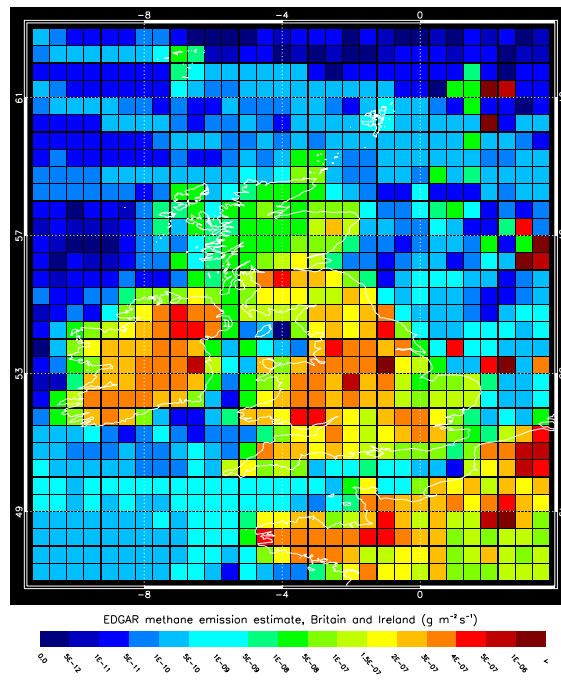


FIGURE 4.2: The EDGAR emission inventory utilised to produce the synthetic measurements. This is also used as the a priori in the inversion algorithm.

do not have a large impact on the receptor. This is a weakness in the chosen mathematical inversion model, as the system is able to calculate negative flux values, i.e. sinks. This displays the need to group source regions further out from the receptor together. It is interesting to compare the measurement footprint (Figure 4.3) to the error in the inverted fluxes (Figure 4.4b) As expected, the error is greatest in the areas where the observations do not sample the surface layer well. The error estimate shows a large uncertainty in the inverted flux east of Britain. The prevailing winds were blowing from the Atlantic ocean towards Europe in the month of August, 2009. The meteorological conditions therefore make any flux estimation, east of Britain difficult.

Figure 4.5 shows the inversion result, when the measurement error is increased to 1 ppbv. The retrieved flux is identical to the EDGAR flux map over the ocean and mainland Europe grid boxes (Figure 4.5a). The error reduction (Figure 4.5c) shows us that the a posteriori error is identical to the error value assigned to the a priori data. The result therefore tells us that there is not enough new information to allow the system to decrease the error in these regions. It was decided, that the next step was to combine all of the grid boxes over the ocean to a single flux region. This would also be done for the emitters in the mainland Europe. Running the inversion at the full resolution would be futile, as the system with a relatively low, simulated measurement error of 1 ppbv has to default to a priori values. The same pattern is expected to be seen, if the observational

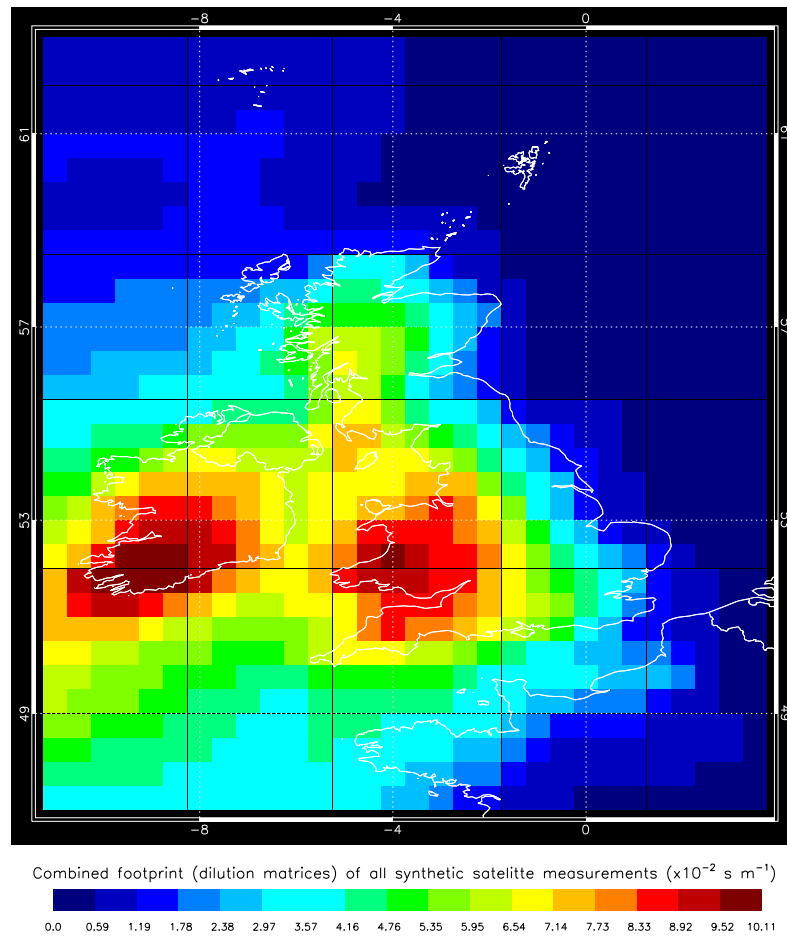
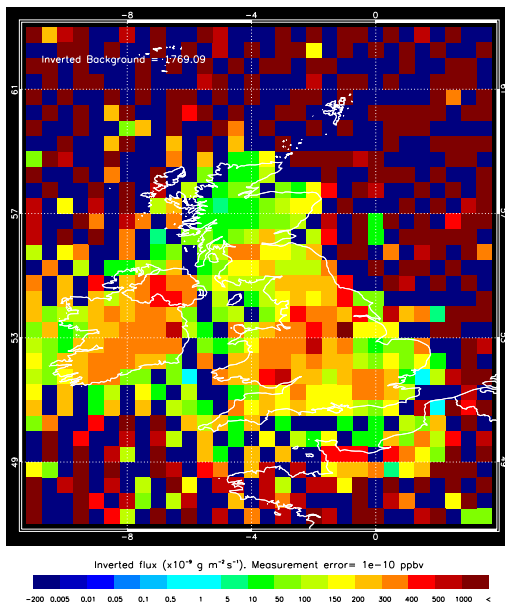


FIGURE 4.3: The average dilution values over the region of interest. This can be taken as a geographical footprint of the measurement.

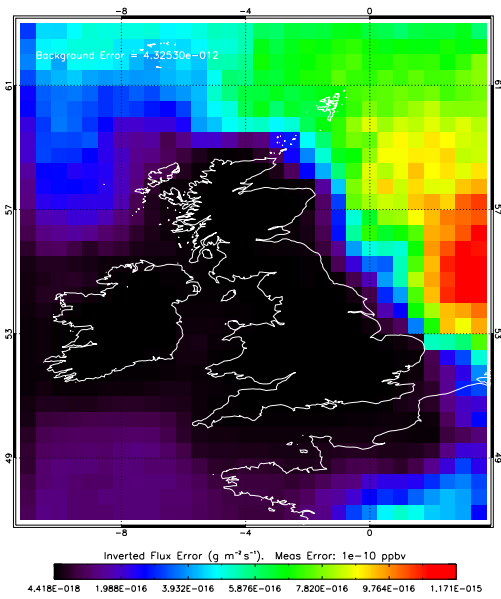
error is to be increased.

#### 4.4 Reducing the number of unknown flux regions

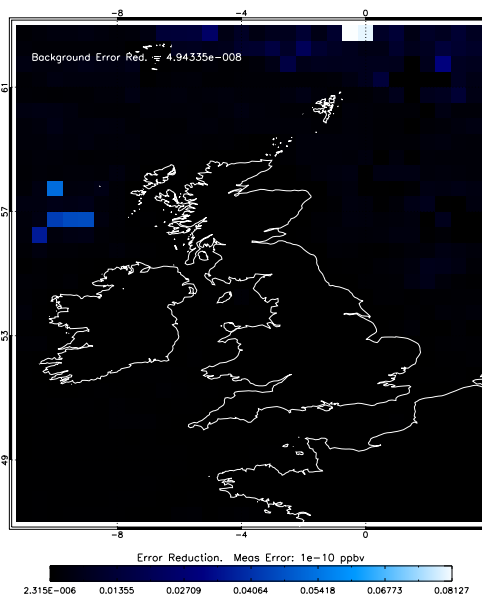
As can be seen in the previous section, the algorithm is not able to reliably retrieve the fluxes over the ocean regions around Britain and Ireland. There is not enough information in the weighting function matrix to constrain the emissions over these regions. It is best to combine the relatively low-emitting ocean grid boxes into a single source region, thus decreasing the number of regions the flux would be inverted for substantially. The resolution of the inverted fluxes over Britain and Ireland would remain at the native NAME run resolution of  $0.5^\circ$ . Britain and Ireland are very well sampled (Figure 4.3), which is expected, as the measurements are made on a regularly sampled grid over the region. Measurements over France and mainland Europe were also combined into a



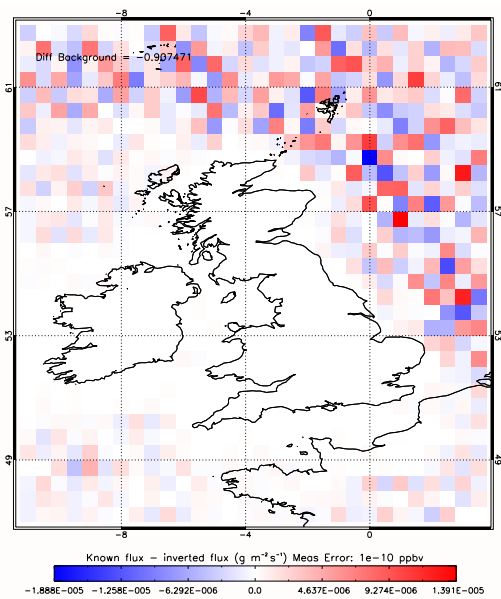
(a)



(b)



(c)



(d)

FIGURE 4.4: Inversion result with a measurement error of  $1 \times 10^{-10}$  ppbv. (a) the inverted flux, (b) the inverted flux error, (c) the error reduction of the inverted flux, assuming a 100% uncertainty in the a priori data, (d) the difference between a known flux value and the inverted flux.

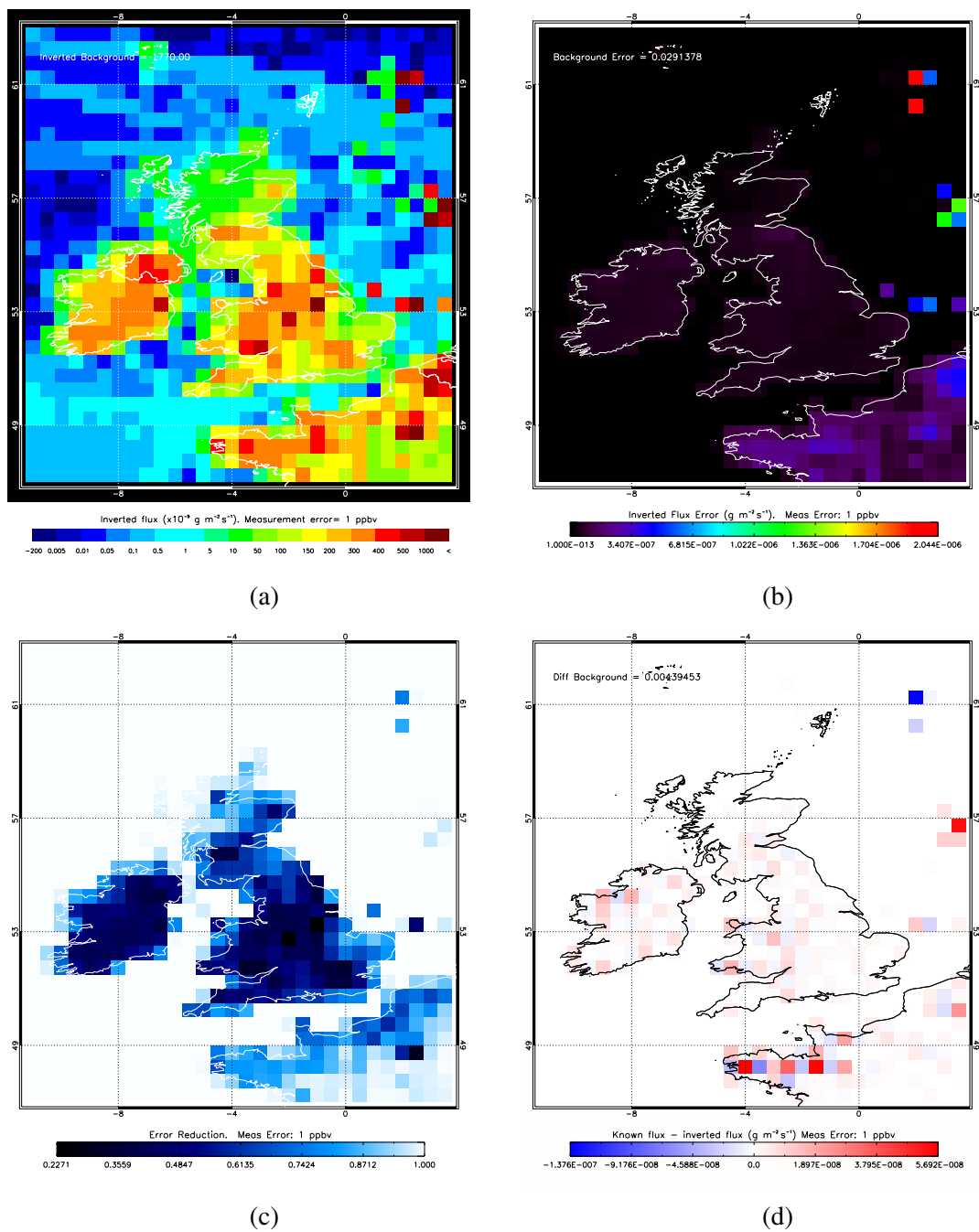


FIGURE 4.5: Inversion result with a measurement error of 1 ppbv. (a) the inverted flux, (b) the inverted flux error, (c) the error reduction of the inverted flux, assuming a 100% uncertainty in the a priori data, (d) the difference between a known flux value and the inverted flux.

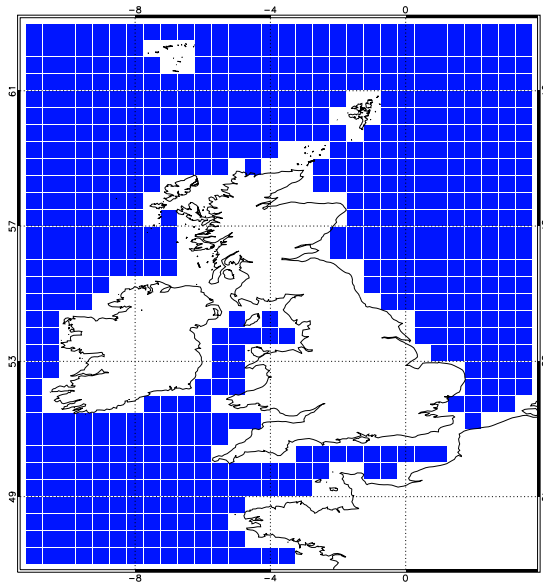


FIGURE 4.6: The sea flag, produced utilising the MODIS instrument. The low-emitting boxes over the ocean are combined into a single value, with the exception of high-emitting oil rigs in the North Sea. The islands north of Scotland were manually assigned a water flag, as the a priori emissions for these regions are very low.

single source. In a mathematical sense, the weighting function  $K$  elements in the corresponding grids are averaged out.  $K$  now has the dimensions: Number of Britain and Ireland grid boxes + 1 ocean emission box + 1 mainland emission box + 1 element with a value of 1 for the background.

The land-sea flag was produced utilising data from the NASA MODIS instrument. The high resolution MODIS data ( $0.1^\circ$  resolution) contains a water flag which is used in this work. All of the MODIS grid boxes in the  $0.5^\circ$  within the defined flux area were first found. The box was flagged as a 'water box' if all of the MODIS pixels were reported being over the sea. The ocean grid boxes designated as the sea were then combined. The exceptions to this were the high-emitting areas in the North Sea. High emissions east of Britain were most likely due to degassing from oil rigs (see EDGAR emissions, Figure 4.2). If the a priori emissions in these boxes were higher than  $1 \times 10^{-7} \text{ g m}^{-2}$ , it was manually designated as a land box. The island north of Scotland with negligible emissions were manually assigned a water flag.

The inversion procedure was repeated and the measurement error was simulated as  $1 \times 10^{-10}$ , 1, 5 and 10 ppbv. As a result of the described procedure, the number of unknown regions was reduced substantially, with a total number of unknown grids decreasing from 961 to 260.

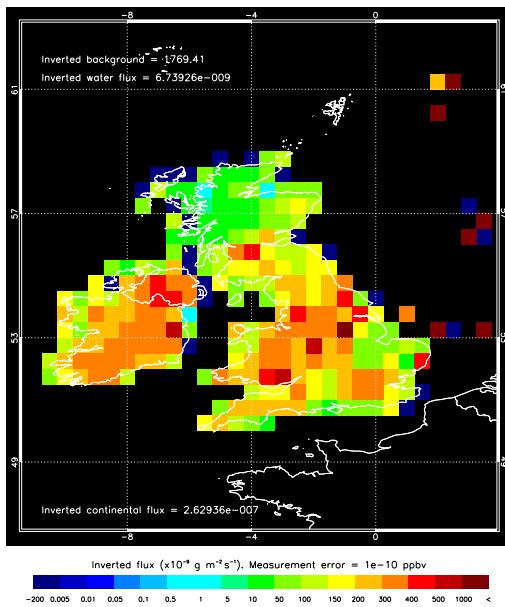
## 4.5 Reduced number of grids - results

The inversion results for the decreased number of unknown flux regions can be seen in Figures 4.7, 4.8, 4.9 and 4.10. The system is generally able to reproduce the fluxes when a measurement error of  $1 \times 10^{-10}$  ppbv is simulated. The error is reduced throughout the whole of the domain. The absolute flux uncertainty is greatest over the high-emitting grid boxes in the North sea. The a posteriori emissions over the North Sea show a so-called dipole - a high-flux cell placed next to a grid box with a negative flux. Despite the high emissions, these grid boxes do not have a big enough impact on the column mixing ratios to be able to assign the flux values correctly (Figure 4.10c). The combined result of the low and high calculated fluxes is 0. The error reduction is low throughout the domain, including the oil rig locations. Even though the values obtained by the system are wrong, the net combined fluxes produce the modelled signal at the observed points.

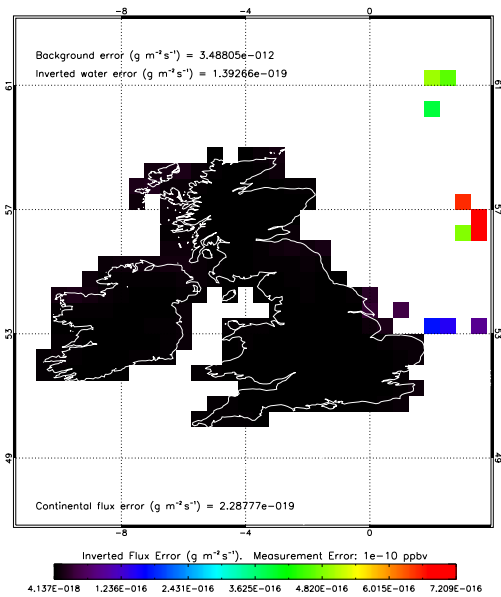
As the measurement uncertainty is increased, the results demonstrate an expected pattern. The inverted flux errors increase and in effect, the ability of the system to decrease the a priori errors gets worse. The system performs best in the areas of high emission, such as in central Britain. (plots 4.8c through to 4.10c) However, the system struggles to estimate the fluxes in areas with the highest measurement errors, such as Scotland.

## 4.6 Decreasing the observation density and inversion spatial resolution

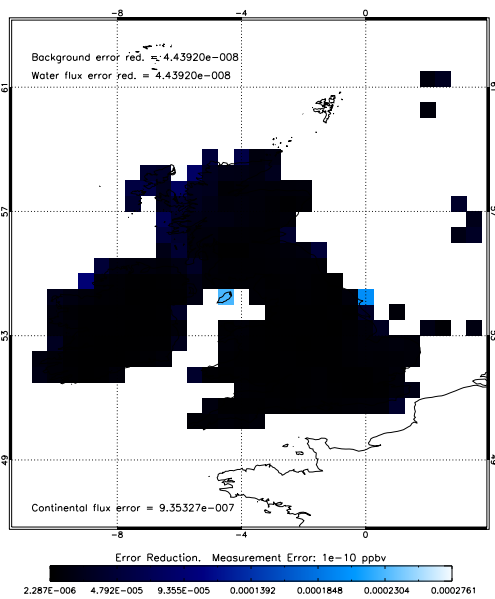
An inversion was also carried out with a decreased number of simulated observations. The observation mesh density was reduced by removing observation grid points from the original observation map (Figure 4.12). This does however lead to a spatial bias, as the observation density is not decreased uniformly. Increasing the spacing between the observation would avoid the spatial bias, however this could not be completed due to time constraints. The total number of daily simulated observation used in the inversion ranged from 16 to 144. This could be said to simulate cloud cover, with the decreasing number of observations representing an increasing proportion of the observations in which the satellite view of the surface would be obstructed. The experiment was also repeated decreasing the spatial resolution of the inverted flux to  $1^\circ$  (see Figure 4.11a for EDGAR a priori emission inventory gridded to  $1^\circ$ ). Running the inversion algorithm at a lower resolution allows us to investigate the effect on the error reduction when different



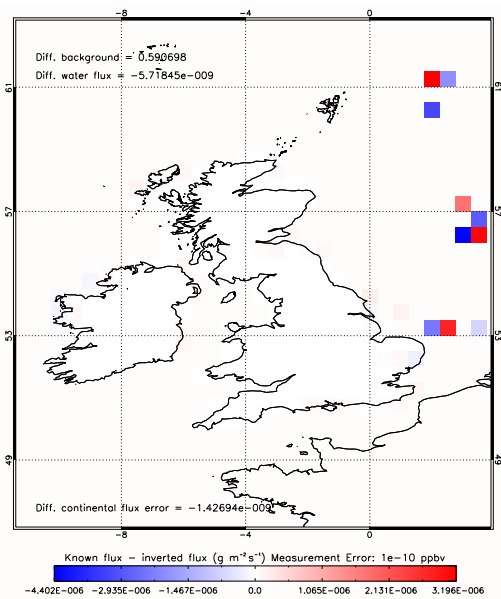
(a)



(b)

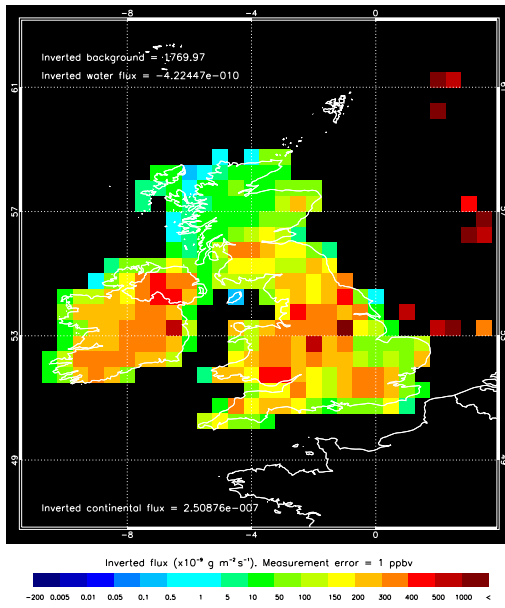


(c)

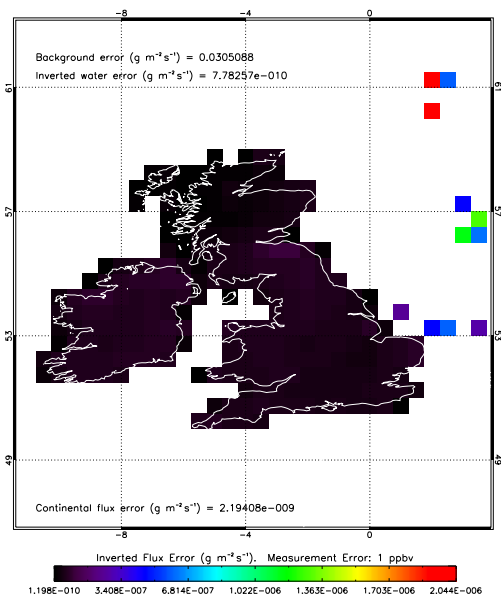


(d)

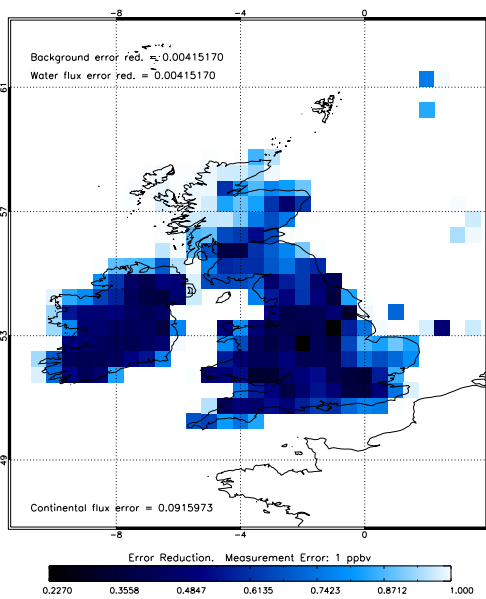
FIGURE 4.7: Inversion result (grouped mainland and water boxes) with a measurement error of  $1 \times 10^{-10}$  ppbv. (a) the inverted flux, (b) the inverted flux error, (c) the error reduction of the inverted flux, assuming 100% uncertainty in the a priori data and (d) the difference between the known and the inverted flux.



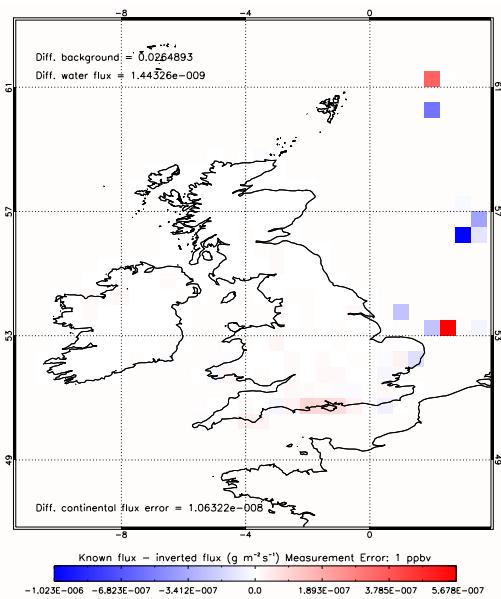
(a)



(b)

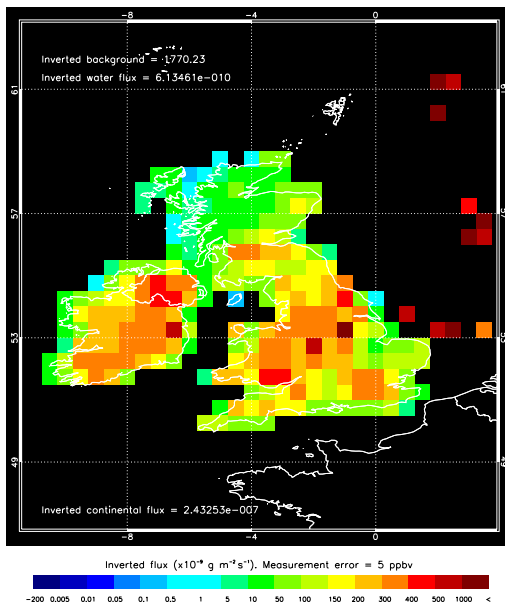


(c)

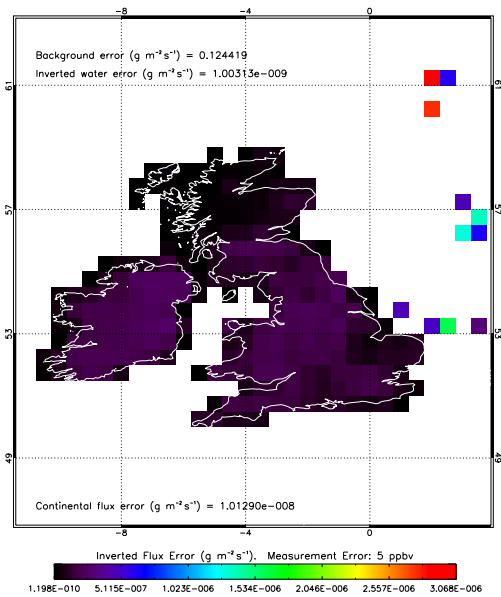


(d)

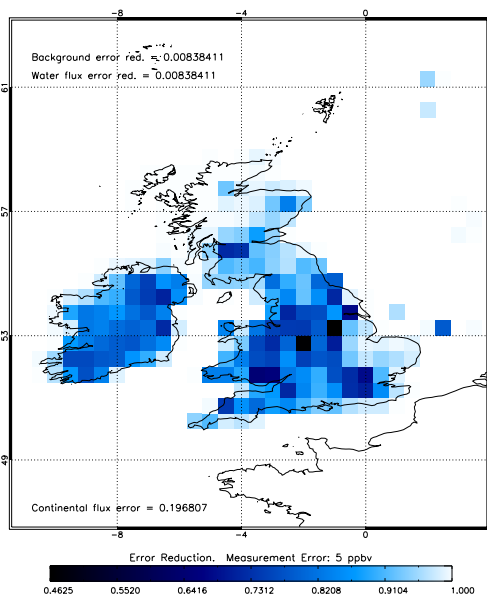
FIGURE 4.8: Inversion result (grouped mainland and water boxes) with a measurement error of 1 ppbv. (a) the inverted flux, (b) the inverted flux error, (c) the error reduction of the inverted flux, assuming 100% uncertainty in the a priori data and (d) the difference between the known and the inverted flux.



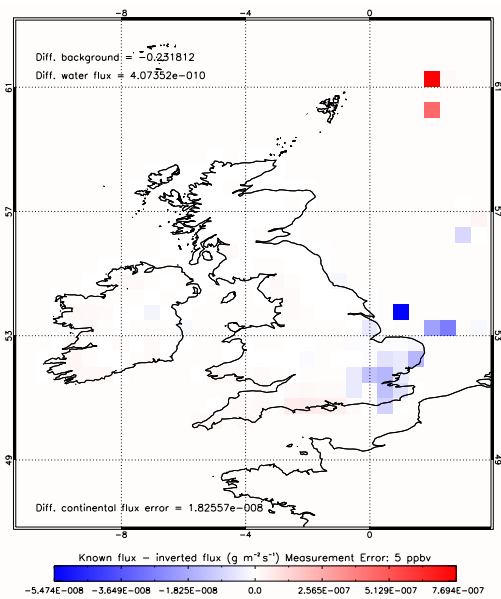
(a)



(b)

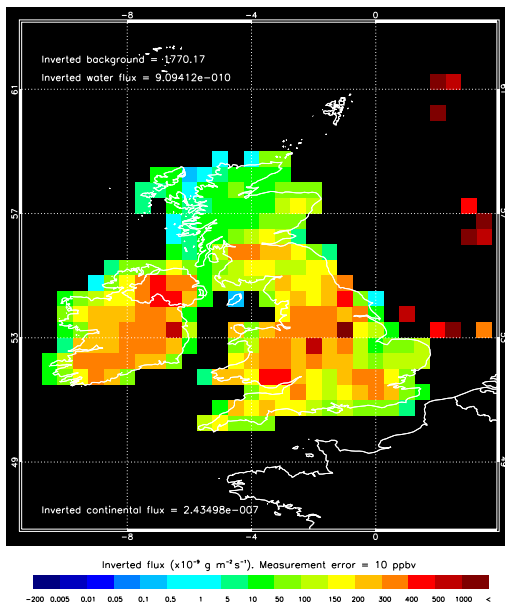


(c)

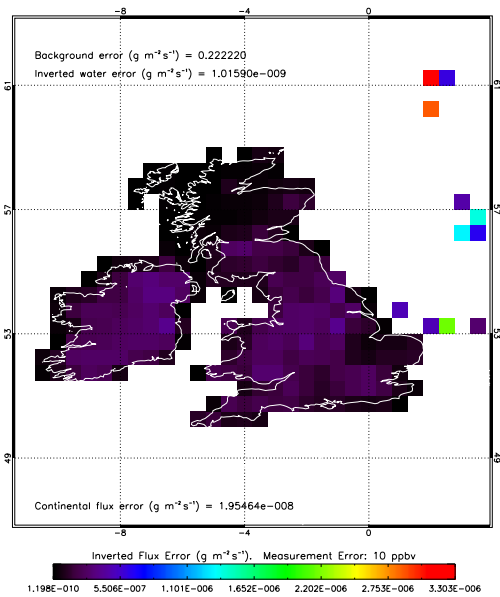


(d)

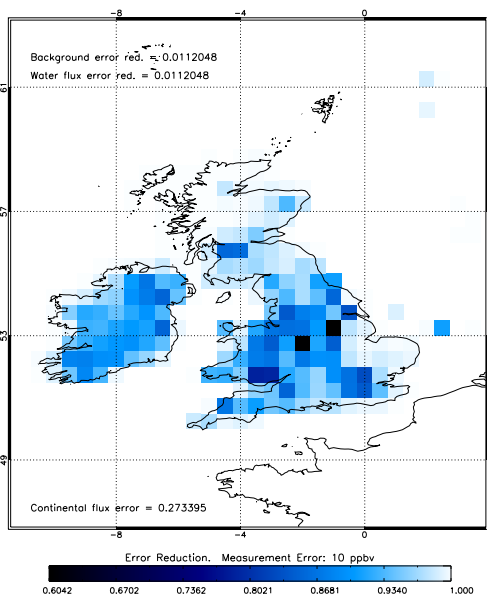
FIGURE 4.9: Inversion result (grouped mainland and water boxes) with a measurement error of 5 ppbv. (a) the inverted flux, (b) the inverted flux error, (c) the error reduction of the inverted flux, assuming 100% uncertainty in the a priori data and (d) the difference between the known and the inverted flux.



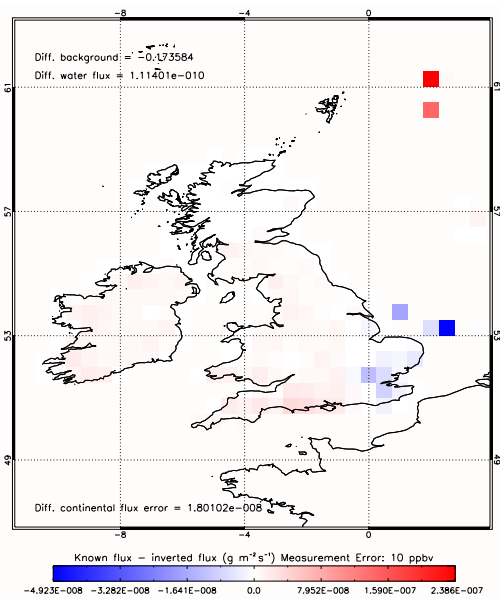
(a)



(b)



(c)



(d)

FIGURE 4.10: Inversion result (grouped mainland and water boxes) with a measurement error of 10 ppbv. (a) the inverted flux, (b) the inverted flux error, (c) the error reduction of the inverted flux, assuming 100% uncertainty in the a priori data and (d) the difference between the known and the inverted flux.

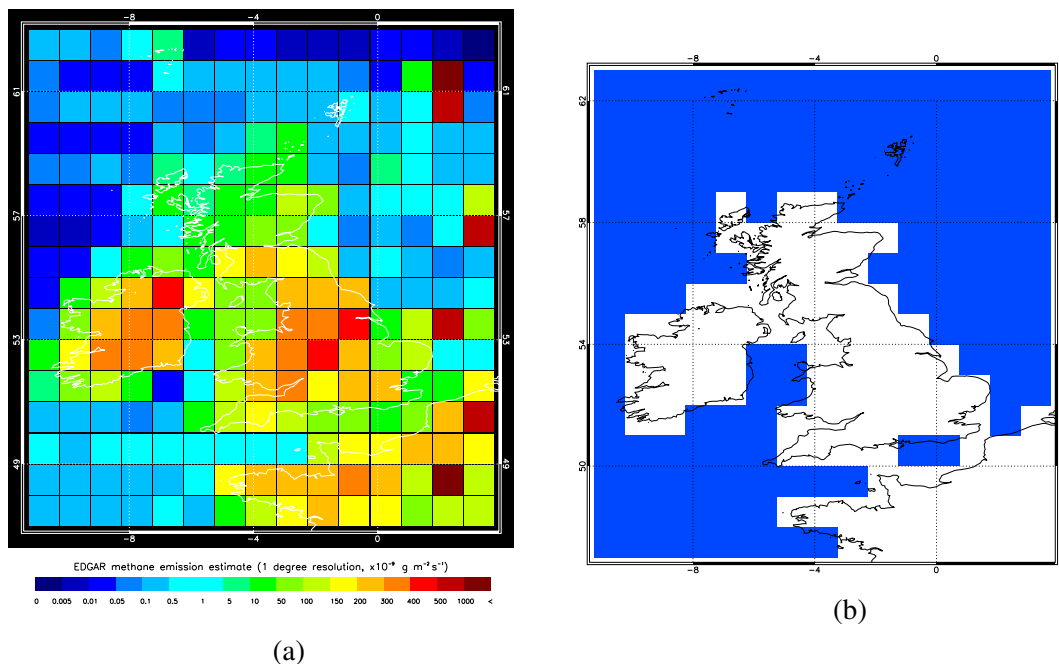


FIGURE 4.11: (a) EDGAR emission inventory gridded to a spatial resolution of  $1^\circ$  and (b) The land sea flag utilised for the inversion at the spatial resolution of  $1^\circ$ . The ocean grid cells are combined to a single average, as is the flux over France. The analysis is concentrated on the the fluxes over the British Isles only.

instruments are used. The EDGAR prior uncertainties are assumed to be 100%. It is assumed that there is no spatial correlation between the cells and no temporal variation in the a priori data.

#### 4.6.1 Application to simulated GOSAT-like instrument measurements

The simulated inversion utilising the minimum number of daily measurements is a number of times higher than the actual number of GOSAT retrieved observations for the whole of August, 2009 (12, see Figure 4.1a). The simulation here estimates the performance of a GOSAT-like instrument, with an ability to measure the column measurements over the British Isles once a day. It is also worth bearing in mind that the actual GOSAT instrument achieves a global coverage only once every 3 days. Figures 4.13a and b with an assumed 20 ppb random measurement error are scenarios most representative of the GOSAT instrument. The simulated error reductions, when 16 daily measurements are used in the inversion (Figure 4.12a), are negligible for inversions with a spatial resolution of  $\sim 0.5^\circ$  and  $1.0^\circ$  ( $\sim 0.98$  and  $\sim 0.94$  respectively). Utilising the full mesh of 166 daily measurements in the inversion decreases the error reduction value at  $0.5^\circ$  degree resolution (a combined error reduction value of 0.87 is achieved). Decreasing the spatial

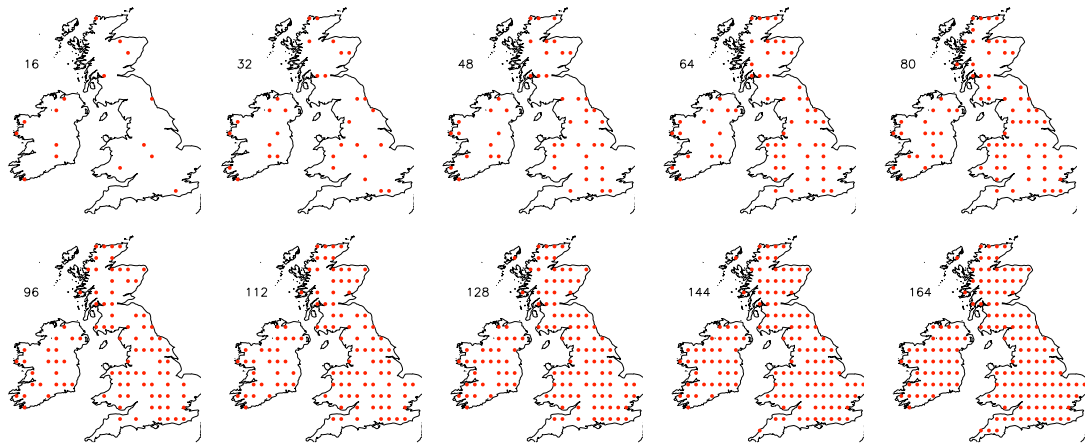


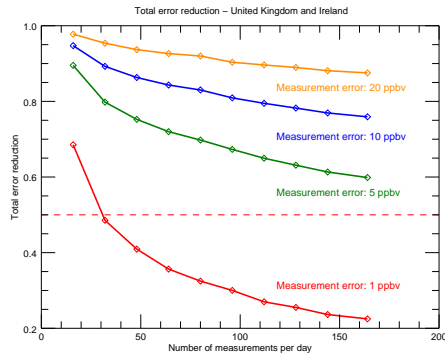
FIGURE 4.12: The locations and the number of the simulated daily measurements. The inversions were repeated with a decreasing number of simulated measurements. A total of 10 simulations were carried out, ranging from 16 daily measurements over the United Kingdom and Ireland (496 total measurements during August) to 164 measurements (a total of 5084 during August).

resolution to  $1.0^\circ$  results in a meancombined error reduction value of  $\sim 0.66$ . An error reduction of 0.5 is not achieved when simulating measurement errors of 20, 10 and 5 ppbv at  $0.5^\circ$  spatial resolution. An error reduction below the 0.5 threshold is calculated when 48 measurements are used, assuming a 1 ppbv random measurement error. The combined grid cell error reduction of  $\sim 6.8 \times 10^{-9}$  is achieved when negligible random measurement error is assumed, even when 16 daily measurements are used in the inversion. This is of course unrealistic, as observational error of  $1 \times 10^{-10}$  ppbv cannot be achieved by GOSAT or any proposed instruments due to the inherent uncertainties in the retrieval process.

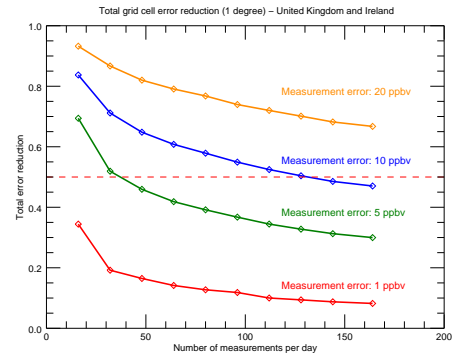
At a spatial resolution of  $1.0^\circ$ , an error reduction of below 0.5 can be achieved (Figure 4.12b) when a measurement error of 10 ppbv is assumed and 128 daily measurements are utilised (see Figure 4.12).

## 4.7 Future $\text{CH}_4$ observing space-borne instruments

In this section, the impact of future remote-sensing, space-borne missions on the methane flux error reduction over the United Kingdom and Ireland is analysed. The simulations will focus on the CarbonSat and Sentinel-5 Precursor instruments (referred to here as Sentinel-5P). The two instruments have a considerably smaller measurement footprint size, which could provide an increased number of observations to be used in future inversion studies. The decreased measurement footprint size is especially important for ob-

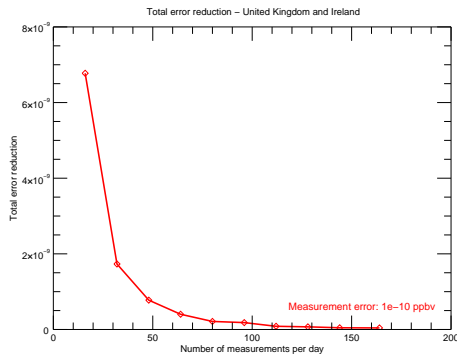


(a)

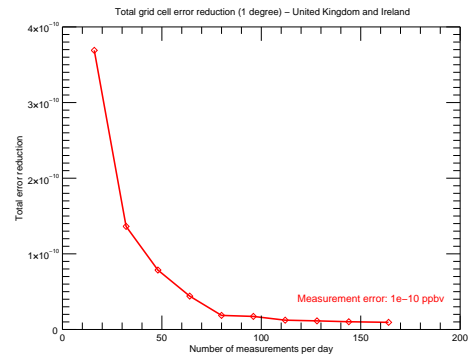


(b)

FIGURE 4.13: The combined error reduction values for the region, with varying number of simulated measurements and error values of 10, 5 and 1 ppbv. (a) The inversion at the spatial resolution of  $0.5^\circ$  and (b) spatial resolution of  $1.0^\circ$



(a)

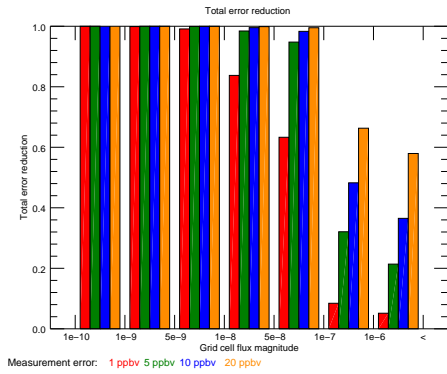


(b)

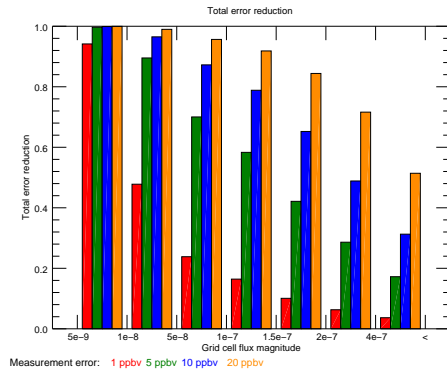
FIGURE 4.14: The combined error reduction values for the region, with varying number of simulated measurements and error value of  $1 \times 10^{-10}$  ppbv. (a) The inversion at the spatial resolution of  $0.5^\circ$  and (b) spatial resolution of  $1.0^\circ$

taining usable measurements over the United Kingdom and Ireland, as currently a high number of GOSAT measurements are affected by clouds. The main characteristics of these instruments are summarised in Table 4.1, which also includes the specifications of GOSAT and SCIAMACHY for comparison purposes. The table shows the measurement swaths, pixel sizes, the global coverage times, the instrument errors and the predicted clear-sky frequencies.

Simulations were run assuming measurement errors of  $1 \times 10^{-10}$  (in effect, no measurement error), 1, 5 and 10 ppbv. Figures 4.13, 4.14, 4.15 and 4.16 summarise the simulation results. Figures 4.13 and 4.14 show the combined grid cell error reduction values over the British Isles as a function of the number of daily simulated measurements used

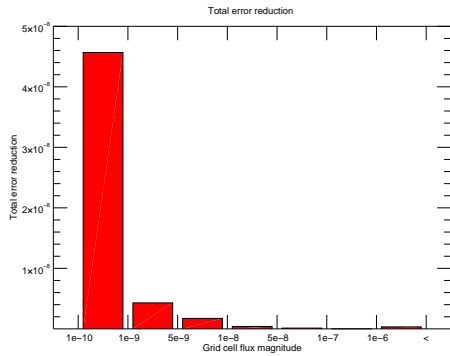


(a)

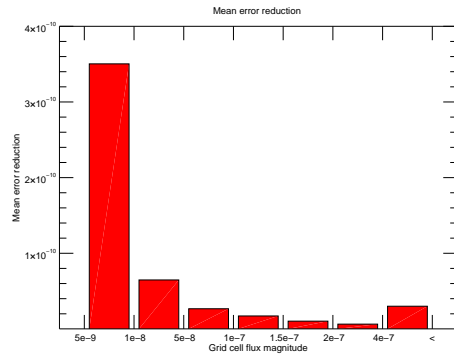


(b)

FIGURE 4.15: The combined cell error reduction values as a fraction of the flux magnitude (measurement errors of 1, 5 and 10 ppbv). The error reduction is greatest at largest fluxes. (a) the inversion at the spatial resolution of  $0.5^\circ$  (b) the inversion at the spatial resolution of  $1.0^\circ$ . The  $x$  scale is changed for the spatial resolution of  $1.0^\circ$  inversion due to largest and lowest fluxes decreasing with decreasing resolution.



(a)



(b)

FIGURE 4.16: The combined cell error reduction values as a fraction of the flux magnitude (measurement error of  $1 \times 10^{-10}$  ppbv). The error reduction is greatest at largest fluxes. The inversions at the spatial resolutions of (a)  $0.5^\circ$  and (b)  $1.0^\circ$ . The  $x$  scale is changed for the spatial resolution of  $1.0^\circ$  inversion due to the largest and lowest fluxes decreasing with decreasing resolution.

**CH<sub>4</sub>** sensing SWIR space-borne instruments

Instrument	Swath	Pixel size	Repeat Orbit	Accuracy	Clear-sky frequency
SCIAMACHY	1000 km	30 x 60 km	3 days	1–3%	5%
GOSAT	~ 150 km separation between measurement points	~ 10.5 km ellipsoid	3 days	17 ppb	13%
CARBONSAT	300* km	2 x 3 km	12* days	< 10 ppb	23%
SENTINEL 5-PRECURSOR	2600 km	7 x 7 km	17 days	1%	18%

Table 4.1: A list of the current and planned methane sensing space-borne instruments. The instrument footprint characteristics and the corresponding percentage predicted clear-sky fractions are shown. The CarbonSat specifications are still not finalised and are subject to change (Buchwitz et al., 2013; Meijer et al., 2012; Miller et al., 2007).

in the inversion (Figure 4.12 for more detail). As expected, the error reduction values decrease as the number of simulation measurements are increased. Also, increasing the simulated measurement error results in a decreased error reduction. Figures 4.15 and 4.16 display the error reduction as the fraction of the methane flux. The error reduction is greatest over the high CH<sub>4</sub> emitting cells increasing as the spatial resolution of the inversion is decreased to 1°.

The simulations are run with one measurement per 0.5° grid cell, an approach identical to that described in Section 4.2. To simulate the CarbonSat or Sentinel-5 P instrument measurements, 2 approaches can be utilised. The first approach is to compute the footprint of every single measurement pixel at the native measurement resolution. CarbonSat has a footprint of 2 x 3 km<sup>2</sup>, which would result over 500 simulated column releases in a 0.5° x 0.5° degree grid cell (varies depending on latitude). The number is less for Sentinel-5 P instrument simulations due to the coarser measurement spatial resolution, however this is still computationally unfeasible. The approach used here is to calculate the reduced random error of all the measurements that would be obtained if the simulations were to be carried out. This allows us to use the existing simulation outputs in the analysis. The reduced random error of the measurements that fall within the individual grid cells is calculated:

$$\sigma = \frac{\sigma_O}{\sqrt{n}}, \quad (4.2)$$

where  $\sigma$  is the reduced random error,  $\sigma_O$  is the random error for a single observation

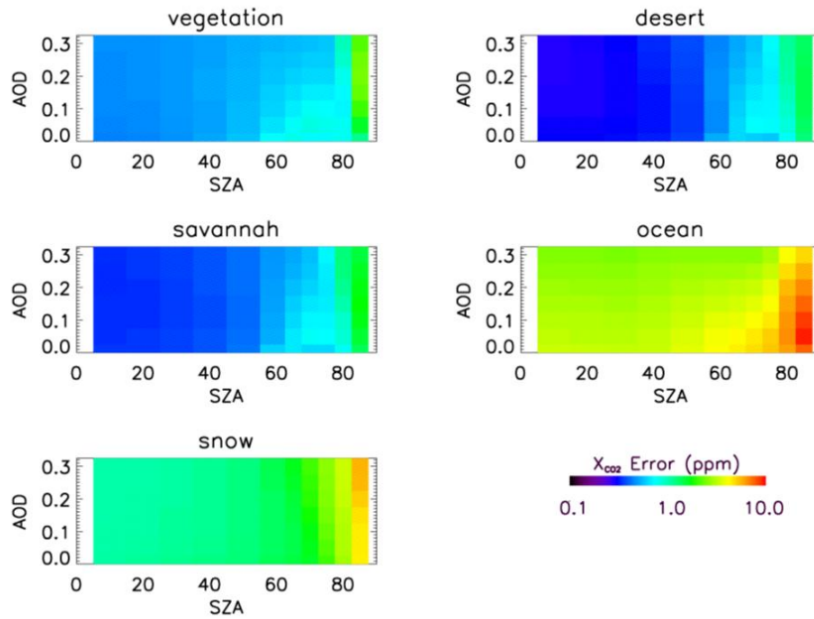


FIGURE 4.17: The simulated XCO<sub>2</sub> retrieval errors from a SWIR-sensing instrument (OCO-2) as a function of SZA and AOD for nadir simulations for the five different surface types (and in turn, albedo) with a surface pressure of 1000 hPa. A similar effect will be observed for CarbonSat and Sentinel-5 Precursor instruments (Boesch et al., 2011).

and  $n$  is the number of observations in a grid box. This is of course an overly optimistic assumption. Estimating a single observation error alone is however difficult. An observational error would be scene-dependent and a function of factors, such as the aerosol optical depth (AOD), solar zenith angle (SZA) and surface pressure. The effect of these factors on the errors in data obtained from a SWIR-sensing instrument can be seen in Figures 4.17 and 4.18. The two figures show the modelled results for a CO<sub>2</sub> sensing instrument, OCO-2. A simulated XCO<sub>2</sub> retrieval error is shown as a function of SZA and AOD for different surface types for nadir and glint observations. CarbonSat and Sentinel-5 Precursor instruments (as well as GOSAT) are also sensitive to the changes shown, although the absolute error value calculated by Boesch et al. (2011) will not be used here.

Combining the observations within a certain area would result in a smaller uncertainty than the individual errors, the magnitude of which depends on error correlations. The error correlations are unknown for the future instruments, and due to the complexity and time constraints, such simulations are beyond the scope of this thesis. The model transport and representation errors are also ignored. The reduced errors calculated utilising Equation 4.2 are therefore underestimated. The Sentinel-5P and CarbonSat instrument measurements errors will be correlated and would have a higher reduced random

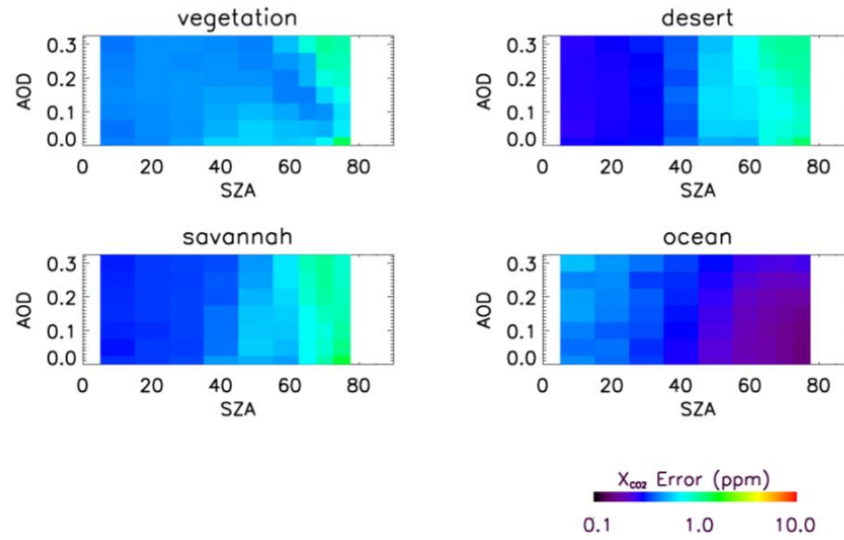


FIGURE 4.18: The Simulated XCO<sub>2</sub> retrieval errors for a SWIR-sensing instrument (OCO-2) as a function of SZA and AOD for glint simulations for the four different surface types (and in turn, albedo) with a surface pressure of 1,000 hPa. A similar effect will be observed for CarbonSat and Sentinel-5 Precursor instruments (Boesch et al., 2011).

error than assumed utilising Equation 4.2. To calculate a more realistic reduced measurement error value, an additional inversion will be carried out with the following equation being used (Palmer et al., 2011)

$$\sigma = \sigma_O \sqrt{\frac{1}{n} + \alpha \left(1 - \frac{1}{n}\right)}, \quad (4.3)$$

where,  $\sigma_O$  is the random error for a single measurement,  $n$  is the number of clear-sky observations and  $\alpha$  is the assumed error correlation coefficient between two observations within a grid box. A value for  $\alpha$  is taken as 0.2, as described by Palmer et al. (2011).

The simulations for the CarbonSat and Sentinel-5 Precursor instruments were carried out for 2 months, in January and July 2011. The choice of the two months will simulate the performance of the instruments during the northern hemispheric winter and summer months. The two different a priori flux maps will be used to forward model the synthetic CarbonSat and Sentinel-5 Precursor measurements, reflecting the changes in natural CH<sub>4</sub> emissions during the seasons. Natural CH<sub>4</sub> emissions in the northern hemispheric winter are expected to be lower for example due to slowdown in bacterial activity. The a priori uses a combined emission inventory, the individual components of which are described in Section 3.6.2. The solar zenith angle, instrument orbits and cloud cover will all be taken into account in these simulations.

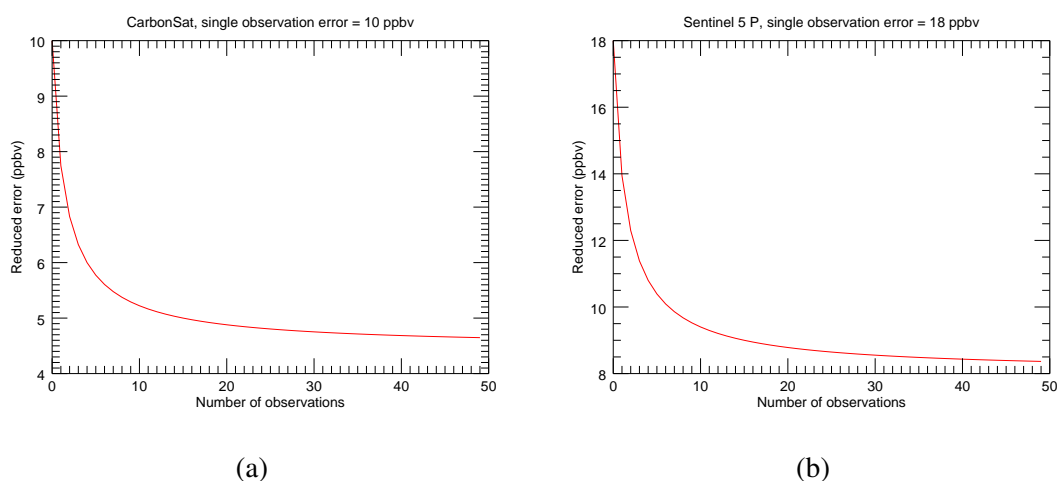


FIGURE 4.19: The reduced errors as a fraction of a number of observations when calculated using Equation 4.3 for (a) CarbonSat, assuming a single observation error of 10 ppbv and (b) Sentinel-5 Precursor, assuming a single observation error of 18 ppbv.

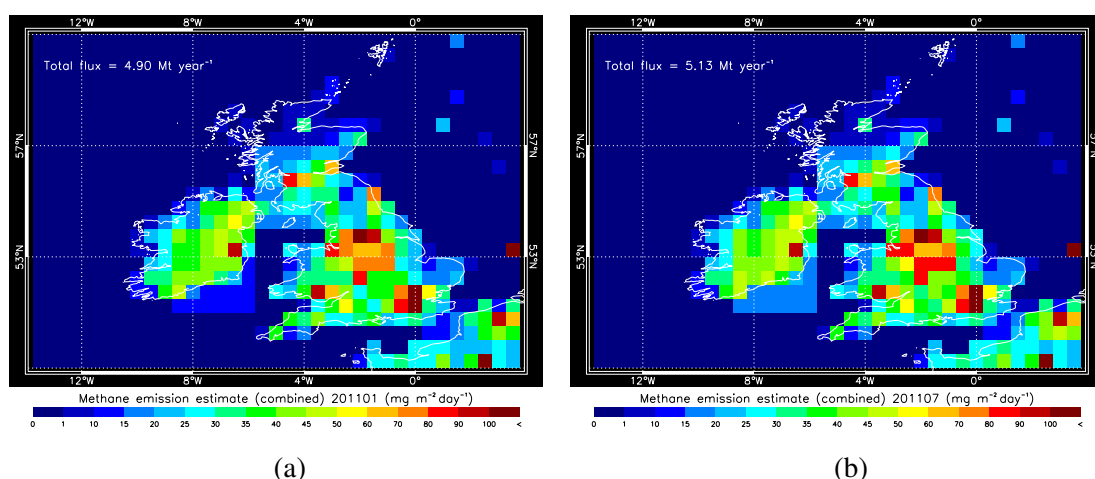


FIGURE 4.20: The combined  $\text{CH}_4$  emission inventory for (a) January 2011 and (b) July 2011, used as the a priori to simulate the CarbonSat and Sentinel-5 Precursor observations taken during the month.

The solar zenith angle is the angle measured from directly overhead to the geometric centre of the sun’s disc. If the solar zenith angle is higher than 75, it will be assumed that no  $\text{XCH}_4$  can be retrieved from the satellite observations. This does lead to there being no simulated measurements that can be used in the inversion over Great Britain and Ireland in early January. More measurements become available to be entered into the inversion system as the SZA decreases throughout January. Figure 4.21a and 4.21b show the solar zenith angle for the centre of each  $0.5^\circ$  grid box used in the NAME simulation at 13:00 on the 19<sup>th</sup> of January and the 19<sup>th</sup> of July, 2011. The SZA is calculated for each day in the two months of the simulation period. In the northern hemispheric summer, the sun is

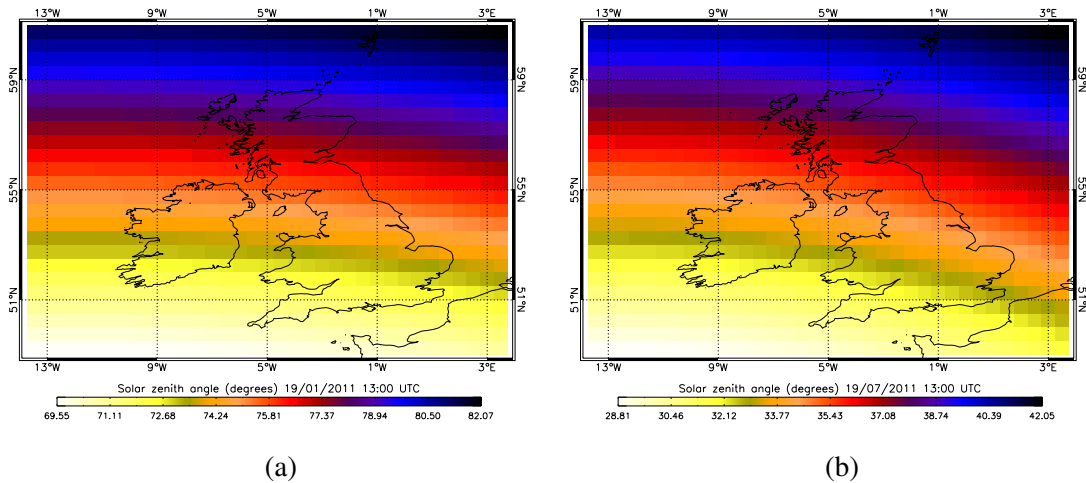


FIGURE 4.21: The solar zenith angle at (a) 13:00 UTC 19/01/2011 and (b) 13:00 UTC 19/07/2011. 13:00 is the simulated overpass time for the proposed instruments.

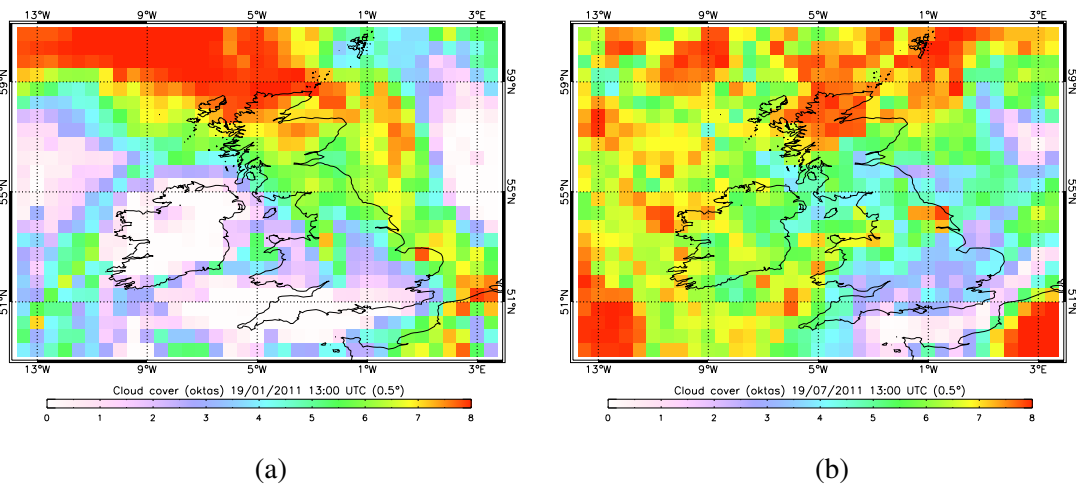


FIGURE 4.22: The cloud cover derived from the NAME meteorological data at (a) 13:00 UTC 19/01/2011 and (b) 13:00 UTC 19/07/2011. 0 represents a cloud-free scene, whilst 8 signifies a scene that is completely covered by clouds.

high above the horizon (SZA at the time of the satellite overpass is low) and thus all of the simulated observations can be used. NAME is requested to provide the cloud cover over the simulation scene for at time of the synthetic observations. The cloud cover for the selected days in January and July can be seen in Figures 4.22a and 4.22b respectively. Oktas (World Meteorological Organisation (2014)) is the measure of the amount of cloud cover at any given location. Sky conditions are estimated in terms of how many eighths of the sky are covered in cloud, ranging from 0 oktas (completely clear sky) to 8 oktas (completely overcast). When calculating the number of measurements that are assumed to be obtained in a grid box, the covered fraction is removed from the total number

of measurements in an area of the box. For example, if 50 measurements were to be obtained in a grid box (assuming the SZA is below  $75^\circ$ ) and the cloud cover would be returned by NAME to be 4 oktas, 25 measurements would be used to calculate the reduced error (i.e. half the observations would be removed). If cloud cover of 6, 7 or 8 oktas is outputted by NAME however, then it is assumed that no observations will be obtained over the grid box. The effects of the specific proposed orbits on the inversion will be discussed in the sections describing CarbonSat (Section 4.7.1) and Sentinel-5 Precursor (Section 4.7.2) results.

It is expected that the methane flux error reductions for January will be less than that for July owing to a fewer possible atmospheric measurements, leading in turn to a higher reduced error.

#### **4.7.1 Application to simulated CarbonSat measurements**

To simulate the performance of the CarbonSat instrument, the orbit of the instrument also has to be taken into account. This is due to a relatively narrow proposed measurement swath. The exact instrument orbit and the swath are yet to be finalised, thus CarbonSat is here assumed to have a 12-day repeat orbit. The swath is assumed to have a width between 240 and 300 km, however this is dependent on the latitude of the observation. The measurements are obtained at the 2 grid boxes east and west of the CarbonSat overpass location, as well as the grid box the instrument directly orbits. The simulated orbit is displayed in Figure 4.23. The satellite is assumed to follow Day 1 path on the 1<sup>st</sup> of January returning to overpass labelled 'Day 1' on the 13<sup>th</sup> of January.

Britain is located at approximately  $51^\circ\text{N}$  to  $59^\circ\text{N}$  of latitude. At  $51^\circ\text{N}$ , the latitude and longitude distance in km per degree is  $\sim 111.12$  km and  $\sim 70$  km respectively. The distance in longitude per degree decreases to  $\sim 57$  km at  $59^\circ\text{N}$ . As the measurement footprint of CarbonSat is  $2 \times 3$  km, the number of CarbonSat measurements within the  $0.5^\circ$  NAME simulated grid box therefore ranges from  $\sim 267$  to  $\sim 337$ . To obtain the number of individual observations that would be obtained in the  $0.5^\circ$  grid box, the area of each grid is initially calculated. The number of measurements obtained each day is dependent on the cloud cover, SZA (Section 4.18) and the orbit of the instrument. Figures 4.24a and b show the number of measurements to be obtained on a selected days in January and July. Assuming the measurement precision is 10 ppbv and the measurement errors are uncorrelated, the combined measurement errors are calculated to have a minimum of 0.55 ppbv and a maximum of 1.16 ppbv in January, using the Equation 4.1. In July 2011, the minimum calculated error is 0.59 ppbv whilst the maximum error is estimated to be

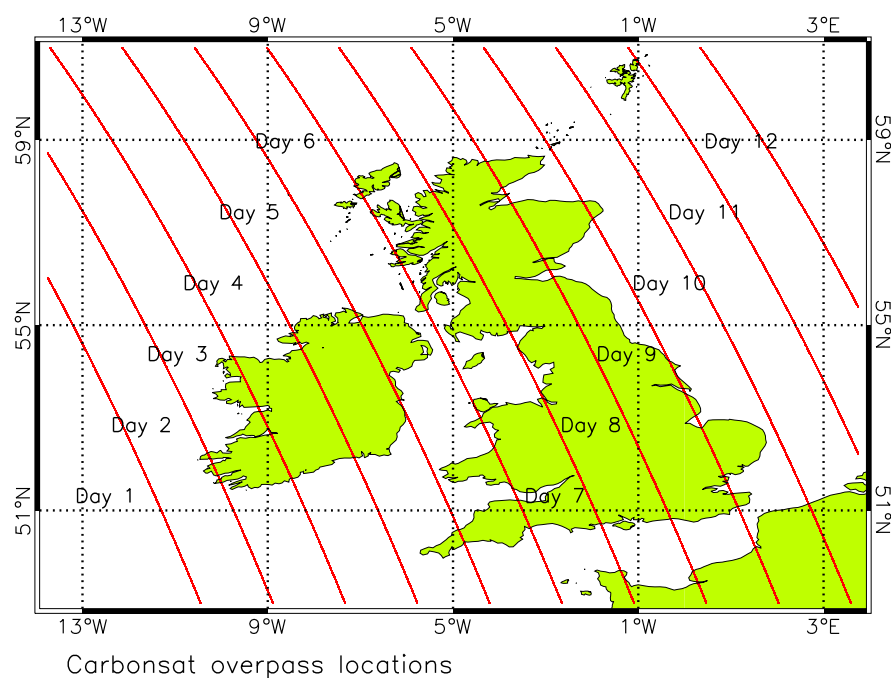


FIGURE 4.23: CarbonSat simulated orbit with a 12 day repeat cycle. The overpass locations for days 1-12 are shown.

1.19 ppbv. If the method by Palmer et al. (2011) is used to calculate the reduced error, the minimum and maximum errors of 4.50 ppbv and 4.59 ppbv are estimated. Figures 4.25a, b and 4.25c, d show the simulated error reduction that can be achieved for January and July respectively utilising the two methods of computing the reduced error. For a full summary of results, see Table 4.2.

In January, CarbonSat can achieve a flux uncertainty error reduction of 0.74 for England, 0.70 for Wales, 0.79 for Scotland, 0.82 and 0.65 for Northern and the Republic of Ireland, respectively. A minimal error reduction for northern France, 0.96 is simulated. In July, the error reduction values of 0.54 and 0.45 are obtained for England and Wales. The flux uncertainty is reduced to 0.56, 0.71, 0.65 and 0.83 from the original uncertainty values in Scotland, Northern Ireland, the Republic of Ireland and northern France, respectively.

Minimal error reductions are simulated for January, for all regions when utilising the Palmer et al. (2011) method of calculating the reduced measurement errors. An uncertainty reduction of 0.93 for England, 0.94 for Wales, 0.93 for Scotland, 0.98 and 0.91 for Northern and the Republic of Ireland respectively and 0.97 for northern France. In July, the results are better. A value of 0.85 is obtained for England, 0.82 for Wales, 0.87 for Scotland and 0.94 for both Northern and Republic of Ireland. An error reduction

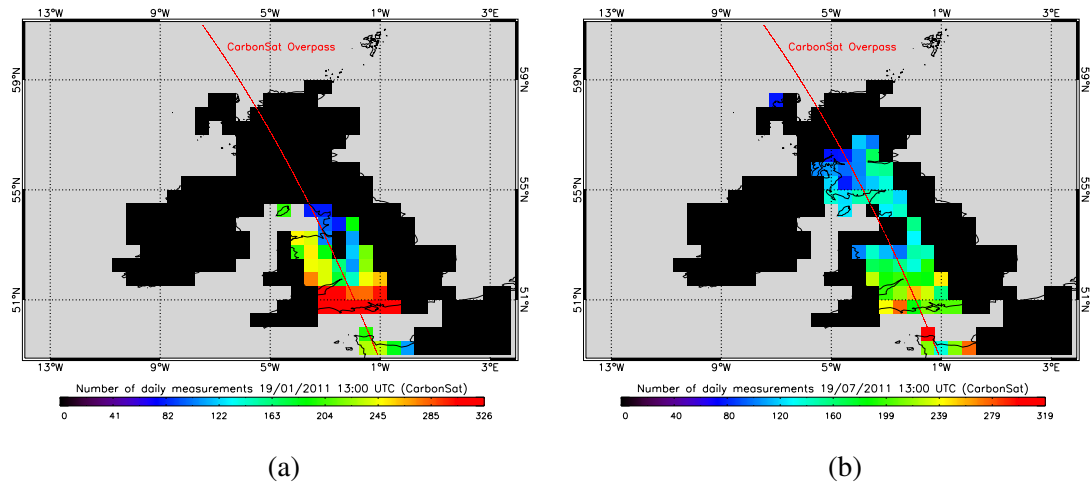


FIGURE 4.24: The number of measurements that would be expected to be obtained by CarbonSat on (a) 19/01/2011 and (b) 19/07/2011. The SZA, cloud cover and the simulated orbit are taken into account.

of 0.97 is achieved for fluxes over northern France.

## 4.7.2 Application to Sentinel-5 Precursor measurements

The measurement footprint of the Sentinel-5P is 7 x 7 km. The number of Sentinel-5P measurements within the 0.5° NAME model run grid box therefore ranges from ~32 to ~40 over the United Kingdom and Ireland. Owing to a wide instrument swath of 2600 km, it is assumed that Sentinel-5 Precursor will be able to make measurements over the whole of the simulation domain daily. Assuming a single measurement error is 18 ppbv and the measurement errors are uncorrelated, the minimum reduced random error during both, January and July, can be calculated using Equation 4.1 to be at the minimum value of 2.85 ppbv and maximum value of 6.36 ppbv. If the method by Palmer et al. (2011) is used to calculate the reduced error, the minimum and maximum errors of 8.44 ppbv and 9.86 ppbv are estimated. Figures 4.26a, b and 4.26c, d show the error reduction in CH<sub>4</sub> fluxes that can be achieved for January and July respectively utilising the different methods of calculating the reduced error. For a full summary of results, see Table 4.2. It is found that in January, Sentinel-5 Precursor can achieve error reductions of 0.79 for England, 0.80 for Wales and Scotland, 0.86 and 0.81 for Northern and the Republic of Ireland, respectively. A minimal error reduction of 0.95 is calculated for northern France owing to only observations over Britain being simulated. In July, the error reduction values of 0.54 and 0.56 are obtained for England and Wales. The flux uncertainty is reduced to 0.66, 0.78, 0.72 and 0.82 from the original values in Scotland,

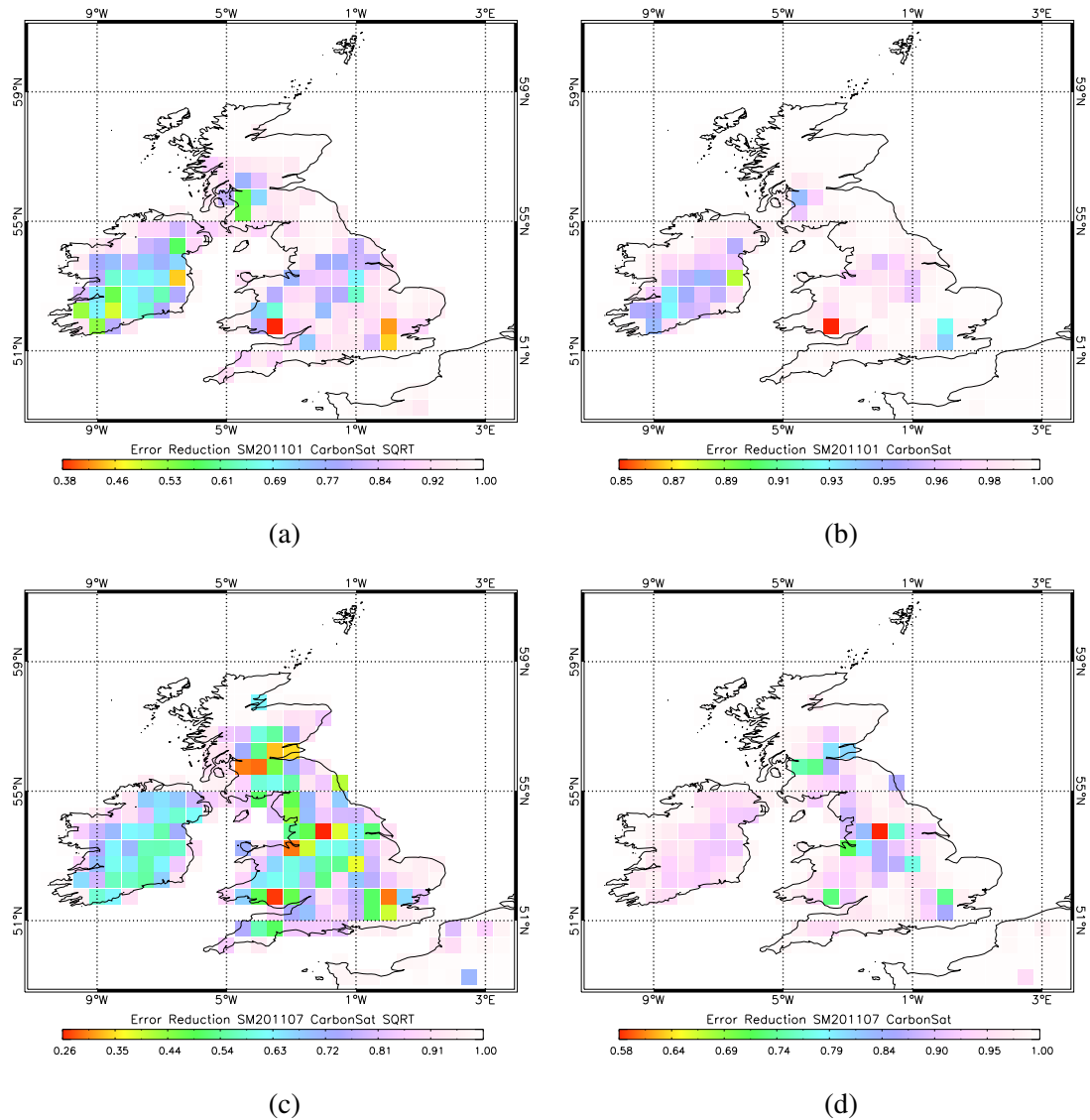


FIGURE 4.25: The error reduction in uncertainty of CH<sub>4</sub> fluxes achieved over Britain and Ireland utilising CarbonSat measurements on (a) January, 2011 and (b) July, 2011. The calculation assumes a 100% uncertainty in the a priori and that the reduced error decreases by a square root of a number of observations in a grid box. (c) and (d) show the error reduction achieved for the months of January and July, respectively, when Equation 4.3 is used to calculate the reduced error.

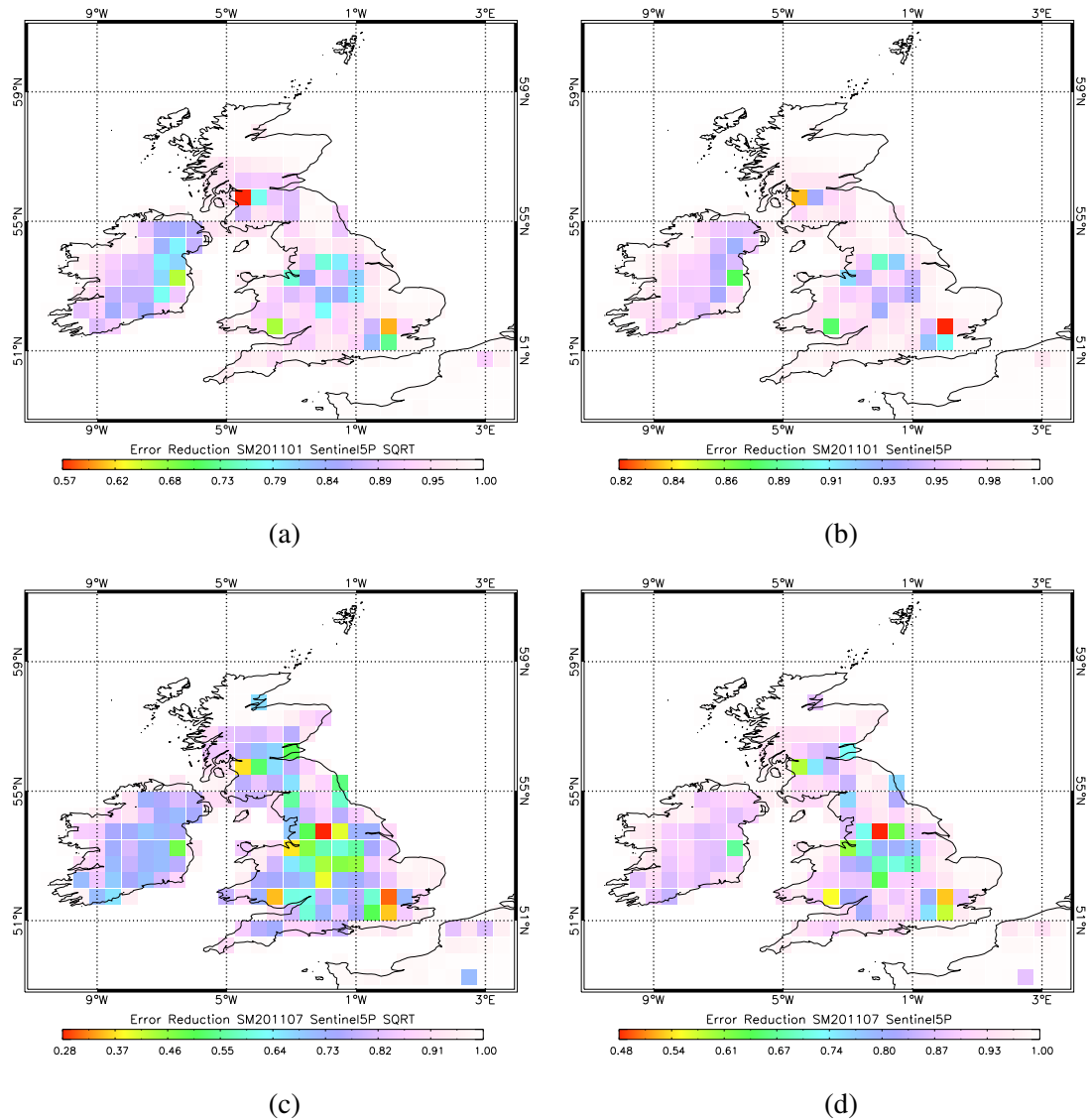


FIGURE 4.26: The error reduction in uncertainty of CH<sub>4</sub> fluxes achieved over Britain and Ireland utilising Sentinel-5 Precursor on (a) January, 2011 and (b) July, 2011. The calculation assumes a 100% uncertainty in the a priori and that the reduced error decreases by a square root of a number of observations in a grid box. (c) and (d) show the error reduction achieved for the months of January and July, respectively, when Equation 4.3 is used to calculate the reduced error.

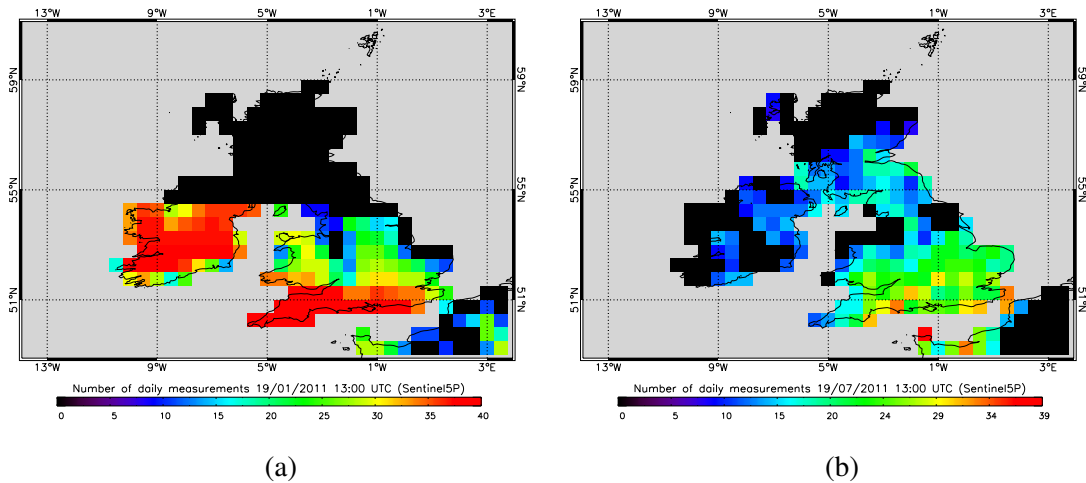


FIGURE 4.27: The number of measurements that would be expected to be obtained by Sentinel-5 Precursor on (a) 19/01/2011 and (b) 19/07/2011. The SZA, cloud cover and the simulated orbit are taken into account.

Northern Ireland, the Republic of Ireland and northern France respectively.

The error reductions are as expected, significantly lower when utilising the Palmer et al. (2011) method of calculating the reduced measurement errors. Error reduction of  $\sim 0.9$  is achieved for all of the regions in January. In July, the results are better. A value of 0.72 is obtained for England, 0.71 for Wales, 0.81 for Scotland, 0.91 and 0.86 for Northern and the Republic of Ireland respectively. An error reduction of 0.92 is achieved for fluxes over northern France.

### 4.7.3 Suitability of future instruments for inversion studies

In this section, the suitability of CarbonSat and Sentinel-5 Precursor instrument data to be used in inversion studies is discussed. The simulation results are summarised in Table 4.2. The table shows the error reduction for 6 individual regions within the simulation domain. The individual regions are shown in Figure 4.28 and the combined error reduction is calculated utilising Equation 3.13. It is expected, that the error reduction achieved is sensitive to the assumed measurement error. This has been shown in Sections 3.3.5 and 4.6.1. The inversion result is demonstrated here to be sensitive to the method of calculating the combined error reductions within the model grid boxes. An assumption that the combined error decreases as a square root of the number of individual measurements multiplied by the error on a single measurement, returns high error reduction values. It is an overly simplistic approach, which results in unreasonably low reduced error values to be calculated. Utilising this method therefore results in low error reduction values

to be calculated by the inversion. Calculating a more realistic reduced error value does yield a worse result, which is still overoptimistic. No model error is taken into account in these synthetic tests for example. Also, no satellite averaging kernel is included in the analysis, although as these simulated test rely on the weighting matrix and a priori flux uncertainties to derive the result, the absence of averaging kernels will not have a noticeable impact on the result.

The error reduction is also sensitive to the season the measurement is taken on as well as the magnitude of the a priori fluxes during the season. No observations from either of the future instruments are available to be used in the inversion at the beginning of January owing to the large calculated solar zenith angles. Some measurements can be obtained in southern Britain as the month progresses however, the number of observations to be used is much lower than in July. The increased cloud cover in January also adds to the decreased number of observations that can be used in the inversion system.

The future instruments will, however, offer more measurements than can be obtained by the existing satellites. CarbonSat and Sentinel-5 Precursor instruments will have more potential for constraining methane emissions. CarbonSat achieves consistently lower error reduction values when assuming a square root decrease in the observational error with an increasing number of measurements. Utilising the Palmer et al. (2011) method reveals that Sentinel-5 Precursor will provide more information into the inversion algorithm. The wide measurement swath results in a daily overpass over the whole of Britain, which is not the case for CarbonSat. The ability of CarbonSat to reduce the fluxes is limited by poor geographical daily sampling in the region investigated here. Realistically, Sentinel-5 Precursor can reduce the flux uncertainty by  $\sim 30\%$  over England and Wales in July with the remaining regions achieving a reduction of  $\sim 8\text{-}14\%$ . In contrast, the CarbonSat error reduction values are expected to range from  $3\%$  to  $18\%$ .

## 4.8 Conclusion

In this chapter, the inversion system developed in Chapter 3 was tested in a number of theoretical studies. A series of daily measurements for a space-borne  $\text{CH}_4$  sensing instrument over the British Isles was first simulated using the forward model utilising the EDGAR emission inventory. The tests simulated various random measurement error scenarios, from  $1 \times 10^{-10}$  to  $10$  ppbv. The number of daily measurements over the region of interest was then reduced and the simulations repeated. It was found that the error reductions are greatest when the highest number of observations are used along with a

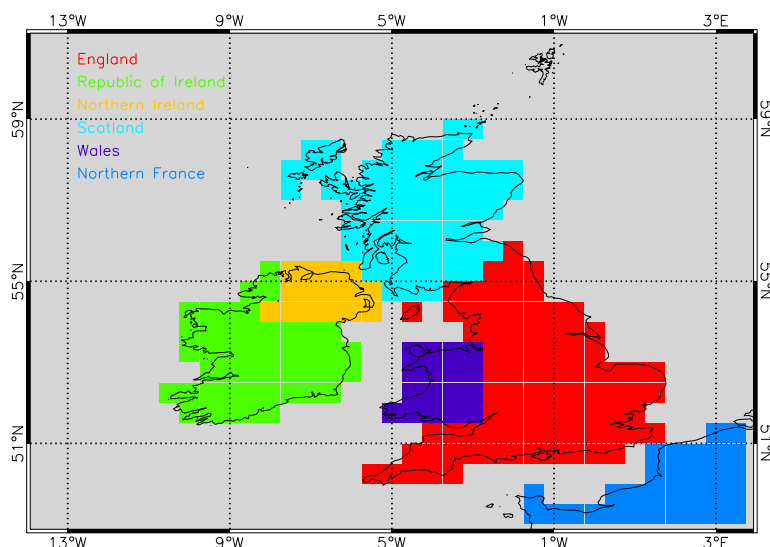


FIGURE 4.28: The regions for which the total error reduction is calculated.

	Sentinel 5 Precursor				CarbonSat			
	January 2011		July 2011		January 2011		July 2011	
	SQRT	Palmer et al.	SQRT	Palmer et al.	SQRT	Palmer et al.	SQRT	Palmer et al.
<b>England</b>	0.79	0.90	0.54	0.72	0.74	0.93	0.54	0.85
<b>Wales</b>	0.80	0.93	0.56	0.71	0.70	0.94	0.45	0.82
<b>Scotland</b>	0.80	0.90	0.66	0.81	0.79	0.93	0.56	0.87
<b>Northern Ireland</b>	0.86	0.95	0.78	0.91	0.82	0.98	0.71	0.94
<b>Republic of Ireland</b>	0.81	0.91	0.72	0.86	0.65	0.91	0.65	0.94
<b>Northern France</b>	0.95	0.96	0.82	0.92	0.96	0.97	0.83	0.97

Table 4.2: The error reduction values achieved for the different regions in the inversion domain. The results are for January and July 2011, utilising two methods for calculating the reduced error of an observation within a single model grid box.

lowest random measurement error, as expected. The flux error reduction was greatest in the highest emitting grid cells, owing to the greatest impact on the signal at the measurement site. The effect of reducing the inversion spatial resolution was also investigated. The algorithm is able to achieve a greater reduction of the flux errors as the spatial resolution of the inversion is reduced from  $0.5^\circ$  to  $1^\circ$ . The simulation was used to estimate the impact of using GOSAT-like instrument observations for inverting fluxes over the British Isles. The simulation assumed a typical GOSAT measurement characteristic, although the number of observations simulated in this study was more than obtained over the region of interest. The results therefore will be better than would be seen if actual

measurements were used. When using 16 daily measurements in the inversion, the error reductions are found to be small with spatial resolutions of  $0.5^\circ$  and  $1.0^\circ$ , assuming an observation error of 20 ppbv ( $\sim 0.98$  and  $\sim 0.93$  respectively). Utilising the full mesh of 166 daily measurements in the inversion decreases the error reduction value at  $0.5^\circ$  to  $\sim 0.87$ .

In this chapter, simulations are also carried out to model the performance of future instruments in the region studied here. Assuming each individual measurement error is uncorrelated, a reduced measurement error can be calculated by dividing the error of a single measurement by the square root of the total number of measurement in an area. CarbonSat is expected to have a ground pixel size of 2 x 3 km and can achieve a greater reduced error within an area when compared to Sentinel-5P with a ground pixel size of 7 x 7 km in the synthetic tests. When a more realistic approach to calculating the reduced error is used, reduced flux uncertainty of  $\sim 30\%$  is found for Sentinel-5P over England and Wales in July, with the remaining regions achieving a reduction of  $\sim 8-14\%$ . In contrast, CarbonSat error reduction values are expected to range from 3% to 18%. The error reductions achieved in January were considerably worse, owing to the increased cloud cover and the SZA. The future instruments will, however, in combination with in situ measurements, play a considerable part in constraining the uncertain methane emissions.

# Chapter 5

## Application of a forward model to GOSAT data

### 5.1 Introduction

In this chapter, the forward model of the algorithm developed in Chapter 3 is used to simulate satellite XCH<sub>4</sub> observations. Measurements at GOSAT overpass locations are modelled and compared against the XCH<sub>4</sub> data retrieved at the University of Leicester. The forward model could be used to critically test the validity of high resolution emission inventories with lesser computational cost than simulations using a Eulerian global transport model.

The chapter builds on the previous work, the main addition being a development of a method to determine the background atmospheric methane values calculated by integrating the high resolution NAME outputs within global Eulerian CTM fields. The calculated background values are then used here and could be utilised when inverting observation data from next generation satellite instruments, which will provide a higher number of observations at a higher spatial resolution. To summarise, the aims of this chapter are to:

1. Develop a method to retrieve the atmospheric background, taking into account atmospheric transport.
2. Simulate GOSAT XCH<sub>4</sub> measurements at GOSAT overpass locations and compare the results to the XCH<sub>4</sub> data retrieved at the University of Leicester.

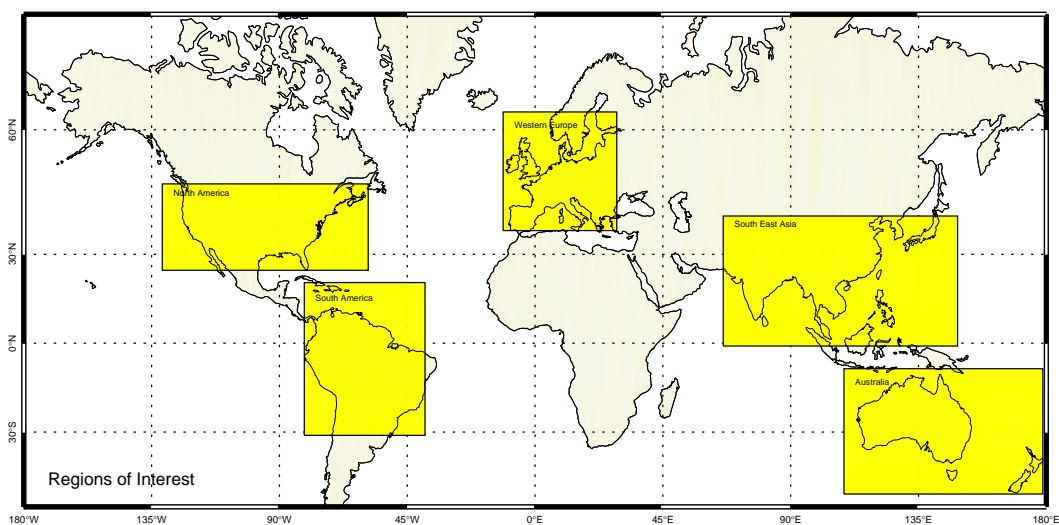


FIGURE 5.1: The regions of for which simulations are carried out.

## 5.2 Regions to be simulated

The  $\text{XCH}_4$  measurements to be simulated utilising the forward modelling approach developed in Chapter 3 were retrieved at the University of Leicester, as described in Section 3.1. There are over 220000 usable GOSAT methane measurements over a year worldwide (222709 in the period of 06/2009 - 05/2010). It is not feasible to simulate each and every one of the measurements. Each simulation requires the NAME model to be run at the measurement co-ordinates and time for 10 days back, which is computationally very expensive. It is therefore necessary to select a smaller measurement time frame as well as regions of interest, in which the satellite data are going to be reproduced. This selection is further limited by the availability of meteorological data, as well as by the difficulties in synchronising the different versions of the meteorological files. It was therefore decided to simulate the measurements taken during the June, July, August and September months of 2009. The months chosen would reflect the emission increase of rice fields, thus displaying at least part of the methane emission cycle. The number of measurements taken over these months were still too high, however. There were  $\sim 20000$  worldwide measurements per month during the dates chosen. The data during the first week (days 1 – 7) of each month are therefore used.

The regions of interest were limited to Europe, North and South America, parts of South East Asia and Australasia. These were chosen to be representative of varying emission sources and magnitudes worldwide. Europe, for example, has fairly uniform emissions, from mainly anthropogenic sources. These do not display great temporal

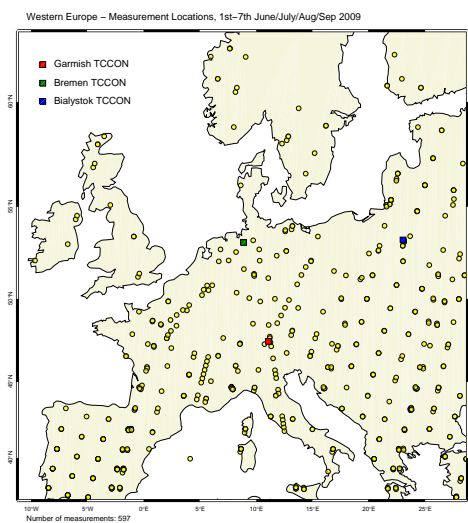


FIGURE 5.2: The locations of GOSAT measurements, Western Europe for the time period of 1<sup>st</sup> - 7<sup>th</sup> Jun /Jul /Aug /Sep, 2009.

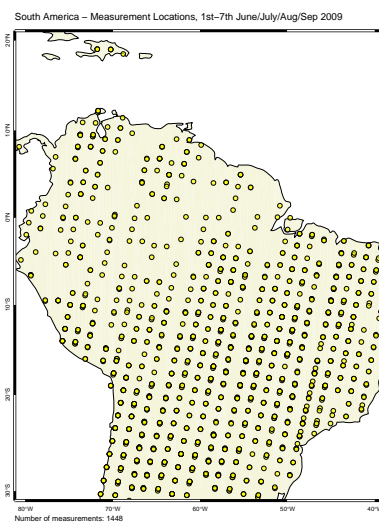


FIGURE 5.3: The locations of GOSAT measurements, South America for the time period of 1<sup>st</sup> - 7<sup>th</sup> Jun /Jul /Aug /Sep, 2009.

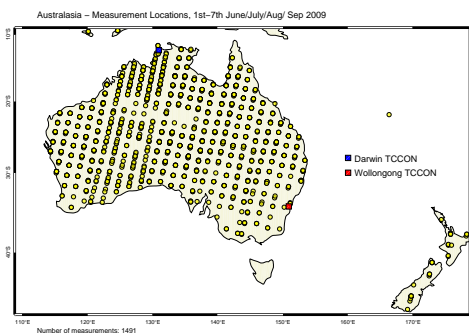


FIGURE 5.4: The locations of GOSAT measurements, Australasia for the time period of 1<sup>st</sup> - 7<sup>th</sup> Jun /Jul /Aug /Sep, 2009.

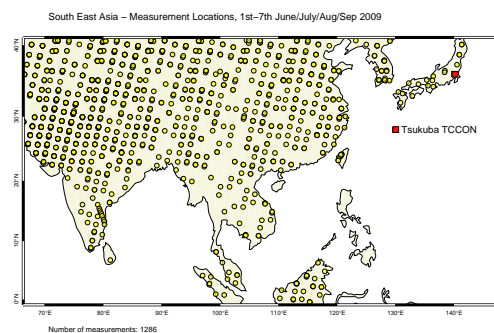


FIGURE 5.5: The locations of GOSAT measurements, South East Asia for the time period of 1<sup>st</sup> - 7<sup>th</sup> Jun /Jul /Aug /Sep, 2009.

variation. Emissions from South East Asia on the other hand are dominated by biogenic wetland and rice field production. The amounts of methane released vary in magnitude over the course of the year, with rice fields emitting highest the amounts of methane during August and September. The simulated data locations in the regions to be modelled (i.e. the GOSAT measurement locations) can be seen in Figures 5.2 through to 5.6. No measurements within the African continent were simulated. There are no significant CH<sub>4</sub> sources in Northern Africa, whilst the emissions from the equatorial African tropical regions would be representative of those over South America. Limiting the dates for which the model was run and imposing geographical constraints resulted in 6140 simulations.

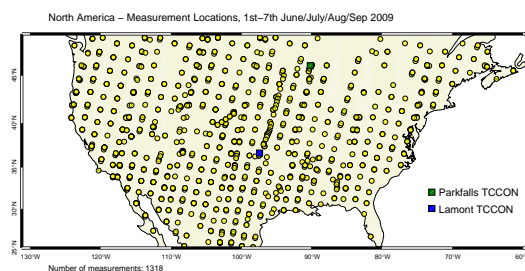


FIGURE 5.6: The locations of GOSAT measurements, North America for the time period of 1<sup>st</sup> - 7<sup>th</sup> Jun /Jul /Aug /Sep, 2009.

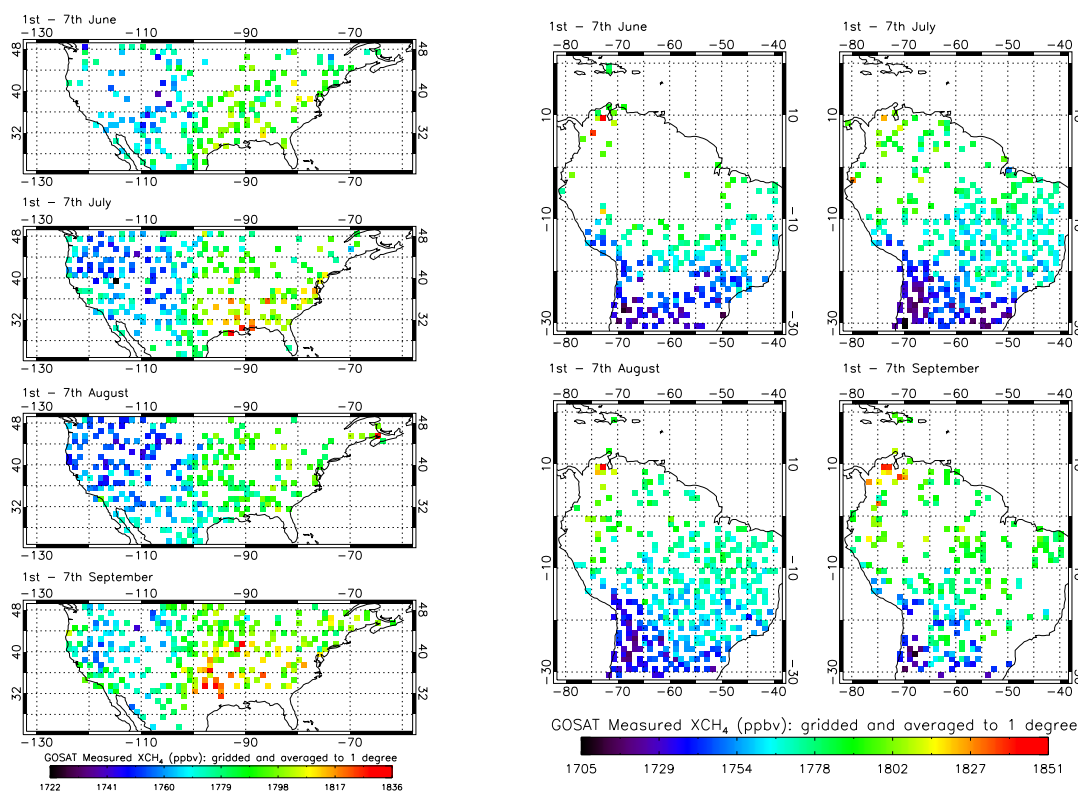


FIGURE 5.7: North America - the mean GOSAT proxy XCH<sub>4</sub> measurements retrieved at Leicester (gridded to 1 degree).

FIGURE 5.8: South America - the mean GOSAT proxy XCH<sub>4</sub> measurements retrieved at Leicester (gridded to 1 degree).

Figures 5.7 through Figure 5.11 show the mean Leicester retrieved GOSAT concentrations during the first week of June, July, August and September, 2009. Measurement data in each 1 degree grid box is taken and the mean calculated.

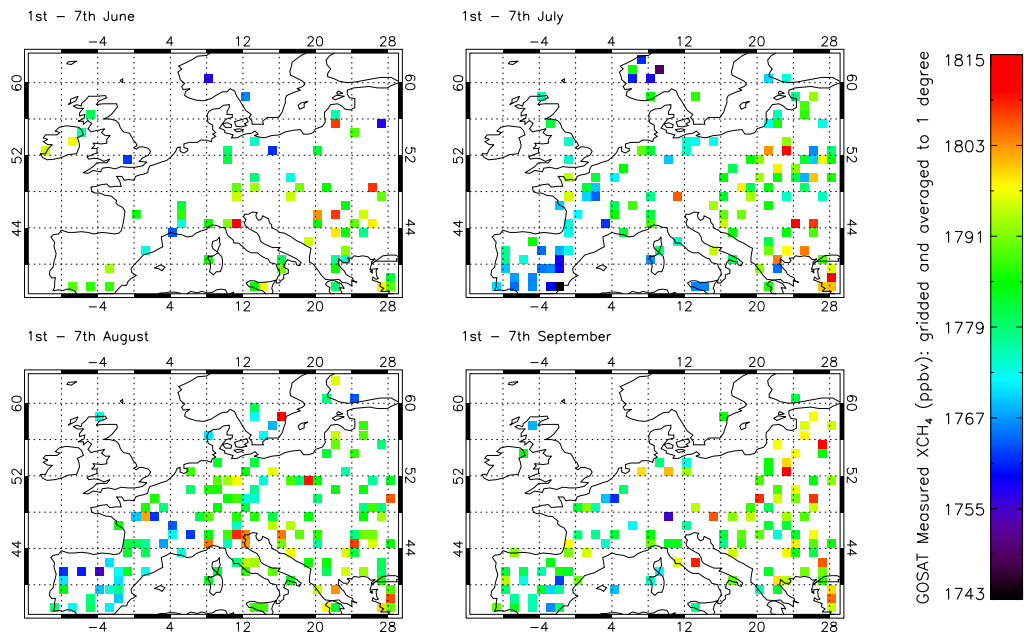


FIGURE 5.9: Western Europe - the mean GOSAT proxy XCH<sub>4</sub> measurements retrieved at Leicester (gridded to 1 degree).

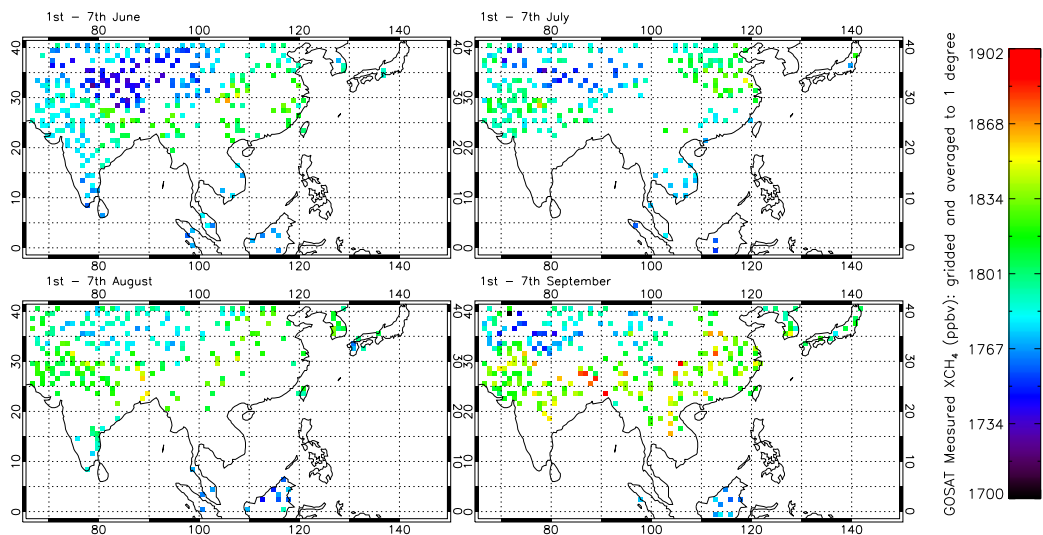


FIGURE 5.10: South East Asia - the mean GOSAT proxy XCH<sub>4</sub> measurements retrieved at Leicester (gridded to 1 degree).

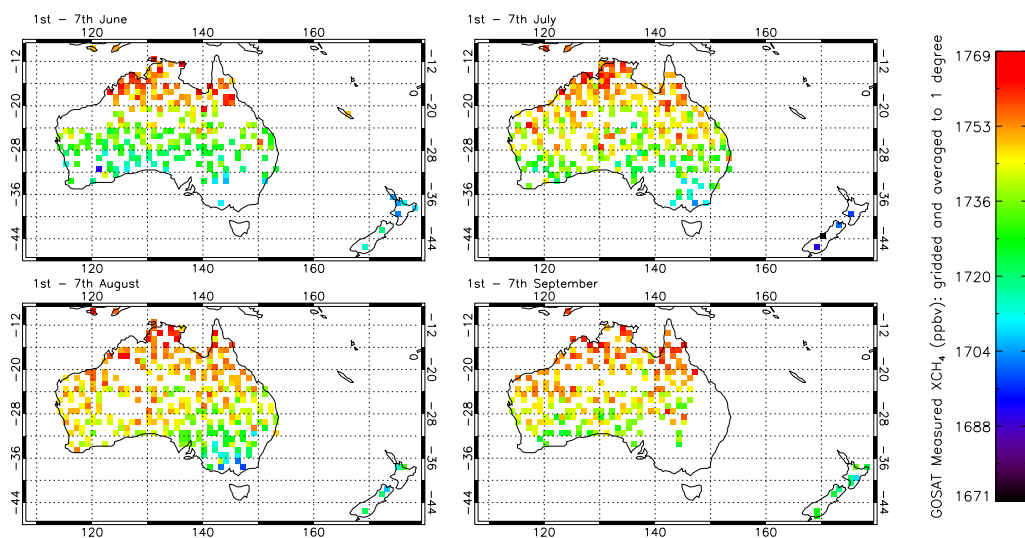


FIGURE 5.11: Australasia - the mean GOSAT proxy XCH<sub>4</sub> measurements retrieved at Leicester (gridded to 1 degree).

### 5.3 Combining emission inventories

In this section, the combined emission inventories to be used in simulating the GOSAT measurements are presented. For the emission inventories (described in Section 3.6.2) to be used together in the forward model, the inventories first have to be combined. As the different emission inventories have different resolutions, the inventories described here were all re-gridded to the 0.5° to match the spatial resolution NAME was run at. Emission hot spots visible in the high resolution EDGAR inventory over the ocean or regions such as southern Ireland, are a result of this process, smoothed out. Other emission inventories, have on the other hand a lower spatial resolution, than 0.5°. For instance, the wetland emission estimates derived by Bloom et al. (2012), have a geographical grid resolution of 3 by 3 degrees. To be used by the modelling system, a box was simply split up into 9 grid boxes. At coastal regions, artefacts are introduced displaying higher than expected emissions over the sea grid boxes. Where the emission inventories are extremely low (parts of Australia), a region can be a net sink of methane. This is where the soil absorption is higher than the combined positive emissions in the region. Figures 5.12, 5.13, 5.14, 5.15 and 5.16 show the resulting combined emission inventories for the simulation domains under consideration here. The flux estimates were then converted to  $\text{g m}^{-2} \text{s}^{-1}$ , as required to be used in the forward simulation system. The final emission inventories used in the model to simulate the final inventories can be seen in Figures 5.12, through to 5.16. The enhancement due to these local emissions will be added to the calculated background, resulting in the final simulated observations.

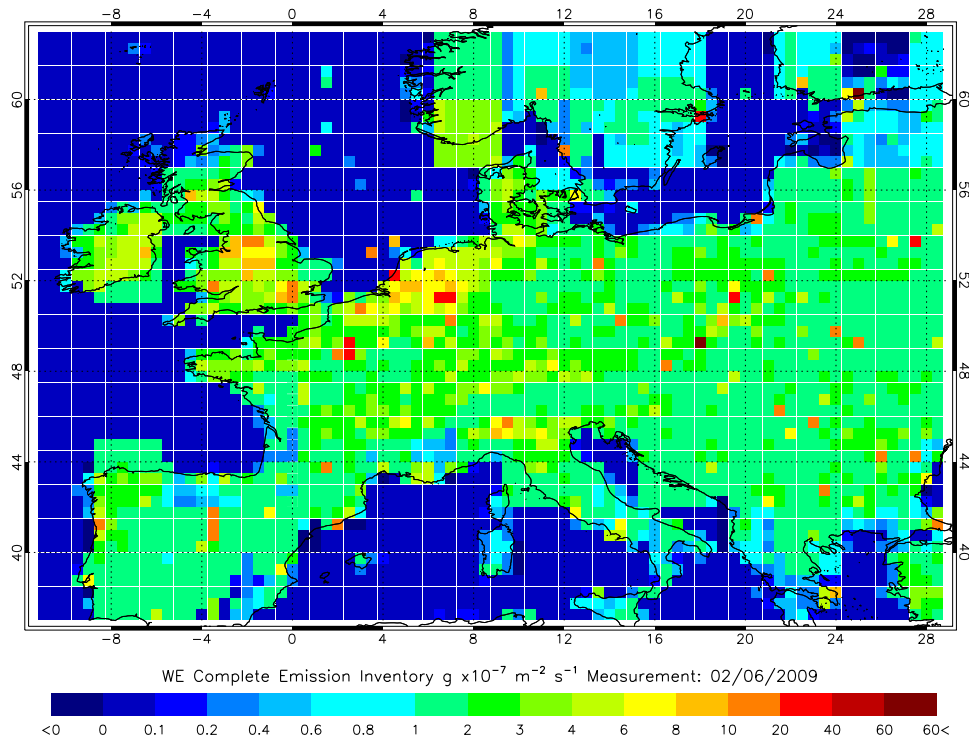


FIGURE 5.12: Western Europe - The final combined methane emission inventory.

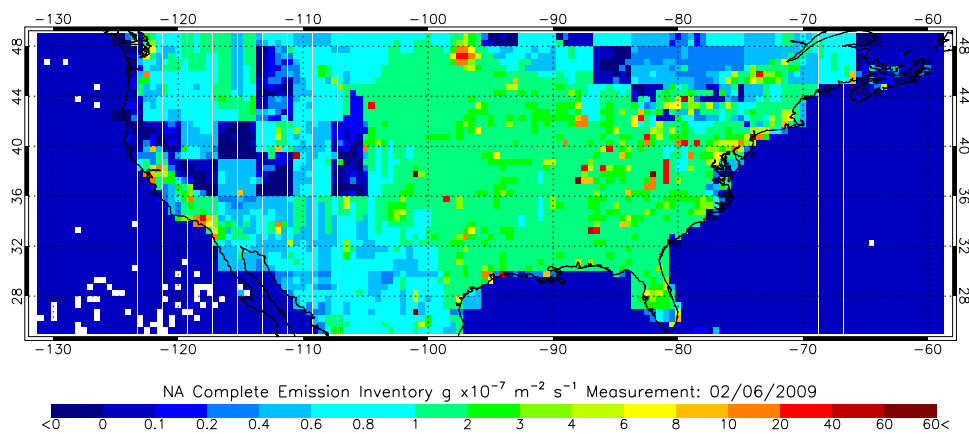


FIGURE 5.13: North America - The final combined methane emission inventory.

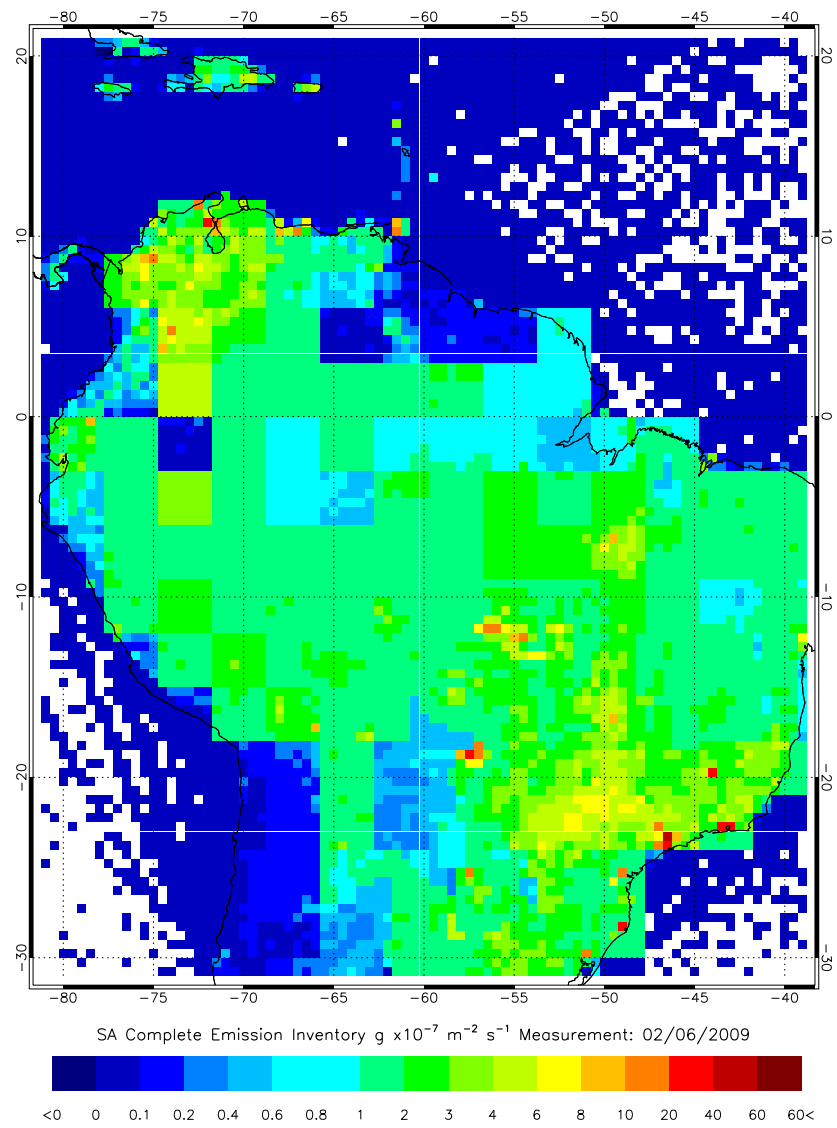


FIGURE 5.14: South America - The final combined methane emission inventory.

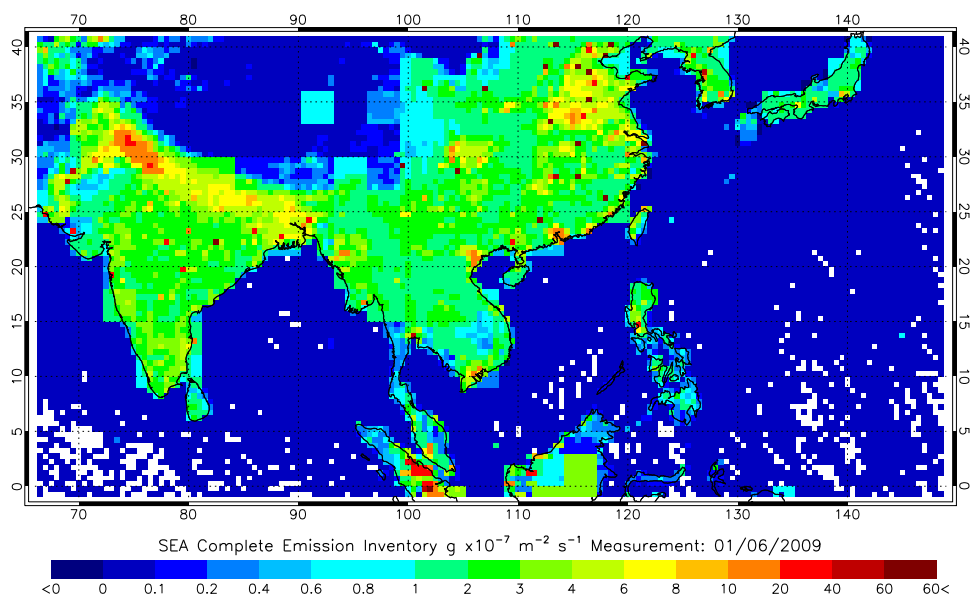


FIGURE 5.15: South East Asia - The final combined methane emission inventory.

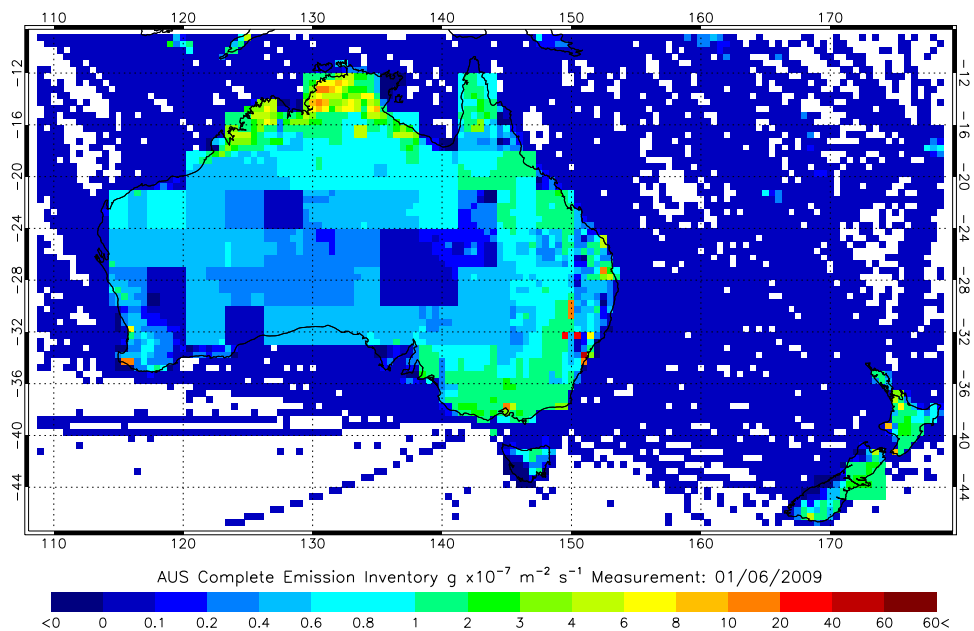


FIGURE 5.16: Australasia - The final combined methane emission inventory.

## 5.4 Determining the atmospheric background

In this section, a method to calculate the atmospheric background of methane is developed. The background (also referred to as baseline in this text) can be defined as the concentration of the pollutant in the air entering the domain of interest, excluding the influence of local simulated emissions. For long-lived gases, such as  $\text{CH}_4$ , this is the major fraction of the measured signal and an enhancement in measured concentrations caused by the regional emissions will be small in comparison. It is therefore essential to compute the background, which will be added to the simulated enhancement.

A number of methods of calculating the baseline have been proposed in previous inversion studies. Manning et al. (2011) used NAME in conjunction with high-frequency measurements from Mace Head to estimate the methane and nitrous oxide emissions from NW Europe. The background concentrations were defined as those that have not been influenced by significant emissions from previous 12 days of travel en route to Mace Head. In effect, only the measurements obtained when strong easterly winds were dominating were recorded as background. As Mace Head is a coastal measurement station, it is reasonable to assume that the air arriving from the Atlantic is well mixed i.e. 'clean'. There is a strong hemispheric gradient in global methane concentrations, therefore Manning et al. (2011) also excluded southern air when modelling the background. For each hour in the measurement time series that passed the analysis, the remaining baseline points were then fitted in a 40-day running window using a quadratic function. The  $\text{CH}_4$  concentration value was extracted for the hour in question, with the baseline time series then smoothed within a moving 20-day time window. Stohl et al. (2009) used a dispersion model and data from a number of ground measurement stations to infer the magnitudes of halocarbon emissions. The data used was obtained from a number of measurement locations, therefore an objective method that could be applied for all stations was required. Stohl et al. defined the baseline as "part of the measured concentration averaged over 31 days that cannot be explained by emissions occurring on the 20-day time scale of the model calculations". The background value was calculated by treating the baseline as another vector of unknowns in the mathematical inversion algorithm, which is solved iteratively.

In this study, satellite measurements are used and this presents new challenges. The Manning et al. (2011) method cannot be utilised, as the measurements are not coastal. A vast majority of observations are inland, which cannot simply be classified as background due to local emission influences. This is further compounded by the large measurement footprint. Ideally,  $\text{XCH}_4$  measured on the domain borders, or coasts depending on the

region, would be added to the calculated enhancement. It would be advisable to employ the same instrument to measure this baseline and obtain  $XH_4$  used in the inversion itself. This would eliminate any cross-calibration errors. Unfortunately, owing to the geographical location of the GOSAT measurements and the relatively sparse observation density, the instrument cannot be used to initialise the background in most regions. GOSAT is able to utilise the sun-glint mode over the equator, which could in theory be used to compute the baseline in the South East Asia region modelled here. Sun-glint retrievals are not, however, performed by the Leicester group as of late 2013. As various retrieval algorithms perform differently, owing to the variations in the retrieval algorithms and use of different a priori data, using the official NIES product in conjunction with the proxy Leicester retrieved data would introduce its own issues. Regardless, sun-glint measurements are not available over high-latitude regions (Western Europe and North America).

As measurements from the GOSAT instrument cannot be used to directly measure the  $XCH_4$  entering the simulated domains, it was decided to use the chemical data fields from a global Eulerian chemical transport model to calculate the baseline. Here, data from the University of Edinburgh GEOSCHEM methane model was used. GEOSCHEM has been compared with GOSAT (Parker et al., 2011) and found to be in good overall agreement, thus it was suitable for background calculations (see Section 3.6.1). The obtained chemical fields have 47 vertical levels, and are pressure weighed using the method described in section giving us  $XCH_4$  to be used in this study. The developed method does not require any modification to the CTM itself therefore in theory, any model could be used for this purpose.

To calculate the background, it is necessary to account for  $CH_4$  leaving the area of interest. There is variation in  $CH_4$  concentrations around the edge of the domain, as can be seen in Figure 5.17a, which shows example GEOSCHEM  $XCH_4$  over Western Europe on 24/07/2009. The  $XCH_4$  that will be carried into this simulation domain on this day will depend on the direction of the wind entering the regions. Air entering the domain from the west on this day would bring in 1766 – 1770 ppbv, whilst air entering the domain from the west carries a lower baseline value in the range of 1761 – 1766 ppbv (Figure 5.17a). NAME is again used here to model the transport of air until it leaves the domain of interest. The model is requested to output an integrated 10-day tracer particle concentration at the border of the region of interest. This, in effect, provides us with the locations, where the NAME tracer particles enter the high resolution domain (as the model is run backwards) over the 10 days prior to the measurement. The information on the air mass history contained within the model output is used in combination with the GEOSCHEM fields to calculate the baseline. The NAME output resolution matches

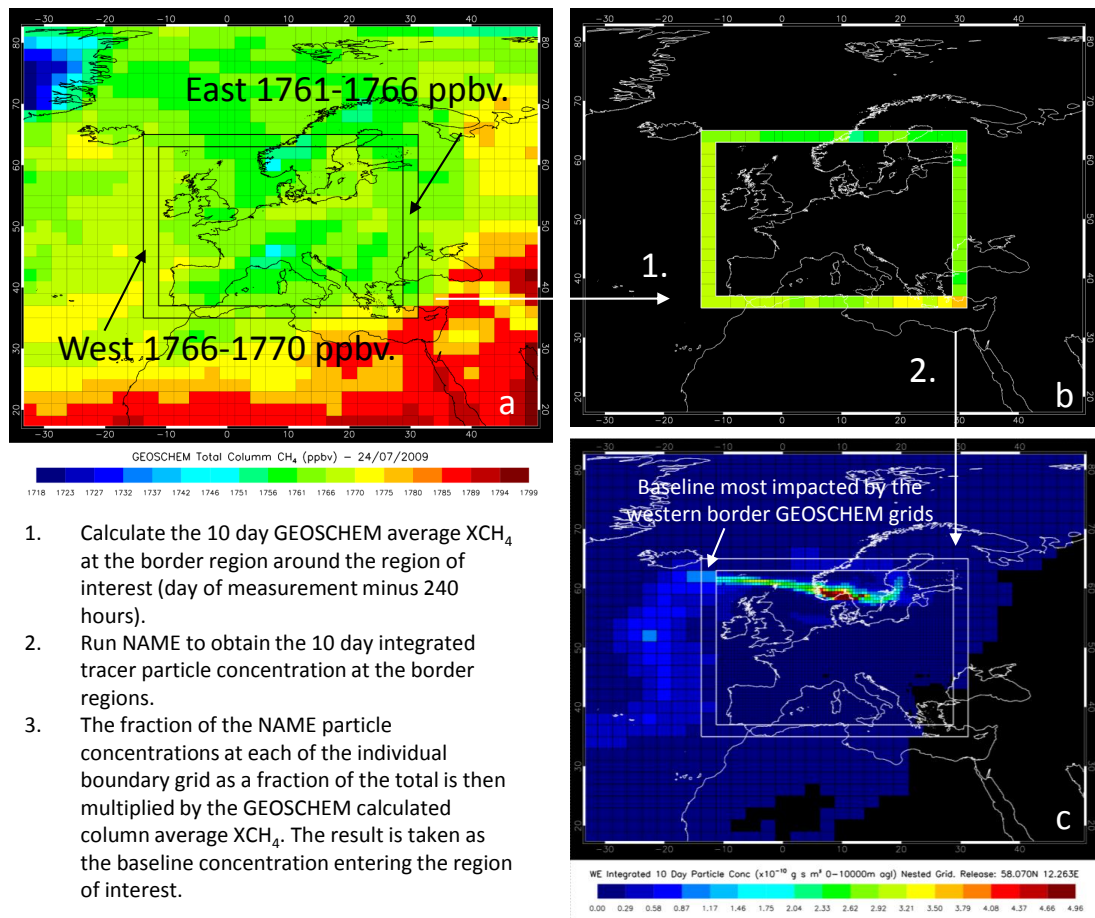


FIGURE 5.17: (a) GEOSCHEM  $XCH_4$  concentration over Western Europe on 24/07/2009. (b) The GEOSCHEM modelled  $XCH_4$  from the highlighted regions is taken into account when calculating the baseline. (c) NAME outputs the residence time of the particles 10 days prior to reaching the measurement co-ordinate at the border region around the domain of interest.

that of the GEOSCHEM model, making the datasets immediately usable together in the modelling framework. The fraction of the NAME particle concentrations at each of the individual boundary grid boxes (10-day integrated) as a fraction of the total is multiplied by the GEOSCHEM-calculated column  $XCH_4$  averaged over 10 days. The result is taken as the baseline concentration entering the region of interest (Figure 5.17 and Section 5.5). The simulated baseline does therefore take into account the meteorology 10 days prior to the measurement being taken.

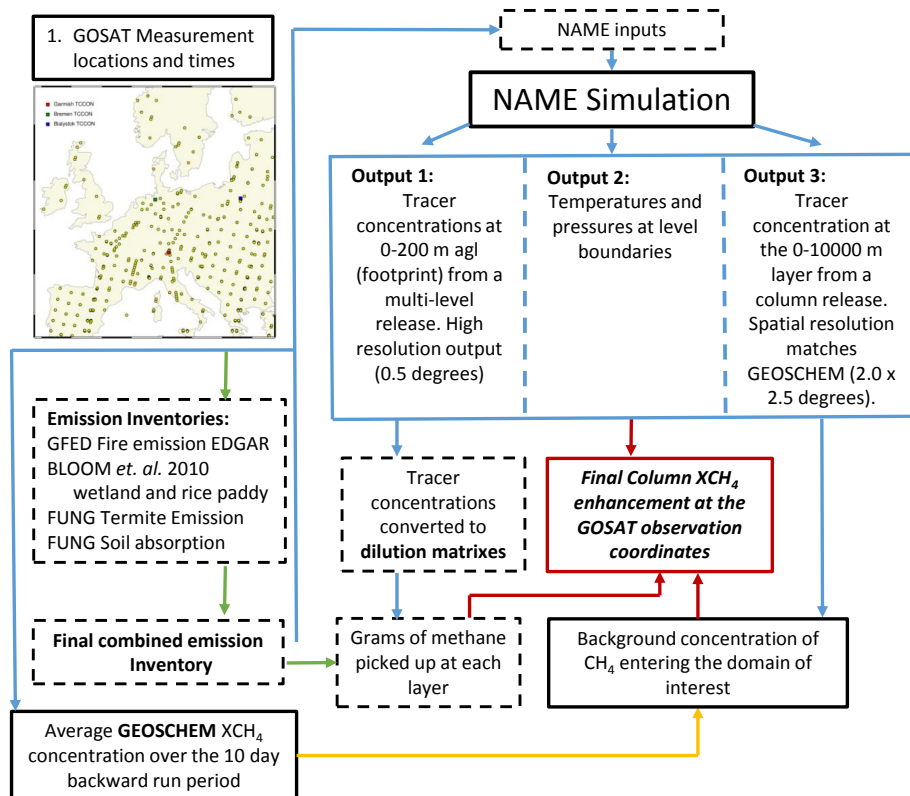


FIGURE 5.18: An overview of the forward modelling system used to simulate the GOSAT measured  $XCH_4$ . The time and location of the GOSAT measurements are used to produce the NAME inputs. High-resolution, multi-level model output is converted to the dilution matrix and combined with the emission inventories to obtain the enhancement in concentration due to local emission. The emission inventory is different for each release day. The low-resolution NAME output, in conjunction with the GEOSCHEM concentrations, provides the baseline.

## 5.5 Simulating satellite $XCH_4$ observations

To simulate atmospheric GOSAT observations of  $XCH_4$ , the forward modelling component of the inversion system developed in Chapter 3 is used.

NAME is required to provide the link between the local emissions and the final concentration enhancement at the measurement point, as well as to the atmospheric background. The overview of the forward system used here and the requested NAME outputs can be seen in Figure 5.18. NAME simulations provide 3 outputs required for this task. Output 1 is a high resolution output ( $0.5^\circ$ ) of the tracer concentration within the bottom level of the model (0 – 200m) from the release at various heights, from the surface

to 10000 m (see Section 3.4.1 for a detailed description). The resolution of the output would match the resolution of the a priori emission inventories. Output 2 provides the temperatures and pressures at the release level boundaries. This will enable conversion of the mass of methane gained at each level to the ppbv enhancement as well as calculating the pressure weighting functions (Section 3.3.3). The resultant dilution matrices can be multiplied by the final emission inventories (described in Section 5.3) to give the enhancement in  $XCH_4$  due to local emissions.

Output 3 gives low resolution ( $2.5^\circ \times 2^\circ$ ) tracer concentration within a column of 0 – 10000 m above the ground level. The air arriving from heights above the planetary boundary layer is also therefore being taken into account. The Eulerian model provides the boundary conditions for the high-resolution model (Section 5.4) and the high-resolution NAME output is then used to model the concentration enhancement due to the local emissions. The modelled local concentration enhancement is added to the previously calculated background, resulting in the final modelled GOSAT measurements. The high-resolution Lagrangian model output can be said to be nested within the low-resolution global Eulerian model.

Visualisation of the requested high and low resolution NAME outputs in the regions of interest are shown in Figures 5.19 through to 5.23. The grid boxes enclosed by the white border signifies the edge of the high-resolution domain. The tracer concentration within the white borders is used to calculate the baseline. Only the emissions within the high-resolution region are going to be simulated, and thus have an impact on the simulated observations.

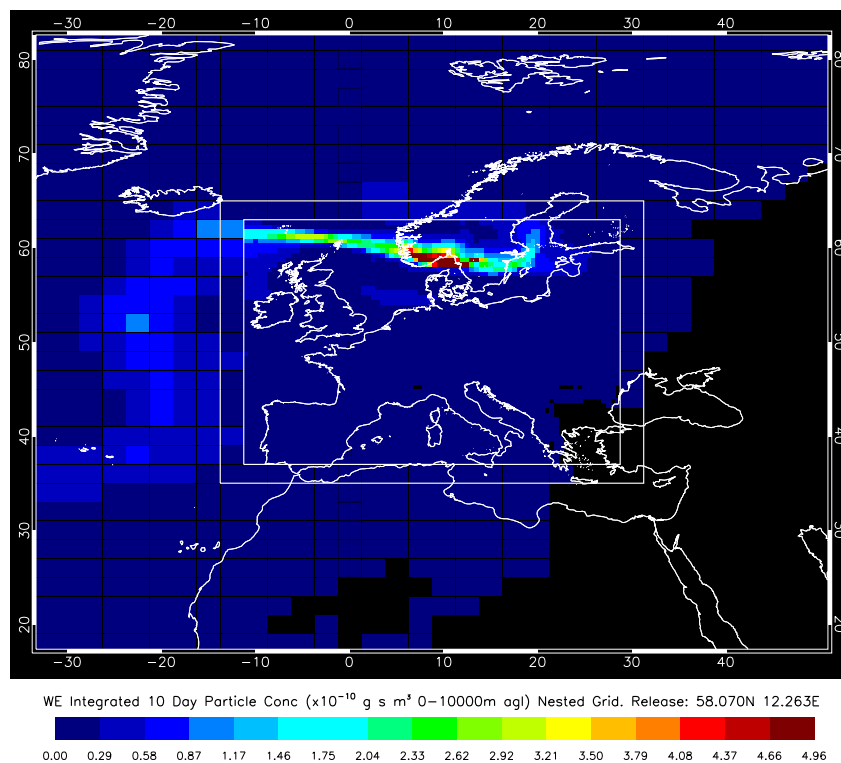


FIGURE 5.19: Western Europe - the requested nested NAME output. The low-resolution output (within the white borders) is used for calculating the background, whilst the high-resolution tracer concentration is used to calculate the  $XCH_4$  enhancement due to local emissions.

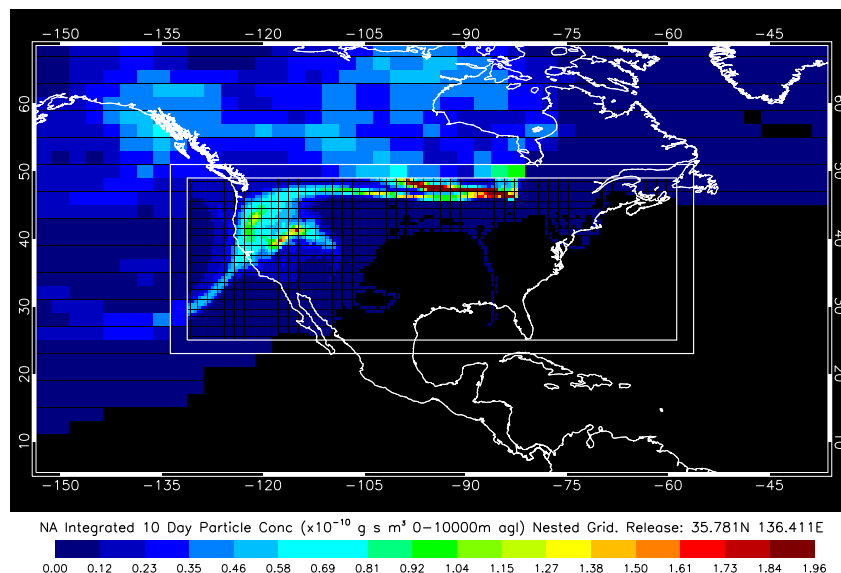


FIGURE 5.20: North America - the requested nested NAME output. The low-resolution output (within the white borders) is used for calculating the background, whilst the high-resolution tracer concentration is used to calculate the  $XCH_4$  enhancement due to local emissions.

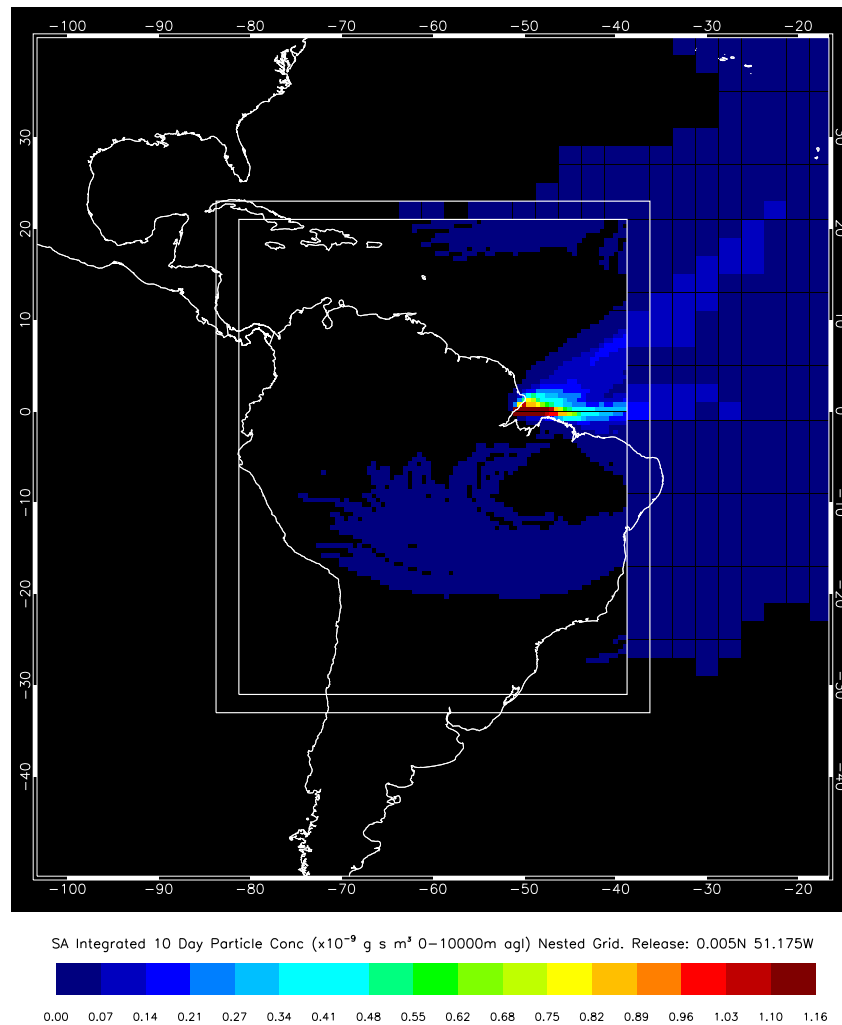


FIGURE 5.21: South America - the requested nested NAME output. The low-resolution output (within the white borders) is used for calculating the background, whilst the high-resolution tracer concentration is used to calculate the  $XCH_4$  enhancement due to local emissions.

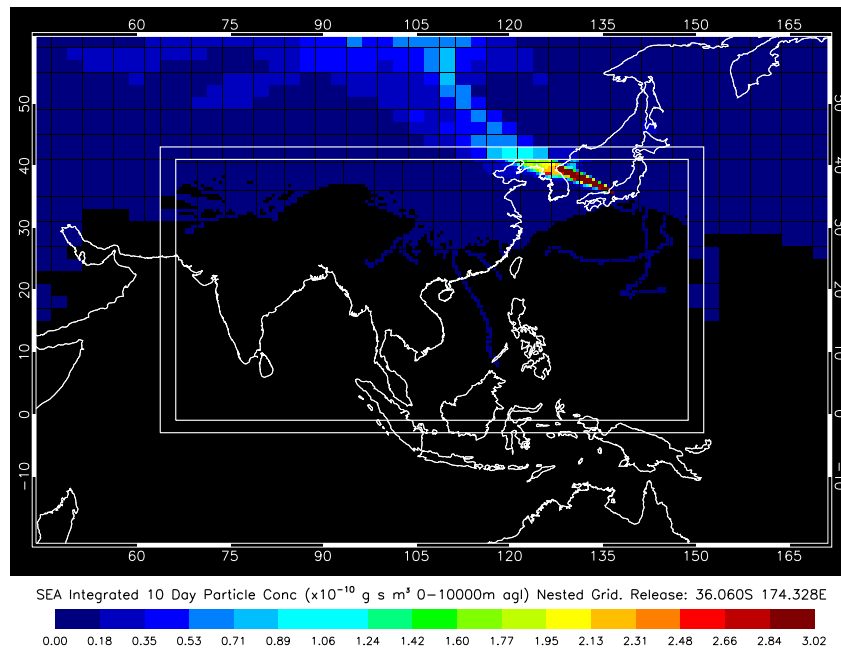


FIGURE 5.22: South East Asia - the requested nested NAME output. The low-resolution output (within the white borders) is used for calculating the background, whilst the high-resolution tracer concentration is used to calculate the  $XCH_4$  enhancement due to local emissions.

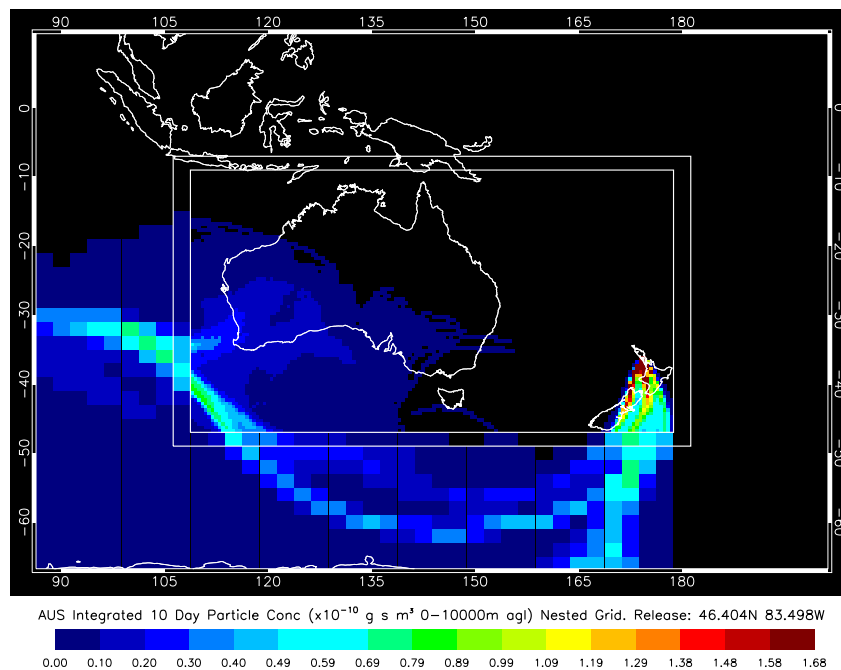


FIGURE 5.23: Australasia - the requested nested NAME output. The low-resolution output (within the white borders) is used for calculating the background, whilst the high-resolution tracer concentration is used to calculate the  $XCH_4$  enhancement due to local emissions.

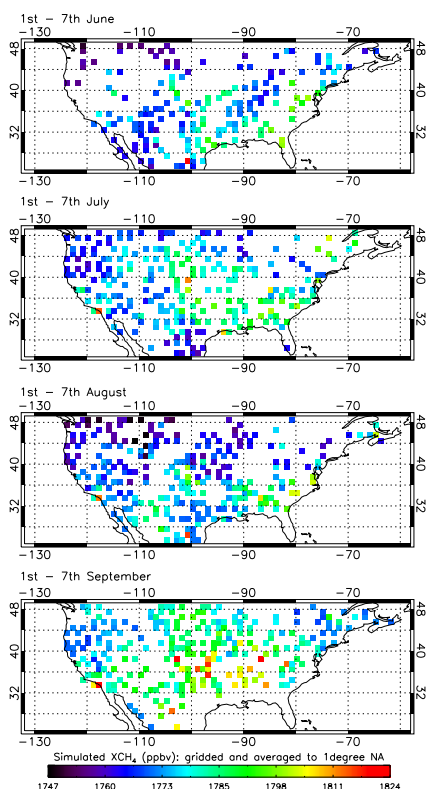


FIGURE 5.24: North America - simulated GOSAT measurements.

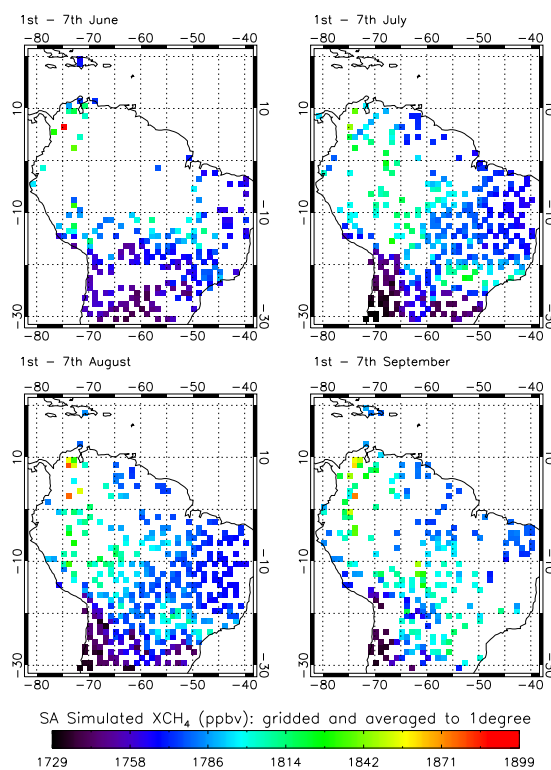


FIGURE 5.25: South America - simulated GOSAT measurements.

## 5.6 Results and analysis

Figures 5.24, 5.25, 5.26, 5.27 and 5.28 show the mean simulated GOSAT concentrations during the first week of June, July, August and September, 2009. The simulated GOSAT measurements are averaged over  $1^\circ \times 1^\circ$  boxes. This allows for the comparison to the averaged GOSAT data to be made. Figures 5.33, 5.34, 5.35, 5.36 and 5.37 display the difference between the gridded GOSAT observation and the simulated measurement mean values. The grid boxes in blue indicate regions where the mean simulated measurement is larger than the mean GOSAT observation. The red grid boxes indicate a larger mean observation to the simulated mean value.

The resulting simulated, satellite-observed atmospheric  $\text{CH}_4$  concentrations are plotted against the GOSAT measured time series in Figures 5.29, 5.30, 5.31, 5.32. The calculated baseline is plotted in red, the simulated measurements in blue and the actual GOSAT observations in black. The figures show the simulated enhancement as well as the baseline, thus displaying the relative contribution of emissions in the local region to each individual measurement. The Pearson's correlation coefficient between the observations and the simulations is also calculated.

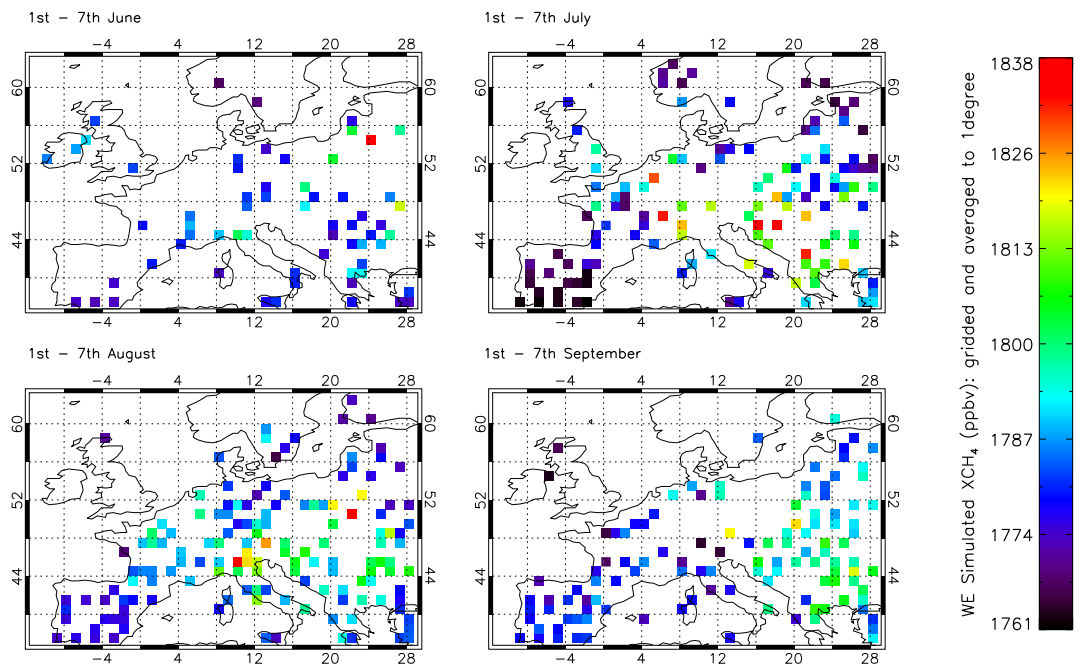


FIGURE 5.26: Western Europe - simulated GOSAT measurements.

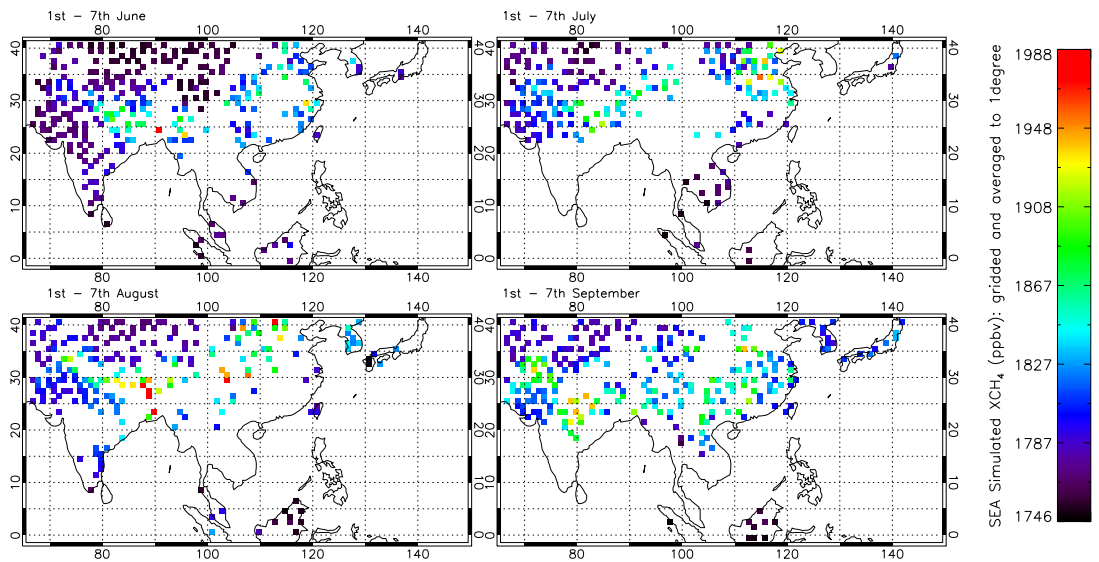


FIGURE 5.27: South East Asia - simulated GOSAT measurements.

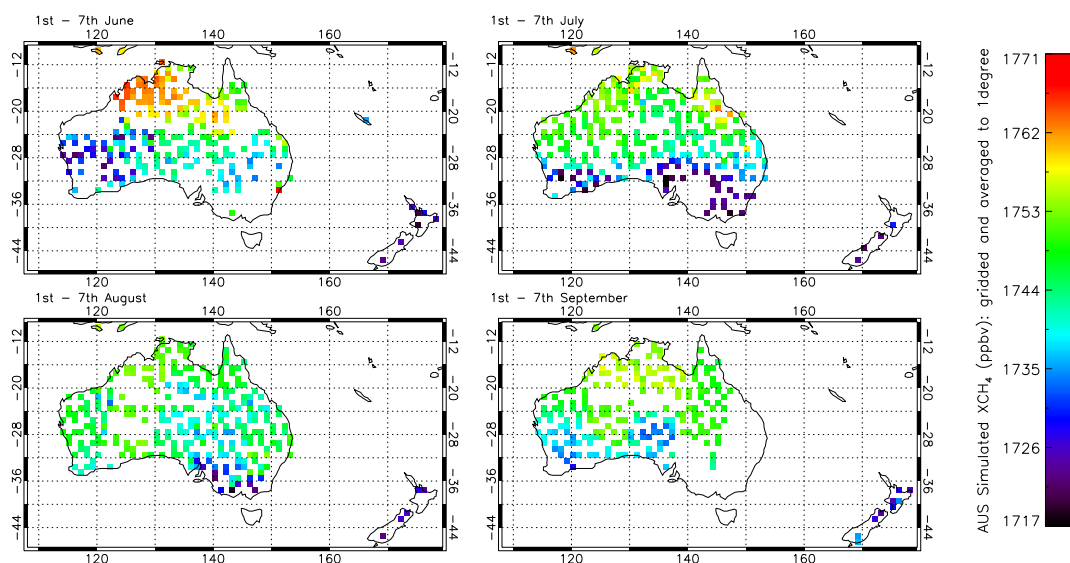


FIGURE 5.28: Australasia - simulated GOSAT measurements.

Figure 5.29 is a comparison of GOSAT observations against the simulated measurements for the first week of June, 2009. The correlation between the observation and the model has a correlation value of  $r=0.18$  in Western Europe. The very low correlation could be a result of the very heterogeneous anthropogenic emissions (EDGAR, also see the inventory contribution breakdown shown in Figure 5.39) that dominate in this particular region. By running NAME at a relatively low spatial resolution of  $0.5^\circ$ , it is possible for the emission hot spots (such as landfill sites) to be diluted over larger areas. The effect would result in an emission hot spot having an influence over a wider modelled geographical area. Simulated GOSAT measurements in such regions would experience a lower enhancement due to the influence of the geographically dispersed flux. In contrast, an actual GOSAT measurement taken over the high-emitting site would experience a greater enhancement over the background than the modelled observations. Running NAME at a higher spatial resolution does, as discussed in Chapter 3, require higher resolution meteorological data than available to be used for this study. The correlation coefficient does increase in the first week of July (Figure 5.30) to  $r=0.56$  before decreasing in August and September to  $r=0.38$  (Figure 5.31) and  $r=0.24$  (Figure 5.32), respectively. Figure 5.38 displays the correlations between all of the measurements and simulated data in the Western Europe region. The correlation is found to be  $r=0.43$ . Figure 5.35 displays the geographical distribution of the differences between the  $1^\circ$  gridded GOSAT observations and simulated measurements. There are no significant geographical biases in the differences visible for the Western Europe simulation region in the time frame of the simulations.

The measurements over North America, similarly to Western Europe, were also largely influenced by the EDGAR emission inventories ( Figures 5.39 to 5.42) The agreement between the simulations and the observations is relatively poor at  $r=0.41$ ,  $r=0.42$ ,  $r=0.31$  and  $r=0.46$  in June, July, August and September (Figures 5.29 to 5.32). The spatial biases in differences between the observations and simulations are present over North America and can be seen in Figure 5.33. The GOSAT measurements east of  $\sim 100^\circ\text{W}$  are in general higher than the simulated observations over all of the months simulated in this study. Similarly, the GOSAT observations west of  $\sim 100^\circ\text{W}$  tend to be lower than the expected simulated values. This suggests that the emission inventories in the eastern United States underestimate the  $\text{CH}_4$  emissions, whilst those in west of  $\sim 100^\circ$  are over estimated. Another possibility is that the bias is introduced in the calculation of the atmospheric background.

In general, the simulated measurements over South America display a good agreement with GOSAT observations. The correlations of  $r=0.73$ ,  $r=0.74$ ,  $r=0.68$  and  $r=0.64$  in June, July, August and September are calculated. This high agreement seems to confirm the hypothesis that regions in which the anthropogenic sources have the greatest influence, have the lowest agreement between the observation and the simulation. In South America, the Bloom et al. emission inventory has an increased impact on the enhancement over the atmospheric background (53%, see Table 5.38). It is also clear, that the framework used to calculate the atmospheric background using the GEOSCHEM needs modification. It is shown (looking at measurements 210 onwards over South America, Figure 5.29), that the calculated background is around  $\sim 50$  ppbv higher than the GOSAT measurement. It is clear that any local emissions will be added to the background, increasing the discrepancy between the model and the observation. Currently, the background is calculated by multiplying the fraction of the integrated 10-day tracer particle concentration in the border of the region of interest by the GEOSCHEM modelled concentrations. The model output does not differentiate when and how many particles left the domain during the time-frame of the simulation. It would be desirable for NAME to record the exact time and the grid box that all of the released particles leave the calculation domain. The particles could then be deleted preventing them from re-entering the domain and contributing to the NAME output. Time constraints prevent this modification from being made.

South East Asia shows an agreement between the synthetic observation and the GOSAT measurement of  $r=0.58$  in June dropping to  $r=0.51$  in July. The Pearson's correlation rises again to  $r=0.63$  in September. Figure 5.38 shows that the overall correlation is calculated to be 0.6. A large fraction of the modelled observations is significantly

higher than the GOSAT observations (see scatter in Figure 5.38d). The maximum disagreement of 172 ppbv shows that the forward model performs very poorly in South East Asia. The geographical distribution of the gridded difference values is displayed in Figure 5.36. The synthetic measurements are consistently higher than the GOSAT measurements in the region. As in South America, the atmospheric background is overestimated which will lead to simulations that are higher than the observations.

In Australasia, the agreement between the data sets is generally good (correlations of  $r=0.71$ ,  $r=0.70$ ,  $r=0.40$  and  $r=0.61$  in June, July, August and September). The correlation between all of the measurements is found to be  $r=0.6$  overall (Figure 5.38). The highest differences between the model and the observations are seen in June, where the the simulated  $XCH_4$  values are consistently overestimated. This is owing to the vast majority of the GOSAT observations being lower than the calculated background value (Figure 5.37). The forward-modelled concentrations are closer in magnitude to the observations in the latter months, however a decreased Pearson's correlation between the observation and the modelled values is seen.

### **5.6.1 Analysis of inventory contribution to enhancement**

It is desirable to break down the synthetic observations into the constituent contributions from the different emission inventories used in the study. The algorithm developed here could be used to analyse any GOSAT observation in the future and potentially explain any anomalous values. Enhancements in observed concentrations could, for example be observed due to fire emissions, which would be visible in this type of analysis (subject to availability of inventories in the time frame of the simulations). Figures 5.39, 5.40, 5.41 and 5.42 display the attributions to the  $CH_4$  enhancements owing to the a priori emission inventories used to forward model the synthetic GOSAT observations. The final simulated observation is calculated by adding the atmospheric background to the values shown. Figure 5.39 displays the modelled observed enhancements in June, 2009, for the different regions modelled here. The contribution to the  $CH_4$  enhancement is dominated by the EDGAR and Bloom et al. wetland and rice inventories over Western Europe. On average, the EDGAR anthropogenic and Bloom et al. emissions contribute  $\sim 75\%$  and  $\sim 27\%$  to local enhancement, respectively. Table 5.1 shows the average percentage contribution of a priori emission inventories to the modelled  $CH_4$  enhancement over the background for all the months and regions. The fire and termite emissions are very small ( $\sim 1\%$ ) over Europe for all of the months investigated in the study. GFED fire emission inventory contribution does however show a minimal monthly increase from

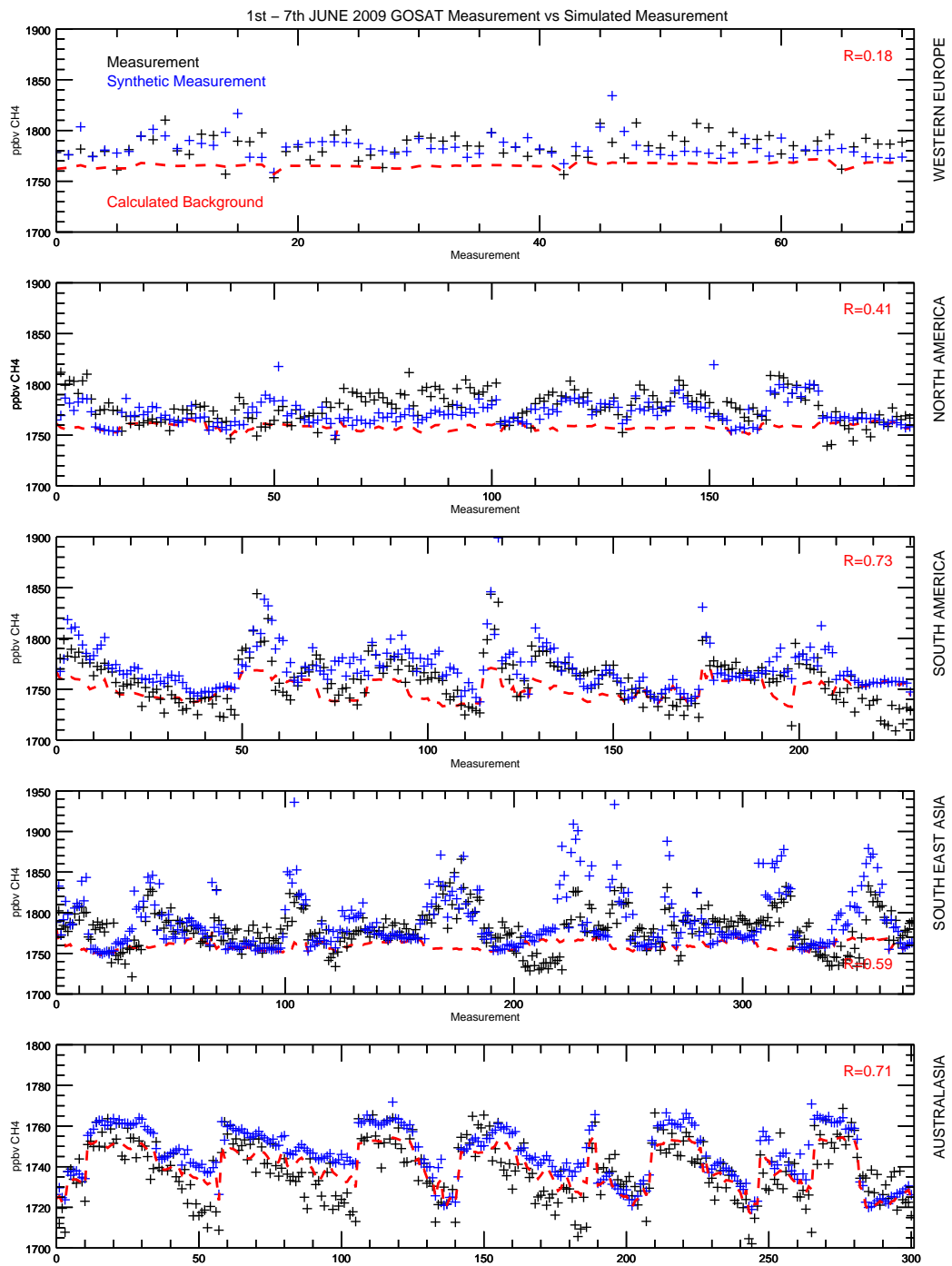


FIGURE 5.29: Simulated GOSAT observations compared with actual measurements - 1<sup>st</sup> to 7<sup>th</sup> June, 2009.

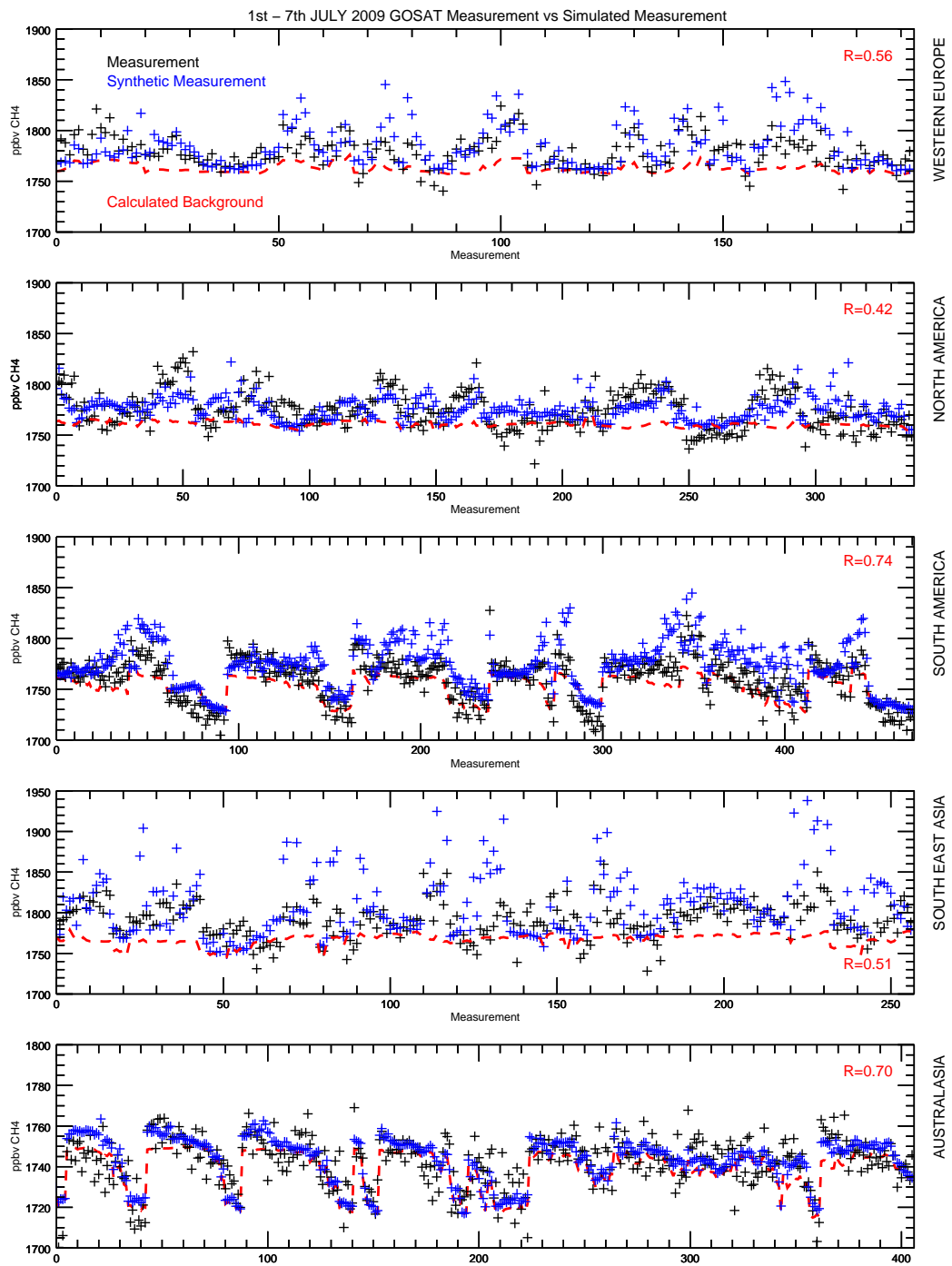


FIGURE 5.30: Simulated GOSAT observations compared with actual measurements - 1<sup>st</sup> to 7<sup>th</sup> July, 2009.

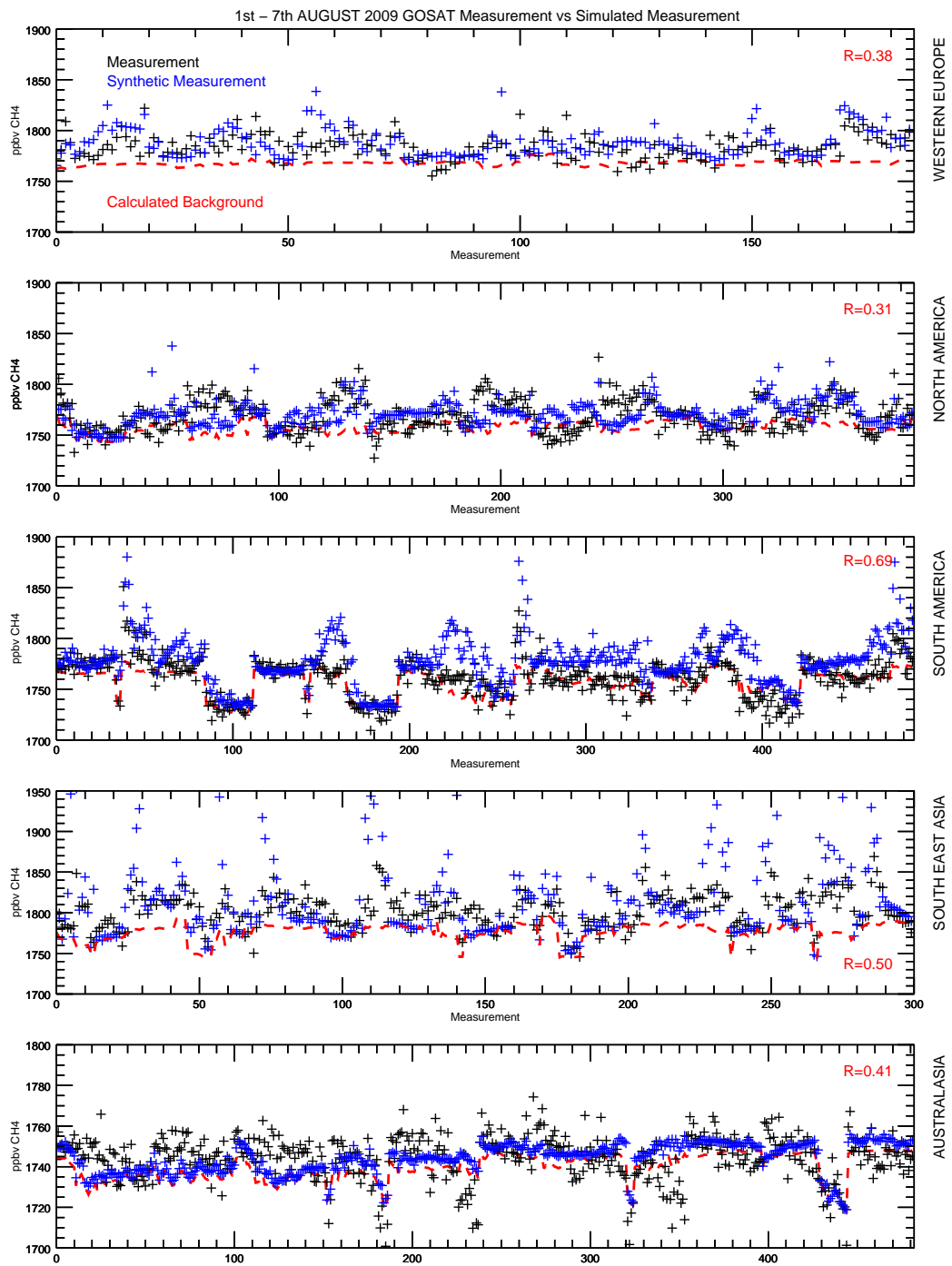


FIGURE 5.31: Simulated GOSAT observations compared with actual measurements - 1<sup>st</sup> to 7<sup>th</sup> August, 2009.

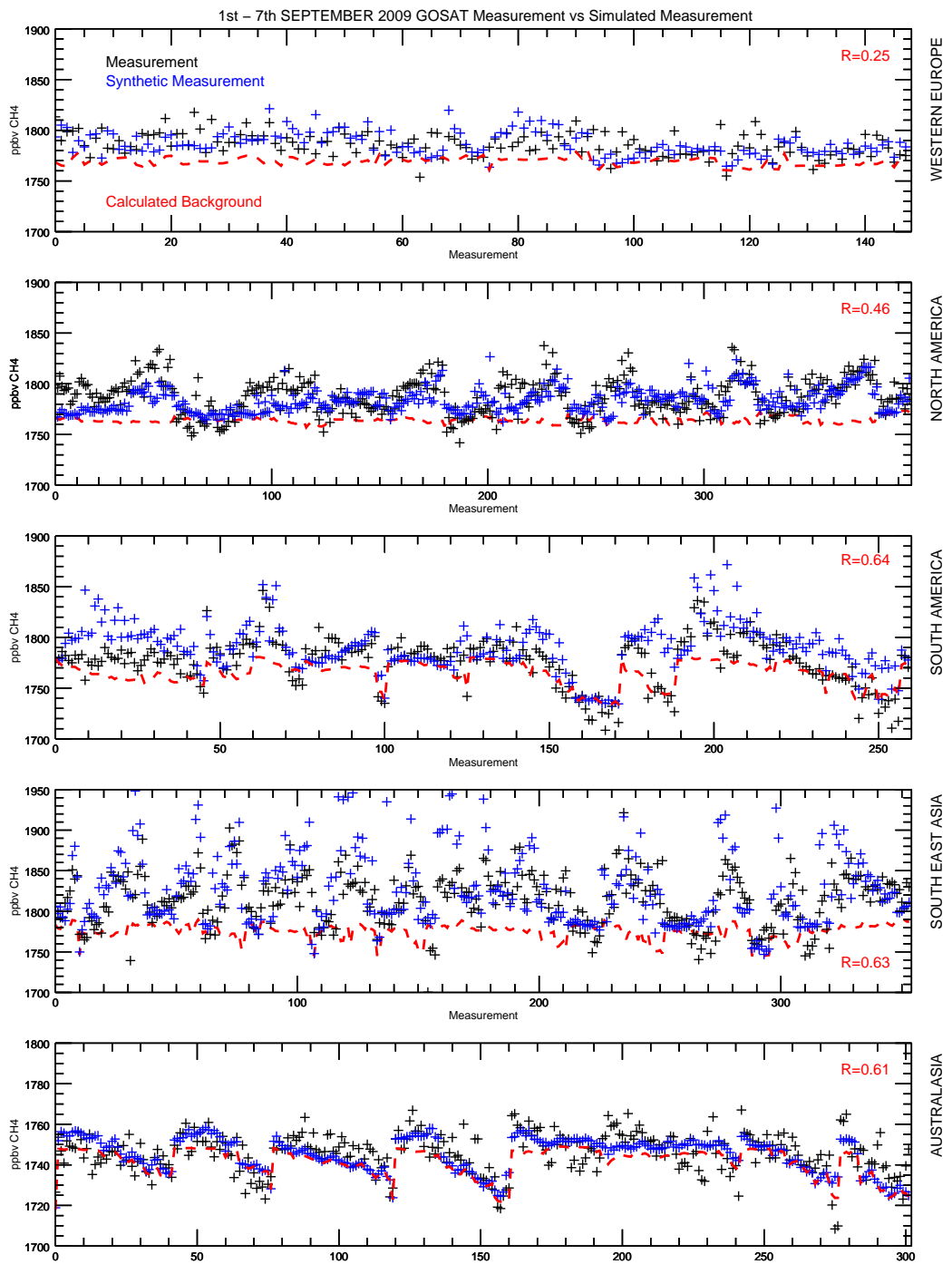


FIGURE 5.32: Simulated GOSAT observations compared with actual measurements - 1<sup>st</sup> to 7<sup>th</sup> September, 2009.

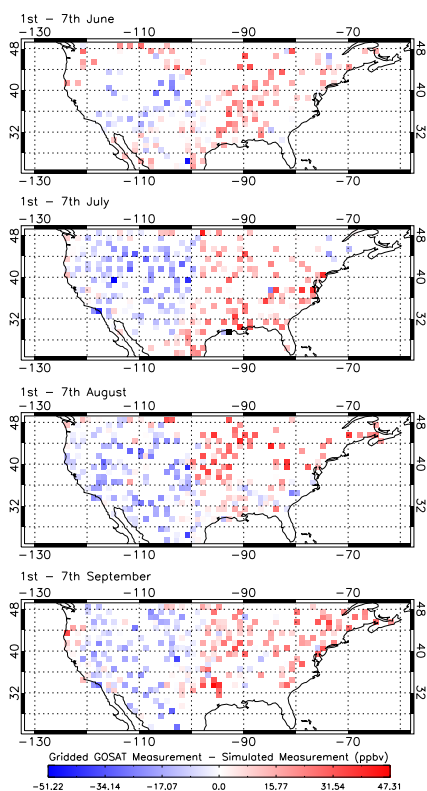


FIGURE 5.33: North America: GOSAT measurements minus simulated GOSAT measurements.

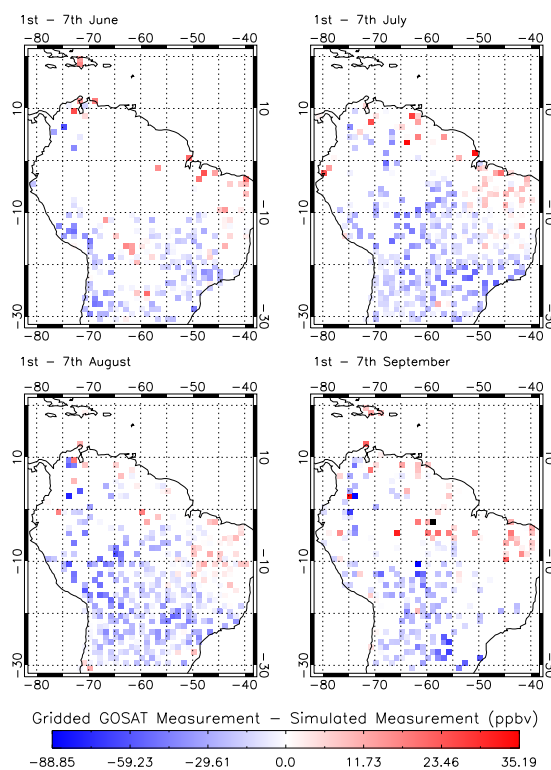


FIGURE 5.34: South America: GOSAT measurements minus simulated GOSAT measurements.

0 % in June (Figure 5.39) to 0.4 % in September (Figure 5.42). Throughout the time period of the study, the soil absorption is a sink of  $\sim 3.5$  % of the synthetic ppbv enhancement. The Fung et al. soil absorption inventory used here is aseasonal (as is the case with EDGAR), only wetland emission and fire emission inventories take into account temporal variability. A major factor in all of the modelled methane concentration enhancements is the meteorology acting on the measurement site 10 days prior to the measurement. Stable wind conditions over the 6 modelled days in any month considered here, could potentially bias the contribution to a particular inventory. The effect is minimised by calculating an average contribution over a large geographical area.

North America displays a similar average magnitude in methane signal enhancement over the background to Europe ( $\sim 20$  ppbv). The influence of Bloom et al. inventories is on average 10% larger than over Europe. The signal from the EDGAR emission inventory shows a corresponding, on average a 10 % decrease in influence over mean enhancement values in each of the months. The observed reduction in the mean anthropogenic source contribution is in part due to the western part of the United States emitting less methane due to human activity as the fraction of the total emissions than

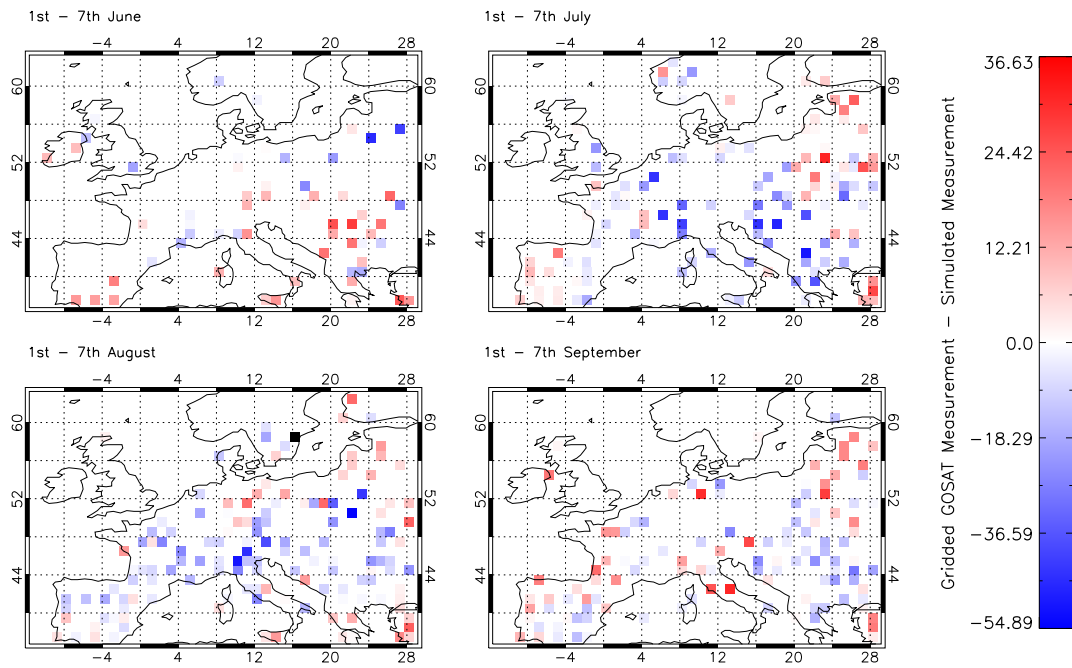


FIGURE 5.35: Western Europe : GOSAT measurements minus simulated GOSAT measurements.

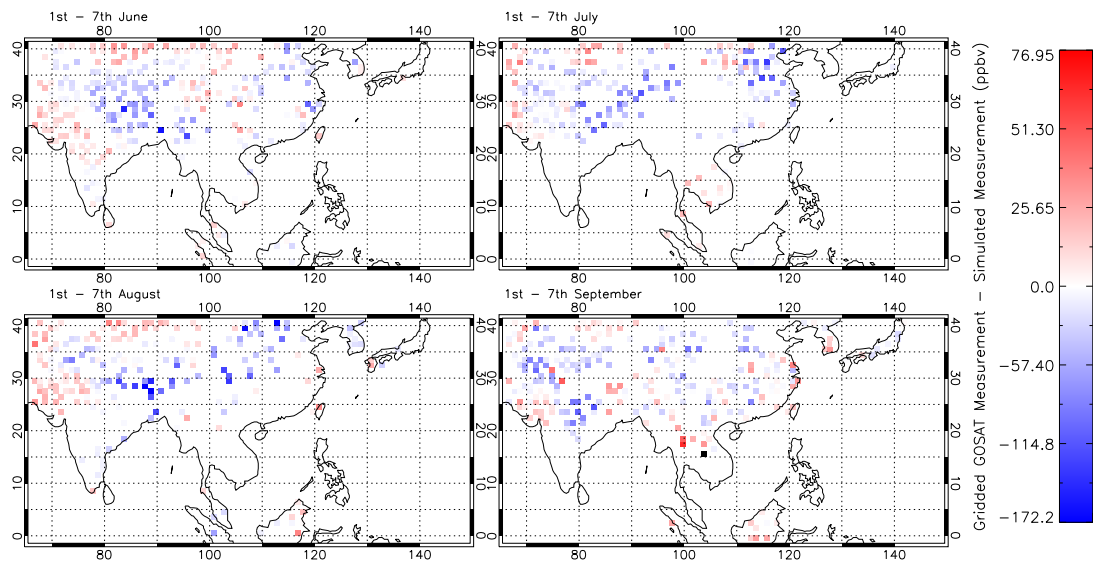


FIGURE 5.36: South East Asia: GOSAT measurements minus simulated GOSAT measurements.

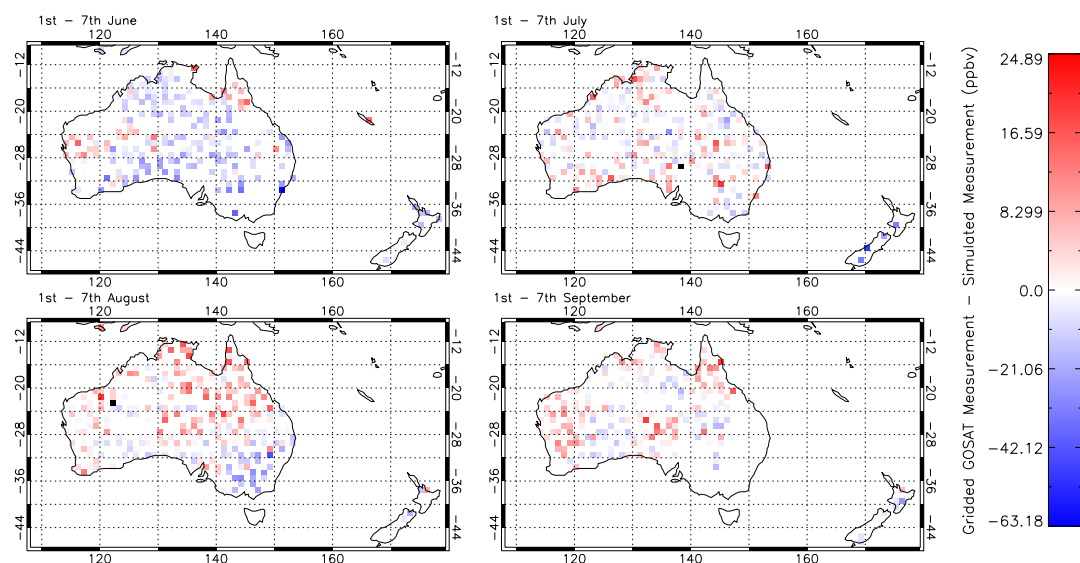


FIGURE 5.37: Australasia: GOSAT measurements minus simulated GOSAT measurements.

the east coast (see Figure 3.24). In effect, the higher fraction of the fluxes due to human activity in the east is offset by the west having fewer anthropogenic sources.

In South America, the wetland and rice field Bloom et al. emission inventory contributes the majority of the signal to the enhancement from the 1<sup>st</sup> until the 7<sup>th</sup> of June, 2009 (Figure 5.39). EDGAR contributes an average of ~42%, whilst wetlands and rice fields contribute ~53 % to the simulated enhancement. The EDGAR emission inventory percentage contribution shows a significant decrease (~33 % in July, ~31 % in August and ~23 % in September). The wetland contribution on the other hand increases significantly from ~53% in July, ~66 % in September). The biomass burning can also be seen to have a considerable impact on the measurement in September. GFED is calculated to contribute on average ~5%. It must be noted that in truth, some synthetic observations are more affected by the fires than others and the figure here is a mean. As can be seen in Figure 5.42 in South America a number of measurements (0 - 40) show that ~10 % - 15 % of the enhancement is owing to the GFED emission inventory influence. Other measurements are less affected owing to the prevailing wind directions and geographical locations of the measurements. Termite emissions are also seen to have a greater influence on the enhancement than either over Europe (mean of ~1 % over the four months studied here) or North America (mean of ~2 %). Termites are found to contribute ~5 % to the modelled total emissions. The soil sink absorbs less methane as a fraction of the total emission (~-1.5 %), due to the greater total enhancement in observations. The absorption contribution value is less than that over Europe or North America despite the

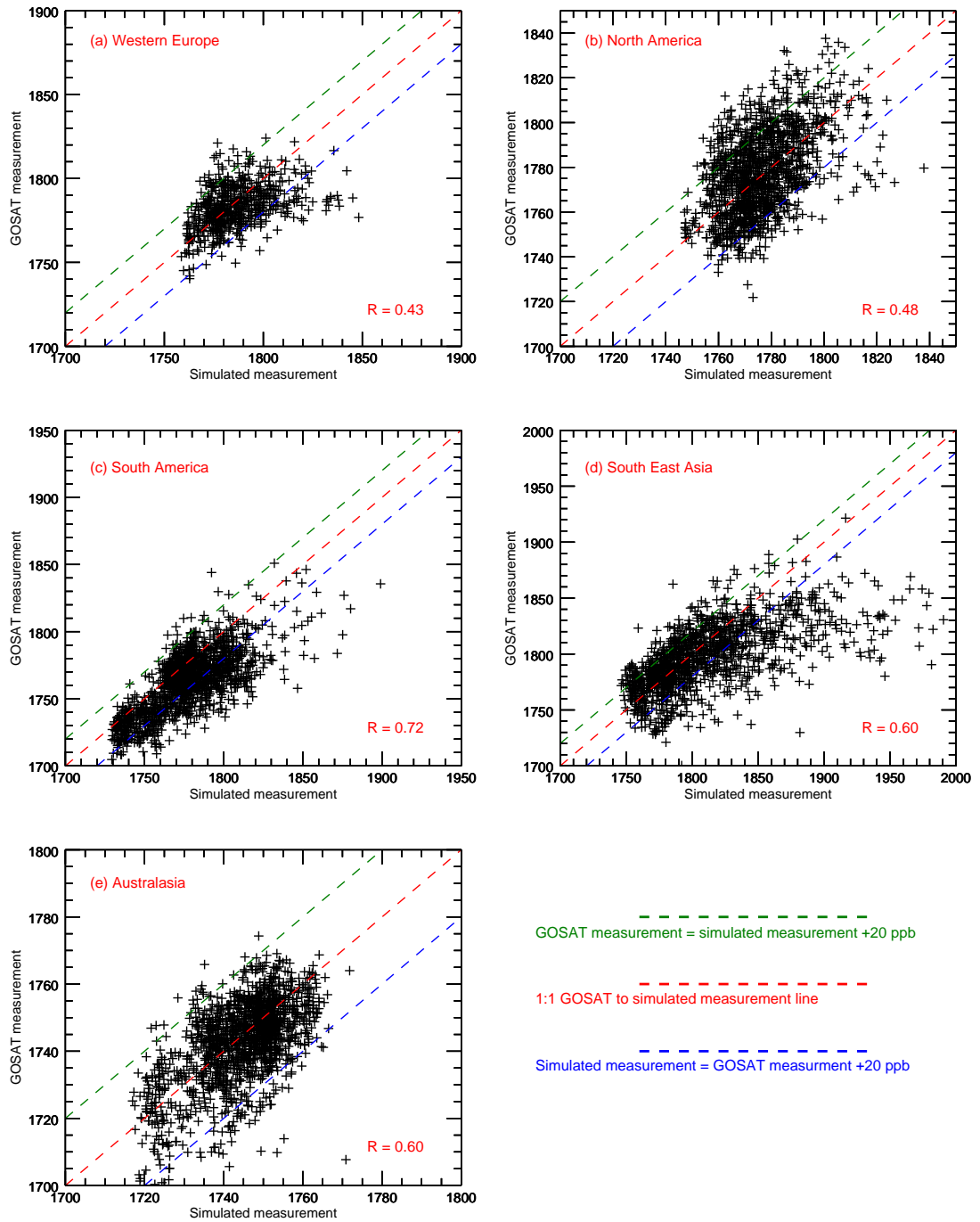


FIGURE 5.38: GOSAT observations vs simulated GOSAT measurements. All four months included in the analysis.

absolute absorption values being approximately 4 times greater in the tropics (see Figure 3.26).

South East Asia displays a clear increase in the enhancement due to wetland and rice field emissions at the latter months of the year. Bloom et al. emission inventory is modelled to contribute ~16 % to the local enhancement in June rising to ~26 % in September. The EDGAR emission inventory does, however dominate the total emissions with percentage contributions of between ~80 % and 70 % in the months of June and September. The soil is modelled to absorb approximately an average of ~-1 % of the total emissions. The fire and termite emissions are comparatively small at each corresponding inventory contributing below ~2 % of the observed enhancement.

Australia has a relatively few anthropogenic sources of CH<sub>4</sub>, as can be seen in Figure 3.24. The emission hot spots are localised mostly to the east coast, in areas with high population density. The total enhancement over the background is consistently low throughout the time scale of the study, averaging at about 7 ppbv. The anthropogenic contribution varies from the high of ~25 % in June to the low of ~14 % in September. The contribution of the Bloom et al. inventory dominates the total methane enhancement with ~70 % contribution. Termites are also modelled to be a significant source of atmospheric methane in Australia. Termites are estimated to contribute ~10 % to the local enhancement. The low total emissions also results in the soil sink being higher as a fraction of the total local flux (~-8 %). It is also expected, that fire emissions would be a high contributor of methane in Australasia. The contribution of the GFED emission inventory is ~1 % in the June, July and August. More fires in September result in the fire contribution increasing to ~5 % of the total local contribution.

### **5.6.2 Comparison of GOSAT measurements, simulated observations and the GEOSCHEM model**

In this section, the performance of the GEOSCHEM model is going to be compared against the GOSAT observations and the simulated GOSAT measurements. Figures 5.43, 5.44, 5.45 and 5.46 show the comparisons of the Eulerian model against the observation over the time frame of the simulation. As GEOSCHEM is run at a resolution of 2° latitude and 2.5° longitude, the concentration in the grid box in which the satellite takes a measurement, is taken to be used in comparisons. It is therefore expected, that the NAME method developed in this study should be able to reproduce localised spikes in observations owing to strong local emission hot spots. The Eulerian model should lose

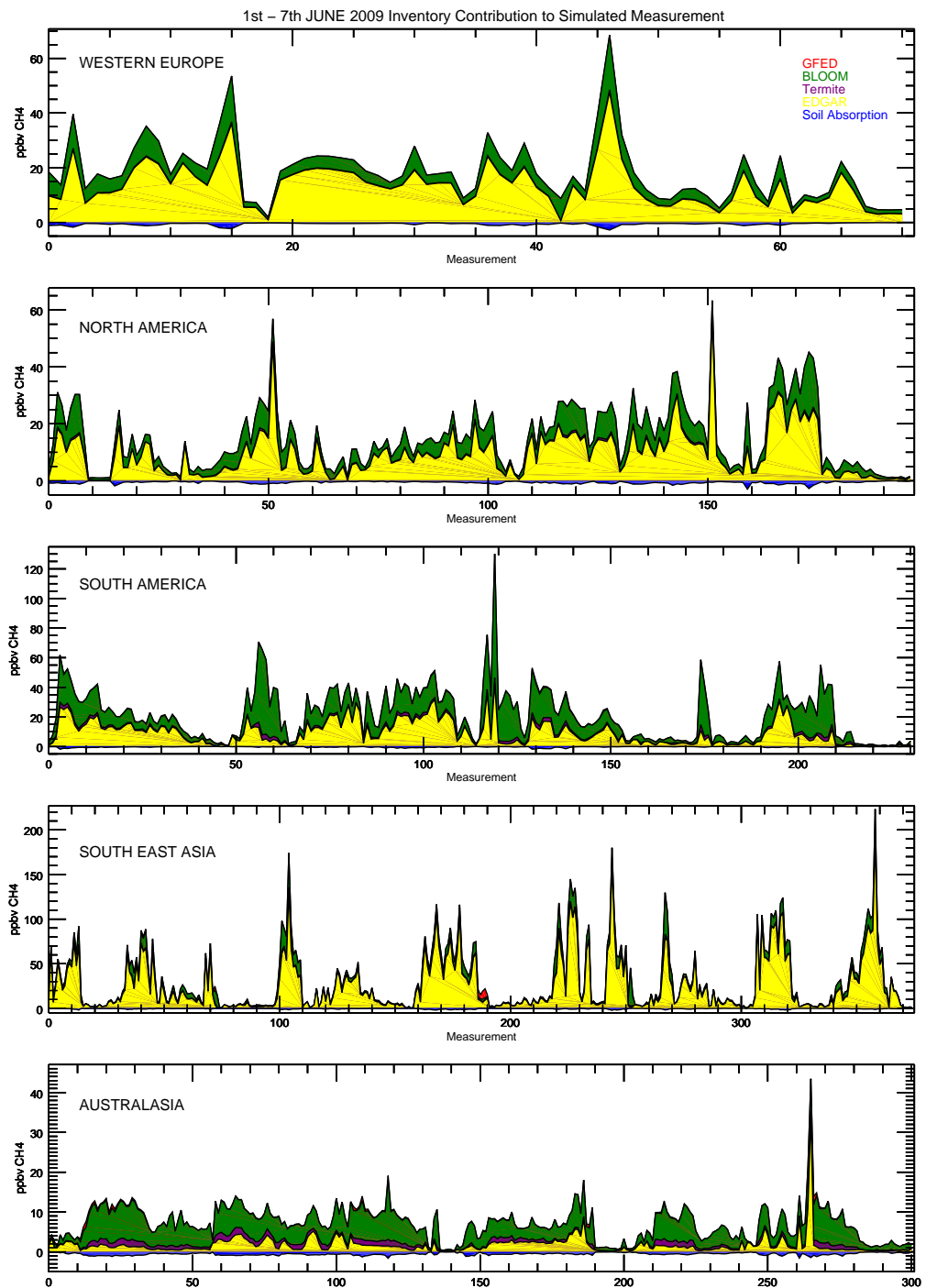


FIGURE 5.39: 1<sup>st</sup> to 7<sup>th</sup> of June, 2009 - the breakdown of the inventory contributions to the enhanced concentration over the atmospheric background. The ppbv volume enhancement by the different emission inventories is highlighted in different colours. All of the individual measurements for the week are listed here

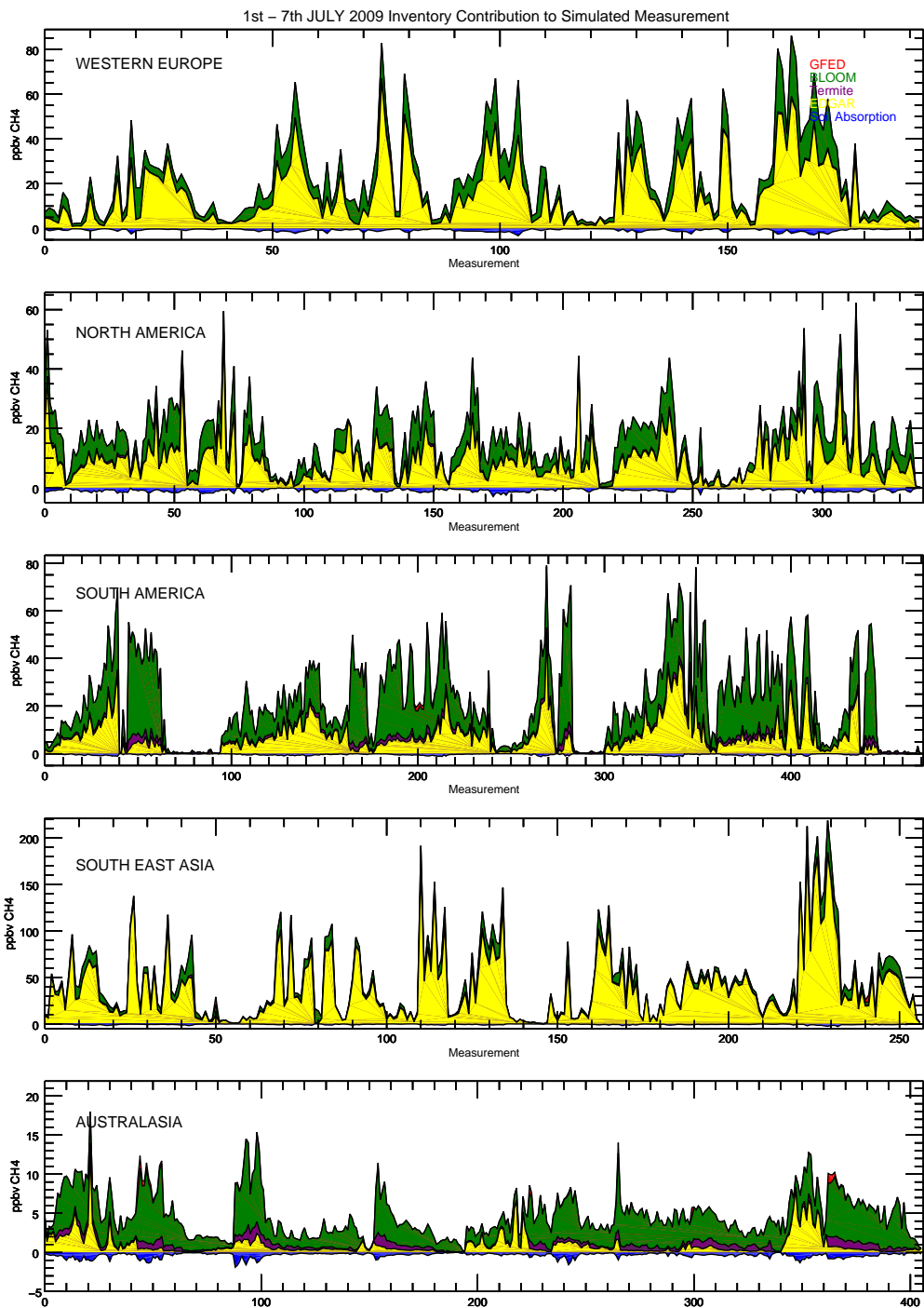


FIGURE 5.40: 1<sup>st</sup> to 7<sup>th</sup> of July, 2009 - the breakdown of the inventory contributions to the enhanced concentration over the atmospheric background. The ppbv volume enhancement by the different emission inventories is highlighted in different colours. All of the individual measurements for the week are listed here

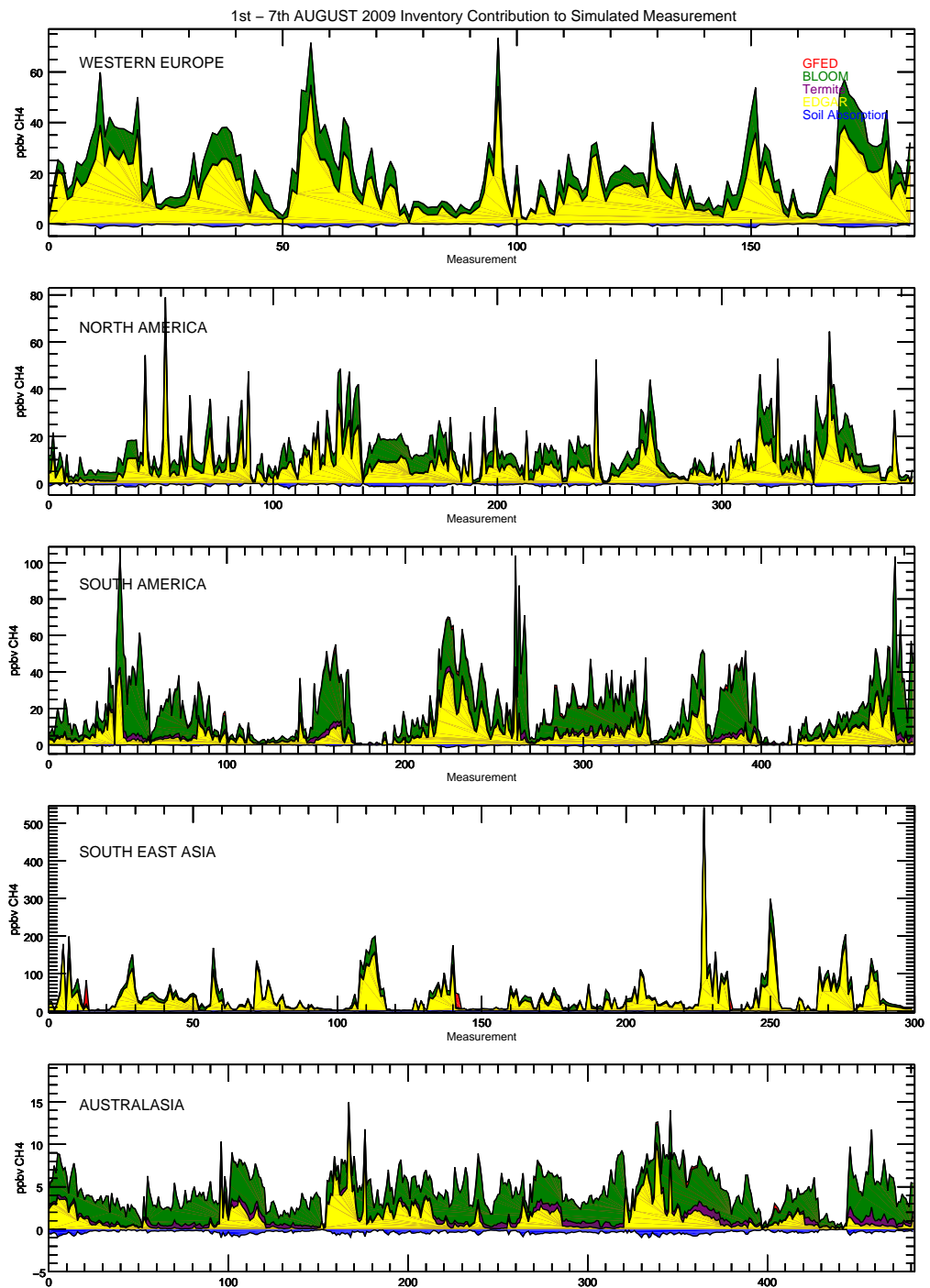


FIGURE 5.41: 1<sup>st</sup> to 7<sup>th</sup> of August, 2009 - the breakdown of the inventory contributions to the enhanced concentration over the atmospheric background. The ppbv volume enhancement by the different emission inventories is highlighted in different colours. All of the individual measurements for the week are listed here.

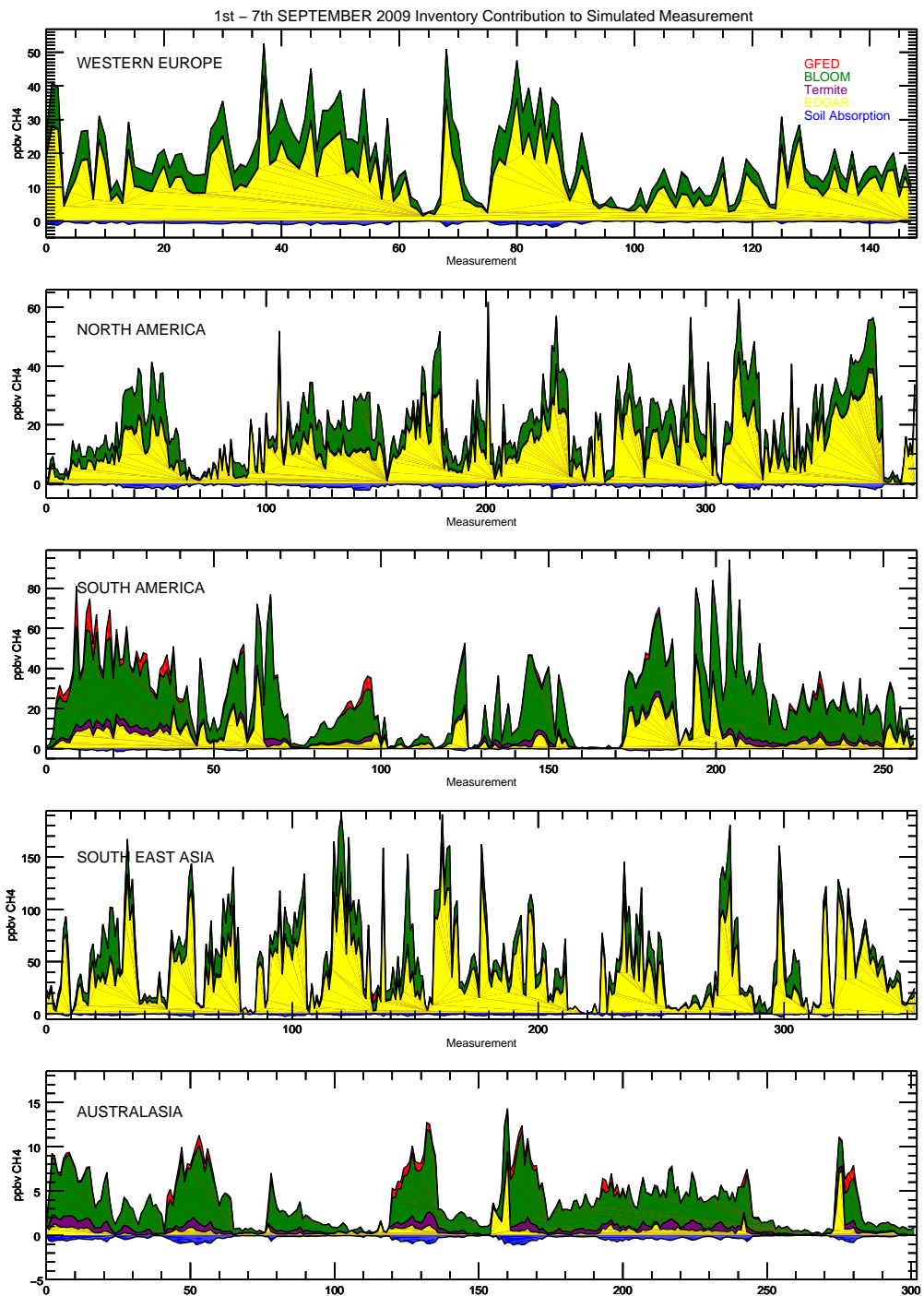


FIGURE 5.42: 1<sup>st</sup> to 7<sup>th</sup> of September, 2009 - the breakdown of the inventory contributions to the enhanced concentration over the atmospheric background. The ppbv volume enhancement by the different emission inventories is highlighted in different colours. All of the individual measurements for the week are listed here.

<b>Western Europe</b>				
	June	July	August	September
EDGAR	74.9 %	70.3 %	69.9 %	70.9 %
BLOOM <i>et.al.</i>	27.3 %	31.9 %	32.1 %	30.8 %
Termite	1.2 %	1.2 %	1.2 %	1.3 %
GFED fire	0.0 %	0.1 %	0.2 %	0.4 %
Soil Absorption	-3.4 %	-3.5 %	-3.3 %	-3.4 %
<b>North America</b>				
EDGAR	66.0 %	61.9 %	60.7 %	65.2 %
BLOOM <i>et.al.</i>	35.9 %	41.4 %	42.1 %	36.8 %
Termite	2.2 %	2.3 %	2.2 %	2.2 %
GFED fire	0.2 %	0.1 %	0.4 %	0.3 %
Soil Absorption	-4.3 %	-5.7 %	-5.4 %	-4.4 %
<b>South America</b>				
EDGAR	42.4 %	32.7 %	30.9 %	22.6 %
BLOOM <i>et.al.</i>	53.4 %	62.0 %	62.2 %	67.5 %
Termite	5.1 %	5.9 %	5.7 %	5.9 %
GFED fire	0.7 %	1.2 %	2.7 %	5.1 %
Soil Absorption	-1.6 %	-1.7 %	-1.5 %	-1.0 %
<b>South East Asia</b>				
EDGAR	82.0 %	84.9 %	78.5 %	73.3 %
BLOOM <i>et.al.</i>	16.8 %	14.6 %	19.4 %	26.2 %
Termite	1.6 %	1.6 %	1.6 %	1.8 %
GFED fire	1.0 %	0.3 %	1.8 %	0.1 %
Soil Absorption	-1.4 %	-1.3 %	-1.2 %	-1.5 %
<b>Australasia</b>				
EDGAR	25.4 %	20.7 %	30.1 %	14.2 %
BLOOM <i>et.al.</i>	69.5 %	75.4 %	67.3 %	77.5 %
Termite	11.3 %	10.9 %	9.1 %	11.0 %
GFED fire	1.9 %	1.3 %	1.1 %	5.6 %
Soil Absorption	-8.0 %	-8.2 %	-7.7 %	-8.4 %
<b>Global emissions (bottom up estimates)</b>				
	Anthropogenic sources	58.9 %		
	Wetland	38.6 %		
	Fire emissions	0.5 %		
	Termite	2.0 %		
	Soil sink	-5.0 %		

Table 5.1: The percentage contribution of a priori emission inventories to the modelled XCH<sub>4</sub> enhancement over the background.

information owing to the resulting spike in concentration being lost due to averaging over a larger geographical area.

Generally, the GEOSCHEM simulated XCH<sub>4</sub> observations are lower than the GOSAT measurements over North America and South East Asia. GEOSCHEM is in better agreement with GOSAT than the NAME simulated observations over South East Asia, especially as it does not overestimate the methane concentrations in the region. The modelled concentrations are at most ~30 ppbv lower than GOSAT inferred measurements. The NAME method on the other hand tends to simulate concentration enhancements that are at times ~100 ppbv higher than GOSAT. The magnitude in differences between the observations and NAME simulations are especially large in September (Figure 5.46). GEOSCHEM fails to capture spikes in the observed concentrations visible in Figures 5.43, 5.44, 5.45 and 5.46 over South America. This is likely an artefact resulting from running the Eulerian model at a relatively low resolution. GEOSCHEM also over-estimates the concentrations over Australasia in June (Figure 5.43), where the GOSAT-observed XCH<sub>4</sub> values are generally lower. As GEOSCHEM is used to estimate the background in all of the NAME simulated GOSAT observations, the over-estimated background values leads to errors in the simulated observations.

### 5.6.3 Comparison with TCCON sites

In this subsection, the modelled and observed XCH<sub>4</sub> values are compared to the observations from the ground network of Fourier transform spectrometers (TCCON). For more details on the TCCON measurement sites, see Chapter 2. TCCON instruments point directly at the sun and have a much higher signal-to-noise ratio than it is possible to obtain by an Earth observation instrument, such as GOSAT. The TCCON recorded XCH<sub>4</sub> values are referred to as the truth here. Figures 5.47, 5.48, 5.49, 5.50 show the time series of TCCON station measurements in the regions studied here. South America does not have any TCCON sites in the year of 2009 and therefore comparisons with ground data cannot be carried out for this region.

Figure 5.47 shows the measured CH<sub>4</sub> concentrations at the Parkfalls and Lamont TCCON sites. The gaps in any measurements are due to the ground instrument not being operational. The synthetic GOSAT measurements are systematically lower than the Parkfalls observations in June, July and August, 2009. In June, the value is ~30 ppbv lower than the observation at the TCCON site. The actual GOSAT-measured XCH<sub>4</sub> is higher than the Parkfalls TCCON retrieved value. The simulation is closer to the truth in the month of September, where the concentration is underestimated by ~30 ppbv.

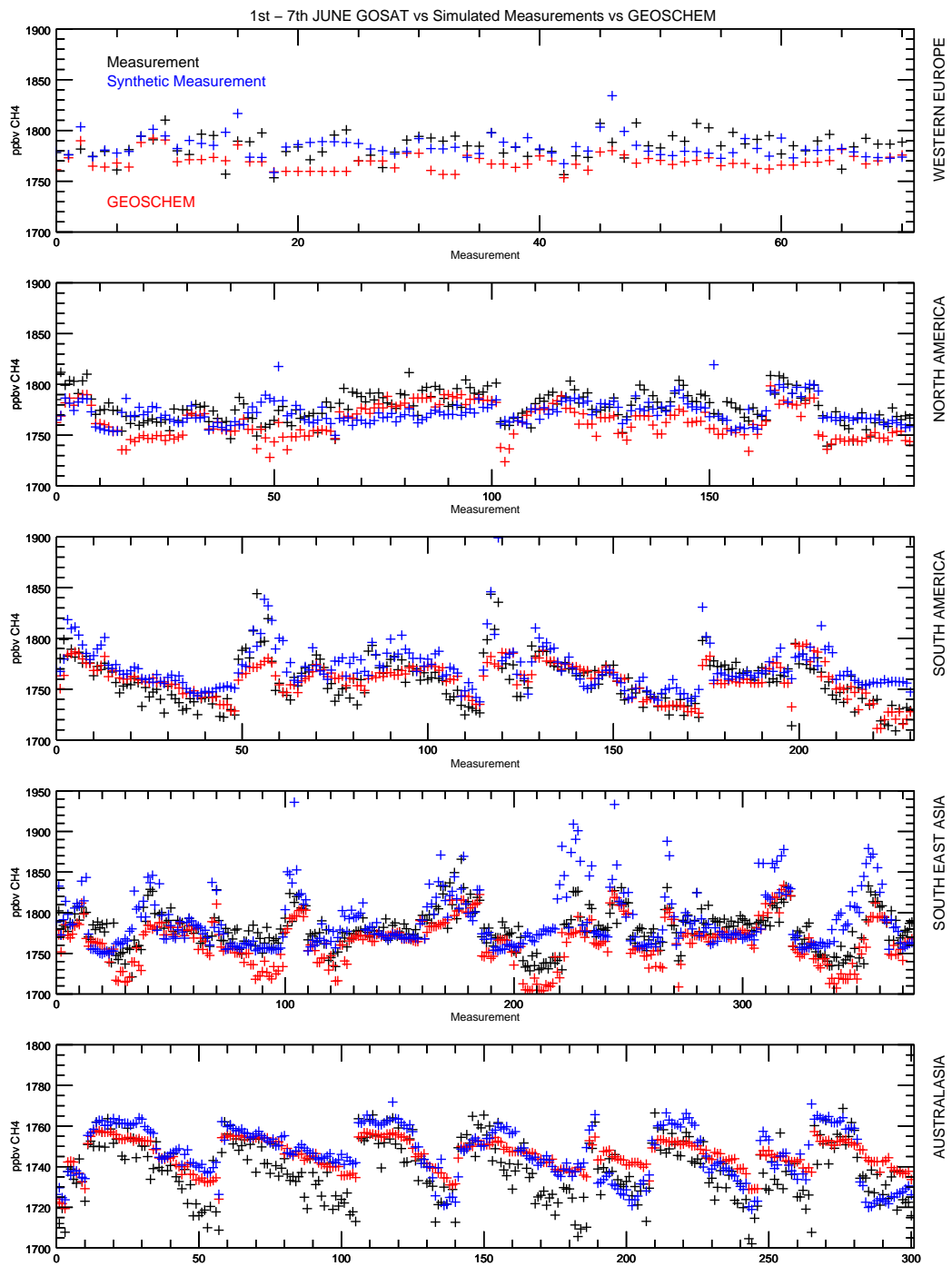


FIGURE 5.43: June 1<sup>st</sup> - 7<sup>th</sup>, a comparison of the GOSAT measurement with the simulated GOSAT observations and the GEOSCHEM model.

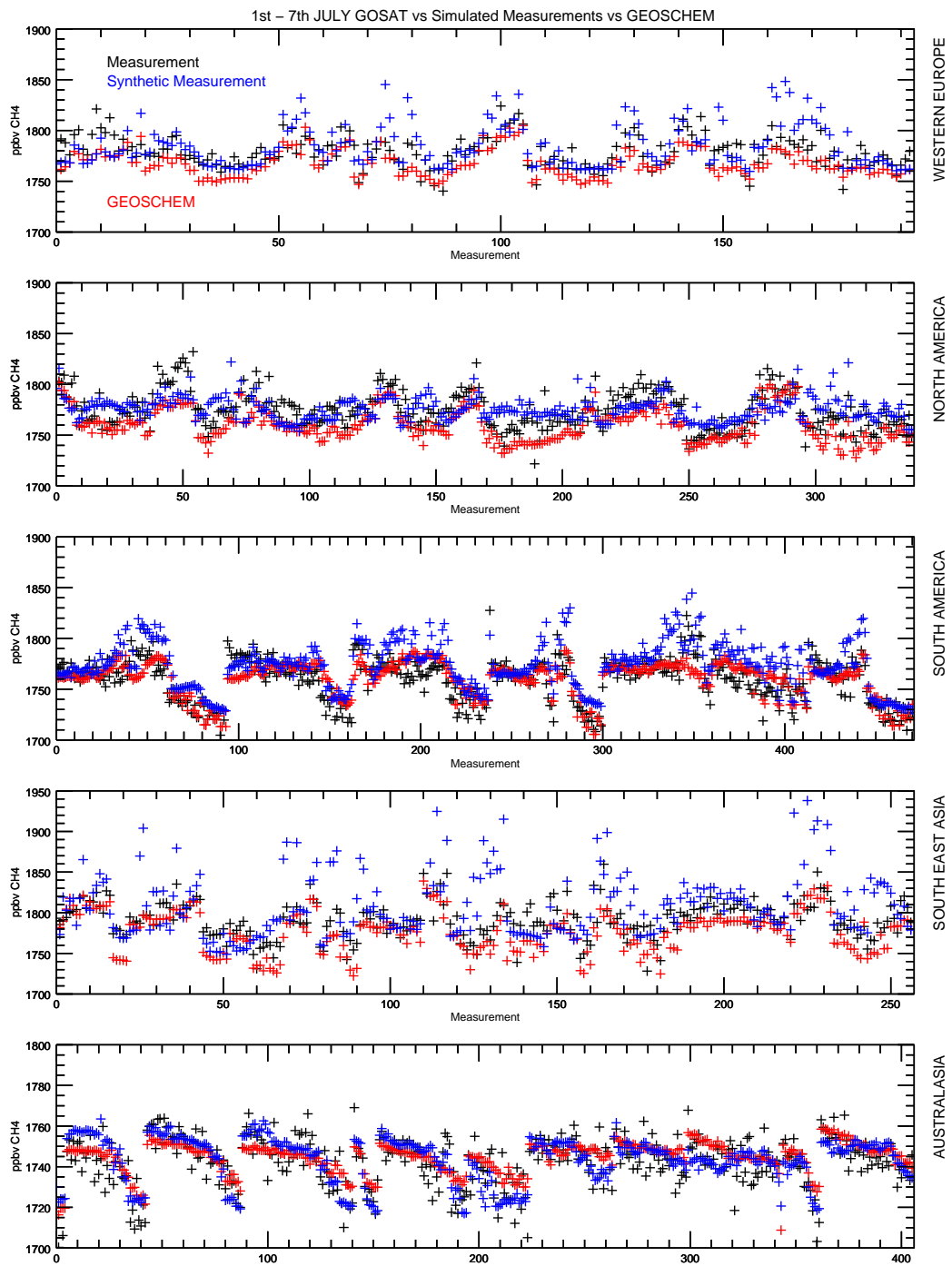


FIGURE 5.44: July 1<sup>st</sup> - 7<sup>th</sup>, a comparison of the GOSAT measurement with the simulated GOSAT observations and the GEOSCHEM model.

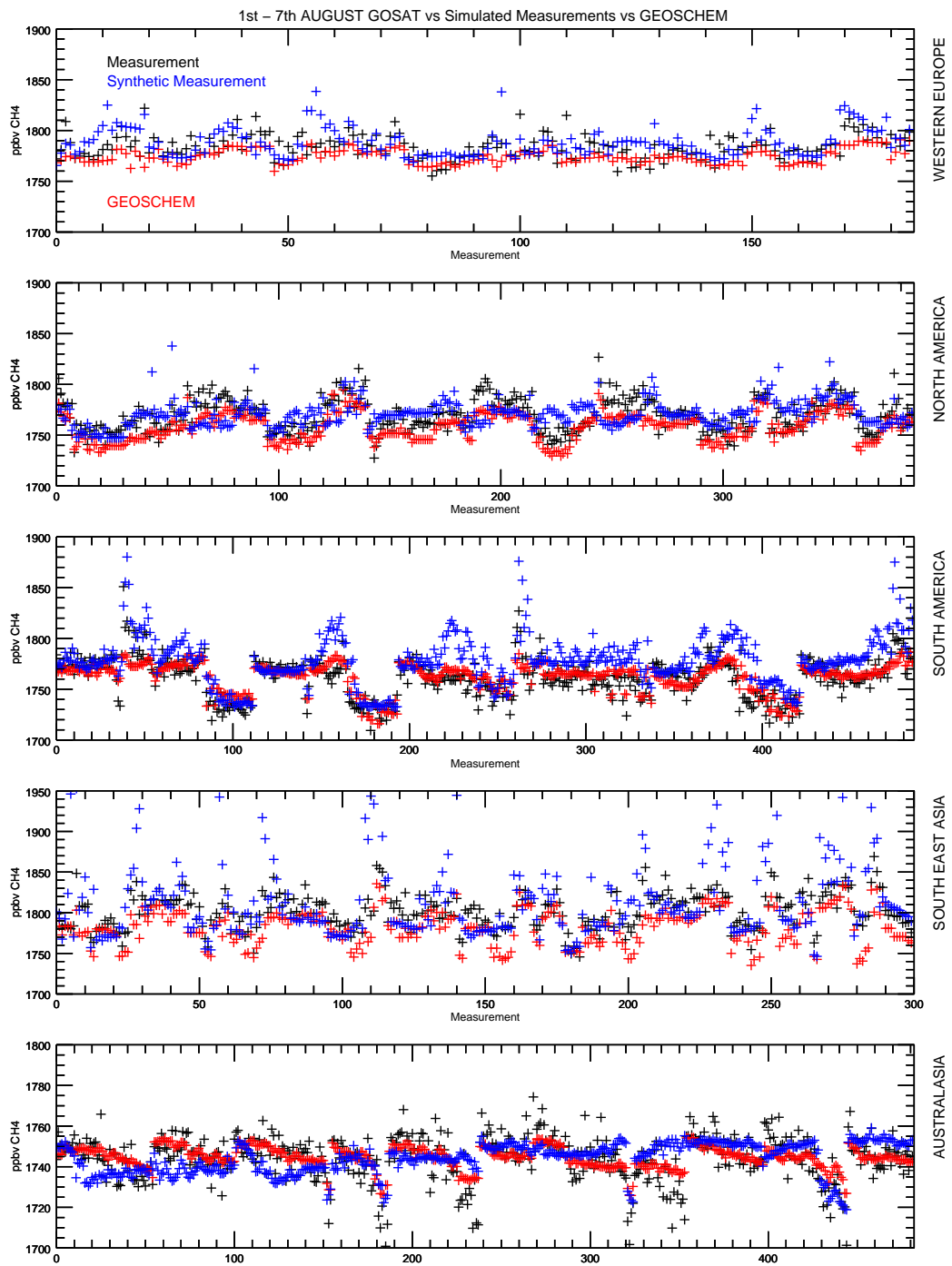


FIGURE 5.45: August 1<sup>st</sup> - 7<sup>th</sup>, a comparison of the GOSAT measurement with the simulated GOSAT observations and the GEOSCHEM model.

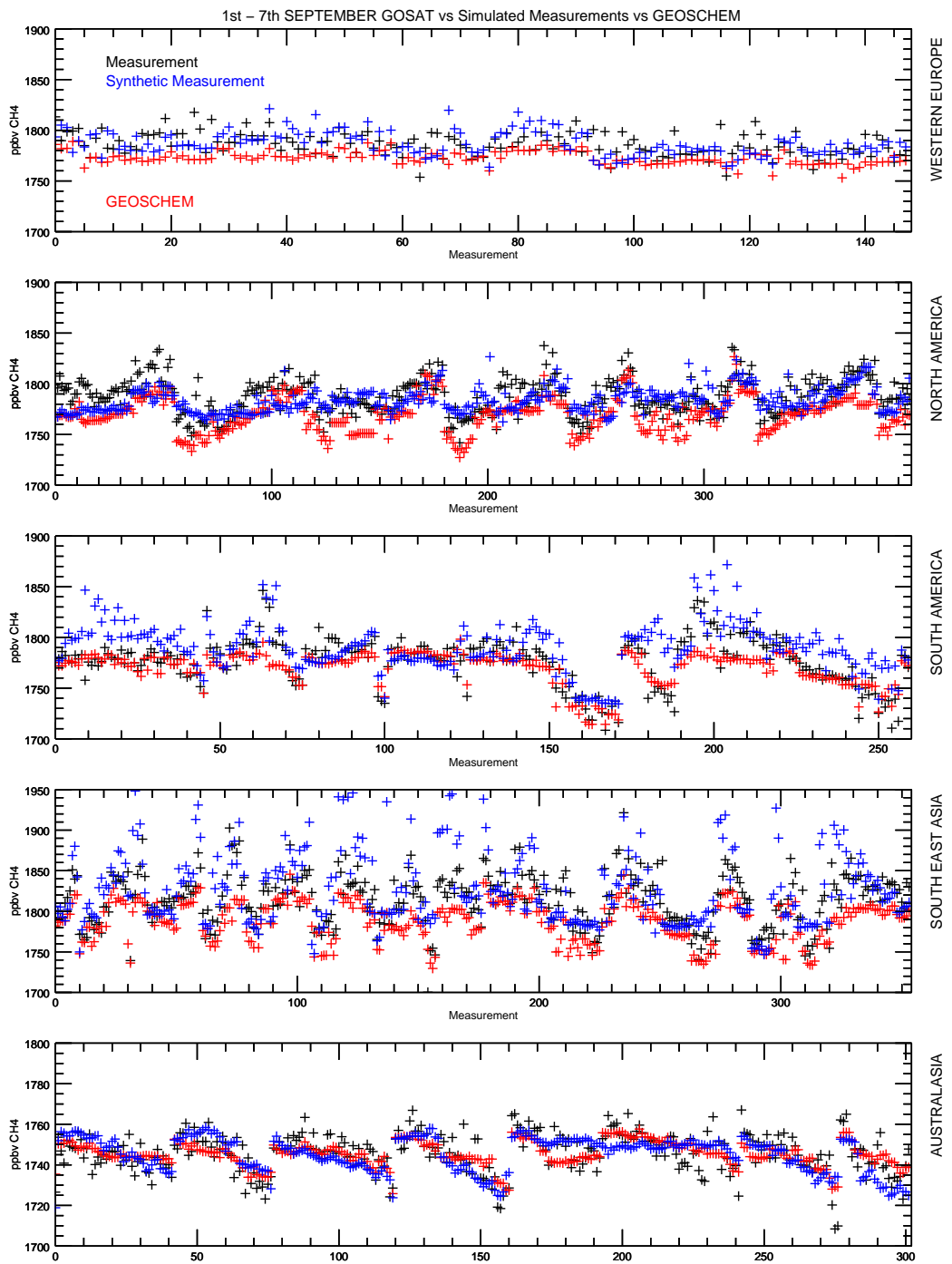


FIGURE 5.46: September 1<sup>st</sup> - 7<sup>th</sup>, a comparison of the GOSAT measurement with the simulated GOSAT observations and the GEOSCHEM model.

The simulated measurements compare more favourably with the Lamont TCCON site measured XCH<sub>4</sub> values. The modelled concentration is within the scatter of the Lamont observations in June, although only the space-borne data on the 6<sup>th</sup> of June, 2009 is available. The synthetic values compare well with the Lamont observations in July, but tend to overestimate the XCH<sub>4</sub> on the 5<sup>th</sup> of August and the 4<sup>th</sup> and the 7<sup>th</sup> of September.

Figure 5.48 displays the measured CH<sub>4</sub> time-series at the Tsukuba TCCON site. The instrument was not operational in the first 7 days of July and August, 2009, therefore no comparisons can be made in these months. The available TCCON data is also very sparse in June and September, making it difficult to draw any conclusion on the accuracy of the simulations. The synthetic observations are within the range of TCCON measurements on the 2<sup>nd</sup> of September and comparisons in the latter days of the week are more problematic due to there being no GOSAT and Tsukuba TCCON measurements taken on the same day. Assuming that the concentrations over the week do not vary significantly, interpolation from the TCCON measurements on the 6<sup>th</sup> and 7<sup>th</sup> of September would suggest that the simulations overestimate the methane XCH<sub>4</sub> by ~20-30 ppbv. It is desirable to investigate the performance of the simulation in a region, where there is the greatest disagreement between the actual and the simulated GOSAT measurement. The Tsukuba site is located at the edge of the simulation domain for South East Asia and is not under the direct influence of rice fields or wetlands.

The TCCON sites in Europe also do not provide continuous uninterrupted measurement time-series in the time-scale of the analysis. Figure 5.49 displays the measured time series at the Bialystok, Bremen and Garmisch TCCON sites. The simulated (and GOSAT) measurements are higher than the observations at the Bialystok site in June and the 3<sup>rd</sup> of August, with the remainder of the simulations being in a better agreement (within ~20 ppbv). The Bremen TCCON site has a very few observations in the first week of all of the months analysed here. The observations on the 5<sup>th</sup> of August are within ~20 ppbv of the simulations. However, the total number of GOSAT and TCCON observations is too low to draw any definite conclusions. The observations at the TCCON sites at Wollongong and Darwin are also too sporadic for any meaningful analysis.

As the number of observations in most of the TCCON sites is very few, definite conclusions cannot be drawn on the accuracy of the simulations based on the analysis in this section. It would be advantageous to run the simulations for a longer time period (a whole month, for example) to increase the possibility of the TCCON data being available within the time frame of the experiment. The results are also uncertain due to the relatively loose co-location criteria used to select the satellite measurements that are thought to be representative of the observations at the TCCON sites. It is assumed that the col-

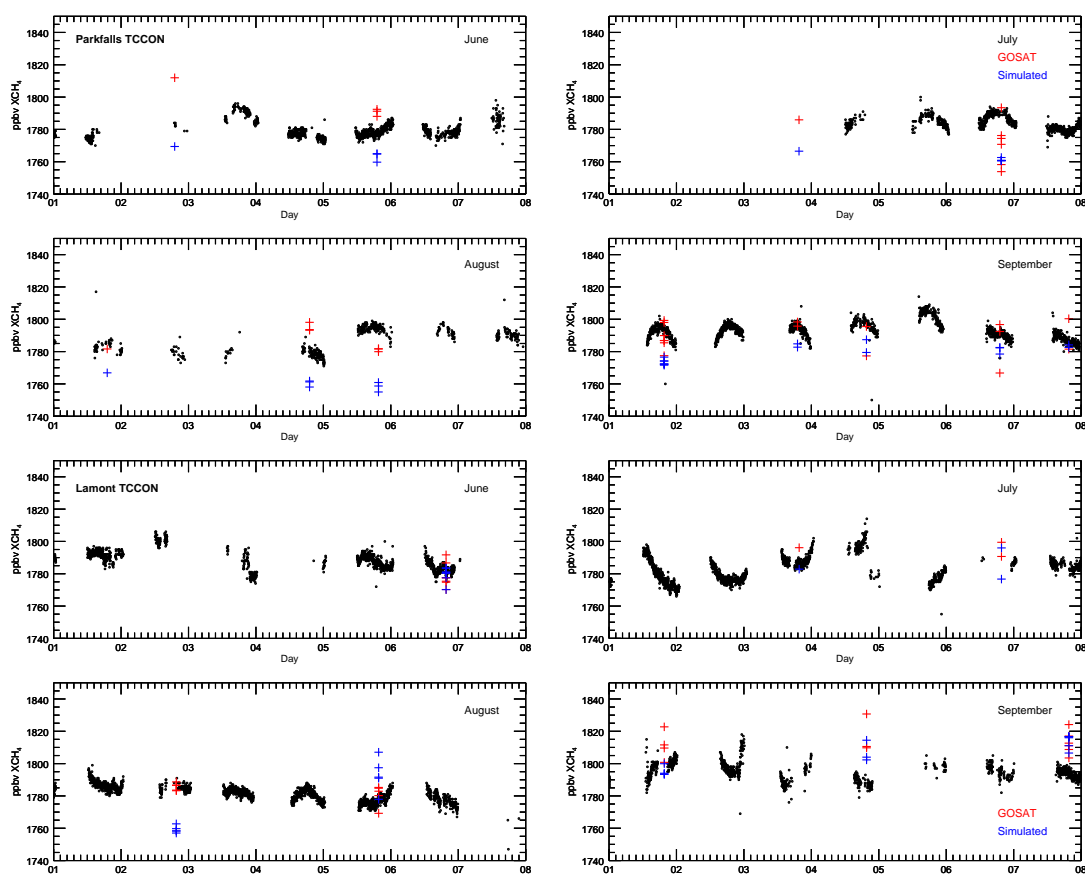


FIGURE 5.47: North America - The time-series of TCCON measurements in the North America region (Parkfalls and Lamont). The actual GOSAT measurements within  $2^\circ$  of the measurement site are overplotted in red and the simulated measurements in blue.

umn atmospheric  $\text{CH}_4$  concentrations are identical within the  $2^\circ$  of the TCCON site. It would be desirable to simulate the TCCON observations utilising the forward model used in this chapter. The comparisons between the simulated observation and the more accurate TCCON measurements would allow us to critically analyse the performance of the forward model.

## 5.7 Conclusion

In this chapter, the forward model developed in Chapter 4 is utilised to simulate GOSAT observations over a selected number of regions. The specific regions are chosen to be under the influence of emissions from various sources. Measurements over Western Europe, for example, are sensitive to anthropogenic emissions, whilst those over South America are more affected by wetland fluxes. This allows us to test the performance

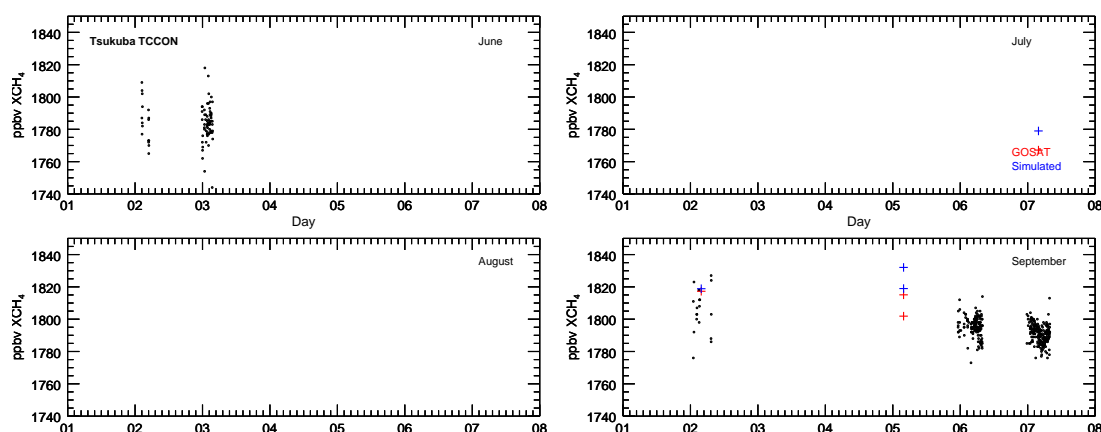


FIGURE 5.48: South East Asia - The time-series of TCCON measurements in the South East Asia region (Tsukuba). The actual GOSAT measurements within  $2^\circ$  of the measurement site are overlotted in red and the simulated measurements in blue.

of the forward model under various conditions. The main scientific development in this chapter is the coupling of the Lagrangian model to a GEOSCHEM model to obtain the atmospheric background, which is then added to the modelled enhancement when calculating the synthetic observations.

the methods of calculating the background in previous studies have been subjective, relying on measurements from coastal station measurements taken under specific meteorological conditions (Manning et al. (2011)) or iteratively retrieving the baseline as another unknown in the inversion (Stohl et al. (2009)). In this chapter, a method was developed that allows for the background to be obtained objectively, for any region under investigation. This method could potentially be used at any time period and uses a Lagrangian model to take into account the atmospheric transport of the air mass into the domain being simulated. The transport model is, in essence, asked to output the residence time of the tracer particles in the border region of the domain. The output is known as the baseline, which together with the GEOSCHEM model fields, is used to estimate the  $XCH_4$  entering the area. Eulerian global atmospheric transport models suffer from numerical diffusion, meaning that they are poor at representing sub-grid processes, a disadvantage which the Lagrangian models do not display. The use of a nested Lagrangian-Eulerian system allows us to generate the global background concentrations of  $XCH_4$  from the Eulerian model, which are then used as the baseline for the Lagrangian model. For the Eulerian model to be used in calculating the baseline, the CTM concentration fields and the GOSAT observations would, ideally, be identical. This is not the case for GEOSCHEM and GOSAT as described in Section 3.6.1. The miss-match between the GOSAT observations and the model data is highly variable, both in space and

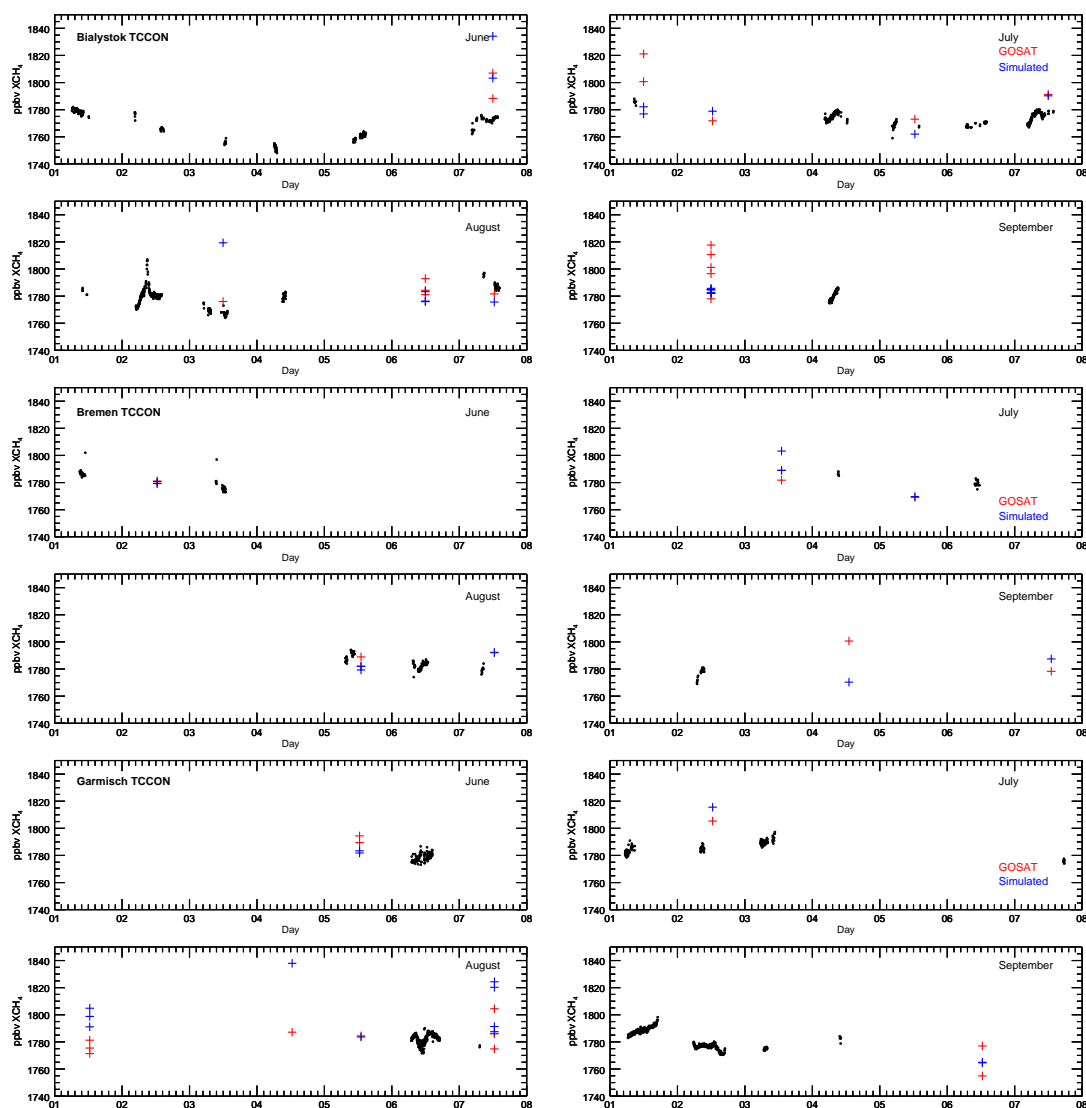


FIGURE 5.49: Western Europe - The time-series of TCCON measurements in the Western Europe region (Bialystok, Bremen and Garmisch). The actual GOSAT measurements within  $2^\circ$  of the measurement site are overlotted in red and the simulated measurements in blue.

time. An offset would ideally be introduced to match the datasets, but this is not done in this study. A mean GOSAT  $XCH_4$  within a GEOSCHEM grid box could be calculated and an offset added to the chemical model data to match the space-borne observations. This particular method would introduce its own problems, as GEOSCHEM is run at a relatively low resolution of  $2.5^\circ \times 2^\circ$ . There would ideally be a number of observations within the GEOSCHEM grid area, sampling different regions. However, owing to the sampling pattern of GOSAT, complete sampling of a GEOSCHEM grid box is not possible. Any applied offset therefore might in itself introduce biases owing to the limited data

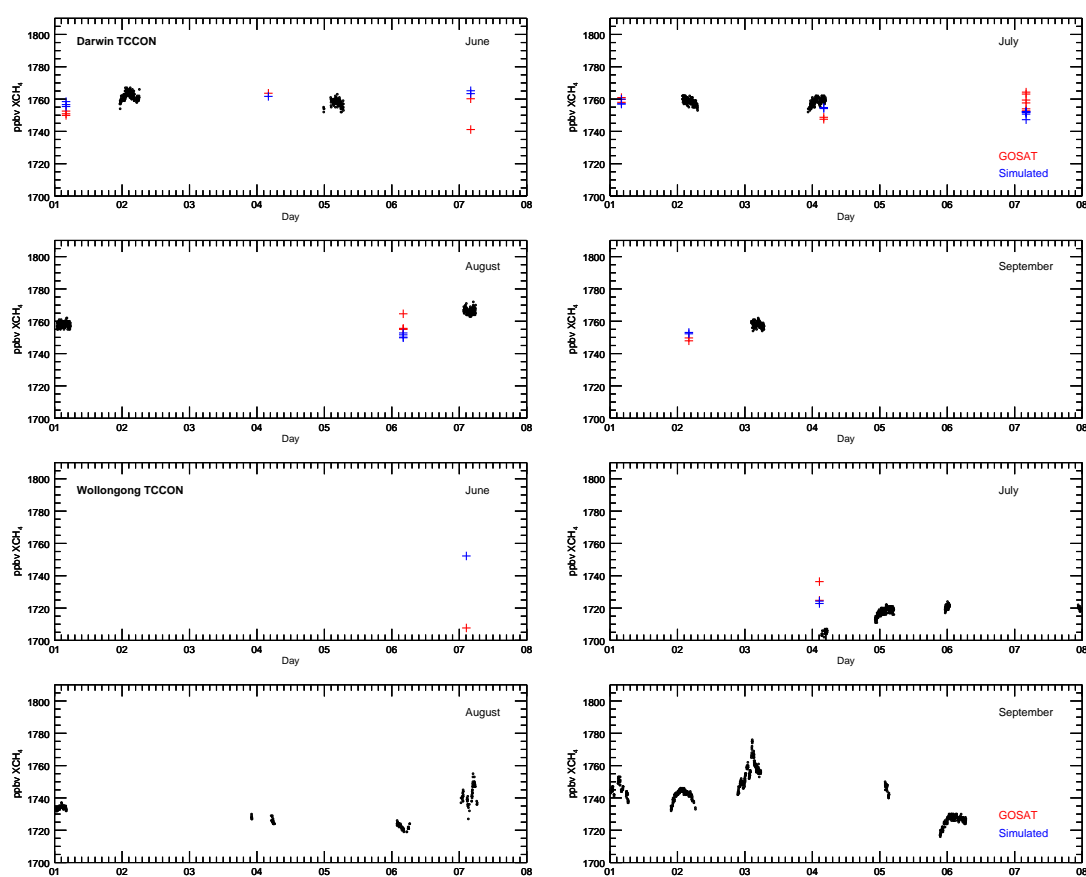


FIGURE 5.50: Australasia - The time-series of TCCON measurements in the Australasia region (Darwin and Wollongong). The actual GOSAT measurements within  $2^\circ$  of the measurement sites are overlotted in red and the simulated measurements in blue.

used to calculate the offset. The GEOSCHEM model is found to simulate column concentrations that are generally lower than those using the NAME method. The Eulerian model is also not able to simulate spikes in the observed concentration (South America) due to the relatively coarse geographical resolution of the model. Any enhancement is averaged out over the grid cell.

The background concentrations calculated using this method are overestimated. In a number of cases (Figure 5.29, South East Asia), it is found that the GOSAT observations are significantly lower than the calculated background. The addition of the modelled concentration enhancement to the calculated baseline leads to a high difference between the simulations and the GOSAT measurements. A modification to the background retrieval is suggested, although it cannot be implemented here due to time constraints. In the current set-up, the particles released into the Lagrangian model atmosphere are free to leave and re-enter the simulation domain. This can result as the tracer particles contributing to the background calculation twice, by having an impact on two different

boxes. The CTM concentration grid box would then be taken into account twice, when calculating the baseline. A solution would be to kill the particles, as they exit the domain. This would ensure that the contribution to the baseline by a particle would only be counted once.

The calculated Pearson's correlation coefficients between GOSAT XCH<sub>4</sub> observations and the modelled values are  $r=0.43$  over Western Europe,  $r=0.48$  over North America,  $r=0.72$  over South America,  $r=0.60$  over South East Asia and  $r=0.60$  over Australasia. The fraction contributions from the different emission inventories to the concentration enhancements are also calculated. The results show that in general, the modelled XCH<sub>4</sub> values are in a better agreement with observations where natural emissions dominate. The regions with high anthropogenic emissions result in observations, that correlate poorly with GOSAT data (Western Europe and North America). The modelled values are also found to be considerably larger than the observations in South East Asia, in the later months of the year. This could be owing to the emission inventories in South East Asia overestimating the emissions in the region.

The GOSAT observations and the modelled XCH<sub>4</sub> have been compared to TCCON measurements and the GEOSCHEM model. There are not enough TCCON observations in the time frame of the study to draw any conclusions on the accuracy of the simulations. It is also disappointing that no TCCON sites exist in South America or China, where large wetland emissions are predicted and observed. In the future, it would be desirable to simulate the TCCON observations utilising the forward model developed here. This removes the need to have a so-called 'co-location' criteria, where the column concentrations within a certain distance of the TCCON site are assumed to be representative at the site.

The emissions by termites can be assumed to be overestimated in the simulations in this chapter, as termites are thought to emit 2-22 Tg year<sup>-1</sup> according to the recent review by Kirschke et al. (2013). The total emissions by termites as used in this work, as calculated by Fung et al. (1991), is 50 Tg year<sup>-1</sup>. It would be possible to scale the Fung et al. (1991) flux field down to the current lower estimates, however the GEOSCHEM model is also run assuming the termite emission value of 50 Tg year<sup>-1</sup>. It was therefore decided to keep to the provided estimates, in order to avoid introducing additional biases. With the exception of Australia, termites do not contribute significantly to the local enhancements in the other regions simulated here. Assuming that the termite emissions over Australia were to be halved, the contribution of the termite emissions to Australian enhancements would be reduced from ~10% to 5%.

## Chapter 6

### Conclusions

Methane ( $\text{CH}_4$ ) is the second most important anthropogenic greenhouse gas after  $\text{CO}_2$  (Nykänen et al., 2002; Shine et al., 2005). In this study, the UK Met Office Lagrangian Atmospheric Modelling Environment (NAME), is used to link satellite  $\text{CH}_4$  observations to the ground level  $\text{CH}_4$  fluxes. A number of previous studies have used Lagrangian dispersion models for inversions. NAME, specifically, has been used to investigate the emissions of various gases by Manning et al. (2003) and Manning et al. (2011). Most of the existing, studies where a Lagrangian dispersion model is used, including Stohl et al. (2009), Kort et al. (2008) and Lin et al. (2004), run it in backwards, in a so-called 'receptor-oriented' mode. This is owing to increased computational efficiency, when there are more source grid boxes present than there are receptors (measurement locations). Various mathematical methods are used to estimate the fluxes. Manning et al. (2011) uses an iterative best-fit technique, which is a simulated annealing method, to derive regional emission estimates for various gases. The method does not rely on a priori, calculates the flux map from the observations and NAME output alone. Manning et al. (2011) uses only the data from a single measurement station, Mace Head. Stohl et al. (2009) utilises measurements from more stations, as well as an a priori. This thesis builds and improves on such work, exploiting the advantages of the Lagrangian models (such as computational efficiency and high resolution) with important additional developments.

The objective of this work was to develop a high-resolution inversion algorithm to invert space-borne column  $\text{XCH}_4$  observations utilising a Lagrangian dispersion model to simulate transport from the emitters to the observation location. Space-borne instruments have a number of advantages over in-situ measurement systems, as used in the studies by Stohl et al. (2009) and Manning et al. (2011). Surface sites are accurate but geographically sparse. The spatial distribution of these in situ measurement sites there-

fore leaves large parts of the globe poorly sampled. Space-borne instruments can fill in the measurement gaps by providing high-density observations over most of the Earth's surface. The space-borne measurements, in combination with in situ observations, can help to constrain the highly uncertain CH<sub>4</sub> fluxes. Column observations from instruments, such as SCIAMACHY and GOSAT, have already been used in inversion studies, helping constrain the emissions of greenhouse gases (Bergamaschi et al., 2013; Fraser et al., 2013). The existing studies typically run the global Eulerian transport models at a relatively low horizontal resolution, such as 4° × 6° in the case of Bergamaschi et al. (2013) or 2° × 2.5° in the case of Fraser et al. (2013). In building the inversion system, this thesis aims to answer a number of questions:

- *Can a high resolution inversion system be set up to use a Lagrangian model dispersion model in conjunction with space-borne XCH<sub>4</sub> observations?*

In this study, a Bayesian approach as described by Rodgers (2000), is adapted to calculate the CH<sub>4</sub> fluxes from atmospheric XCH<sub>4</sub> observations. The inversion algorithm is tested on modelled data from a Mace Head site, simulated using an EDGAR emission inventory as an assumed flux map. To allow the algorithm to accept column measurements, modifications to the NAME set-up have to be made. A satellite, in contrast to an in situ site sampling air at a single location, observes an integrated column concentration of methane. The air arriving at different column altitudes might be under the influence of different meteorological conditions and potentially, sources. To best represent the column in the NAME model atmosphere, the tracer particles are released into the NAME model atmosphere at different heights (Section 3.4). The NAME outputs are pressure-weighted and then can be used in the inversion system. The high-resolution algorithm has therefore been successfully set up to use a Lagrangian dispersion model in conjunction with space-borne observations.

- *Can GOSAT be used to constrain high-resolution CH<sub>4</sub> emission inventories over the UK?*

GOSAT data cannot be used to constrain CH<sub>4</sub> emissions when the model is run at a high resolution owing to the lack of measurements in the time period studied here. There are only 12 GOSAT retrieved observations for the whole of August, 2009 over the UK. 12 measurements are too few to constrain CH<sub>4</sub> flux uncertainties at a requested 0.5° resolution. The inversion was instead carried out with simulated GOSAT-like instrument data. The results showed that the algorithm is not able to reliably invert the fluxes over

the poorly sampled regions, further away from the British Isles (Section 4.3). It was decided to combine all of the ocean grid boxes and mainland Europe boxes into a single mean flux values to be retrieved. The simulation assumed a number of observation error scenarios, including an error of 20 ppbv, which represents a typical GOSAT error. Simulations were carried out, with varying number of observations removed from the inversion. This removal of data simulates cloud cover or any other factor that might result in the observation not being obtained. Assuming an observation error of 20 ppbv, an error reduction, when 16 daily measurements are used in the inversion, are found to be approximately 2% for inversions at a spatial resolution of  $0.5^\circ$  and ~6% for  $1.0^\circ$  (~0.98 and ~0.94 respectively). Utilising the full mesh of 166 daily measurements in the inversion decreases the error reduction value at  $0.5^\circ$  to a 23% reduction in error (a total error reduction of 0.87 for the region is achieved). As expected, minimal flux constrains can be achieved at a desired spatial resolution of  $0.5^\circ$ . The low error reductions achieved, are despite the number of observations simulated in this study being over-estimated compared to what can be realistically obtained by GOSAT over the the British Isles and Ireland. The results suggest that GOSAT is better suited for regional or continental scale  $\text{CH}_4$  flux studies.

- *How well can future instruments, such as Sentinel-5 Precursor and CarbonSat constrain  $\text{CH}_4$  emissions inventories over the UK?*

The ability of the inversion algorithm to retrieve the fluxes over the region depends on a number of factors, such as the number of observations over a region, the random observation measurement error and the spatial resolution of the inversion. This study quantified the ability of the inversion algorithm to reduce the uncertainties in the flux as a function of these factors. As was shown by the results of the theoretical study in Chapter 4, a GOSAT-like instrument alone cannot be used to reliably constrain the fluxes over the British Isles at a resolution of  $0.5^\circ$  or  $1.0^\circ$ . This is owing to the low measurement precision and the limited number of measurements over the region.

Next, simulations were carried out to determine how well Sentinel-5 Precursor and CarbonSat instruments will be able to decrease the uncertainties of  $\text{CH}_4$  emissions over the simulation domain. The number of measurements the future remote sensing instruments are expected to obtained are higher than the current ones. This is owing to higher resolution of measurement footprints. CarbonSat is expected to have a ground pixel size of 2 x 3 km whilst Sentinel-5 Precursor is expected to have a ground pixel size of 7 x 7 km. The inversion calculation simulating the performance of the future instruments was carried out by computing a reduced measurement error of all of the measurements that

would be obtained in a NAME modelled grid box. The important factors, such as the solar zenith angle, cloud cover and the instrument orbits, were all taken into account in the calculation. Two different mathematical methods were then used to calculate the reduced measurement error. In the initial tests, it was assumed that the measurement errors were not correlated. This is of course unreasonably optimistic, resulting in combined measurement errors of below 1 ppbv. A more realistic method assumes that the error can only be reduced to an inherent threshold, where adding more observations results in a negligible reduction in combined observational error. The results were obtained for two months, January and July, 2011. The two months are representative of the different cloud cover, SZA and fluxes that the instrument could be expected to be under the influence of in the northern hemispheric winter and summer. It is shown that Sentinel-5 Precursor can reduce the flux uncertainty by ~30% over England and Wales in July with the remaining regions achieving a reduction of ~8-14%. In contrast, CarbonSat error reduction values are expected to range from 3% to 18%. The study has shown, that the higher precision XCH<sub>4</sub> measurements offered by CarbonSat and Sentinel-5 Precursor, will allow for the flux uncertainties to be reduced over Britain.

- *How well do the synthetic GOSAT measurements modelled utilising the forward modelling component of the inversion framework compare against Leicester University retrieved XCH<sub>4</sub> data?*

The synthetic and the Leicester retrieved XCH<sub>4</sub> values display varying degrees of correlation, varying spatially and temporally. The simulations show that in general, the modelled XCH<sub>4</sub> values are in a better agreement with observations, in which natural emissions dominate. The regions with high anthropogenic emissions result in simulated observations that correlate poorly with GOSAT data (Western Europe and North America). The modelled values are also found to be considerably larger than the observations in South East Asia, in the later months of the year. It is difficult to validate the synthetic observations owing to the lack of TCCON observations in the time period of the simulations. The developed system offers a number of advantages over Eulerian models when simulating observations. It allows us to perform high resolution studies off-line, tailoring the study to a specific region of interest. As can be seen in Section 5.6.2, Eulerian global models, which are run at low resolutions, fail to capture localised enhancements in observed concentration due to methane emission hot spots.

The central challenge of this work is that of calculating the background. In this study a method utilising the GEOSCHEM model is developed, although the resulting inferred background values are at times higher than the GOSAT observations. A modification

to the background retrieval system is suggested in Section 5.6. The miss-match could be owing to the particles being counted twice when leaving the domain. It could be desirable to remove the tracer particles from the NAME simulation, once they leave the domain.

## **6.1 Future work and potential applications**

The spatial and temporal variability of CH<sub>4</sub> fluxes are currently not well understood (Bloom et al., 2010; Fiore et al., 2006; Kai et al., 2011). Emissions are especially uncertain for important natural sources, such as wetlands (Bloom et al., 2010). Therefore inversion studies are crucial for progressing our understanding of these uncertainties. The inversion algorithm described in this thesis, allows for monitoring of CH<sub>4</sub> emissions, both natural and anthropogenic and allows for verification of existing inventories. The monitoring of fugitive methane emissions from natural gas production from recent emergence of fracking and shale gas, or emissions from the melting methane hydrates owing to climate change, are notably of current scientific interest. Existing instruments, such as GOSAT, are not sensitive enough to quantify the emissions of individual sources. The large measurement footprint, in combination with a high measurement error, make the instrument more suitable for regional or continental-scale inversion studies. CarbonSat and Sentinel 5-Precursor will have a smaller measurement footprint and provide more and higher quality data allowing us to potentially monitor individual methane hot-spots. The future instruments will certainly be able to constrain the methane fluxes to a degree, that was not possible with the current and past instruments.

The forward model, described in Chapter 5, can also be a useful investigative tool. The forward model can, with minimal modification, be used to model space-borne instrument observations using any emission inventory as the potential source. It allows us to estimate the contribution to the enhanced concentrations from the different input sources, providing the investigator with a break-down of the contribution to the local by the different inventories. Once the changes to the background estimation system are implemented, a study critically evaluating the emission inventories can be carried out. This allows us to critically test the validity of the inventories and compliance with international treaties, such as the Kyoto protocol, monitored.

# Bibliography

Agency for Toxic Substances and Disease Registry (2001), 'Landfill Gas Primer - An Overview for Environmental Health Professionals', <http://www.atsdr.cdc.gov/HAC/landfill/html/ch2.html>.

AIRS, N. (2013), 'How AIRS Works', <https://airs.jpl.nasa.gov/>.

Andrews, A. E., Kofler, J. D., Trudeau, M. E., Williams, J. C., Neff, D. H., Masarie, K. A., Chao, D. Y., Kitzis, D. R., Novelli, P. C., Zhao, C. L., Dlugokencky, E. J., Lang, P. M., Crotwell, M. J., Fischer, M. L., Parker, M. J., Lee, J. T., Baumann, D. D., Desai, A. R., Stanier, C. O., de Wekker, S. F. J., Wolfe, D. E., Munger, J. W., Tans, P. P. (2013), 'CO<sub>2</sub>, CO and CH<sub>4</sub> measurements from the NOAA Earth System Research Laboratory's Tall Tower Greenhouse Gas Observing Network: instrumentation, uncertainty analysis and recommendations for future high-accuracy greenhouse gas monitoring efforts', *Atmospheric Measurement Techniques Discussions* **6**(1), 1461–1553.

Archer, D. (2005), 'Destabilization of methane hydrates: A risk analysis. Externe Expertise für das WBGU-Sondergutachten Die Zukunft der Meere—zu warm, zu hoch, zu sauer', [http://www.wbgu.de/fileadmin/templates/dateien/veroeffentlichungen/sondergutachten/sn2006/wbgu\\_sn2006\\_ex01.pdf](http://www.wbgu.de/fileadmin/templates/dateien/veroeffentlichungen/sondergutachten/sn2006/wbgu_sn2006_ex01.pdf).

Archer, D., Buffett, B., Brovkin, V. (2009), 'Ocean methane hydrates as a slow tipping point in the global carbon cycle', *Proceedings of the National Academy of Sciences* **106**(49), 20596–20601.

Aselmann, I., Crutzen, P. (1989), 'Global distribution of natural freshwater wetlands and rice paddies, their net primary productivity, seasonality and possible methane emissions', *Journal of Atmospheric Chemistry* **8**(4), 307–358.

Aydin, M., Verhulst, K. R., Saltzman, E. S., Battle, M. O., Montzka, S. A., Blake, D. R., Tang, Q., Prather, M. J. (2011), 'Recent decreases in fossil-fuel emissions of ethane and methane derived from firn air', *Nature* **476**(7359), 198–201.

- Barrie, L. A. (2005), 'The WMO global atmosphere watch (GAW) programme', *70 The Swiss Contribution to the WMO Global Atmosphere Watch Programme—Achievements of the First Decade and Future Prospects* p. 7.
- Bartlett, K. B., Bartlett, D. S., Harriss, R. C., Sebacher, D. I. (1987), 'Methane emissions along a salt marsh salinity gradient', *Biogeochemistry* **4**(3), 183–202.
- Bergamaschi, P., Frankenberg, C., Meirink, J. F., Krol, M., Villani, M. G., Houweling, S., Dentener, F., Dlugokencky, E. J., Miller, J. B., Gatti, L. V., others (2009), 'Inverse modeling of global and regional CH<sub>4</sub> emissions using SCIAMACHY satellite retrievals', *Journal of Geophysical Research* **114**(D22), D22301.
- Bergamaschi, P., Houweling, S., Segers, A., Krol, M., Frankenberg, C., Scheepmaker, R. A., Dlugokencky, E., Wofsy, S. C., Kort, E. A., Sweeney, C., Schuck, T., Brenninkmeijer, C., Chen, H., Beck, V., Gerbig, C. (2013), 'Atmospheric CH<sub>4</sub> in the first decade of the 21st century: Inverse modeling analysis using SCIAMACHY satellite retrievals and NOAA surface measurements', *Journal of Geophysical Research: Atmospheres* **118**(13), 7350–7369.
- Bergamaschi, P., Krol, M., Dentener, F., Vermeulen, A., Meinhardt, F., Graul, R., Ramonet, M., Peters, W., Dlugokencky, E. J. (2005), 'Inverse modelling of national and European CH<sub>4</sub> emissions using the atmospheric zoom model TM5', *Atmospheric Chemistry and Physics* **5**(9), 2431–2460.
- Bergamaschi, P., Krol, M., Meirink, J. F., Dentener, F., Segers, A., van Aardenne, J., Monni, S., Vermeulen, A. T., Schmidt, M., Ramonet, M., Yver, C., Meinhardt, F., Nisbet, E. G., Fisher, R. E., O'Doherty, S., Dlugokencky, E. J. (2010), 'Inverse modeling of European CH<sub>4</sub> emissions 20012006', *Journal of Geophysical Research: Atmospheres* **115**(D22).
- Bloom, A. A., Palmer, P. I., Fraser, A., Reay, D. S. (2012), 'Seasonal Variability of Tropical Wetland CH<sub>4</sub> emissions: the role of the methanogen-available carbon pool', *Biogeosciences Discussions* **9**(1), 387–409.
- Bloom, A. A., Palmer, P. I., Fraser, A., Reay, D. S., Frankenberg, C. (2010), 'Large-Scale Controls of Methanogenesis Inferred from Methane and Gravity Spaceborne Data', *Science* **327**(5963), 322–325.
- Boesch, H., Baker, D., Connor, B., Crisp, D., Miller, C. (2011), 'Global characterization of CO<sub>2</sub> column retrievals from shortwave-infrared satellite observations of the Orbiting Carbon Observatory-2 mission', *Remote Sensing* **3**(2), 270–304.

- Bousquet, P., Ciais, P., Miller, J., Dlugokencky, E., Hauglustaine, D., Prigent, C., Van der Werf, G., Peylin, P., Brunke, E.-G., Carouge, C., others (2006), 'Contribution of anthropogenic and natural sources to atmospheric methane variability', *Nature* **443**(7110), 439–443.
- Bousquet, P., Ringeval, B., Pison, I., Dlugokencky, E., Brunke, E.-G., Carouge, C., Chevallier, F., Fortems-Cheiney, A., Frankenberg, C., Hauglustaine, D., others (2011), 'Source attribution of the changes in atmospheric methane for 2006–2008', *Atmospheric Chemistry and Physics* **11**(8), 3689–3700.
- Brauman, A., Kane, M. D., Labat, M., Breznak, J. A. (1992), 'Genesis of acetate and methane by gut bacteria of nutritionally diverse termites.', *Science(Washington)* **257**(5075), 1384–1387.
- Bron, F.-M., Ciais, P. (2010), 'Spaceborne remote sensing of greenhouse gas concentrations', *Comptes Rendus Geoscience* **342**(45), 412 – 424.
- Brook, E. J., Harder, S., Severinghaus, J., Steig, E. J., Sucher, C. M. (2000), 'On the origin and timing of rapid changes in atmospheric methane during the last glacial period', *Global Biogeochemical Cycles* **14**(2), 559–572.
- Browning, K. A., Gurney, R. J. (1999), *Global energy and water cycles*, Cambridge University Press.
- Buchwitz, M. (2007), 'Image gallery: SCIAMACHY Methane', [http://www.iup.uni-bremen.de/sciamachy/NIR\\_NADIR\\_WFM\\_DOAS/wfmd\\_image\\_gallery\\_ch4.html](http://www.iup.uni-bremen.de/sciamachy/NIR_NADIR_WFM_DOAS/wfmd_image_gallery_ch4.html).
- Buchwitz, M. (2010), 'Carbon Monitoring Satellite - CarbonSat', <http://www.iup.uni-bremen.de/carbonsat/>.
- Buchwitz, M., Beek, R. d., Burrows, J., Bovensmann, H., Warneke, T., Notholt, J., Meirink, J., Goede, A., Bergamaschi, P., Körner, S., others (2005), 'Atmospheric methane and carbon dioxide from sciamachy satellite data: initial comparison with chemistry and transport models', *Atmospheric Chemistry and Physics* **5**(4), 941–962.
- Buchwitz, M., Reuter, M., Bovensmann, H., Pillai, D., Heymann, J., Schneising, O., Rozanov, V., Krings, T., Burrows, J. P., Boesch, H., Gerbig, C., Meijer, Y., Löscher, A. (2013), 'Carbon Monitoring Satellite (CarbonSat): assessment of scattering related atmospheric CO<sub>2</sub> and CH<sub>4</sub> retrieval errors and first results on implications for inferring city CO<sub>2</sub> emissions', *Atmospheric Measurement Techniques Discussions* **6**(3), 4769–4850.

- Burgin, L., Gloster, J., Mellor, P. (2009), 'Why were there no outbreaks of bluetongue in the UK during 2008?', *The Veterinary Record* **164**(13), 384–387.
- Center for Global Environmental Research, NIES (2010), 'GOSAT project', <http://www.cger.nies.go.jp/en/activities/supporting/publications/>.
- Chahine, M. T., Pagano, T. S., Aumann, H. H., Atlas, R., Barnet, C., Blaisdell, J., Chen, L., Divakarla, M., Fetzer, E. J., Goldberg, M., Gautier, C., Granger, S., Hannon, S., Irion, F. W., Kakar, R., Kalnay, E., Lambrigtsen, B. H., Lee, S.-Y., Le Marshall, J., McMillan, W. W., McMillin, L., Olsen, E. T., Revercomb, H., Rosenkranz, P., Smith, W. L., Staelin, D., Larrabee Strow, L., Susskind, J., Tobin, D., Wolf, W., Zhou, L. (2006), 'AIRS: Improving Weather Forecasting and Providing New Data on Greenhouse Gases.', *Bulletin of the American Meteorological Society* **87**, 911–926.
- Ciais, P., Dolman, A. J., Bombelli, A., Duren, R., Peregón, A., Rayner, P. J., Miller, C., Gobron, N., Kinderman, G., Marland, G., Gruber, N., Chevallier, F., Andres, R. J., Balsamo, G., Bopp, L., Bréon, F.-M., Broquet, G., Dargaville, R., Battin, T. J., Borges, A., Bovensmann, H., Buchwitz, M., Butler, J., Canadell, J. G., Cook, R. B., DeFries, R., Engelen, R., Gurney, K. R., Heinze, C., Heimann, M., Held, A., Henry, M., Law, B., Luysaert, S., Miller, J., Moriyama, T., Moulin, C., Myneni, R. B., Nussli, C., Obersteiner, M., Ojima, D., Pan, Y., Paris, J.-D., Piao, S. L., Poulter, B., Plummer, S., Quegan, S., Raymond, P., Reichstein, M., Rivier, L., Sabine, C., Schimel, D., Tarasova, O., Valentini, R., van der Werf, G., Wickland, D., Williams, M., Zehner, C. (2013), 'Current systematic carbon cycle observations and needs for implementing a policy-relevant carbon observing system', *Biogeosciences Discussions* **10**(7), 11447–11581.
- Clerbaux, C., Drummond, J. R., Flaud, J.-M., Orpha, J. (2011), Chapter 3 - Thermal Infrared: Absorption and Emission Trace Gases and Parameters, in C. Clerbaux, J. R. Drummond, J.-M. Flaud, J. Orphal, eds, 'The Remote Sensing of Tropospheric Composition from Space', Springer Verlag, Heidelberg.
- Connor, B. J., Boesch, H., Toon, G., Sen, B., Miller, C., Crisp, D. (2008), 'Orbiting Carbon Observatory: Inverse method and prospective error analysis', *Journal of Geophysical Research: Atmospheres* **113**(D5).
- Conrad, R. (2002), 'Control of microbial methane production in wetland rice fields', *Nutrient Cycling in Agroecosystems* **64**(1-2), 59–69.
- Crutzen, P. (1973), 'A discussion of the chemistry of some minor constituents in the stratosphere and troposphere', *Pure and Applied Geophysics* **106**(1), 1385–1399.

- Delmas, R. (1994), 'An overview of present knowledge on methane emission from biomass burning', *Nutrient Cycling in Agroecosystems* **37**(3), 181–190.
- Dentener, F., Stevenson, D., Cofala, J., Mechler, R., Amann, M., Bergamaschi, P., Raes, F., Derwent, R. (2005), 'The impact of air pollutant and methane emission controls on tropospheric ozone and radiative forcing: CTM calculations for the period 1990–2030', *Atmospheric Chemistry and Physics* **5**(7), 1731–1755.
- Devenish, B., Thomson, D., Marenco, F., Leadbetter, S., Ricketts, H., Dacre, H. (2012), 'A study of the arrival over the United Kingdom in April 2010 of the Eyjafjallajökull ash cloud using ground-based lidar and numerical simulations', *Atmospheric Environment* **48**, 152–164.
- Dils, B., Buchwitz, M., Reuter, M., Schneising, O., Boesch, H., Parker, R., Guerlet, S., Aben, I., Blumenstock, T., Burrows, J. P., Butz, A., Deutscher, N. M., Frankenberg, C., Hase, F., Hasekamp, O. P., Heymann, J., De Mazière, M., Notholt, J., Sussmann, R., Warneke, T., Griffith, D., Sherlock, V., Wunch, D. (2013), 'The Greenhouse Gas Climate Change Initiative (GHG-CCI): comparative validation of GHG-CCI SCIAMACHY/ENVISAT and TANSO-FTS/GOSAT CO<sub>2</sub> and CH<sub>4</sub> retrieval algorithm products with measurements from the TCCON network', *Atmospheric Measurement Techniques Discussions* **6**(5), 8679–8741.
- Dlugokencky, E., Bruhwiler, L., White, J., Emmons, L., Novelli, P. C., Montzka, S. A., Masarie, K. A., Lang, P. M., Crotwell, A., Miller, J. B., others (2009), 'Observational constraints on recent increases in the atmospheric CH<sub>4</sub> burden', *Geophysical Research Letters* **36**(18).
- Dlugokencky, E. J., Nisbet, E. G., Fisher, R., Lowry, D. (2011), 'Global atmospheric methane: budget, changes and dangers', *Philosophical Transactions of the Royal Society A: Mathematical, Physical and Engineering Sciences* **369**(1943), 2058–2072.
- Dlugokencky, E. J., Steele, L. P., Lang, P. M., Masarie, K. A. (1995), 'Atmospheric methane at Mauna Loa and Barrow observatories: Presentation and analysis of in situ measurements', *Journal of Geophysical Research: Atmospheres (1984–2012)* **100**(D11), 23103–23113.
- EDGAR (2009), Emission Database for Global Atmospheric Research (EDGAR), release version 4.0, Technical report, European Commission, Joint Research Centre (JRC)/Netherlands Environmental Assessment Agency (PBL). <http://edgar.jrc.ec.europa.eu>.

- Eggleston, H., Buendia, L., Miwa, K., Ngara, T., Tanabe, K. (2006), 2006 IPCC Guidelines for National Greenhouse Gas Inventories, Technical report, Intergovernmental panel on climate change, IPCC.
- Ehret, G., Amediek, A., Quatrevalet, M. (2012), Towards a Greenhouse Gas Lidar in Space, *in* U. Schumann, ed., 'Atmospheric Physics', Research Topics in Aerospace, Springer Berlin Heidelberg, pp. 799–813.
- Enting, I., Trudinger, C., Francey, R. (1995), 'A synthesis inversion of the concentration and  $\delta^{13}\text{C}$  of atmospheric  $\text{CO}_2$ ', *Tellus B* **47**(1-2), 35–52.
- EPA (2012), Global anthropogenic non- $\text{CO}_2$  greenhouse gas emissions: 1990-2030, Technical report, United States Environmental Protection Agency.
- Farquhar, G. J., Rovers, F. (1973), 'Gas production during refuse decomposition', *Water, Air, and Soil Pollution* **2**(4), 483–495.
- Fey, A., Chin, K. J., Conrad, R. (2001), 'Thermophilic methanogens in rice field soil', *Environmental Microbiology* **3**(5), 295–303.
- Fiore, A. M., Horowitz, L. W., Dlugokencky, E. J., West, J. J. (2006), 'Impact of meteorology and emissions on methane trends, 1990–2004', *Geophysical Research Letters* **33**(12).
- Fiore, A. M., West, J. J., Horowitz, L. W., Naik, V., Schwarzkopf, M. D. (2008), 'Characterizing the tropospheric ozone response to methane emission controls and the benefits to climate and air quality', *Journal of Geophysical Research: Atmospheres* **113**(D8).
- Frankenberg, C., Aben, I., Bergamaschi, P., Dlugokencky, E. J., van Hees, R., Houweling, S., van der Meer, P., Snel, R., Tol, P. (2011), 'Global column-averaged methane mixing ratios from 2003 to 2009 as derived from SCIAMACHY: Trends and variability', *Journal of Geophysical Research: Atmospheres* **116**(D4).
- Frankenberg, C., Bergamaschi, P., Butz, A., Houweling, S., Meirink, J. F., Notholt, J., Petersen, A. K., Schrijver, H., Warneke, T., Aben, I. (2008), 'Tropical methane emissions: A revised view from SCIAMACHY onboard ENVISAT', *Geophysical Research Letters* **35**(15).
- Frankenberg, C., Meirink, J., Bergamaschi, P., Goede, A., Heimann, M., Körner, S., Platt, U., Van Weele, M., Wagner, T. (2006), 'Satellite cartography of atmospheric methane from sciamachy on board envisat: Analysis of the years 2003 and 2004'.

- Frankenberg, C., Meirink, J., Van Weele, M., Platt, U., Wagner, T. (2005), ‘Assessing methane emissions from global space-borne observations’, *Science* **308**(5724), 1010–1014.
- Fraser, A., Palmer, P. I., Feng, L., Boesch, H., Cogan, A., Parker, R., Dlugokencky, E. J., Fraser, P. J., Krummel, P. B., Langenfelds, R. L., O’Doherty, S., Prinn, R. G., Steele, L. P., van der Schoot, M., Weiss, R. F. (2013), ‘Estimating regional methane surface fluxes: the relative importance of surface and GOSAT mole fraction measurements’, *Atmospheric Chemistry and Physics* **13**(11), 5697–5713.
- Fraser, P., Rasmussen, R., Creffield, J., French, J., Khalil, M. (1986), ‘Termites and global methane another assessment’, *Journal of Atmospheric Chemistry* **4**(3), 295–310.
- Fung, I., John, J., Lerner, J., Matthews, E., Prather, M., Steele, L. P., Fraser, P. J. (1991), ‘Three-dimensional model synthesis of the global methane cycle’, *Journal of Geophysical Research: Atmospheres* **96**(D7), 13033–13065.
- Gerbig, C., Lin, J., Wofsy, S., Daube, B., Andrews, A., Stephens, B., Bakwin, P., Grainger, C. (2003), ‘Toward constraining regional-scale fluxes of CO<sub>2</sub> with atmospheric observations over a continent: 2. Analysis of COBRA data using a receptor-oriented framework’, *Journal of geophysical research* **108**(D24), 4757.
- Gloor, M., Bakwin, P., Hurst, D., Lock, L., Draxler, R., Tans, P. (2001), ‘What is the concentration footprint of a tall tower?’, *Journal of Geophysical Research: Atmospheres* **106**(D16), 17831–17840.
- Gloster, J., Champion, H., Sørensen, J., Mikkelsen, T., Ryall, D., Astrup, P., Alexandersen, S., Donaldson, A. (2003), ‘Airborne transmission of foot-and-mouth disease virus from Burnside Farm, Heddon-on-the-Wall, Northumberland, during the 2001 epidemic in the United Kingdom.’, *The Veterinary Record* **152**(17), 525–533.
- Hamazaki, T. (2005), ‘GOSAT Mission Overview’, Presentation to Carbon from Space, ESA.
- Heimann, M. (2006), The Global Atmospheric Tracer Model TM2, Technical Report Tech. Rep. 10., Max-Planck-Institute für Meteorologie, Hamburg, Germany.
- Heimann, M. (2011), ‘Atmospheric science: enigma of the recent methane budget’, *Nature* **476**(7359), 157–158.

- Hornibrook, E. H. (2005), 'Biogeochemical processes of methane emission and uptake', Presentation, Bristol Biogeochemistry Research Centre, Department of Earth Sciences, University of Bristol.
- Hornibrook, E. R. C., Bowes, H. L., Culbert, A., Gallego-Sala, A. V. (2008), 'Methanotrophy potential versus methane supply by pore water diffusion in peatlands', *Biogeosciences Discussions* **5**(3), 2607–2643.
- Houweling, S., Kaminski, T., Dentener, F., Lelieveld, J., Heimann, M. (1999), 'Inverse modeling of methane sources and sinks using the adjoint of a global transport model', *Journal of Geophysical Research: Atmospheres* **104**(D21), 26137–26160.
- Hurst, D., Dutton, G., Romashkin, P., Elkins, J., Herman, R., Moyer, E., Scott, D., May, R., Webster, C., Grecu, J., others (2000), 'Comparison of in situ N<sub>2</sub>O and CH<sub>4</sub> measurements in the upper troposphere and lower stratosphere during STRAT and POLARIS', *Journal of Geophysical Research: Atmospheres (1984–2012)* **105**(D15), 19811–19822.
- Jacob, D. (1999), *Introduction to atmospheric chemistry*, Princeton University Press.
- Jamali, H., Livesley, S. J., Hutley, L. B., Fest, B., Arndt, S. K. (2013), 'The relationships between termite mound CH<sub>4</sub>/CO<sub>2</sub> emissions and internal concentration ratios are species specific', *Biogeosciences* **10**(4), 2229–2240.
- Jones, A. (2013), User Guide for NAME, Technical Report MD15/8(version 1.0), Met Office, Exeter, UK.
- Jones, A., Thomson, D., Hort, M., Devenish, B. (2007), The UK Met Office's next-generation atmospheric dispersion model, NAME III, in 'Air Pollution Modeling and its Application XVII', Springer, pp. 580–589.
- Juottonen, H. (2008), Archaea, Bacteria, and methane production along environmental gradients in fens and bogs, PhD thesis, Helsingin yliopisto.
- Kai, F. M., Tyler, S. C., Randerson, J. T., Blake, D. R. (2011), 'Reduced methane growth rate explained by decreased northern hemisphere microbial sources', *Nature* **476**(7359), 194–197.
- Karamouz, M., Nazif, S., others (2012), *Hydrology and Hydroclimatology: Principles and Applications*, CRC Press.

- Keeling, C., Whorf, T. (2004), 'Atmospheric CO<sub>2</sub> concentrations derived from flask air samples at sites in the SIO network. In Trends: A Compendium of Data on Global Change.'
- Kepler, F., Hamilton, J. T., Braß, M., Röckmann, T. (2006), 'Methane emissions from terrestrial plants under aerobic conditions', *Nature* **439**(7073), 187–191.
- Khalil, M. A. K. (2000), *Atmospheric methane: Its role in the global environment*, Springer.
- Kiemle, C., Quatrevalet, M., Ehret, G., Amediek, A., Fix, A., Wirth, M. (2011), 'Sensitivity studies for a space-based methane lidar mission', *Atmospheric Measurement Techniques* **4**(10), 2195–2211.
- Kirschke, S., Bousquet, P., Ciais, P., Saunois, M., Canadell, J. G., Dlugokencky, E. J., Bergamaschi, P., Bergmann, D., Blake, D. R., Bruhwiler, L., others (2013), 'Three decades of global methane sources and sinks', *Nature Geoscience* **6**(10), 813–823.
- Koppmann, R., von Czapiewski, K., Reid, J. S. (2005), 'A review of biomass burning emissions, part I: gaseous emissions of carbon monoxide, methane, volatile organic compounds, and nitrogen containing compounds', *Atmospheric Chemistry and Physics Discussions* **5**(5), 10455–10516.
- Kort, E. A., Eluszkiewicz, J., Stephens, B. B., Miller, J. B., Gerbig, C., Nehr Korn, T., Daube, B. C., Kaplan, J. O., Houweling, S., Wofsy, S. C. (2008), 'Emissions of CH<sub>4</sub> and N<sub>2</sub>O over the United States and Canada based on a receptor-oriented modeling framework and COBRA-NA atmospheric observations', *Geophysical Research Letters* **35**(18).
- Lassey, K., Allan, W., FLETCHER, S. M. (2011), 'Seasonal inter-relationships in atmospheric methane and companion  $\delta^{13}\text{C}$  values: effects of sinks and sources', *Tellus B* **63**(3), 287–301.
- Lelieveld, J., Lechtenböhmer, S., Assonov, S. S., Brenninkmeijer, C., Dienst, C., Fishedick, M., Hanke, T. (2005), 'Greenhouse gases: Low methane leakage from gas pipelines', *Nature* **434**(7035), 841–842.
- Levin, I., Veidt, C., Vaughn, B., Brailsford, G., Bromley, T., Heinz, R., Lowe, D., Miller, J., Poss, C., White, J. (2012), 'No inter-hemispheric  $\delta^{13}\text{C}$  trend observed', *Nature* **486**(7404), E3–E4.

- Levine, J., Wolff, E., Jones, A., Sime, L., Valdes, P., Archibald, A., Carver, G., Warwick, N., Pyle, J. (2011), ‘Reconciling the changes in atmospheric methane sources and sinks between the last glacial maximum and the pre-industrial era’, *Geophysical Research Letters* **38**(23).
- Lin, J. C. (2013), *Lagrangian Modeling of the Atmosphere: An Introduction*, American Geophysical Union, pp. 1–11.
- Lin, J. C., Gerbig, C., Wofsy, S. C., Andrews, A. E., Daube, B. C., Grainger, C. A., Stephens, B. B., Bakwin, P. S., Hollinger, D. Y. (2004), ‘Measuring fluxes of trace gases at regional scales by Lagrangian observations: Application to the CO<sub>2</sub> Budget and Rectification Airborne (COBRA) study’, *Journal of Geophysical Research: Atmospheres* **109**(D15).
- Lin, J. C., Gerbig, C., Wofsy, S. C., Chow, V. Y., Gottlieb, E., Daube, B. C., Matross, D. M. (2007), ‘Designing Lagrangian experiments to measure regional-scale trace gas fluxes’, *Journal of Geophysical Research: Atmospheres* **112**(D13).
- Lin, J., Gerbig, C., Wofsy, S., Andrews, A., Daube, B., Davis, K., Grainger, C. (2003), ‘A near-field tool for simulating the upstream influence of atmospheric observations: The Stochastic Time-Inverted Lagrangian Transport (STILT) model’, *Journal of Geophysical Research: Atmospheres (1984–2012)* **108**(D16).
- Lu, Y., Wassmann, R., Neue, H., Huang, C. (1999), ‘Impact of phosphorus supply on root exudation, aerenchyma formation and methane emission of rice plants’, *Biogeochemistry* **47**(2), 203–218.
- Manning, A. J. (2011), ‘The challenge of estimating regional trace gas emissions from atmospheric observations’, *Philosophical Transactions of the Royal Society A: Mathematical, Physical and Engineering Sciences* **369**(1943), 1943–1954.
- Manning, A. J., O’Doherty, S., Jones, A. R., Simmonds, P. G., Derwent, R. G. (2011), ‘Estimating UK methane and nitrous oxide emissions from 1990 to 2007 using an inversion modeling approach’, *Journal of Geophysical Research: Atmospheres* **116**(D2).
- Manning, A. J., Ryall, D. B., Derwent, R. G., Simmonds, P. G., O’Doherty, S. (2003), ‘Estimating European emissions of ozone-depleting and greenhouse gases using observations and a modeling back-attribution technique’, *Journal of Geophysical Research: Atmospheres* **108**(D14).
- Maresi, L., Van Der Meulen, W., De Vries, J. (2013), ‘TROPOMI, A Stepping Stone for Global Troposphere Monitoring’.

- Meijer, Y., Ingmann, P., Löscher, A., Sierk, B., Bovensmann, H., Buchwitz, M. (2012), CarbonSat: ESAs Earth Explorer 8 Candidate Mission, in 'EGU General Assembly Conference Abstracts', Vol. 14, p. 2474.
- Meirink, J. F., Bergamaschi, P., Frankenberg, C., d'Amelio, M. T. S., Dlugokencky, E. J., Gatti, L. V., Houweling, S., Miller, J. B., Rckmann, T., Villani, M. G., Krol, M. C. (2008), 'Four-dimensional variational data assimilation for inverse modeling of atmospheric methane emissions: Analysis of SCIAMACHY observations', *Journal of Geophysical Research: Atmospheres* **113**(D17).
- Meirink, J. F., Bergamaschi, P., Krol, M. C. (2008), 'Four-dimensional variational data assimilation for inverse modelling of atmospheric methane emissions: method and comparison with synthesis inversion', *Atmospheric Chemistry and Physics* **8**(21), 6341–6353.
- Melton, J., Wania, R., Hodson, E., Poulter, B., Ringeval, B., Spahni, R., Bohn, T., Avis, C., Beerling, D., Chen, G., others (2013), 'Present state of global wetland extent and wetland methane modelling: conclusions from a model inter-comparison project (WETCHIMP)', *Biogeosciences* **10**(2), 753–788.
- Mer, J. L., Roger, P. (2001), 'Production, oxidation, emission and consumption of methane by soils: A review', *European Journal of Soil Biology* **37**(1), 25 – 50.
- Miller, B. R., Weiss, R. F., Salameh, P. K., Tanhua, T., Grealley, B. R., Muhle, J., Simmonds, P. G. (2008), 'Medusa: A Sample Preconcentration and GC/MS Detector System for in Situ Measurements of Atmospheric Trace Halocarbons, Hydrocarbons, and Sulfur Compounds', *Analytical Chemistry* **80**(5), 1536–1545. PMID: 18232668.
- Miller, C., Crisp, D., DeCola, P., Olsen, S., Randerson, J. T., Michalak, A., Alkhaled, A., Rayner, P., Jacob, D., Suntharalingam, P., others (2007), 'Precision requirements for space-based data', *Journal of Geophysical Research: Atmospheres (1984–2012)* **112**(D10).
- Monks, P., Granier, C., Fuzzi, S., Stohl, A., Williams, M., Akimoto, H., Amann, M., Baklanov, A., Baltensperger, U., Bey, I., others (2009), 'Atmospheric composition change—global and regional air quality', *Atmospheric Environment* **43**(33), 5268–5350.
- Monteil, G., Houweling, S., Dlugokencky, E., Maenhout, G., Vaughn, B., White, J., Rockmann, T. (2011), 'Interpreting methane variations in the past two decades using

- measurements of CH<sub>4</sub> mixing ratio and isotopic composition', *Atmospheric Chemistry and Physics* **11**(17), 9141–9153.
- Montzka, S., Dlugokencky, E., Butler, J. (2011), 'Non-CO<sub>2</sub> greenhouse gases and climate change', *Nature* **476**(7358), 43–50.
- Montzka, S., Krol, M., Dlugokencky, E., Hall, B., Jöckel, P., Lelieveld, J. (2011), 'Small interannual variability of global atmospheric hydroxyl', *Science* **331**(6013), 67–69.
- Morgenstern, O., Zeng, G., Luke Abraham, N., Telford, P. J., Braesicke, P., Pyle, J. A., Hardiman, S. C., O'Connor, F. M., Johnson, C. E. (2013), 'Impacts of climate change, ozone recovery, and increasing methane on surface ozone and the tropospheric oxidizing capacity', *Journal of Geophysical Research: Atmospheres* .
- Mosher, B. W., Czepiel, P. M., Harriss, R. C., Shorter, J. H., Kolb, C. E., McManus, J. B., Allwine, E., Lamb, B. K. (1999), 'Methane Emissions at Nine Landfill Sites in the Northeastern United States', *Environmental Science & Technology* **33**(12), 2088–2094.
- Naik, V., Voulgarakis, A., Fiore, A. M., Horowitz, L., Lamarque, J.-F., Lin, M., Prather, M. J., Young, P., Bergmann, D., Cameron-Smith, P., others (2013), 'Preindustrial to present-day changes in tropospheric hydroxyl radical and methane lifetime from the Atmospheric Chemistry and Climate Model Intercomparison Project (ACCMIP)', *Atmospheric Chemistry and Physics* **13**(10), 5277–5298.
- NASA (2013), 'AIRS and Composition Science', <https://airs.jpl.nasa.gov>.
- National Oceanic and Atmospheric Administration (2013), 'Measuring and analyzing greenhouse gases: Behind the scenes', [http://www.esrl.noaa.gov/gmd/ccgg/behind\\_the\\_scenes/](http://www.esrl.noaa.gov/gmd/ccgg/behind_the_scenes/).
- Neef, L., van Weele, M., van Velthoven, P. (2010), 'Optimal estimation of the present-day global methane budget', *Global Biogeochemical Cycles* **24**(4).
- Nykänen, H., Vasander, H., Huttunen, J. T., Martikainen, P. J. (2002), 'Effect of experimental nitrogen load on methane and nitrous oxide fluxes on ombrotrophic boreal peatland', *Plant and Soil* **242**(1), 147–155.
- Palmer, P., Feng, L., Bösch, H. (2011), 'Spatial resolution of tropical terrestrial CO<sub>2</sub> fluxes inferred using space-borne column CO<sub>2</sub> sampled in different earth orbits: the role of spatial error correlations', *Atmospheric Measurement Techniques* **4**(9), 1995–2006.

- Pan, L. L. e. (2010), 'The StratosphereTroposphere Analyses of Regional Transport 2008 Experiment', *American Meteorological Society* **91**, 327–342.
- Parker, R., Boesch, H., Cogan, A., Fraser, A., Feng, L., Palmer, P. I., Messerschmidt, J., Deutscher, N., Griffith, D. W. T., Notholt, J., Wennberg, P. O., Wunch, D. (2011), 'Methane observations from the Greenhouse Gases Observing SATellite: Comparison to ground-based TCCON data and model calculations', *Geophysical Research Letters* **38**(15).
- Pillai, D., Gerbig, C., Kretschmer, R., Beck, V., Karstens, U., Neininger, B., Heimann, M. (2012), 'Comparing Lagrangian and Eulerian models for CO<sub>2</sub> transport a step towards Bayesian inverse modeling using WRF/STILT-VPRM', *Atmospheric Chemistry and Physics* **12**(19), 8979–8991.
- Pison, I., Bousquet, P., Chevallier, F., Szopa, S., Hauglustaine, D. (2009), 'Multi-species inversion of CH<sub>4</sub>, CO and H<sub>2</sub> emissions from surface measurements', *Atmospheric Chemistry and Physics* **9**(14), 5281–5297.
- PLANETA (2013), 'MetOp Polar-Orbiting Satellite System'.
- Polson, D., Fowler, D., Nemitz, E., Skiba, U., McDonald, A., Famulari, D., Di Marco, C., Simmons, I., Weston, K., Purvis, R., others (2011), 'Estimation of spatial apportionment of greenhouse gas emissions for the UK using boundary layer measurements and inverse modelling technique', *Atmospheric Environment* **45**(4), 1042–1049.
- Prigent, C., Papa, F., Aires, F., Rossow, W. B., Matthews, E. (2007), 'Global inundation dynamics inferred from multiple satellite observations, 1993–2000', *Journal of Geophysical Research: Atmospheres* **112**(D12).
- Quantifying Methane Emissions from Livestock (2012), 'Greenhouse gas emissions: quantifying methane emissions from livestock', *Am. J. Engg. & Applied Sci* **5**(1), 1–8.
- Ratering, S., Conrad, R. (1998), 'Effects of short-term drainage and aeration on the production of methane in submerged rice soil', *Global Change Biology* **4**(4), 397–407.
- Rice, A. L., Tyler, S. C., McCarthy, M. C., Boering, K. A., Atlas, E. (2003), 'Carbon and hydrogen isotopic compositions of stratospheric methane: 1. High-precision observations from the NASA ER-2 aircraft', *Journal of Geophysical Research: Atmospheres* **108**(D15).

- Rigby, M., Manning, A. J., Prinn, R. G. (2011), 'Inversion of long-lived trace gas emissions using combined Eulerian and Lagrangian chemical transport models', *Atmospheric Chemistry and Physics* **11**(18), 9887–9898.
- Rigby, M., Prinn, R. G., Fraser, P. J., Simmonds, P. G., Langenfelds, R. L., Huang, J., Cunnold, D. M., Steele, L. P., Krummel, P. B., Weiss, R. F., O'Doherty, S., Salameh, P. K., Wang, H. J., Harth, C. M., Mhle, J., Porter, L. W. (2008), 'Renewed growth of atmospheric methane', *Geophysical Research Letters* **35**(22).
- Rodenbeck, C., Houweling, S., Gloor, M., Heimann, M. (2003), 'CO<sub>2</sub> flux history 1982–2001 inferred from atmospheric data using a global inversion of atmospheric transport', *Atmospheric Chemistry and Physics* **3**(6), 1919–1964.
- Rodgers, C. D. (2000), *Inverse methods for atmospheric sounding*, World Scientific.
- Ryall, D., Derwent, R., Manning, A., Simmonds, P., O'Doherty, S. (2001), 'Estimating source regions of European emissions of trace gases from observations at Mace Head', *Atmospheric Environment* **35**(14), 2507 – 2523.
- Saito, R., Patra, P. K., Sweeney, C., Machida, T., Krol, M., Houweling, S., Bousquet, P., Agustí-Panareda, A., Belikov, D., Bergmann, D., Bian, H., Cameron-Smith, P., Chipperfield, M. P., Fortems-Cheiney, A., Fraser, A., Gatti, L. V., Gloor, E., Hess, P., Kawa, S. R., Law, R. M., Locatelli, R., Loh, Z., Maksyutov, S., Meng, L., Miller, J. B., Palmer, P. I., Prinn, R. G., Rigby, M., Wilson, C. (2013), 'TransCom model simulations of methane: Comparison of vertical profiles with aircraft measurements', *Journal of Geophysical Research: Atmospheres* **118**(9), 3891–3904.
- Sanders, C. J., Burgin, L., Pallot, A., Barber, J., Golding, N., Carpenter, S., Gloster, J. (2010), 'A study of potential bluetongue vectors and meteorology in Jersey', *Weather* **65**(1), 21–26.
- Sawadogo, J. B., Dianou, D., Traoré, A. S. (2011), 'Effects of Temperature and Termite-Substrate on Methane and Carbon Dioxide Emissions from *Macrotermes bellicosus* and *Microcerotermes dubius* Cultures', *Middle-East Journal of Scientific Research* **9**(1), 75–83.
- Schimel, J. (2004), 'Playing scales in the methane cycle: From microbial ecology to the globe', *Proceedings of the National Academy of Sciences of the United States of America* **101**(34), 12400–12401.

- Schuck, T. J., Brenninkmeijer, C. A. M., Slemr, F., Xueref-Remy, I., Zahn, A. (2009), 'Greenhouse gas analysis of air samples collected onboard the CARIBIC passenger aircraft', *Atmospheric Measurement Techniques* **2**(2), 449–464.
- Schultz, M. (2002), 'On the use of ATSR fire count data to estimate the seasonal and interannual variability of vegetation fire emissions', *Atmospheric Chemistry and Physics* **2**(5), 387–395.
- Seibert, P., Frank, A. (2004), 'Source-receptor matrix calculation with a Lagrangian particle dispersion model in backward mode', *Atmospheric Chemistry and Physics* **4**(1), 51–63.
- Seiler, W., Conrad, R., Scharffe, D. (1984), 'Field studies of methane emission from termite nests into the atmosphere and measurements of methane uptake by tropical soils', *Journal of Atmospheric Chemistry* **1**(2), 171–186.
- Seiler, W., Crutzen, P. (1980), 'Estimates of gross and net fluxes of carbon between the biosphere and the atmosphere from biomass burning', *Climatic Change* **2**(3), 207–247.
- Shine, K. P., Fuglestvedt, J. S., Hailemariam, K., Stuber, N. (2005), 'Alternatives to the global warming potential for comparing climate impacts of emissions of greenhouse gases', *Climatic Change* **68**(3), 281–302.
- Simpson, I. J., Andersen, M. P. S., Meinardi, S., Bruhwiler, L., Blake, N. J., Helmig, D., Rowland, F. S., Blake, D. R. (2012), 'Long-term decline of global atmospheric ethane concentrations and implications for methane', *Nature* **488**(7412), 490–494.
- Solomon, S., Qin, D., Manning, M., Chen, Z., Marquis, M., Averyt, K., Tignor, M., Miller, H. (2007), 'IPCC, 2007: Climate Change 2007: The Physical Science Basis', *Contribution of Working Group I to the fourth assessment report of the Intergovernmental Panel on Climate Change* .
- Spahni, R., Wania, R., Neef, L., van Weele, M., Pison, I., Bousquet, P., Frankenberg, C., Foster, P. N., Joos, F., Prentice, I. C., van Velthoven, P. (2011), 'Constraining global methane emissions and uptake by ecosystems', *Biogeosciences* **8**(6), 1643–1665.
- Stocker, T., Qin, D., Plattner, G., Tignor, M., Allen, S., Boschung, J., Nauels, A., Xia, Y., Bex, V., Midgley, P. (2013), 'IPCC, 2013: Climate Change 2013: The Physical Science Basis. contribution of Working Group i to the Fifth Assessment Report of the Intergovernmental Panel on Climate Change'.

- Stohl, A., Forster, C., Frank, A., Seibert, P., Wotawa, G. (2005), ‘Technical note: The Lagrangian particle dispersion model FLEXPART version 6.2’, *Atmospheric Chemistry and Physics* **5**(9), 2461–2474.
- Stohl, A., Seibert, P., Arduini, J., Eckhardt, S., Fraser, P., Grealley, B., Lunder, C., Maione, M., Mühle, J., O’doherly, S., others (2009), ‘An analytical inversion method for determining regional and global emissions of greenhouse gases: Sensitivity studies and application to halocarbons’, *Atmospheric Chemistry and Physics* **9**(5), 1597–1620.
- Streets, D. G., Canty, T., Carmichael, G. R., de Foy, B., Dickerson, R. R., Duncan, B. N., Edwards, D. P., Haynes, J. A., Henze, D. K., Houyoux, M. R., Jacob, D. J., Krotkov, N. A., Lamsal, L. N., Liu, Y., Lu, Z., Martin, R. V., Pfister, G. G., Pinder, R. W., Salawitch, R. J., Wecht, K. J. (2013), ‘Emissions estimation from satellite retrievals: A review of current capability’, *Atmospheric Environment* **77**(0), 1011 – 1042.
- Tanaka, T., Miyamoto, Y., Morino, I., Machida, T., Nagahama, T., Sawa, Y., Matsueda, H., Wunch, D., Kawakami, S., Uchino, O. (2012), ‘Aircraft measurements of carbon dioxide and methane for the calibration of ground-based high-resolution Fourier Transform Spectrometers and a comparison to GOSAT data measured over Tsukuba and Moshiri’, *Atmospheric Measurement Techniques* **5**(8), 2003–2012.
- Tarantola, A. (2005), *Inverse Problem Theory and Methods for Model Parameter Estimation*, Society for Industrial and Applied Mathematics.
- Terao, Y., Mukai, H., Nojiri, Y., Machida, T., Tohjima, Y., Saeki, T., Maksyutov, S. (2011), ‘Interannual variability and trends in atmospheric methane over the western Pacific from 1994 to 2010’, *Journal of Geophysical Research: Atmospheres* **116**(D14).
- Trenberth, K. E., Fasullo, J. T. (2012), ‘Tracking Earth’s energy: From El Niño to global warming’, *Surveys in Geophysics* **33**(3-4), 413–426.
- Trenberth, K. E., Fasullo, J. T., Kiehl, J. (2009), ‘Earth’s global energy budget’, *Bulletin of the American Meteorological Society* **90**(3), 311–323.
- Trenberth, K. E., Stepaniak, D. P. (2004), ‘The flow of energy through the Earth’s climate system’, *Quarterly Journal of the Royal Meteorological Society* **130**(603), 2677–2701.
- Turner, A. J., Henze, D. K., Martin, R. V., Hakami, A. (2012), ‘The spatial extent of source influences on modeled column concentrations of short-lived species’, *Geophysical Research Letters* **39**(12).

- Uglietti, C., Leuenberger, M., Brunner, D. (2011), 'European source and sink areas of CO<sub>2</sub> retrieved from Lagrangian transport model interpretation of combined O<sub>2</sub> and CO<sub>2</sub> measurements at the high alpine research station Jungfraujoch', *Atmospheric Chemistry and Physics* **11**(15), 8017–8036.
- United States Environmental Protection Agency (2010), 'Methane and Nitrous Oxide Emissions From Natural Sources', <http://www.epa.gov/methane/pdfs/Methane-and-Nitrous-Oxide-Emissions-From-Natural-Sources.pdf>.
- U.S. Government (2013), 'Electronic Code of Federal Regulations', <http://www.ecfr.gov/>.
- van der Werf, G. R., Randerson, J. T., Giglio, L., Collatz, G. J., Mu, M., Kasibhatla, P. S., Morton, D. C., DeFries, R. S., Jin, Y., van Leeuwen, T. T. (2010), 'Global fire emissions and the contribution of deforestation, savanna, forest, agricultural, and peat fires (1997–2009)', *Atmospheric Chemistry and Physics* **10**(23), 11707–11735.
- van Groenigen, K. J., Osenberg, C. W., Hungate, B. A. (2011), 'Increased soil emissions of potent greenhouse gases under increased atmospheric CO<sub>2</sub>', *Nature* **475**(7355), 214–216.
- Veefkind, J., Aben, I., McMullan, K., Förster, H., de Vries, J., Otter, G., Claas, J., Eskes, H., de Haan, J., Kleipool, Q., others (2012), 'TROPOMI on the ESA Sentinel-5 Precursor: A GMES mission for global observations of the atmospheric composition for climate, air quality and ozone layer applications', *Remote Sensing of Environment* **120**, 70–83.
- Vermeulen, A., Eisma, R., Hensen, A., Slanina, J. (1999), 'Transport model calculations of nw-european methane emissions', *Environmental Science & Policy* **2**(3), 315–324.
- Vigano, I., Van Weelden, H., Holzinger, R., Keppler, F., Röckmann, T., others (2008), 'Effect of UV radiation and temperature on the emission of methane from plant biomass and structural components', *Biogeosciences Discussions* **5**(1), 243–270.
- Walter, K. M., Smith, L. C., Chapin, F. S. (2007), 'Methane bubbling from northern lakes: present and future contributions to the global methane budget', *Philosophical Transactions of the Royal Society A: Mathematical, Physical and Engineering Sciences* **365**(1856), 1657–1676.
- Webster, H., Carroll, E., Jones, A., Manning, A., Thomson, D. (2007), 'The Buncefield oil depot incident: a discussion of the meteorology', *Weather* **62**(12), 325–330.

- Webster, H., Thomson, D., Johnson, B., Heard, I., Turnbull, K., Marengo, F., Kristiansen, N., Dorsey, J., Minikin, A., Weinzierl, B., others (2012), ‘Operational prediction of ash concentrations in the distal volcanic cloud from the 2010 Eyjafjallajökull eruption’, *Journal of Geophysical Research: Atmospheres (1984–2012)* **117**(D20).
- Wecht, K. J., Jacob, D. J., Wofsy, S. C., Kort, E. A., Worden, J. R., Kulawik, S. S., Henze, D. K., Kopacz, M., Payne, V. H. (2012), ‘Validation of TES methane with HIPPO aircraft observations: implications for inverse modeling of methane sources’, *Atmospheric Chemistry and Physics* **12**(4), 1823–1832.
- Werf, G. v. d., Morton, D., DeFries, R., Giglio, L., Randerson, J., Collatz, G., Kasibhatla, P., others (2009), ‘Estimates of fire emissions from an active deforestation region in the southern Amazon based on satellite data and biogeochemical modelling.’, *Biogeosciences* **6**(2), 235–249.
- West, J., Fiore, A., Horowitz, L. (2012), ‘Scenarios of methane emission reductions to 2030: abatement costs and co-benefits to ozone air quality and human mortality’, *Climatic Change* **114**(3-4), 441–461.
- Whalen, S. (2005), ‘Biogeochemistry of methane exchange between natural wetlands and the atmosphere’, *Environmental Engineering Science* **22**(1), 73–94.
- Whiticar, M. J. (1999), ‘Carbon and hydrogen isotope systematics of bacterial formation and oxidation of methane’, *Chemical Geology* **161**(1), 291–314.
- WMO (2013), ‘Global Atmosphere Watch’, <http://www.wmo.int/gaw/>.
- Wofsy, S. C. (2011), ‘HIAPER Pole-to-Pole Observations (HIPPO): fine-grained, global-scale measurements of climatically important atmospheric gases and aerosols’, *Philosophical Transactions of the Royal Society A: Mathematical, Physical and Engineering Sciences* **369**(1943), 2073–2086.
- World Meteorological Organisation (2014), ‘Definition of oktas’, <http://worldweather.wmo.int/oktas.htm>.
- Wunch, D., Toon, G. C., Blavier, J.-F. L., Washenfelder, R. A., Notholt, J., Connor, B. J., Griffith, D. W. T., Sherlock, V., Wennberg, P. O. (2011), ‘The Total Carbon Column Observing Network’, *Philosophical Transactions of the Royal Society A: Mathematical, Physical and Engineering Sciences* **369**(1943), 2087–2112.
- Wunch, D., Toon, G. C., Wennberg, P. O., Wofsy, S. C., Stephens, B. B., Fischer, M. L., Uchino, O., Abshire, J. B., Bernath, P., Biraud, S. C., Blavier, J.-F. L., Boone, C.,

- Bowman, K. P., Browell, E. V., Campos, T., Connor, B. J., Daube, B. C., Deutscher, N. M., Diao, M., Elkins, J. W., Gerbig, C., Gottlieb, E., Griffith, D. W. T., Hurst, D. F., Jiménez, R., Keppel-Aleks, G., Kort, E. A., Macatangay, R., Machida, T., Matsueda, H., Moore, F., Morino, I., Park, S., Robinson, J., Roehl, C. M., Sawa, Y., Sherlock, V., Sweeney, C., Tanaka, T., Zondlo, M. A. (2010), ‘Calibration of the Total Carbon Column Observing Network using aircraft profile data’, *Atmospheric Measurement Techniques* **3**(5), 1351–1362.
- Xiong, X., Barnet, C., Maddy, E. S., Gambacorta, A., King, T. S., Wofsy, S. C. (2013), ‘Mid-upper tropospheric methane retrieval from IASI and its validation’, *Atmospheric Measurement Techniques* **6**(9), 2255–2265.
- Xiong, X., Barnet, C., Maddy, E., Sweeney, C., Liu, X., Zhou, L., Goldberg, M. (2008), ‘Characterization and validation of methane products from the Atmospheric Infrared Sounder (AIRS)’, *Journal of Geophysical Research: Biogeosciences* **113**(G3).
- Xiong, X., Barnet, C., Maddy, E., Wei, J., Liu, X., Pagano, T. S. (2010), ‘Seven Years Observation of Mid-Upper Tropospheric Methane from Atmospheric Infrared Sounder’, *Remote Sensing* **2**(11), 2509–2530.
- Yoshida, Y., Kikuchi, N., Morino, I., Uchino, O., Oshchepkov, S., Bril, A., Saeki, T., Schutgens, N., Toon, G. C., Wunch, D., Roehl, C. M., Wennberg, P. O., Griffith, D. W. T., Deutscher, N. M., Warneke, T., Notholt, J., Robinson, J., Sherlock, V., Connor, B., Rettinger, M., Sussmann, R., Ahonen, P., Heikkinen, P., Kyrö, E., Mendonca, J., Strong, K., Hase, F., Dohe, S., Yokota, T. (2013), ‘Improvement of the retrieval algorithm for GOSAT SWIR XCO<sub>2</sub> and XCH<sub>4</sub> and their validation using TCCON data’, *Atmospheric Measurement Techniques* **6**(6), 1533–1547.
- Zhao, C., Andrews, A. E., Bianco, L., Eluszkiewicz, J., Hirsch, A., MacDonald, C., Nehr Korn, T., Fischer, M. L. (2009), ‘Atmospheric inverse estimates of methane emissions from Central California’, *Journal of Geophysical Research: Atmospheres* **114**(D16).
- Zimmerman, P., Greenberg, J., Wandiga, S., Crutzen, P. (1982), ‘Termites: a potentially large source of atmospheric methane, carbon dioxide, and molecular hydrogen’, *Science* **218**(4572), 563–565.
- Zimov, S. A., Schuur, E. A., Chapin III, F. S. (2006), ‘Permafrost and the global carbon budget’, *Science(Washington)* **312**(5780), 1612–1613.